MOLECULES IN MEMBRANES: WHERE THEY ARE, WHAT THEY DO

EFFECTS OF VARIOUS MOLECULES ON THE STRUCTURE AND DYNAMICS OF LIPID MEMBRANES

By

LAURA TOPPOZINI, M.A.Sc., M.Sc., H.B.Sc.

A Thesis
Submitted to the School of Graduate Studies
in Partial Fulfillment of the Requirements
for the Degree
Doctor of Philosophy

McMaster University

DOCTOR OF PHILOSOPHY (2015)
(Physics)

McMaster University
Hamilton, Ontario

TITLE: Effects of Various Molecules on the Structure and Dynamics of Lipid Membranes

AUTHOR: Laura Toppozini, M.A.Sc., M.Sc., H.B.Sc.(McMaster University, McMaster University, Lakehead University)

SUPERVISOR: Dr. Maikel C. Rheinstädter

NUMBER OF PAGES: vi, 126

Abstract

In my time at the Laboratory of Membrane and Protein Dynamics at McMaster University it has been our goal to investigate the fundamental properties of model membranes and how some common membrane molecules, namely water, ethanol, and cholesterol, interact with the bilayer. Our studies employ highly-oriented, solid-supported membranes in order to extract unambiguous structural information perpendicular to and in the plane of the membranes, with the exception of the hydrated powder samples used in probing the effects on ethanol. Both X-ray and neutron scattering were employed to investigate the structural properties of the membranes and neutron scattering was used to infer the dynamical properties.

A variety of neutron scattering techniques were used to determine the properties of hydrated lipid bilayers, as described in the first two publications listed [1, 2]. Instruments including a neutron backscattering spectrometer, reflectometer, and time-of-flight spectrometer were used to observe bilayer structure, lipid/water coupling, and water diffusion. We found that hydrated, solid-supported single-bilayers showed no strong coupling between hydration water and lipid tails and the out-of-plane structure of stacked fluid bilayers as well as the anisotropic and anomalous behaviour of hydration water compared to bulk water.

Both X-ray and neutron scattering experiments were done to determine the effect of a 2mol% concentration of ethanol on a hydrated lipid powder [3]. X-ray scattering was used to determine the structural changes due to the addition of ethanol and the location of ethanol within the bilayer. This was accomplished by determining areas of increased electron density in the head group and among the acyl tails. The presence of ethanol also attributed to a decrease in lateral lipid diffusion constant in the gel phase, while no significant change was found in fluid bilayers.

In the final study outlined in this thesis, the result of a 32.5% concentration of cholesterol in a hydrated, fluid phospholipid membrane is discussed [4]. Coarse-grained molecular simulations and measurements of the lateral structure of the membrane via neutron spectrometry were able to determine the heterogeneous nature of the liquid-ordered phase and the structure of each of the domains in the membrane.

The following thesis will introduce model membranes, their relevant components and the scattering of X-rays and neutrons from such matter. Next, experimental techniques, sample constituents, sample preparations, and instruments used in experiments will be described. Then, each study will be introduced and discussed which will showcase the progress made in the field of model membranes. Lastly, an overview of the studies will lead in to future directions for each model system in terms of suggested experiments and general path.

Acknowledgements

I have had a great deal of support during the past four years which has been dedicated to the studies contained in this thesis and other fruitful projects, and for this tremendous support I would like to give thanks.

First, I would like to thank my supervisor Dr. Maikel C. Rheinstädter for always being there to help me think about the particular physics problem with which I was struggling. I would also like to thank you for all of your guidance and mentorship; your excitement for science is infectious and I was lucky enough to have shared in this excitement.

I would also like to thank past and present students that I have had the pleasure of working with, learning from, and occasionally having super fun times with: Clare, Matt, Fei-Chi, and Rick. As for collaborators, I would like to thank a few that were an extraordinary pleasure to work with and always kept me motivated throughout the projects: Dr. David Deamer, Dr. Vicky García Sakai, Dr. Felix Roosen-Runge. All of the instrument scientists that I have ever had the pleasure of working with also deserve a big thank you for all their dedication, expertise and help: Norbert Kučerka, Zahra Yamani, Antonio Faraone, Michihiro Nagao, Robert Bewley, Robert Dalgliesh, and Madhusudan Tyagi.

Finally, I would like acknowledge all of the support from my family and friends over the years. I would like to thank my sisters and brothers Lisa, Kimberly, Johnny, and Will and my parents Barbara and John for helping to shape me as a person and giving me support over the years. Next, I would like to thank Chad for always being there for me and helping me keep everything in perspective. To my friends Clare, Phil, Paul, Mark, Brit, Jia jia and Kieran, thank you for what you do best, being amazing friends.

Contents

1 Preface **1**

1.1 Scientific Contributions 2

1.2 Thesis Overview 5

2 Introduction **7**

2.1 Model Membrane Components 7

2.1.1 Lipids 7

2.1.2 Cholesterol 10

2.1.3 Ethanol 13

2.2 Model Membrane Systems 14

2.3 Scattering Theory of X-rays and Neutrons 20

3 Experimental Considerations **29**

3.1 Sample Preparation 29

3.1.1 Materials 29

3.1.2 Preparation Protocol of Single, Solid-Supported Bilayers 31

3.1.3 Preparation of Multi-Lamellar, Highly-Oriented Bilayers with Non-Polar Solvents 32

3.1.4 Preparation of a Hydrated Powder of Lipids 34

3.2 X-ray Instrumentation 35

3.2.1 X-Ray Diffractometer: BLADE at McMaster University 35

3.3 Neutron Instrumentation 38

3.3.1 Neutron Reflectometer: OFFSPEC at ISIS 38

3.3.2 Triple-Axis Spectrometer: N5 at Canadian Neutron Beam Center 39

3.3.3 Backscattering spectrometer: HFBS at NIST 41

3.3.4 Time-of-Flight Spectrometer: Low Energy Transfer at ISIS 44

4 Properties of Hydration Water in Fluid Lipid Membranes: Publications I & II 49
4.1 Introduction 49
4.2 Preface to Publication I: "*Hydration Water Freezing in Single Supported Lipid Bilayers*" 50
4.3 Preface to Publication II: "*Anomalous and Anisotropic Nanoscale Diffusion of Hydration Water in Fluid Lipid Membranes*" 59

5 The Location and Effect of Ethanol in Single-Component Lipid Bilayers: Publication III 79
5.1 Preface 79

6 The Structure of Cholesterol in Lipid Rafts: Publication IV 93
6.1 Preface 93

7 Conclusions & Outlook 101
7.1 Conclusions 101

A Supplementary Information of Publications 105
A.1 Supplementary Material for "*Structure of Cholesterol in Lipid Rafts*" 105

B Copyright Information for Publications 115
B.1 ISRN Publication 115
B.2 Soft Matter Publications 115
B.3 Physical Review Letters Publication 115

Chapter 1

Preface

Biological membranes are a ubiquitous feature of living things, they can occur as an external envelope like the plasma membrane or envelopes for organelle interior to cells, such as the nucleus or mitochondria. Membranes provide a barrier for the interior components from the exterior, being selective in molecules that pass through it. Cell membranes are of particular interest as they are the envelope that protects cell contents and are implicated in a variety of specific and non-specific interactions. In biological membranes, molecules commonly interact with the membrane through specific interactions driven by chemical interactions, for instance a molecule binding to a receptor. However, many molecules interact with the membrane via physical interactions, and such as hydrogen bonding and hydrophobic interactions, such non-specific interactions will be covered in this thesis.

Our experimental model system is a simple construction of a membrane that captures the relevant attributes from biological membranes. We regard the lack of detail in our models as a strength, allowing us to have insight into the fundamental mechanisms and properties that drive a studied interaction. Model membranes, such as the ones addressed in this thesis, are two-dimensional, viscous fluids consisting of at most two components. A well-used model for the study of biological membranes is the fluid-mosaic membrane model, outlined by Singer and Nicolson [5]. Since its inception in 1972, some slight modifications have been made to the model [6, 7, 8] to include structural elements like lipid rafts [7], however the general model still holds. Essentially, the model states that a lipid bilayer forms a long-range mosaic where lipids and proteins float freely amongst each other. Our model membranes focus on the viscous fluid lipid matrix and interactions with this matrix as our subject of study.

A main advantage to probing solid-supported model membranes with X-ray and neutron scattering is that we are able to unambiguously measure the scattering parallel and perpendicular to the membranes. This allows us to determine the relative positions of membrane components out of the plane of the membrane. By adding molecules that interact with the membranes, we can infer their effect on the membranes by observing the changes in structural information to gain a better understanding of this interaction. We investigated the structure and dynamics of hydration water in

bilayers, ethanol's effect on the structure and dynamics of lipid bilayers, and structure of cholesterol lipid rafts in bilayers.

Our investigations of hydration water in single and stacked bilayers measure the change in elastic neutron scattering to show that hydration water dynamics are not strongly coupled to the dynamics of the membrane lipids and using a state-of-the-art time-of-flight instrument, for the first time we measure a two-dimensional mapping of the hydration water that is both anomalous and anisotropic. By combining molecular dynamics and Brownian dynamics simulations, the microscopic origins for the anomalous and anisotropic behaviours of hydration water were investigated. Brownian dynamics have previously been used to analyse quasi-elastic neutron data, to model the diffusive motions in model membrane systems. However, by using large two-dimensional detectors we were able to gain a larger picture of the system and determine its non-Brownian characteristics.

Alcohol (ethanol, ethyl alcohol) is a commonly used substance around the world and many studies have attempted to observe its effect on membranes. Our investigation of the ethanol's effect on single component lipid bilayer found the location and quantity of ethanol molecules accumulated amongst the head groups of a single-species phospholipid membrane for a 2mol% ethanol solution. We were also able to confirm that ethanol increases the permeability of the membranes, as we were able to use X-ray diffraction measurements to observe increased electron density in the bilayer core. We also used neutron scattering to observe the decrease in diffusion of lipids in the gel phase with the addition of ethanol.

High cholesterol concentrations in phospholipid bilayers were investigated using a new neutron scattering technique pioneered by recent experiments performed by the Laboratory for Membrane and Protein Dynamics [9, 10], using a triple-axis spectrometer to determine that the cholesterol/phospholipid liquid-ordered phase (l_o) is not a homogeneous phase, but a heterogeneous phase that forms domains with three distinct structures. These findings are important for further investigations of the mechanism of formation of biological lipid rafts and their properties.

These works detailed in this thesis contribute significantly to the knowledge base of fundamental properties of model membranes: the characteristics of the water hydrating these membranes, the membrane's interaction with ethanol, and the response to the addition of membrane cholesterol, a major component in biological membranes.

1.1 Scientific Contributions

First Author Publications

- **Toppozini, L.**, Roosen-Runge, F., Bewley, R., Dalgliesh, R., Glyde, H.R., Perring, T., García Sakai, V., Rheinstädter, M.C. *Anomalous and Anisotropic Nanoscale Diffusion of Hydration Water in Fluid Lipid Membranes.* Soft Matter, DOI: 10.1039/C5SM01713K

- **Toppozini, L.**, Meinhardt, S., Armstrong, C.L., Yamani, Z., Kučerka, N., Schmid, F., Rhe-

instädter, M.C. *Structure of Cholesterol in Lipid Rafts.* Physical Review Letters 2014, 113, 228101

- **Toppozini, L.**, García Sakai, V., Bewley,R., Dalgliesh, R., Perring, T., Rheinstädter, M.C. *Lateral and Transmembrane Diffusion in Membranes: Towards a Two-Dimensional Diffusion Map.* EPJ Web of Conferences, 83, 02019 (2015)
- **Toppozini, L.**, Dies, H., Deamer, D., Rheinstädter, M.C. *Adenosine monophosphate forms ordered arrays in multilamellar lipid matrices: Insights into assembly of nucleic acid for primitive life.* PLOS ONE 8(5): e62810 (2013)
- Poinapen, D.*, **Toppozini, L.***, Dies, H., Brown, D., Rheinstädter, M.C. *Static Magnetic Fields Enhance Lipid Order in Native Plant Plasma Membrane.* Soft Matter, 2013, 9, 6804-6813 (* co-first author)
- **Toppozini, L.**, Armstrong, C.L., Barrett, M.A., Zheng, S., Luo, L., Nanda, H., García Sakai, V., Rheinstädter, M.C. *Partitioning of ethanol into lipid membranes and its effect on fluidity and permeability as seen by X-ray and neutron scattering.* Soft Matter, 2012, 8, 11839-11849
- **Toppozini, L.**, Armstrong, C.L., Tyagi, M., Jenkins, T., Rheinstädter, M.C. *Hydration water freezing transition in single supported lipid bilayers.* ISRN Biophysics, 2012, Article ID 520307

Other Publications

- Alsop, R.J., Armstrong, C.L., Maqbool, A., **Toppozini, L.**, Rheinstädter,M.C. *Cholesterol Expels Ibuprofen from the Hydrophobic Membrane Core and Stabilizes Lamellar Phases in Lipid Membranes Containing Ibuprofen.* Soft Matter, 2015, 11 (24), 4756-4767
- Alsop, R., **Toppozini, L.**, Marquardt, A., Kučerka, N., Harroun, T., Rheinstädter, M.C. *Aspirin Inhibits Formation of Cholesterol Rafts in Fluid Lipid Membranes.* Biochimica et Biophysica Acta 1848 (2015) 805812
- Rheinstädter, M.C., Dies, H., **Toppozini, L.** *The Interaction of Bio-Molecules with Lipid Membranes Studied by X-ray Diffraction.* Zeitschrift für Physikalische Chemie, 228:11051120 (2014)
- Dies, H., **Toppozini, L.**, Rheinstädter, M.C. *The Interaction Between Amyloid-β Peptides and Anionic Lipid Membranes Containing Cholesterol and Melatonin.* PLoS ONE 9(6):e99124 (2014)
- Barrett, M.A., Zheng, S., **Toppozini, L.**, Alsop, R.J., Dies, H., Wang, A., Jago, N., Moore, M., Rheinstädter, M.C. *Solubility of Cholesterol in Lipid Membranes and the Formation of Immiscible Cholesterol Plaques at High Cholesterol Concentrations.* Soft Matter, 2013, 9(39), 9342-9351

- Armstrong, C.L., Barrett, M., **Toppozini, L.**, Kučerka, N., Yamani, Z., Katsaras, J., Fragneto, G., Rheinstädter, M. C. *Co-existence of Gel and Fluid Lipid Domains in Single-component Phospholipid Membranes.* Soft Matter, 2012, 8, 4687-4694

- Pedri, L.J., **Toppozini, L.**, Gallagher, M.C. *Au-induced nanofaceting and the stoichiometry of the Si(775)-Au surface.* Surface Science 2007, 601, 924-930

Contributed Talks

- **Toppozini, L.**, Armstrong, C., Meinhardt, S., Kučerka, N., Schmid, F., Rheinstädter, M.C. *Cholesterol Structure in Lipid Rafts.* Canadian Association of Physicists Congress, Sudbury, Ontario, 06/2014

- **Toppozini, L.**, Bewley,R, García Sakai, V., Rheinstädter, M.C. *Two-Dimensional Diffusion of Water in Lipid Membranes. American Conference on Neutron Scattering*, Knoxville, Tennessee, 05/2014

- **Toppozini, L.**, Armstrong, C., Meinhardt, S., Kučerka, N., Schmid, F., Rheinstädter, M.C. *Cholesterol Structure in Lipid Rafts.* Chemical Biophysics Symposium, Toronto, Ontario, 05/2014

- **Toppozini, L.**, Armstrong, C., Kučerka, N., Rheinstädter, M.C. *Membranes:From model to biological.* Canadian Institute for Neutron Scattering Annual General Meeting, Hamilton, Ontario, 10/2013

- **Toppozini, L.**, Deamer, D., Rheinstädter, M.C. *Nucleotide Confinement by Lipid Membranes.* International Conference on Applied Mathematics, Modeling and Computational Science, Waterloo, Ontario, 08/2013

Poster Presentations

- **Toppozini, L.**, Roosen-Runge, F., Bewley, R., Dalgliesh, R., Perring, T., Seydel, T., Glyde, H.R., García Sakai, V., Rheinstädter, M.C. *Anomalous and Anisotropic Nanoscale Diffusion of Hydration Water Molecules in Fluid Lipid Membranes.* European Biophysical Societies' Association, Dresden, Germany, 07/2015

- **Toppozini, L.**, Roosen-Runge, F., Glyde, H.R.,García Sakai, V.,Seydel, T., Bewley, R., Dalgliesh, R.,Rheinstädter, M.C. *A Two-Dimensional Diffusion Map of Membrane Hydration Water.* Chemical Biophysics Symposium. Toronto, Ontario, 04/2015

- **Toppozini, L.**, Bewley, R., García Sakai, V., Rheinstädter, M.C. *Lateral and transmembrane diffusion: A 2D membrane diffusion map.* QENS2014/WINS2014, Autrans, France, 05/2014
- **Toppozini, L.**, Armstrong, C., Meinhardt, S., Kučerka, N., Schmid, F., Rheinstädter, M.C. *Cholesterol Structure in Lipid Rafts.* Neutrons in Biology and Biotechnology, Grenoble, France, 02/2014
- **Toppozini, L.**, Deamer, D., Rheinstädter, M.C. *From Nucleotides to RNA: Searching for the Origins of Life.* Chemical Biophysics Symposium. Toronto, Ontario, 04/2013
- **Toppozini, L.**, Armstrong, C.L., Barrett, M.A., Zheng, S., Luo, L., Nanda, H., García Sakai, V., Rheinstädter, M.C. *Interaction and partitioning of ethanol with lipid membranes as seen by X-ray and neutron scattering.* American Conference on Neutron Scattering (ACNS), Washington, D.C., 06/2012
- **Toppozini, L.**, Deamer, D., Rheinstädter, M.C. *Making RNA: Searching for the origins of life.* Chemical Biophysics Symposium. Toronto, Ontario, 03/2012

1.2 Thesis Overview

Contained within this thesis is a description of a subset of the work done to characterize phospholipid model membranes and how these membranes change by the addition of select molecules. These works, executed by myself and collaborators, aim to bring about a more complete understanding of the commonly used model membrane system and how interactions with common molecules affect its characteristics.

Chapter 2 is an introduction to the membrane components, model membranes employed in our experiments and common techniques that are used to characterize model membranes. A survey of lipids found in biological membranes will be presented with an emphasis on lipids used in our experiments as well as ethanol and cholesterol molecules and their biological relevance. including nuclear magnetic resonance spectroscopy, fluorescence spectroscopy, and simulations. By presenting a survey of membrane models and techniques with which to measure them, we aim to highlight advances made through our experiments. Finally, scattering theory of X-rays and neutrons and their interactions with matter will be covered.

Next, Chapter 3 will guide the reader through the different components used in the experiments in this thesis. Materials used, sample preparation and experiments, and sample preparation techniques for each of the different types of samples will be discussed. General descriptions of the X-ray diffractometer and neutron instruments used in these experiments will be followed by more specific details of the settings and configurations of the particular instruments used.

Chapters 4, 5, and 6 will outline four projects that have been completed in my time as a Ph.D. student at McMaster University. The publications are divided into three chapters. First, hydrated membranes and the properties of their hydration water is the subject of Chapter 4, which introduces the coupling of dynamics in a solid-supported single-bilayer system in the publication

"*Hydration Water Freezing in Single Supported Lipid Bilayers*" and the two-dimensional diffusion dynamics of the hydration water of solid-supported, stacked bilayers in the submission "*Anomalous and Anisotropic Nanoscale Diffusion of Hydration Water in Fluid Lipid Membranes*". Chapter 5 introduces the effect of the ubiquitous molecule ethanol on model membranes in both the gel and fluid phases found by the structural and dynamical changes of the membrane in the publication "*Partitioning of ethanol into lipid membranes and its effect on fluidity and permeability as seen by X-ray and neutron scattering*".

Cholesterol's effect on solid-supported, fluid, stacked lipid bilayers is described in Chapter 6 in the context of a binary lipid membrane. The structure of the domains found within the cholesterol/lipid membrane is informed by coarse-grained molecular dynamics simulations and neutron spectroscopy, which are in excellent agreement. The findings of the simulations and experiment are discussed in the publication "*The Structure of Cholesterol in Lipid Rafts*".

Lastly, Chapter 7 will outline the main findings of these publications and an outlook will then be offered on the directions of future research given the advances made here and the climate of research in this field.

Chapter 2

Introduction

2.1 Model Membrane Components

2.1.1 Lipids

Lipids are the primary constituents of biological membranes and their amphiphilic nature gives rise to the bilayer structure of membranes. In general, the anatomy of a lipid consists of a hydrophilic head group and a hydrophobic tail region. In aqueous solutions, lipids will naturally form vesicles or micelles in order for the acyl chains to be shielded from the aqueous solution. Biological membranes are complex, containing a wealth of species of proteins, carbohydrates, and lipids.

Membrane lipids come in three basic classifications: sphingolipids, sterols, and glycerophospholipids (or simply phospholipids). Sphingolipids are a class of structural lipid which have a hydrophobic ceramide backbone and their tails are typically saturated. Sterols, the major non-polar lipid of membranes, have a small hydrophobic head group, a rigid four-ring sterol backbone, and a terminal group such as cholesterol's hydrocarbon tail. Glycerophospholipids or phospholipids are the major structural lipids in eukaryotic membranes [12]; this type of lipid is classified by its glycerol group bound to a phosphate group.

The variation in glycerophospholipid species is determined by additional group bound to the phosphate group. Phosphatidylcholine (PC) lipids have a choline (C_5H_14NO) attached to the phosphate, ethanolamine (C_2H_7NO) is bound to the phosphate in phosphatidylethanolamine (PE) lipids, a serine group (C_3H_7NO3) is bound in phosphatidylserine (PS), phosphatidylinositol (PI) lipids have inotsitol ($C_6H_12O_6$), and phosphatidic acid (PA) is the name for the acid forms of the above lipids [12]. The cylindrical geometry (i.e., the area of the head group is similar to that of the tails) of the phosphatidylcholine lipids means that they self-assemble into planar bilayers which is advantageous for making a solid-supported stacked bilayer system.

Though biological membranes have such a variety of different lipid species, the experiments covered in this thesis are only concerned with a single group of glycerophospholipids, phosphatidylcholines due to their biological prevalence and experimental advantages. We use PC lipids as they

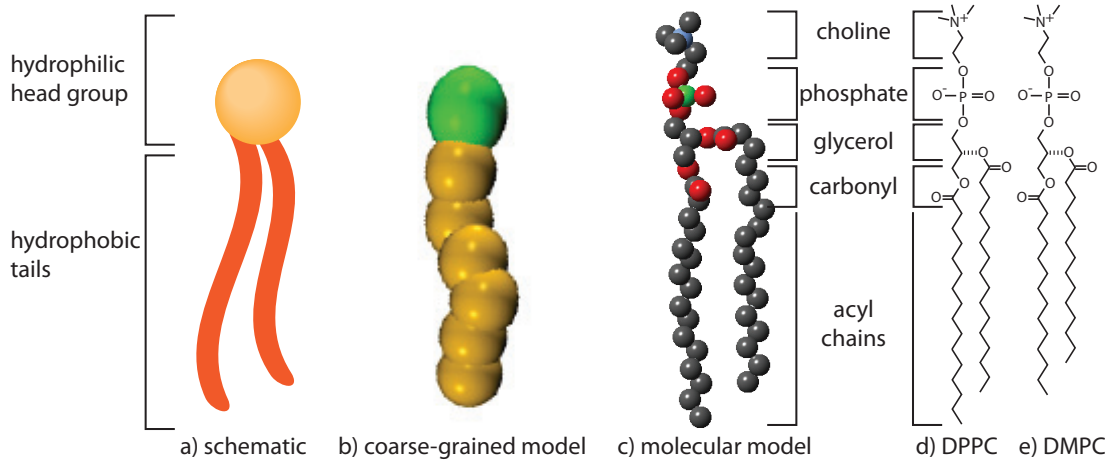

Figure 2.1: Various representations of phospholipids. (a) Schematic of a lipid highlighting the hydrophilic head group and hydrophobic tails. (b) Coarse-grained model of a DPPC molecule. A hydrophilic bead acts as the head group and 6 hydrophobic beads act as the hydrophobic acyl chains. Image from Toppozini *et al.* [4]. (c) Molecular model of DPPC: carbon atoms (gray), nitrogen (green), phosphorus (blue) oxygen (red), hydrogen (not shown). DPPC molecule taken from Wennberg *et al.* [11] and rendered in CrystalMaker software. (d) Chemical structure drawing of DPPC (16-carbon acyl chains). (e) Chemical structure drawing of DMPC (14-carbon acyl chains).

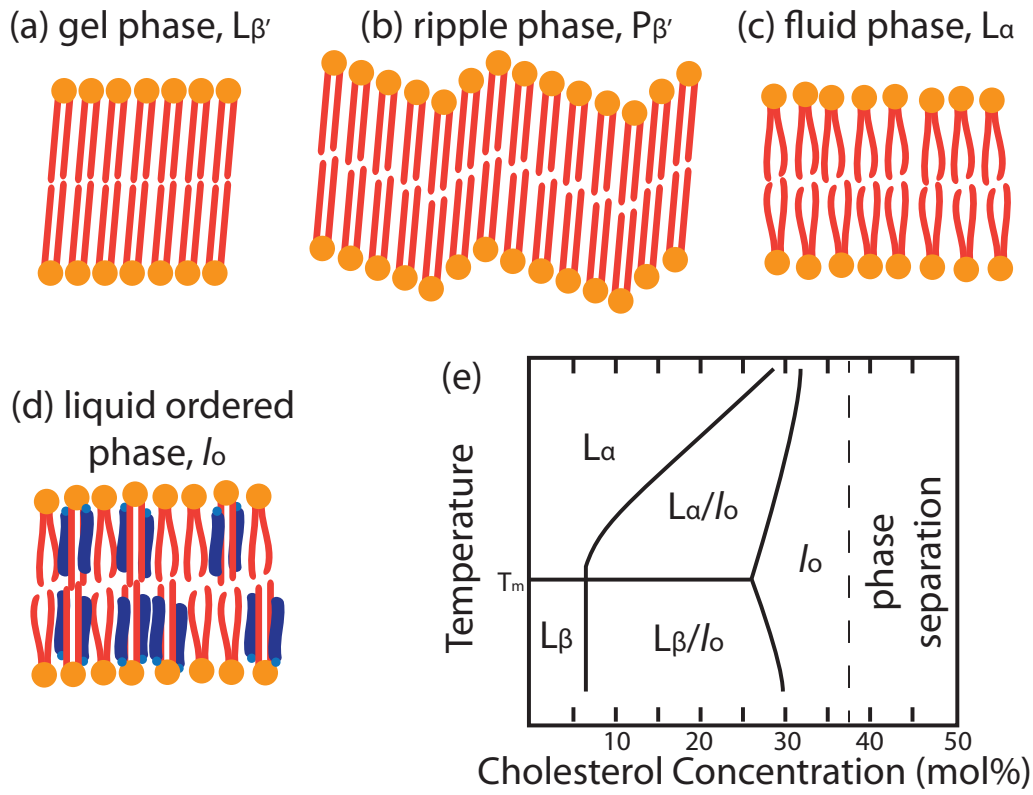

Figure 2.2: Main transitions of phospholipid bilayer systems. (a) The solid-ordered (gel) phase, $L_{\beta'}$. (b) The ripple phase (pre-transition) $P_{\beta'}$. (c) Fluid, or liquid-disordered phase, L_{α}. (d) Liquid-ordered phase, l_o. This phase only occurs for lipid-cholesterol mixtures. (e) Phase diagram of phospholipid phases as a function of temperature and molar cholesterol concentration. This diagram was modified from Armstrong *et. al* [10]

account for more than 50% of most eukaryotic membrane phospholipids [12]. The experiments outlined in the works of this thesis contain two types of the phosphatidylcholine class of lipids, specifically, DMPC (1,2-dimyristoyl-sn-glycero-3-phosphocholine) and DPPC (1,2-dipalmitoyl-sn-glycero-3-phosphocholine). These lipids have identical PC head group consisting of a choline bound to a phosphate bound to the third hydroxyl group of a glycerol. The two remaining glycerol hydroxyl groups are connected to saturated fatty acid chains by a carbonyl. The difference between DMPC and DPPC is the length of the fatty acid chains are 14-carbons and 16-carbons long as can be see in Figure 2.1 (c) and (d).

Bilayer structures, such as planar bilayers or vesicles, are readily formed by phosphatidylcholine lipids, giving rise to our model membrane system. The amphipathic nature of the lipids drives the aggregation of the acyl tails such that the head groups are in contact with the aqueous solution while

their cylindrical geometry drives bilayer formation, i.e., as opposed to micelles, for instance [13].

The most biologically relevant phase is the fluid phase, also referred to as the liquid-disordered , liquid crystalline, or simply the L_α phase. Lipid phases are commonly referred to by two labels: (1) the positional degree of freedom, solid or liquid, and (2) the conformation of the acyl tails, ordered or disordered [13]. In the L_α phase (liquid-disordered), the lipids can be thought of as a viscous, two-dimensional liquid with disordered acyl chains. X-ray and neutron scattering measurements have been used to characterize hydrated, fluid phospholipid bilayers; the area per lipid of DMPC in a bilayer is ~ 60.5 Å^2 [14] and the DPPC area per lipid is ~ 63.0Å^2 [15]. The main transition temperature, T_m, is 23°C for DMPC and 41.5°C for DPPC [16]. The liquid-disordered phase can be arrived at through the main transition (gel-to-fluid). The gel phase $L_{\beta'}$, which is also referred to as the solid-ordered phase (S_o), corresponds to a smaller area per lipid due to fully-stretched, all-trans configuration of the acyl tails. The solid-ordered phase is further defined by L_β, which denotes the case where the acyl chains are parallel to the bilayer normal and $L_{\beta'}$, which denotes acyl chains at an angle to the bilayer normal [17]. The tilt angle for the gel phase is dependent on hydration, the higher the level of hydration the higher the tilt angle, i.e., the bilayer spacing in the gel phase decreases with increasing hydration [18, 19]. The ripple phase, $P_{\beta'}$ occurs between the gel and fluid phases, just below the main transition [18, 19]. The reason for its name is the one-dimensional height-modulation in a sawtooth or rippled pattern, this phase is observed to occur in highly hydrated membranes [18, 19, 20]. For DMPC and DPPC the ripple phase occurs at 14°C for DMPC and 35°C for DPPC [16].

In the case of a mixture of cholesterol and phosphatidylcholine lipids, a unique, new phase is introduced: the liquid-ordered phase, l_o [21, 22]. Similar to the solid-ordered phase in single-species lipid bilayers, the acyl tails are restricted by the cholesterol's planar sterol group, the acyl chains become extended. However, the positional degree of freedom is that of a liquid. This is due to cholesterol's condensing effect also referred to as the umbrella model [23]. At low cholesterol concentrations the phase turns into the liquid-disordered phase [21, 22]. The liquid-ordered phase will be discussed in detail in Section 2.1.2.

2.1.2 Cholesterol

Sterols are common in all biological membranes, generally possessing a hydroxyl (OH) group connected to four planar rings, and finally a hydrocarbon chain. Cholesterol is an amphipathic molecule whose structure is shown in Figure 2.3 (c) and (d) and varies considerably from that of the lipids described above. This molecule has a hydroxyl group that acts as a small hydrophilic head group and a hydrophobic four-ringed sterol group with a hydrocarbon chain.

There are a variety of sterols present in animal membranes; however, cholesterol is the most abundant of this class of lipids [13]. Interestingly, the molecular evolution of sterols has been implicated in the evolution of species [13]. And though this is a clear indicator that sterols are important for life, cholesterol specifically has a bad reputation in society as it is linked to common fatalities like heart disease and atherosclerosis. Cholesterol is notably abundant in the plasma membrane of

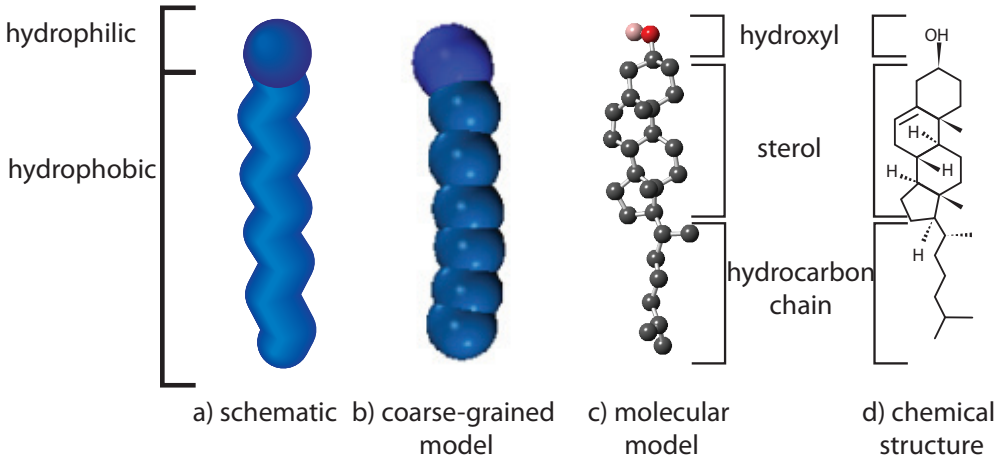

Figure 2.3: Representations of cholesterol. Hydrophilic and hydrophobic regions labelled along with hydroxyl, sterol and hydrocarbon groups. a) Schematic representation of cholesterol. b) Cholesterol represented by seven beads in the coarse-grained simulations. Image from Toppozini *et al.* [4]. c) Molecular model of cholesterol. Cholesterol molecule taken from Wennberg *et al.* [11] and rendered in CrystalMaker software. carbon atoms (gray), oxygen (red), hydrogen (off-white). d) Chemical structure of cholesterol molecule.

mammalian cells where the plasma membrane contains roughly 30%-50%, while organelles in the cell have very low cholesterol content [13].

Introducing cholesterol into lipid bilayers changes the phase diagram of the bilayer. As the cholesterol concentration is increased above $\sim$ 30%, the main transition of the bilayer disappears in lieu of another phase, the liquid-ordered phase, l_o. Cholesterol molecules add structural rigidity to lipid bilayers and have the ability to stabilize lipid bilayers. The liquid-ordered phase is unique to the phase diagram of lipid/cholesterol mixtures. Marsh provides a compendium of experimental and simulated phospholipid/cholesterol phase diagrams [24], Figure 2.2 (e) shows a phase diagram for phospholipid/cholesterol as a function of cholesterol concentration and temperature [10, 24]. At low cholesterol concentration, the lipids act as if no cholesterol is present, i.e., gel phase below T_m and fluid phase above. However, at the mid-range concentrations, less than around 30%, coexistence of the gel and fluid phases with the liquid-ordered phases occurs i.e., $L_{\beta'}+l_o$ and $L_\alpha+l_o$, below and above the T_m, respectively. The position of the main transition is lower in lipid/cholesterol mixtures than simple lipid bilayers.

Beyond this intermediate concentration only the liquid-ordered phase exists for all temperatures until phase separation occurs near 40% cholesterol. Marsh has compiled many phase diagrams from ^{2}H nuclear magnetic resonance(NMR), electron paramagnetic resonance (EPR) spectroscopy, and differential scanning calorimetry (DSC); however, our assessment of the phase for DPPC bilayer with 32.5% cholesterol at 50°C was accomplished using neutron diffraction [4]. Fluorescence microscopy methods have not been successful in observing nanoscale phase separations or raft structures in

binary mixtures (e.g., DPPC/cholesterol) [25]; however, μm-scale phase-separated fluid domains have been observed by fluorescence microscopy in ternary mixtures [26, 25, 27]. Recent work by Meinhardt *et al.* and Toppozini *et al.* have shown existence of nanoscopic and short-lived heterogeneities in the liquid-ordered phase of a binary mixture of DPPC/cholesterol [28, 4]. Thus the liquid ordered phase was observed to be heterogeneous, as had been inferred from ^{2}H NMR spectroscopy studies previously [21], and have three distinct structures using neutron spectroscopy [4].

The condensation effect of cholesterol in lipid membranes is widely known; however, there are some models that describe this effect and how it pertains to various lipids. The condensation effect refers to the stiffening of the lipid acyl chain as a result of interaction with cholesterol above the main transition. This leads to increased order of the tails while the lipids should be in the fluid phase [29, 30]. It should be noted that there is also a fluidizing effect of lipids below the main transition due to their interaction with cholesterol; however, this pertains to the less biologically relevant low temperature range [29, 30]. The order of the lipid tails have increased mobility which the reason for the disappearance of the main transition in cholesterol/lipid mixtures at high cholesterol concentration [29].

Sankaram and Thompson suggested that at low cholesterol concentrations, cholesterol sits in the center of the bilayer, parallel to the lipids [31]. At high cholesterol concentrations, they suggested that cholesterols and lipids coexist in the same configuration as the lipid bilayer; that is, lipids are replaced by cholesterol molecules [31]. However, this organization does not account for the condensation effect. These experiments found evidence for cholesterol's hydroxyl hydrogen-bonding to the lipid's second glycerol-carbonyl bond. This was also suggested by simulations where cholesterol/lipid heterodimers are formed through this interaction [32].

The superlattice model described by Somerharju *et al.* has also been suggested as a configuration of cholesterol/lipid systems wherein lipids tend to adopt a regular lateral organisation rather than a random distributions [33, 34]. A superlattice occurs only for allowed concentrations that are conducive to lattice formations e.g., the number of lipids will be an integer multiple of the cholesterols [33, 34]. It is also suggested that superlattices are in dynamic equilibrium with other superlattices, and randomly distributed cholesterols [33, 34]. These superlattice structures are suggested to form due to a variety of factors such as charge-charge repulsion, steric strain, and the hydrophobic effect [33, 34]. A particular Monte Carlo simulation study by Huang attempted to show that the superlattice model is not a viable model due to some opposing interactions such as the favourable cholesterol/lipid interaction and the unfavorable lipid chain interaction that is proportional to the number of cholesterol contacts [35]. This study also attempted to show that the umbrella model, a competing model for cholesterol/lipid mixtures, was more likely [35].

The umbrella model, coined by Huang and Feigenson, was observed by Monte Carlo simulations informed by solubility limits measured by X-ray diffraction [23]. This model suggests cholesterol is incorporated into the bilayer where the phospholipid head groups shield the hydrophobic sterol rings from exposure to water [23]. The driving mechanism for this arrangement is the exposure of cholesterol's non-polar sterol group to the lipid/water interface, which would yield an unfavourable

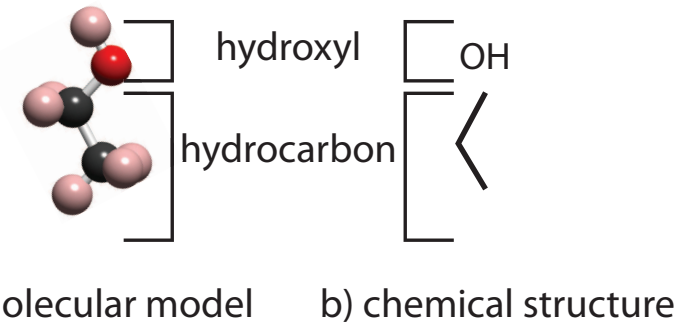

Figure 2.4: Representations of ethanol. Hydroxyl and hydrocarbon regions are labelled. a) Molecular model of ethanol. Carbon atoms (gray), oxygen (red), hydrogen (off-white). b) Chemical structure drawing of ethanol.

gain in the free energy [23]. Under this phosphatidylcholine umbrella two cholesterol molecules can be accommodated which causes the acyl chains to stiffen and elongate, and neither the cholesterol nor the tails are exposed to water [23]. In our neutron diffraction study probing the lateral organisation of cholesterol in DPPC bilayers containing 32.5% cholesterol, we found the cholesterol structure was compatible with the umbrella model, which is discussed in more detail in Chapter 6.

2.1.3 Ethanol

Ethanol and its interaction with cells can take on many different roles: drug, drug enhancer, anaesthetic, and antiseptic. Whether ethanol is taken orally, traveling to your intestines and absorbed into the blood stream, or applied to the skin, there are many membrane barriers with which ethanol has the opportunity to interact. Ethanol is a small amphiphilic molecule with a hydroxyl at one end and a methyl group at the other (as shown in Figure 2.4), which is the reason for its affinity to the hydrophobic-hydrophilic interface of lipid membranes [36, 37, 3]. Ethanol's hydroxyl group prefers a water environment which causes it to avoid entry into the hydrophobic core of the bilayer, though other alcohol with longer hydrophobic chains insert more readily into the hydrophobic core with their hydrophobic chains aligned parallel to the lipid hydrocarbon chains [38].

Some pioneering publications interactions between ethanol and membranes have relied on MD simulations such as those performed by Chanda and Bandyopadhyay [39], and Terama *et al.* NMR experiments [36, 37]. In these studies ethanol has been shown to lower the main transition temperature of a lipid membrane [36, 37], it makes the membrane more disordered, increasing fluidity, and ethanol has also been implicated in an increase in membrane permeability [38].

X-ray and neutron scattering can be used as a method to probe the molecular interactions introduced by ethanol; however these methods are faced with experimental challenges particularly due to the volatility of ethanol when hydrating from the vapour phase. In our combined X-ray and neutron scattering study, which determined the partitioning of ethanol, both experiments used a lipid powder hydrated with ethanol/water such that the amount of ethanol in contact with the

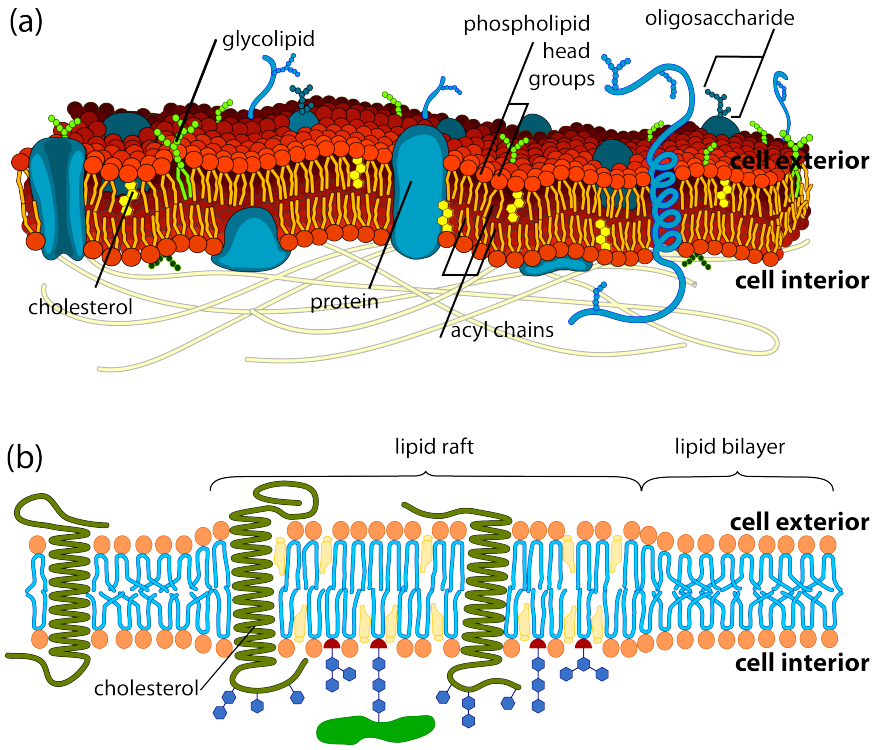

Figure 2.5: (a) Schematic of a fluid bilayer consisting of lipids, proteins, carbohydrates and cholesterol. This figure has been modified from a public domain figure [40]. (b) Schematic of a lipid raft surrounded by a fluid lipid bilayer. This figure has been modified from a public domain figure [41].

membranes was known [3]. It was in this way that our systems were consistent with each other.

2.2 Model Membrane Systems

Cell membranes are integral components of all living organisms; however, biological systems such as native cell membranes are complex with a variety of components. A single-component fluid bilayer is an approximation to the ubiquitous biological cell membrane. Do not let its simplicity fool you, many quantities have been measured in these model systems that elucidate fundamental properties and interactions that can be extended to their complex counterparts. Here, a survey of many properties of model membranes and the various techniques with which they can be measured are presented.

For over four decades the fluid mosaic model has been used to justify the use of our simple model systems. In the fluid mosaic model, membrane proteins float passively in a two-dimensional sea of lipids, as shown in Figure 2.5 a), where the lipids act as the membrane matrix; however structures within the membrane are not addressed [5]. The issue with a passive fluid membrane is that the biological membranes have important functions that are not simply driven by random

fluctuations. Rafts [7, 42, 43] are the proposed provide a mechanism for this functionality, though this phenomenon has yet to be observed directly in cell membranes. Lipid rafts were first conceptualized in the plasma membranes epithelial cells where, through detergent extraction, insoluble complexes were observed [7]. We used a binary mixture of lipids to observe lipid raft structures using neutron scattering and simulations; this is discussed in Chapter 6. A schematic of a lipid raft is shown in Figure 2.5 b).

In this thesis X-ray and neutron scattering are used to probe model membranes prepared with a single phospholipid species and the effects of water, ethanol, and cholesterol are assessed. Many different techniques have been and are currently used to probe model membranes. Below is a brief summary of the findings from techniques that have also made important contributions to the field of model membranes, namely nuclear magnetic resonance, fluorescence microscopy, and simulations.

Nuclear magnetic resonance: Nuclear magnetic resonance spectroscopy exploits the magnetic properties of an atom to observe the local environments of an atomic species. A particular atom in an experimental system is surrounded by a magnetic field that is indicative of the surrounding atoms and changes the resonance frequency, thus giving access to details of the electronic structure of a molecule. The system under investigation is subject to a fixed magnetic field and a sinusoidally varying field giving rise to two time constants, τ_1 and τ_2 [44]. These time constants are the characteristic time for relaxation of the spin components in the plane parallel and perpendicular to the static magnetic field, respectively. τ_1 is the relaxation of magnetic fluctuations due to molecular motions along the direction of the magnetic field and τ_2 is the relaxation time associated with spin coherence in the plane perpendicular to the magnetic field [44]. Using a variety of NMR techniques structural properties, as well as dynamical properties of membranes can be determined. When probing model membranes, the sample consists of a suspension of vesicles (unilamellar or multilamellar), oriented bilayers solid-supported on glass slides, and even bilayers on glass bead substrates [45]. Only those atoms that have a net nuclear magnetic moment will interact with an external magnetic field; in membrane systems ^{1}H, ^{2}H, ^{13}C, ^{14}N, and ^{31}P are typically used. Splitting of the NMR signal is used to determine the degree of ordering in the sample and quantities such as temperature or deuteration can be varied in order to characterize these dependencies [27].

^{1}H NMR or proton NMR spectroscopy has been used to determine the locations of the hydrogen atoms in the system, leaving other atoms essentially invisible. Early studies using ^{1}H NMR to probe lipid phases demonstrated the change in rotational and oscillatory motions of phospholipids when heated through the main transition from gel to fluid phases [46, 47, 48, 24]. In these experiments samples with deuterium labeled tails were measured. ^{2}H NMR of selectively deuterated acyl chains has been used to determine the tail ordering, and thickness of the hydrocarbon region of the bilayer [49] and head group conformation as a function of hydration [50]. The nature and rates of motions of acyl chains and head groups and the effects of interaction of proteins, other lipids, and ions [51], as well as the area per lipid and hydrocarbon tail distribution [52] have also been determined by ^{2}H NMR. Because of the ease with which lipids can be deuterated ^{2}H NMR can be used to isolate the acyl tail signal, even membrane curvature can be studied with this method [45, 53].

Probing the resonance of other atoms in lipid membranes can be advantageous, for instance ^{31}P NMR spectroscopy is an attractive candidate for the study of membranes because there is only one phosphorous atom in a lipid molecule, it is also sensitive to the motions of the lipids as well as the structure [53].

In addition to membrane properties, NMR can be used to investigate the binding of small molecules to a lipid membrane [54, 55]. Some relevant studies are Holte *et al.* who found that ethanol binds to the head groups of phospholipids in membranes [36], Leonard *et al.* found that cholesterol has an affinity to the interior of the lipid bilayers [56], and much larger and complex molecules such as peptides and proteins have various locations depending on the chemistry of the molecules [57, 51]

Fluorescence microscopy: Fluorescence microscopy techniques in membrane studies have the advantage of combining the sensitivity and flexibility of a microscope with the addition of fluorescence spectroscopy, allowing for the collection of spatially resolved information. Relevant timescales in cell biology can be minutes and hours; however, in our model systems we are interested in timescales down to nanoseconds, where molecular and intramolecular motions take place. Using fluorescence microscopy to observe characteristics of lipid membranes, two types of observations are commonly made: local dynamics of lipids by diffusion and domain formation on micrometer length scales. The visual information provided by fluorescence microscopy can be used to overcome the challenge of correlating lateral structure information between model membrane systems and complex mixtures including biological membranes. Many fluorescence techniques have been used to observe the lateral structure on giant unilamellar vesicles (GUVs) including confocal and two-photon fluorescence microscopy [58], Förster resonance energy transfer (FRET) and the lateral motions of molecules in planar bilayers using fluorescence correlation spectroscopy (FCS) and fluorescence recovery after photo-bleaching (FRAP).

The aforementioned structures that are observed with fluorescence techniques are in the form of nano- or microscopic regions of the membrane. For simple lipid mixtures of two or three components, regions of different phases are visible and these fluorescence techniques can inform phase diagrams of binary and ternary mixtures as a function of temperature and concentration. Phase separations were first observed in two-component mixtures of phospholipids where lipids were chosen such that main-transition temperatures were many degrees apart. For similar lipids, with the same head groups for instance, decreasing the tail length or increasing the degree of unsaturation of the lipid tails has the effect of decreasing the transition temperature. Using differential scanning calorimetry (DSC) [59], the heat capacity difference is measured as a function of temperature between a solution and simply the solvent [60] to determine the phase transition(s). Fluorescence microscopy experiments aimed to characterise the size of domains and conditions under which they form; however, the lateral resolution of fluorescence microscopy is $\sim$200 nm [61]. Veatch and Keller observed >1 μm domains below the phase separation temperature in ternary mixtures of cholesterol, DPPC, and DOPC in the form of GUVs employing fluorescence microscopy [25, 27].

Förster resonance energy transfer, FRET, probes structure in that it is a method sensitive to

molecules in close proximity. The basic principle is that when a fluorophore A absorbs a photon then that fluorophore has an electron in an excited state. Upon return to its ground state, the excited electron can non-radiatively transfer that energy to fluorophore B instead of fluorescing [62]. However, these fluorophores must be in close proximity, ∼1-10nm, which means that interactions between the fluorophores are probed and the relative structure can be inferred on this length scale [63]. Thus the formation and observation of domains in lipid bilayers in ternary lipid mixtures have been studied with FRET [64, 65].

Other fluorescence methods allow for the observation of the diffusive motions, i.e., Brownian diffusion, of the membrane constituents such as lipid and proteins. Fluorescence correlation spectroscopy (FCS) is a technique whereby the fluorescence intensity arising from a small volume of fluorescent molecules is correlated, which elucidates processes that arise from fluctuations in the fluorescence intensity, such as Brownian motion [60]. A characterization of a GUVs of a ternary lipid mixture (DLPC/DPPC/cholesterol) was done using confocal fluorescence microscopy to observe phase separations and FCS was used to observe diffusion within the phase domains [66]. Korlach *et al.* compared GUVs with and without cholesterol with confocal microscopy and observed that cholesterol solubilizes DPPC into the fluid phase, however caused a decrease in diffusion constant of this fluid phase [66]. FCS was also used by Banks and Fradin [67] to measure the diffusive motions of fluorescent proteins in a highly concentrated solution of polymer and protein. Though this measurement was made on a very different system its findings were very relevant to our work on diffusion of hydration water in solid-supported, stacked lipid bilayers [68, 2]. They observed a slower-than-Brownian motion, i.e.,anomalous diffusion, in this crowded medium which is described by not just one characteristic timescale of motion (Brownian), but a distribution of times. Biological systems are often crowded such as cell membranes, thus our finding of anomalous diffusion of hydration water in this biomimetic system was informed by this seminal work.

Another fluorescence method used to make diffusion measurements in biological and model systems is fluorescence recovery after photo-bleaching (FRAP). In the context of lipid membranes, this technique measures fluorescence from a fluorophore, which sits amongst the lipids or a mixture in a bilayer in order to assess the motion of the components in the membrane. In FRAP a short, intense pulse of light is incident on a small circular area of the membrane, which contains mobile fluorescent molecules [69]. This pulse serves to irreversibly photo-bleach the fluorophores in that area, rendering them unable to fluoresce. The photo-bleached fluorescent molecules diffuse throughout the sample as well as the non-photo-bleached fluorophores from outside the bleached area. Diffusion coefficients can be determined by measuring the characteristic exponential recovery rate of the fluorescent signal and fitting this curve to the theoretical profile for recovery [69]. Almeida *et al.* performed an extensive study of the lateral diffusion of a binary mixture of DMPC/cholesterol bilayers using the fluorophore (NBD-C(10)PE or N-(7-nitro-2,1,3-benzoxadiazol-4-yl)didecanoylphosphatidylethanolamin) from 0-50 mol% cholesterol concentrations [30]. By comparing with other techniques such as DSC and NMR from other studies they were able to compare phase regions and use the diffusion in the different regions to modify the DMPC/cholesterol phase diagram [30]. The diffusion constants, D, of the

membrane fluorophores generally increased with increasing temperature at any concentration [30]. For a particular isotherm, however, (1) D at high cholesterol concentrations and high temperatures continued to decrease while (2) D at high cholesterol concentrations and low temperatures increased, and (3) D at intermediate concentrations decreased [30]. This study showed that lipid mobility is lowered for fluid phase lipids and increased for gel phase lipids.

Membrane simulations: Computer simulations are becoming an increasingly widespread tool for studying the structure and dynamics of lipid bilayer systems due to the advances in computational processing power and simulation methods. Molecular dynamics (MD) simulations, in particular, are of great interest due to the modelling of lipid, solvent, and additional molecules at the atomic level. MD simulations explicitly solve Newton's equations of motion and an attractive feature of MD simulations is that the membranes systems are treated with atomic realism [70]. However, difficulties arise in the model development and interpretation of MD simulations including many large molecules and systems with inherent disorder. For instance, lipids in the biologically relevant liquid-disordered phase do not have a single conformation, making simple models hard to create [71]. Many parameters from experiment are used, such as bond lengths and force constants; however, the simplified potentials modelled may lead to very different simulated outcomes since the actual potential is surely more complex [70]. Measured quantities from NMR experiments, such as order parameters and bond lengths, are crucial to test simulations for validity, for instance, the force fields of acyl chains [72].

Molecular dynamics simulations produce helpful findings alone or in conjunction with experiments. Simulations can be used to study two-dimensional, fluid phospholipid bilayer and interactions between molecules at high temporal (ps to μs) and spatial resolution (Å to μm) to determine for instance, ordering and phase transitions, which can complement experimental data and inform theoretical models. In simulations, atoms are treated classically. Bonded atoms interact via harmonic oscillator-like potentials and non-bonded atoms have van der Waals and electrostatic interactions valid over a certain cut-off radius [70]. Lipid bilayer simulations can be informed by monolayer simulations at the air/water interface; however, monolayers cannot simply be thought of as half of a bilayer because many properties may be quite different than those of bilayers such as lateral pressure at the ends of the acyl chains [73, 74].

The 'slab model' of a lipid bilayer was introduced by Marrink and Berendsen to describe transport of water through a lipid membrane (DPPC) [75]. In their model, the bilayer consists of four regions of different free energies and diffusivities in each region in the membrane [75]. The four regions are as follows: (1) water furthest away from the bilayer where the water is slightly perturbed by the lipids to lipid water interface; (2) head group region where all water are arranged in hydration shells, $\sim$8Å for phosphatidylcholine head groups; (3) a region of the acyl tail that is partially ordered and have high density, size depends on tail length; and (4) a low density, hydrophobic bilayer center. We found this model instructive in describing the regions of hydration water in our study on the diffusive motions of hydration water in lipid bilayers [2]. Kučerka *et al.* used X-ray and neutron scattering data of DPPC and DOPC membranes of various deuterations with models for volume probability

distributions of membrane components to execute MD simulations [15]. These simulations were able to reasonably reproduce the electron and neutron scattering length density profiles which has led to an improved technique to measure lipid areas in bilayer systems [15].

More recent studies on lipid membranes are of interest as they simulate bilayer systems closely related to our experiments. Hansen *et al.*, von Hansen *et al.* and Holland *et. al* recently investigated the diffusion within a hydrated bilayer of DMPC and DPPC [76, 77]. These studies found that the diffusion of hydration water was anisotropic, decreasing for increasing proximity to the membrane interface [76, 77]. An anomalous diffusion regime was observed by von Hansen *et al.* and simulations in our hydration water dynamics study [2] followed their method where Brownian diffusion constants varied as a function of distance along the membrane normal and a potential energy function [77].

Ethanol's effect on a phospholipid bilayer was simulated for a variety of ethanol concentrations and found that ethanol has an affinity for the head groups of a lipid bilayer [39, 78] and dynamics of both water and lipid molecules were influenced by its presence [39, 78]. Both water and lipid translational diffusion were found to increase or not have much effect; however, our recent quasi-elastic experiments of 2mol% ethanol concentration suggest fluid bilayers show no significant change in diffusion, while the gel phase actually shows a decrease in diffusion constant with the addition of ethanol [3].

MD simulation studies of the addition of cholesterol to single-species phospholipid bilayers have shown a condensing effect for high concentrations of 50 mol% cholesterol in both DPPC and DMPC bilayers [79, 80]. These studies observed a decrease in area (e.g., average lipid area or bilayer area) and increase in the average bilayer thickness, supporting the condensation effect [79, 80]. It should be mentioned that Huang and Feigenson reported that their Monte Carlo simulations have shown the 'umbrella model' as a plausible configuration of the condensation of the cholesterol and phospholipid molecules [23]. This configuration can be explained by the shielding of cholesterol's hydrophobic rings the lipid/water interface by the phosphatidylcholine head group, which can accommodate up to two cholesterol, preventing the unfavourable water/sterol ring [23].

Molecular dynamics simulations are well suited for simulating systems on the atomic level; however, other methods must be employed for probing long length scales due to the vast system size which leads to prohibitively large equilibration times [18]. Monte Carlo (MC) simulations are used to probe larger length scales and can avoid explicit time dependence of the processes in the system. MC simulations sample molecular conformations based on their Boltzmann probability distribution [81]. Recently, Meinhardt *et al.* observed the formation of rafts in coarse-grained simulations where molecular groups such as head groups, sterol rings, methylenes and hydroxyls were modeled by beads with various mobilities [28]. The beads of the coarse-grained cholesterol molecules were stiffer to mimic cholesterol's rigid sterol rings, whereas the lipid beads were much more flexible [28]. Coarse-grained models of a lipid and a cholesterol molecule are shown in Figures 2.1 b) and 2.3 b), respectively. Similar coarse-grained molecular simulations were included in our work on the structure of cholesterol in lipid rafts in order to help us explain our observation of multiple domain structures in a heterogeneous liquid-ordered phase [4]. Though the simulations could not predict the molecular

structure of the domains due to their coarse-grained nature, by monitoring the cholesterol concentration of the simulation box we were able to observe three co-existing regions of different cholesterol concentrations [4]. This observation agreed well with our neutron diffraction observations, which were used to assess the molecular structures of the regions [4].

X-ray and neutron diffraction: X-ray and neutron scattering experiments using vesicles and solid-supported bilayers of phosphatidylcholine lipids have contributed greatly to the structural properties of hydrated, single-species bilayers. The diffraction data comes in the form of bilayer form factors, $F(q_z)$, that can be Fourier transformed to create density profiles along the bilayer normal [72]. Electron density and neutron scattering length density profiles (NSLD) are used to find parameters such as repeat spacing, d_z, head-to-head distance, D_{HH}, and bilayer thickness, D_B [72]. Simulations have been successful in modeling detailed distributions of the various components of the membrane, and we have found these distributions very useful in the structure determination of our DMPC bilayers from neutron reflectometry data [2, 15, 17, 72].

2.3 Scattering Theory of X-rays and Neutrons

Both X-rays and neutrons have wavelengths (electromagnetic and de Broglie) that are on the order of atomic distances in fluid and condensed matter systems making them prime candidates for studying these systems. X-rays and neutrons are both used to probe matter; however, this is accomplished in a different way, though scattering is the probe mechanism in each case. The difference is the interaction with the atoms from which they scatter: X-rays scatter from the distribution, $\rho_e(r)$, of electrons that surround the nucleus, while neutrons scatter from the sharp distribution, $\rho_n(r)$, of the nucleus. The strength of the interaction between X-rays and atoms increases monotonically as a function of the number of electrons, while the strength of the neutron-nucleus interaction is dependent on the nuclear state, nuclear spin and given isotope.

X-ray scattering has some advantages over neutron scattering due to the ease of access, making experiments fast and plentiful, the properties of neutrons, however, may allow a greater depth of information to be accessed from the experimental system. One of the main advantages of neutrons is their lack of charge, which means that the neutron is able to penetrate matter much more than any charged particle because it can bypass the electronic Coulomb barrier. Unlike X-rays, which interact with the electronic distribution of atoms and whose scattering is proportional to the number of electrons in atoms, neutrons can probe uniquely-scattering nuclei. For instance H_2O scatters ~ 10 times less than D_2O, whereas H_2O and D_2O are indistinguishable in X-ray measurements. Another property of the neutron of which we take advantage is that of the energy of thermal neutrons. This energy is on the same order as excitations in the fluid and soft matter systems, making thermal neutrons prime candidates for probing the dynamics of the membranes. In measuring the quasi-elastically or inelastically scattered neutrons from membranes, we observe excitations when the neutron's energy increases as a result of the scattered neutron absorbing the energy of a membrane excitation or decreases as a result of the neutron transferring energy to the membranes, inducing

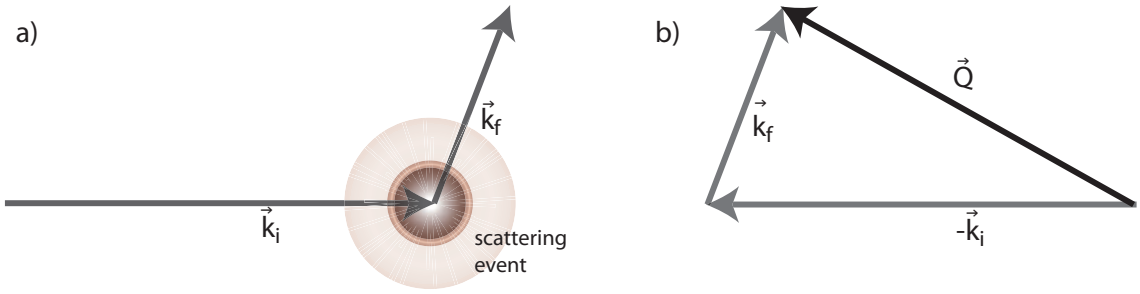

Figure 2.6: a) A plane wave with momentum vector $\vec{k}_i$ is scattered from an atom and the scattered wave vector is $\vec{k}_f$. b) The scattering wave vector, $\vec{Q}$, is defined as the incident wave vector, $\vec{k}_i$, subtracted from the scattered vector, $\vec{k}_f$: $\vec{Q} = \vec{k}_f + (-\vec{k}_i)$.

an excitation. It should be mentioned that neutrons are widely used in magnetic systems since they are a great probe for magnetic properties of matter. However, this thesis will not be concerned with this topic.

The energies of the incident X-rays and neutrons, E_X and E_n are defined as:

$$E_X = \frac{hc}{\lambda_X}\,, \tag{2.1}$$

$$E_n = \frac{1}{2}m_n v^2\,. \tag{2.2}$$

Referring to Eq.(2.1), h is the Planck constant, c is the speed of light, and λ_X is the wavelength of the incident X-rays; for instance the wavelength of X-rays from BLADE (Biological Large Angle Diffraction Experiment) is λ=1.5418 Å, which have energy $E_X \sim 8$ keV. With reference to Eq.(2.2), m_n is the mass of the neutron (m_n=1.675×10^{-27} kg) and v is the neutron's speed. Thermal neutrons at room temperature, $T \sim 300$ K, such as the ones produced at the reactor at the CNBC at Chalk River, have an energy of $E_n \sim 25$ meV corresponding to a speed of $v \sim 2$ km/s.

Consider a plane wave with wave vector, $\vec{k}$

$$|\vec{k}| = \frac{2\pi}{\lambda} \tag{2.3}$$

so that,

$$E_X = \hbar c|\vec{k}|\,, \tag{2.4}$$

$$E_n = \frac{\hbar^2 k^2}{2m}\,, \tag{2.5}$$

where $\hbar = \frac{h}{2\pi}$.

Experiments employing neutron scattering commonly aim to measure two main quantities: (1) the change in neutron wave vector direction due the scattering event and (2) the change in neutron

energy due to the scattering event. The scattering vector, $\vec{Q}$, is defined as the difference between the outgoing wave vector and the incident wave vector,

$$\vec{Q} = \vec{k}_f - \vec{k}_i \,, \tag{2.6}$$

where subscripts f and i denote final and initial, respectively as is seen in Figure 2.6. The scattering vector is related to the momentum transfer: $\vec{p} = \hbar\vec{Q} = \hbar(\vec{k}_f - \vec{k}_i)$. The energy transferred to or from the neutron by a dynamical excitation is

$$E_f - E_i = \hbar\omega = \frac{\hbar}{2m}(k_f^2 - k_i^2) \,. \tag{2.7}$$

In structure determination experiments using X-rays or neutrons we will only be concerned with $\vec{Q}$. However, in dynamical studies of matter with neutrons both $\vec{Q}$ and $\hbar\omega$ are utilized.

How effectively a particular atom scatters X-rays or neutrons is dependent on the scattering cross section of the atom. Scattering cross sections are quantities that are a measure of the interaction of an atom with a wave and can be calculated in the case of X-rays; however, have to be determined experimentally in the case of neutrons. The interaction between a wave and matter can result in the scattering of the wave, which will change the energy and/or direction of the incident wave.

For an incident beam of X-rays or neutrons, N_s is the number of scattering events, proportional to the scattering cross section, σ [82],

$$N_s = \Phi_o \, \sigma \,, \tag{2.8}$$

where Φ_o is the incident flux of the beam in scattering events$\cdot$s^{-1}barn^{-1} (1 barn = 10^{-24}cm^2). Similarly to Eq.(2.8), $N_a = \Phi_o \sigma_a$ describes the number of incident absorptions, N$_a$, by an atom that has absorption cross section σ_a [82].

Our definition of cross section σ, leads to the introduction of the one-dimensional differential cross section $d\sigma/\mathrm{d}\Omega$, proportional to the probability that a scattering event will occur in solid angle element dΩ in the direction $\vec{\Omega}/|\vec{\Omega}|$.

The total cross section σ_{tot}, proportional to the total number of scattering events in all directions θ and ϕ, can be defined as [85]

$$\sigma_{tot} = \int_0^\pi \mathrm{d}\theta \frac{\mathrm{d}\sigma}{\mathrm{d}\Omega} \times 2\pi \sin\theta \,, \tag{2.9}$$

assuming that scattering is axially symmetric and only depends on the zenith angle θ, and not the azimuthal angle ϕ. Experimentally measured cross sections tend to be quoted per atom, and the coherent cross sections for X-rays and neutrons are compared for some biologically relevant atoms in Figure 2.7.

The double-differential cross section $\mathrm{d}^2\sigma/\mathrm{d}\Omega\mathrm{d}E$ is proportional to the probability of particle of incident energy E$_i$, leaving the scatterer in a solid angle dΩ, in direction $\vec{\Omega}/|\vec{\Omega}|$ with change in energy $\hbar\omega = dE = E_f - E_i$. By integrating the double differential cross section over all possible energies, one recovers the differential cross section.

For a monochromatic, collimated beam of X-rays or neutrons, we can model this approximation

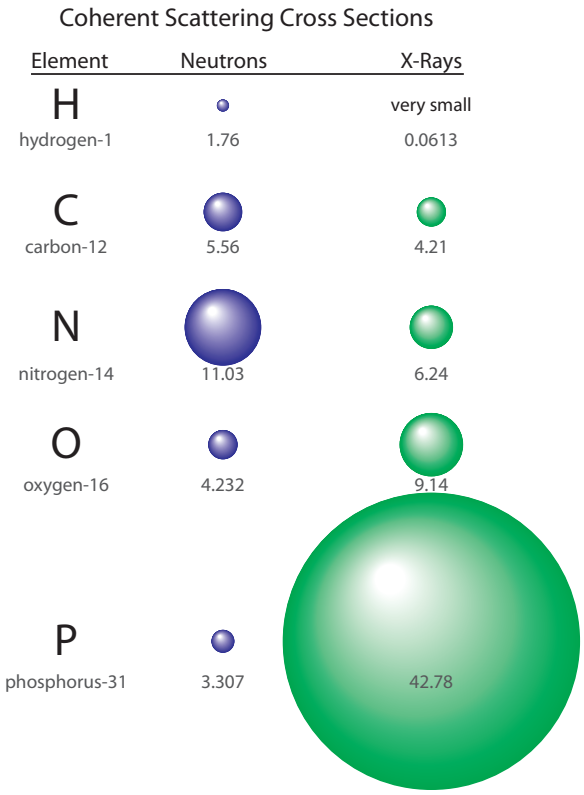

Figure 2.7: Coherent cross sections are compared for some common elements present in biological matter. Shown in order of increasing atomic number: hydrogen, carbon, nitrogen, oxygen . The X-ray scattering cross sections increase monotonously and rely predictably on the number of electrons present. However, the neutron scattering cross sections do not increase monotonically. Cross section units are barns and values are from NIST [83] (neutrons) and [84] (Xrays)

(as these beams will never be completely monochromatic or collimated) as a plane wave with wave vector k_i travelling along $\hat{z}$ and incident on the sample and being scattered by individual atoms as a spherical wave that is detected at a distance r from the scatterer, i.e., the spherical wave front has radius r. We can write the wave functions of the incident and scattered waves as [86, 85]

$$\psi_i = e^{i(k_i z - \omega t)}\,, \tag{2.10}$$

$$\psi_f = -\frac{b}{r} e^{i(\vec{k}_f \cdot \vec{r} - \omega t)}\,. \tag{2.11}$$

In the general case we account for an initial phase ωt of the incident beam. The scattering length, b, characterizes the ability of an atom to scatter, and assumes the interaction is isotropic. The scattering length can be complex where $Re(b)$ represents scattering with a repulsive ($Re(b) > 0$) or an attractive ($Re(b) < 0$) interaction and $Im(b)$ represents absorption [82].

The differential scattering cross section, $d\sigma/d\Omega$ for a single point nucleus impinged upon by a beam of X-rays or neutrons with speed v, flux Φ_o through an area $\mathrm{d}A$ can be calculated using Equations (2.8 and 2.11) [86, 85]

$$v\,\mathrm{d}A|\psi_f|^2 = v\,\mathrm{d}A\frac{b^2}{r^2} = vb^2\mathrm{d}\Omega\,, \tag{2.12}$$

$$\frac{\mathrm{d}\sigma}{\mathrm{d}\Omega} = \frac{N_s}{\Phi_o \mathrm{d}\Omega} = b^2\,. \tag{2.13}$$

The incident flux $\Phi_o = v|\psi_i|^2 = v$ can be expressed as the incident number density multiplied by the speed of the particles, v, for X-rays $v = c$. Also, the differential area can be defined as $\mathrm{d}A = \mathrm{d}\Omega r^2$. The total scattering cross section for the spherically symmetric case is

$$\sigma_{tot} = 4\pi b^2\,. \tag{2.14}$$

In our sample, nuclei are positioned at $\vec{R}_j$ and the Fermi pseudo-potential, $V(\vec{r})$ may defined by

$$V(\vec{r}) = \frac{2\pi\hbar^2}{m}\sum_j b_j\,\delta(\vec{r} - \vec{R}_j)\,, \tag{2.15}$$

where we approximate the nuclear potential as a narrow, short range potential [85].

If we now look at a sample with many nuclear species and a variety of locations of these nuclei, we will have an average scattering length for the system

$$\langle b\rangle = \sum_i n_i b_i\,, \tag{2.16}$$

$$\text{where } \sum_i n_i = 1.$$

Here, the probability of finding a nucleus i with scattering length b_i is simply n_i. We can also show

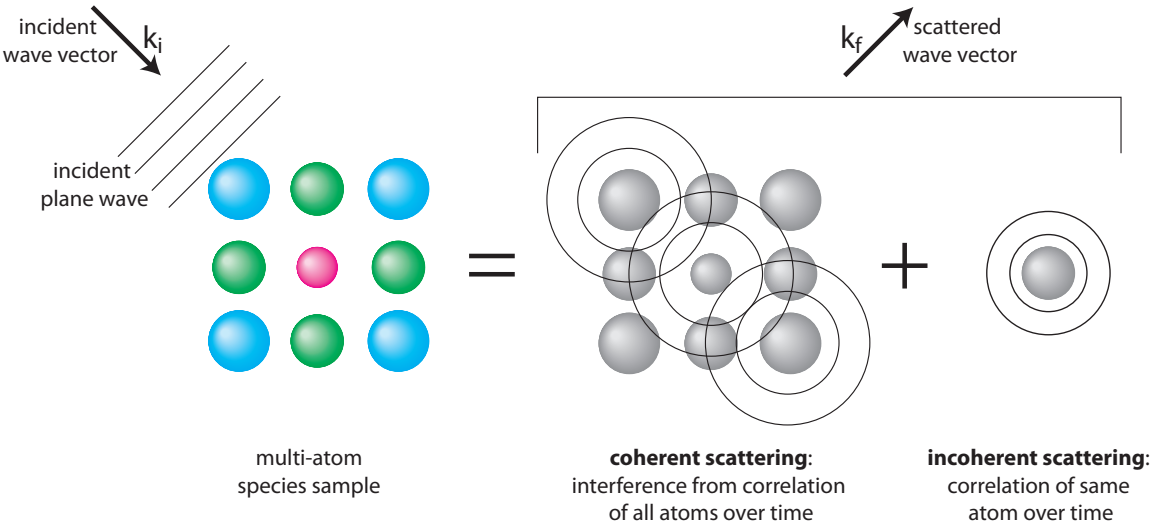

Figure 2.8: A plane wave with wave vector $\vec{k_i}$ is incident on a multi-atom scatterer. The scattering that is produced is generally a combination of coherent scattering and incoherent scattering. Coherent scattering is the scattering as if each atom has the same average cross section of all the atoms, and is an interference effect. Incoherent scattering is the deviation of the position of a particular atom from its mean position.

the average value for b^2

$$\langle b^2 \rangle = \sum_i n_i b_i^2 \,. \tag{2.17}$$

For a distribution of nuclei with scattering length b, we come to a simple expression double-differential cross section [85]

$$\frac{\mathrm{d}^2\sigma}{\mathrm{d}\Omega \mathrm{d}E} = \frac{k_f}{k_i}\frac{1}{2\pi\hbar}\sum_{j'j}\langle b_{j'} b_j \rangle \int \langle e^{i\vec{Q}\cdot(\vec{R}_j(t)-\vec{R}_{j'}(0))}\rangle e^{-i\omega t}\, dt \tag{2.18}$$

$$= \frac{k_f}{k_i}\langle b \rangle^2 \frac{1}{2\pi\hbar}\sum_{j'j(j'\neq j)}\int \langle e^{i\vec{Q}\cdot(\vec{R}_j(t)-\vec{R}_{j'}(0))}\rangle e^{-i\omega t}\, dt \tag{2.19}$$

$$+\frac{k_f}{k_i}\langle b^2 \rangle \frac{1}{2\pi\hbar}\sum_{j}\int \langle e^{i\vec{Q}\cdot(\vec{R}_j(t)-\vec{R}_{j}(0))}\rangle e^{-i\omega t}\, dt.$$

This expression holds for an unpolarized beam incident upon a monatomic material. However, samples that are comprised of a variety of atoms or isotopes will require the scattering length to be incorporated into the integral, making the interaction and the structural information coupled.

We can split this expression into coherent $\left(\frac{\mathrm{d}^2\sigma}{\mathrm{d}\Omega \mathrm{d}E}\right)_{coh}$ and incoherent $\left(\frac{\mathrm{d}^2\sigma}{\mathrm{d}\Omega \mathrm{d}E}\right)_{inc}$ cases of scattering. Coherent term is the case of a correlation between an atom and all other atoms, the interference of scattering from different atoms. Incoherent scattering is the case of a correlation between an atom and itself at later time t. Coherent and incoherent scattering from a multi-atom sample are shown

schematically in Figure 2.8. The two cases for the double-differential cross section are [85]

$$\left(\frac{\mathrm{d}^2\sigma}{\mathrm{d}\Omega \mathrm{d}E}\right)_{coh} = \langle b\rangle^2 \frac{k_f}{k_i}\frac{1}{2\pi\hbar}\sum_{j'j}\int_{-\infty}^{\infty}\langle e^{i\vec{Q}\cdot(\vec{R}_j(t)-\vec{R}_{j'}(0))}\rangle e^{-i\omega t}\,\mathrm{d}t\,, \tag{2.20}$$

$$\left(\frac{\mathrm{d}^2\sigma}{\mathrm{d}\Omega \mathrm{d}E}\right)_{inc} = [\langle b^2\rangle - \langle b\rangle^2]\frac{k_f}{k_i}\frac{1}{2\pi\hbar}\sum_{j}\int_{-\infty}^{\infty}\langle e^{i\vec{Q}\cdot(\vec{R}_j(t)-\vec{R}_j(0))}\rangle e^{-i\omega t}\,\mathrm{d}t\,, \tag{2.21}$$

$$\left(\frac{\mathrm{d}^2\sigma}{\mathrm{d}\Omega \mathrm{d}E}\right)_{tot} = \left(\frac{\mathrm{d}^2\sigma}{\mathrm{d}\Omega \mathrm{d}E}\right)_{coh} + \left(\frac{\mathrm{d}^2\sigma}{\mathrm{d}\Omega \mathrm{d}E}\right)_{inc}. \tag{2.22}$$

The coherent, incoherent and total scattering cross sections are defined as

$$\sigma_{coh} = 4\pi\langle b\rangle^2\,, \tag{2.23}$$

$$\sigma_{inc} = 4\pi[\langle b^2\rangle - \langle b\rangle^2] \tag{2.24}$$

$$\sigma_{tot} = \sigma_{coh} + \sigma_{inc}. \tag{2.25}$$

In neutron scattering experiments, the system can typically be made to maximize the incoherent or coherent scattering from the sample in order to measure motion or structure by selectively deuterating parts of the system. We have taken advantage of this feature of neutrons by using deuterium labelling of organic molecules. For example, to measure the structure of lipid tails in a system we maximize the amount of coherent scattering for a lipid molecule species by replacing the hydrogen-rich acyl chains with deuterium. Since the coherent scattering cross section of D is $\sim$80$\times$ that of H, the scattering signal is dominated by the scattering from the lipid acyl chains. Figure 2.9 compares coherent and incoherent scattering cross sections for some atoms commonly found in organic molecules. In our X-ray experiments probing structure, only coherent scattering is measured and since the scattering length of the atoms depends on the electron density distribution of the atoms, our X-ray experiments are generally sensitive to a much different subset of atoms for the same sample.

From the above double-differential scattering cross sections we can define the intermediate scattering function $I(\vec{Q},t)$, time-dependent pair-correlation function $G(\vec{r},t)$, and scattering function $S(\vec{Q},\hbar\omega)$ [85]

$$I(\vec{Q},t) = \frac{1}{N_n}\sum_{j'j}\langle e^{i\vec{Q}\cdot(\vec{R}_j(t)-\vec{R}_{j'}(0))}\rangle\,, \tag{2.26}$$

$$G(\vec{r},t) = \frac{1}{(2\pi)^3}\int I(\vec{Q},t)\,e^{-i\vec{Q}\cdot\vec{r}}\mathrm{d}\vec{Q}, \tag{2.27}$$

and

$$S(\vec{Q},\omega) = \frac{1}{2\pi\hbar}\int I(\vec{Q},t)\,e^{-i\omega t}\,\mathrm{d}t, \tag{2.28}$$

where N_n denotes the number of nuclei in the sample. It is also to be noted that each of these three

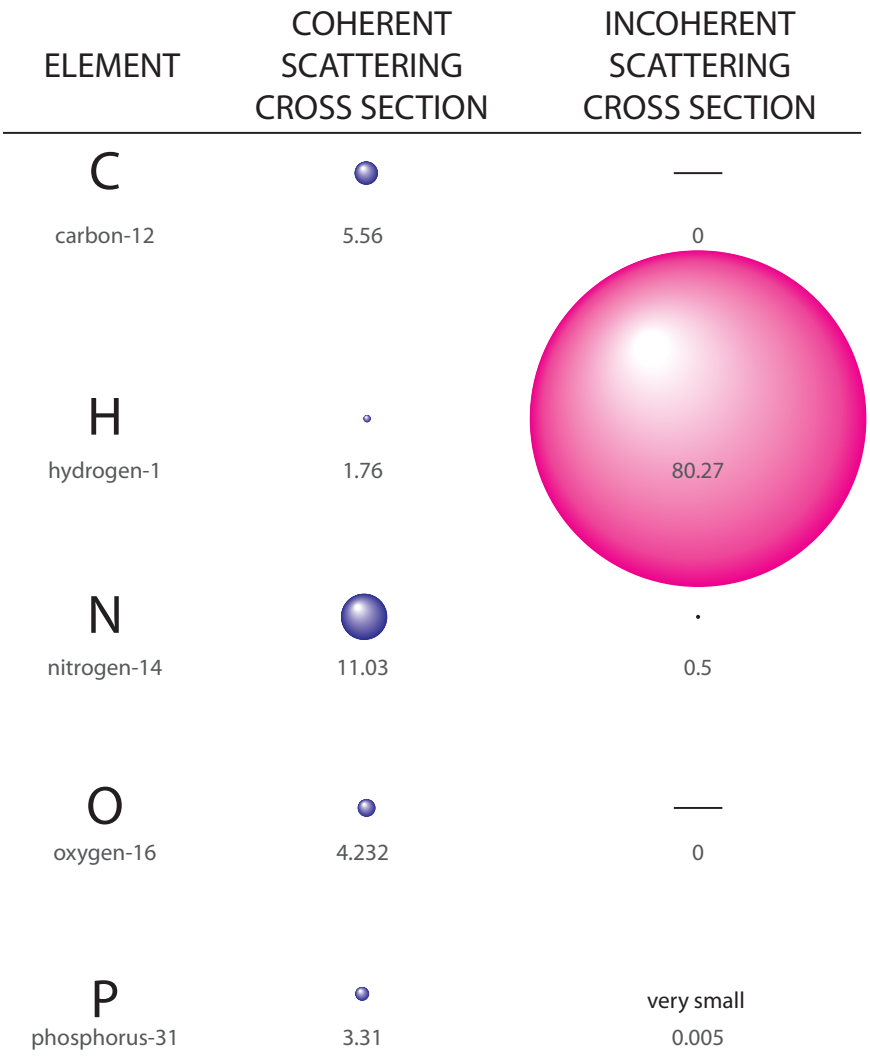

Figure 2.9: Comparison of coherent (blue) and incoherent (magenta) neutron scattering cross sections σ_{coh} and σ_{inc}. To-scale cross sections are listed for common biological elements that are present in our samples: carbon-12, hydrogen, nitrogen-14, oxygen-16, and phosphorus-31. Cross section units are barns and values are from NIST [83].

functions can use the properties of Fourier transforms to become in terms of each other.

The intermediate scattering function can be used to find time scales of correlations over a particular length scale and dynamic heterogeneities in the system. The time-dependent pair-correlation function $G(\vec{r},t)$ gives the probability that an atom, initially at $\vec{r}_o = 0$, $t_o = 0$, will be found at some other position, $\vec{r}$, at some time t later. The scattering function $S(\vec{Q},\omega)$ is the probability that the scattered neutron has changed the energy and momentum of the sample by $\hbar\omega$ and $\hbar\vec{Q}$ [87]. The $\vec{r}$-dependence of $G(\vec{r},t)$, or the $\vec{Q}$-dependence of $S(\vec{Q},\omega)$ and $I(\vec{Q},t)$, gives us information about the structure of the sample. The t-dependence of $G(\vec{r},t)$ and $I(\vec{Q},t)$, or the ω-dependence of $S(\vec{Q},\omega)$ gives us information about the motions in the sample.

Chapter 3

Experimental Considerations

3.1 Sample Preparation

The goal of sample preparation in each experiment was to fabricate a bilayer structure that mimics a particular fundamental property of biological membranes. Typically, stacked, solid-supported, highly-oriented bilayers are used in order to take advantage of the separation of scattering information into in-plane and out-of-plane components. Only in the case of hydrating the bilayers with a volatile solvent [3] was this convention not used. The general method will be discussed below and any variation will be described in detail.

3.1.1 Materials

This section serves to introduce the materials that are mentioned during the explanation of preparation protocols and throughout the remainder of the thesis.

Substrates:

Silicon Wafers: Wafers were ordered in two sizes: 2 ″ and 4 ″. 2 ″ wafers were used exclusively for neutron experiments and 4 ″ wafers were laser cut into 1 cm×1 cm or 2 cm×2 cm squares for X-ray experiments. The polished silicon was cut on the [100] face with a resistivity of 8 to 12 Ω· cm and thickness of 256-306 μm. Round silicon wafers used for neutron experiments were purchased from WRS Materials, USA. Square wafers used for X-ray experiments were purchased from Silchem Corp., Germany.

Glass Slides: Quartz glass slides with a 0.5 mm-deep stone-ground depression were used as a substrate for hydrated powder samples. The depression was ground out to approximately 20 mm×20 mm with rounded corners.

Kapton:

Kapton polyimide sheets of 13μm thickness were cut to size and used for the windows on BLADE's hydration chamber and to seal the hydrated powder in the depression on the Quartz slide. The high

mechanical strength and high X-ray transmission of polyamide foil made it a desirable choice for our window material [88].

Wafer-cleaning solutions:

Methanol (CH_3OH) was used for cleaning wafers during sonication (alternated with water) resulting in a hydrophobic surface.

In order to make a hydrophilic surface, wafers were submerged in an acid solution for 30 minutes. The piranha solution was a 70:30 ratio of sulphuric acid (H_2SO_4) and hydrogen peroxide (H_2O_2) at 90°C. This solution is a strong oxidizing agent capable of removing organic residues while still leaving the oxide layer of the silicon intact.

These substances were purchased from scientific stores in the basement of the Arthur Bourns Building, ABB B166.

Water and lipid solutions:

The Cascade LS Water System dispenses ultrapure water for use in the Laboratory of Membrane and Protein Dynamics, which has a resistivity of 18.2 MΩ·cm.

Solvents used in making lipid solutions in these experiments include chloroform ($CHCl_3$) and 2,2,2-trifluoroethanol ($C_2H_3F_3O$). These solvents were reagent grade and purchased from scientific stores in the basement of the Arthur Bourns Building, ABB B166.

Molecules:

DMPC and DPPC: All lipids used in the preparation of the samples mentioned in this thesis were purchased as powder from Avanti Polar Lipids, Inc. The lipids are packed and transported with solid CO_2 and stored in a freezer at approximately -20°C in the Laboratory for Membrane and Protein Dynamics until use.

DMPC or 1,2-dimyristoyl-sn-glycero-3-phosphocholine has two saturated 14-carbon acyl-chains with a phosphatidylcholine head groups and has the chemical formula $C_{36}H_{72}NO_8P$. DMPC was purchased using product number 850345P (CAS number 18194-24-6). DMPC-D54 has deuterated tails; however, the phosphatidylcholine head group is still protonated with the chemical formula $C_{36}H_{18}NO_8PD_{54}$. DMPC-D54 was purchased using product number 860345P (CAS number 78415-49-3). DPPC or 1,2-dipalmitoyl-sn-glycero-3-phosphocholine has two saturated 16-carbon acyl-chains with a phosphatidylcholine head group and has the chemical formula $C_{40}H_{80}NO_8P$. DPPC was purchased using product number 850355P (CAS number 63-89-8).

Cholesterol: Deuterated cholesterol was purchased from Avanti Polar Lipids Inc. as a powder and was shipped with solid CO_2 and stored in the freezer in the Laboratory for Lipid and Protein Dynamics until sample preparation started. Cholesterol-D7 has a deuterium labelled hydrocarbon chain giving rise to the chemical formula $C_{27}H_{39}OD_7$ and was purchased using product number 700041P (CAS 83199-47-7).

Ethanol: Commercial Alcohols‘ ethyl alcohol of 99.9% purity was purchased from scientific

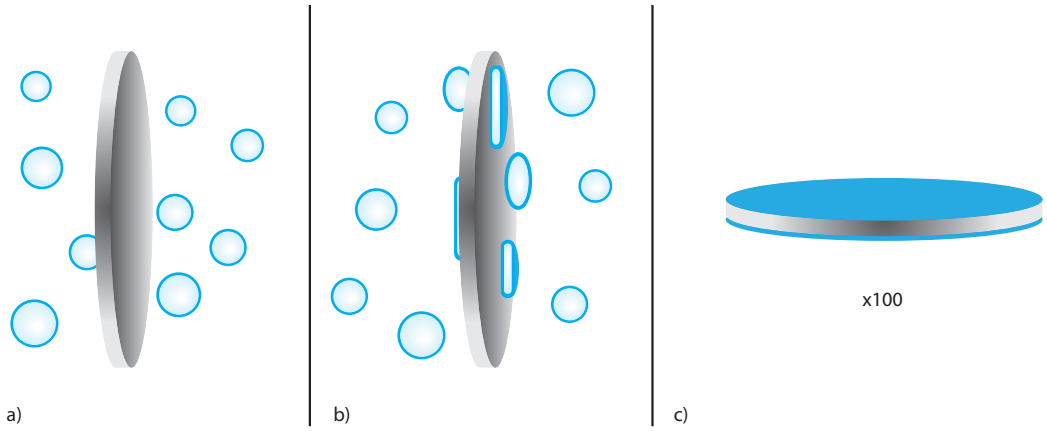

Figure 3.1: Preparing single, solid-supported bilayers. a) Treated silicon wafers are submerged in a solution of DMPC vesicles for one hour. b) DMPC vesicles adsorb to both sides of the treated wafer. Adsorbed vesicles rupture and start forming bilayer patches. c) Continuous bilayer coats each side of the wafer after being rinsed with water.

stores in the basement of the Arthur Bourns Building, ABB B166.

3.1.2 Preparation Protocol of Single, Solid-Supported Bilayers

A single bilayer of DMPC was adsorbed to the surface of a hydrophilic silicon wafer by vesicle fusion [89]. The protocol followed in the publication "*Hydration Water Freezing in Single Supported Lipid Bilayers*" [1] followed that of from Armstrong *et al.* [90] and is explained below.

The 2″ Si wafers were double-side polished and treated in order to render the surfaces hydrophilic. First, the wafers were submerged in a 90°C, so called piranha solution, made of peroxide (H_2O_2) and sulfuric acid (H_2SO_4) (30:70 by volume) for 30 minutes. This ensures removal of all organic contaminants without disturbing the natural SiO_2 layer. Wafers were then rinsed with and submerged in ultrapure water until the vesicle solution was prepared. A 200 mL buffer solution containing 5 mM Hepes, 5 mM $MgCl_2$, and 100 mM KCl was prepared and heated to 55°C. DMPC was then added to a concentration of 1.5 mg/mL.

Initially translucent, the solution was sonicated for 15 hours (duty cycle: 50%, power: 4) until the solution became transparent. This step is crucial as it is the transition from giant multi-lamellar to smaller unilamellar vesicles which are needed to result in a single adsorbed bilayer. The treated wafers were submerged in the 55°C buffer solution for 1 hour to ensure fluid-phase vesicles adsorb to the surface of the wafer. After 1 hour, 2L of ultrapure water was used to remove excess vesicles. As illustrated in Figure 3.1, vesicles adsorbed onto the silicon surface form bilayer patches. After approximately 20-25 minutes, a single bilayer has formed. Wafers were removed from the solution and annealed in 55°C air oven for 72 hours. After annealing, the wafers were mounted in the sample holder and rehydrated. X-ray and atomic force microscopy (AFM) measurements gave evidence for single bilayer coverage free of defects.

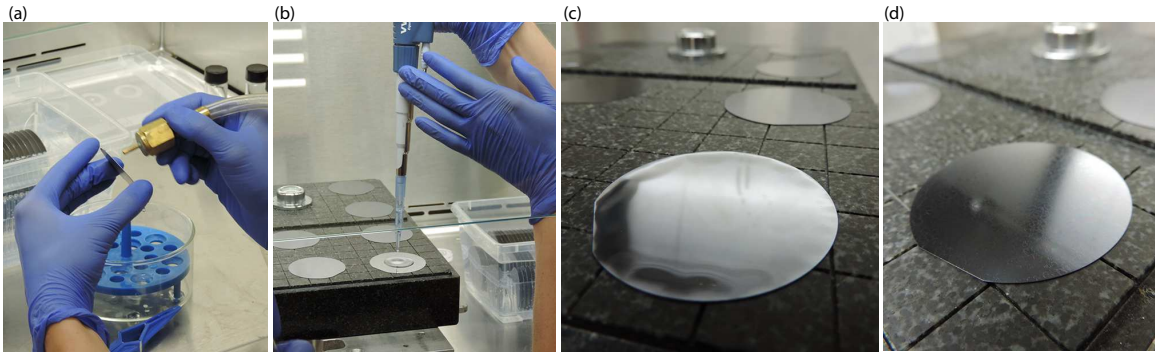

Figure 3.2: Preparation of stacked, oriented, solid-supported bilayers for a neutron scattering experiment. a) After three methanol/water sonication cycles a wafer is dried with nitrogen. b) The wafer is then placed on a heated stage ensuring lipids stay above T_m when solution is deposited. c) After deposition solvent starts to evaporate. d) Solvent has evaporated and the sample is on its way to the vacuum oven to ensure all traces of solvents are gone.

3.1.3 Preparation of Multi-Lamellar, Highly-Oriented Bilayers with Non-Polar Solvents

The silicon wafers were cleaned to make their surface hydrophobic in order for the lipid solution to spread on the wafer. The following was the wafer-cleaning procedure: wafers were submerged into a beaker filled with ultrapure water, this beaker was then placed in a 40°C ultrasonic bath (Branson 2510 Ultrasonic Bath) for 12 minutes, after which wafers were placed in a methanol-filled beaker and sonicated for another 12 minutes at 40°C. Four alternating cycles with water with methanol completed the cleaning.

Wafers were stored in methanol and dried with nitrogen (see Figure 3.2 (a)) before being placed onto a heated granite block (Figure 3.2). Wafers were stored and dried in the fume hood and all deposition occurred in the fume hood. Two granite blocks sat atop an piece of aluminum through which water flowed, in this way thermal conduction heated the granite blocks. The aluminum/granite assembly was heated many hours before sample preparation in order for the entire block to reach equilibrium, a pyrometer was used to ensure the granite surface was above the transition temperature. This heating assembly sat atop an aluminum slab with three screwed feet such that a level surface was achieved by adjusting the screws. In practice a level surface is very important for the spreading of the solutions, thus the level was checked before each round of samples were prepared since the stainless steel tabletop of the fume hood was susceptible to warping over time presumably due to temperature gradients.

Lipids were weighed with a microbalance and mixed with a 1:1 solution of chloroform ($CHCl_3$) and 2,2,2-trifluoroethanol ($C_2H_3F_3O$) to a concentration of 20 mg/mL such that 20 mg of lipid would be deposited in a 1 mL deposition, forming ∼3000 bilayers. However, for sample protocol for the publication entitled "*Structure of Cholesterol in Lipid Rafts*" in which DPPC was the lipid species, the high transition temperature of DPPC (T_m=41°C) [91] and the volatile nature of the

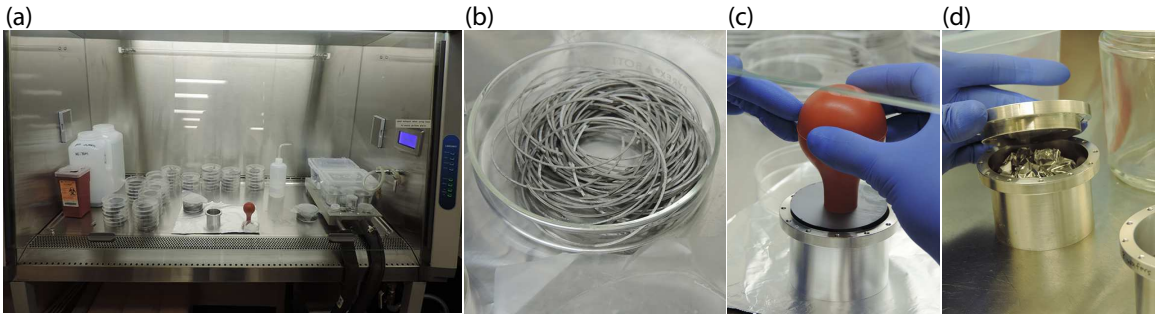

Figure 3.3: Stacked bilayers on wafers are housed in an aluminum sample can for a neutron scattering experiment on Let (Low energy transfer). (a) Laminar flow fume hood containing prepared wafers, spacers and sample can is the sample assembly area. (b) Two $\sim$ 300 μm thick semi-circular spacers are placed at the bottom of the sample can and between each wafer as it is placed in the can. The spacers allow room for water vapour to enter between the wafers. (c) Suction is applied to the unpolished (back) of the wafer. (d) The suction bulb releases the wafer and the wafer sits upon two spacers.

solvents caused the rapid evaporation where the solution would evaporate before reaching the edge of the wafer. Therefore a concentration of 16.67 mg/mL was deposited in a 1.2 mL aliquot was shown to give complete coverage. The solution was kept above the transition temperature of the lipids and deposited on a silicon wafer heated about 5°C above the lipid-specific transition temperature to ensure the lipids are always in the fluid phase until bilayer formation, i.e., solvent evaporation, was complete. After the solvent had evaporated (on the order of minutes) the wafers were placed in individual petri dishes and put into the vacuum oven overnight to ensure all traces of solvent were removed.

Petri dishes are then transferred to the incubator to hydrate and anneal. Wafers were placed in beakers sealed with heavy or light water (or salt solution) and placed in the incubator while at room temperature and the incubator temperature was increased to at least 5°C higher than the transition temperature in increments at a rate of 5 °C/hour. The incubator then housed the wafers for a minimum of 24 hours at above the transition temperature. The wafers were then put into their respective sample holders and/or sample cans.

For the publication entitled "*Anomalous and Anisotropic Nanoscale Diffusion of Hydration Water in Fluid Lipid Membranes*", the wafers were put into the Let sample cans as shown in Figure 3.3 (c) and (d) [2]. The sample can for the Let experiment was 2″ in diameter; the wafers needed to be carefully placed horizontally since even a slight angular deviation would cause the wafer to get stuck. A suction bulb was used to get a firm hold of the wafer's unpolished side. Once the wafer was safely on the spacers which were placed between each wafer, the wafer was released from the bulb. Once all 18 wafers were stacked, aluminum foil was lightly crumpled to provide tension on the wafers such that movement was impossible. A piece of filter paper cut into a 2″-diameter circle was moistened with 0.8 mL of H_2O and laid between the aluminum foil and the sample can lid. Before the lid was screwed on, a length of indium wire was pressed between the can and the lid

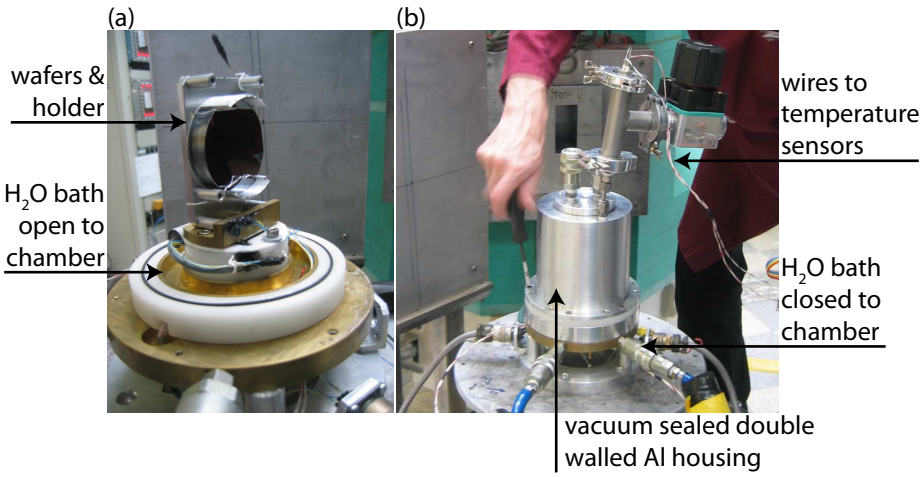

Figure 3.4: Sample in humidity chamber at the triple-axis spectrometer N5 at the Canadian Neutron Beam Centre in Chalk River, ON. (a) 15 wafers are stacked in a sample holder that is seated such that the wafers are vertical. Water sits in the brass well which is in contact with a water bath constantly pumping water through from a temperature controlled water source. (b) The sample is enclosed by the aluminum windows. Temperature sensors in the between the double wall give the temperatures of the inner wall at the top and at the middle of the window.

to ensure a proper seal. Aluminum screws were used to tighten the lid onto the sample can.

For the publication "*Structure of Cholesterol in Lipid rafts*", wafers were stacked into a sample holder as shown in Figure 3.4 (a). The sample holder is just over 2″ inner diameter such that when stacking the wafers and spacers, the top wafer was held in place by tension using aluminum foil. Figure 3.4 (a) shows the sample holder mounted onto a slab of aluminum for heat conduction and temperature sensing. The slab is mounted to the base of the sample chamber where a brass well holds temperature controlled water that flows through an inlet and outlet.

Figure 3.4 (b) shows the cover of the humidity chamber being sealed in order for the hydration of the sample to begin. The cover of the humidity chamber is a aluminum double-walled cylinders, the space between the walls have been evacuated to increase the insulating properties of the double-wall. Two temperature sensors at within the evacuated space were placed near the bottom and top of the cover to measure the temperature gradient within the chamber.

3.1.4 Preparation of a Hydrated Powder of Lipids

Experiments using highly concentrated lipid suspensions were concerned with direct contact of the hydrating solution with the lipids as opposed to a highly oriented sample. This leads to a much simpler preparation protocol of lipid bilayers than highly-oriented samples described previously.

DMPC and an aliquot of lipid-hydrating solution (water or water/ethanol solution) was pipetted onto the lipid powder in a ratio of approximately 1:3 to ensure full hydration. The paste was thoroughly but quickly mixed with a spatula before being sealed. Samples were measured at 20°C

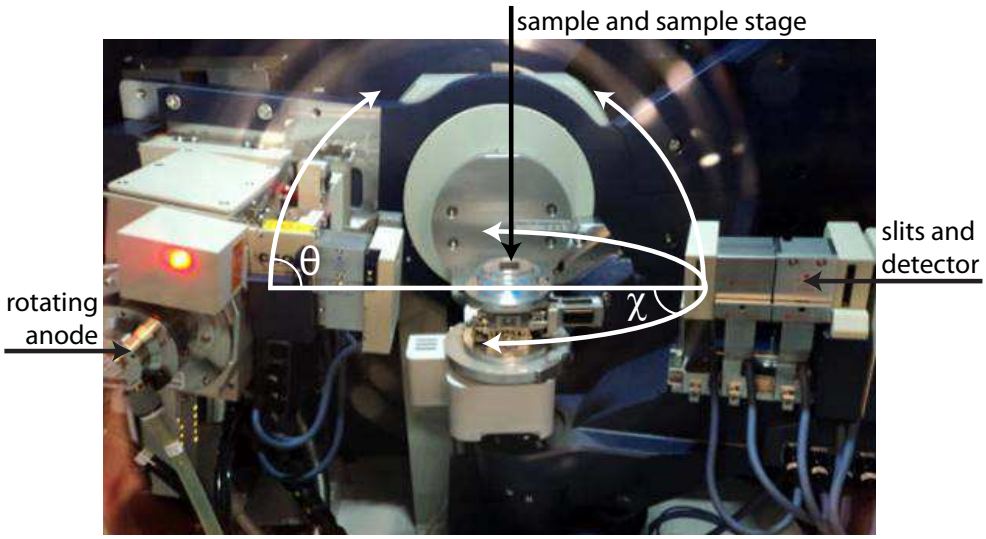

Figure 3.5: X-rays are generated from a moveable rotating anode. The beam is collimated by a series of slits. The X-rays are directed toward the sample and the scattered X-rays travel through another series of slits where they finally arrive at a point detector. The rotating anode moves in a plane about θ and the detector moves through θ and χ.

and 30°C.

X-ray experiments: A microbalance was used to measure approximately 15 mg of DMPC powder into the stone-ground depression (20 mm×20 mm×0.5 mm) of a quartz slide. Lipids were hydrated with either ultrapure H_2O or H_2O and ethanol in a 5 wt% solution. Once reasonably mixed, Kapton polyimide foil (13 μm thick) was then placed over the slide depression and sealed externally with vacuum sealant. Kapton was used to cover the suspension as it has a high transmittance to X-rays.

Neutron experiments: DMPC was measured to approximately 300 mg and mixed with D_2O or D_2O/deuterated ethanol (CD_3CD_2OD, 5 wt% solution). Once reasonably mixed, the suspension was spread onto the walls of an aluminum annulus and sealed.

3.2 X-ray Instrumentation

3.2.1 X-Ray Diffractometer: BLADE at McMaster University

All X-ray scattering data mentioned were obtained using the Rigaku SmartLab X-ray diffractometer within the Laboratory for Membrane and Protein Dynamics at McMaster University. This diffractometer is referred to as the Biological Large Angle Diffraction Experiment (BLADE), see Figure 3.5. X-rays are generated using a rotating anode which uses a 9 kW (45 kV, 200 mA) of power to generate X-rays peaked at a 1.5418 Å wavelength (CuKα). The rotating anode X-ray generator is a vacuum sealed enclosure in which electrons are ejected from a high-voltage filament, by thermionic emission, and travel toward a copper target. The target is rotating and also water-cooled in order to dissipate

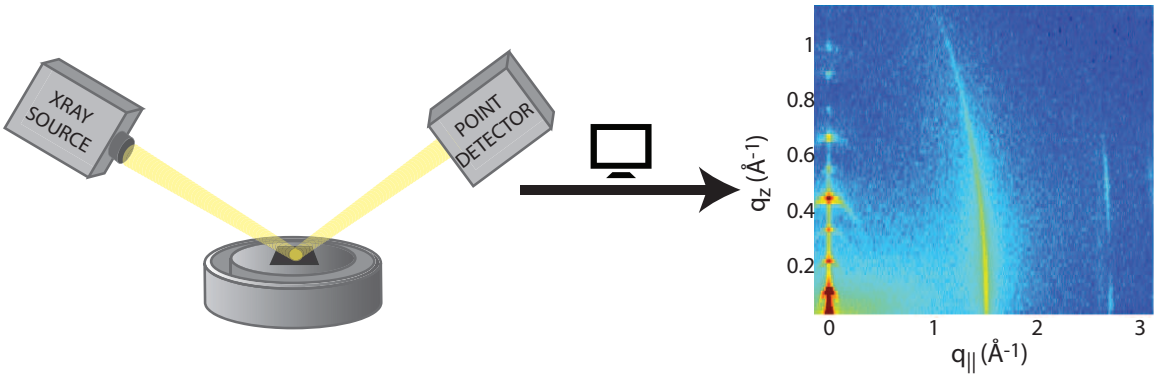

Figure 3.6: X-rays are generated from a rotating anode that is allowed to move along an arc. The collimated beam of X-rays is incident on the sample and the scattered X-rays are detected by a point detector that can move through angles θ and χ. A two-dimensional intensity map is constructed.

heat over a large area, thus ensuring a consistent X-ray flux.

The X-rays emitted as a result of the transition from the two innermost electron shells (L→K) of the copper molecules are selected for use. This radiation is Kα radiation and is much more intense than the broad spectrum of *Bremsstrahlung*, which is emitted when the fast moving electrons are quickly slowed by the copper anode.

A multi-component optics assembly allows our X-ray beam to be both intense and highly collimated. On the way to the sample the X-rays travel through the cross-beam optics (CBO) system, which uses a parabolic multi-layer mirror and a selection slit [92] to generate a parallel beam through focusing. Once the X-rays are scattered from the sample the combination of Soller-slit and parallel-slit analyser directs the scattered X-rays to the "0D" scintillation counter [93]. BLADE's beam geometry provides intensities of up to 10^{10} counts/(mm^2/s), this high-intensity illumination of the samples ensures a high scattering signal. The detector can move up and down along an arc, θ and side-to-side along an arc, this angle χ is shown in Figure 3.5. We commonly measure one-dimensional data, only scanning θ, as in the case of the detection of Bragg peaks (i.e., χ=0). We also commonly measure two-dimensional data, scanning through θ and χ, as is shown in Figure 3.6.

The stacked nature of our system means that by measuring the scattering along the direction of the bilayer normal, we can find the repeat spacing height, d_z, of the membranes by using information from the Bragg reflections using Bragg's law:

$$n\lambda = 2d_z \sin\theta\,. \tag{3.1}$$

Figure 3.7 illustrates this law with Bragg angle, θ, lamellar spacing, d_z where each lamella includes two bilayer leaflets and the water layer between the head groups. The term $2d_z \sin\theta$ is the path length difference between two rays that scatter from the lamellae and constructively interfere. n is the order of the Bragg peak.

Information from the measurement of the out-of-plane Bragg peaks from the membrane stacks

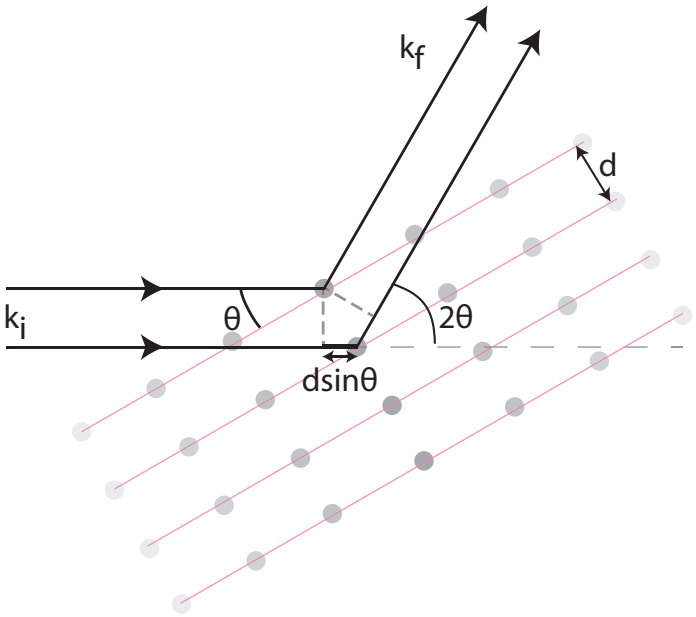

Figure 3.7: A wave with wave vector $\vec{k_i}$ is incident upon a set of planes at an angle θ to the planes. The specularly reflected wave vector $\vec{k_f}$ is scattered at an angle 2θ from $\vec{k_i}$, which is θ from the planes. Bragg's law relates the wavelength of the ray to the path length difference of the light scattered off the planes.

allows the determination of a density profile perpendicular to the plane of the membranes. With X-ray scattering we determine the electron density profile, whereas for neutron scattering we determine a scattering length density profile as is outlined in Section 3.3.1. The Fourier transform in this case is discrete due to the convolution with the lamellar structure factor. The integrated intensities of the out-of-plane Bragg peaks are simply the Fourier components. We use one-dimensional Fourier analysis to approximate the electron density, $\rho(z)$,

$$\begin{aligned} \rho(z) &= \rho_W + \frac{F(0)}{d_z} + \frac{2}{d_z}\sum_{n=1}^{N} F(q_n)\nu_n \cos(q_n z) \\ &= \rho_W + \frac{F(0)}{d_z} + \frac{2}{d_z}\sum_{n=1}^{N} \sqrt{I_n q_n}\nu_n \cos\left(\frac{2\pi n z}{d_z}\right), \end{aligned} \tag{3.2}$$

where N is the highest order of observed Bragg peaks and ρ_W the electron density of water (or other solvent). I_n are the integrated peak intensities, which are combined with the q_z value at which the peak occurs, q_n, to obtain the form factors, $F(q_n)$. The membrane form factor $F(q_z)$, is in general a complex quantity; however, in this case it is real-valued due to centro-symmetry. Therefore, the phase problem of crystallography simplifies to the sign problem: $F(q_z) = \nu_n|F(q_z)|$. A given phase can only take on two values, $\nu_n = \pm 1$. By measuring the bilayer form factor F(q_z) at several q_z

values, we can construct a related, continuous function, T(q_z),

$$T(q_z) = \sum_n \sqrt{I_n q_n} sinc\left(\frac{1}{2} d_z q_z - \pi n\right), \tag{3.3}$$

which can be fit using the data. Fitting the Bragg peak intensities from the data allows for an analytical expression of $T(q_z)$, from which the phases, ν_n can be assessed. The determination of electron density profiles for gel and fluid phase membranes with hydrated with and without ethanol can be seen in "*Partitioning of ethanol into lipid membranes and its effect on fluidity and permeability as seen by X-ray and neutron scattering*" [3].

3.3 Neutron Instrumentation

3.3.1 Neutron Reflectometer: OFFSPEC at ISIS

Neutron reflectometers employ the principles of Bragg diffraction, similar to X-ray diffractometers as discussed in Section 3.2.1. However, this section will be concerned with the advantages of specular reflection of neutrons from our bilayer samples. By treating the neutron as a plane wave with wave vector $\vec{k}$, and measuring the coherent, elastically scattered neutrons, we can use this specular reflection from the sample to gain information about the structure perpendicular to the plane of the membranes. Specular reflection is the reflection captured at angle θ, where the neutrons are incident on the sample at the same angle θ as shown in Figure 3.7 described by Bragg's law, Eq. (3.1).

Since neutron sources tend to have a fixed source (unlike X-ray sources that may change the location of their source) the angle subtended by the incident beam and sample normal is controlled by changing the angle of the sample, while the detector is confined to have an angle of 2θ from the incident beam. For specular reflection, the scattering must be in the same plane, thus, the sample and detector are rotated and moved, respectively. If the incident wavelength is held constant, the scattered neutrons can be measured as a function of $|\vec{Q}|$

$$|\vec{Q}| = |\vec{k}_f - \vec{k}_i| = \frac{4\pi \sin\theta}{\lambda}\,.$$

By measuring the fluctuations in specular intensity as a function of angle or scattering vector, we can obtain the density profile perpendicular to the plane of our solid-supported, oriented membranes. The density profile can allow us to assess, for instance, the level of hydration, the structure of the bilayers [2], or compare to a system with and without a particular molecule to locate the molecule in the bilayers. The profiles are generated using Eqs. (3.2) and (3.3) as in Section 3.2.1; however, instead of electron density as for X-rays, this technique generates a neutron scattering length density (NSLD) profile.

A neutron scattering length density profile is the weighted average of the coherent neutron scattering lengths b_i per volume element (on the order of the wavelength of the neutron), divided by the volume of the volume element. In general the scattering length density may be three-dimensional.

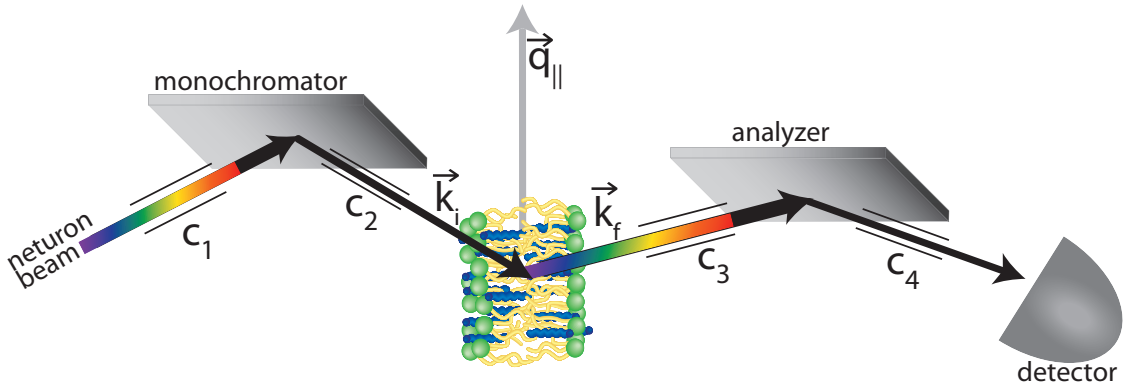

Figure 3.8: A schematic of a triple-axis spectrometer. The three axes of a triple-axis spectrometer are the rotation axes of (1) the monochromator, (2) the sample, and (3)the analyser. The white beam from the reactor is incident on the monochromator, the single wavelength beam is then incident on the sample. The sample scatters neutrons with various $|\vec{k_f}|$ values and a single value of $|\vec{k_f}|$ is chosen by the analyser which is then directed toward the detector. Collimators, c_1, c_2, c_3, c_4, are shown in each leg of the beam.

For our membrane samples, it is assumed that the scattering length densities are decoupled such that the in-plane ($\text{NSLD}_{xy} = \rho(x, y)$) and out-of-plane ($\text{NSLD}_z = \rho(z)$) profiles are independent. The advantage of neutrons is that for the same system, such as hydrated lipid bilayers, hydrogens may be replaced by deuterium atoms to change the scattering of the labelled portion of the sample. For instance, we can highlight the water or the acyl tails in a the sample by using D_2O or tail-deuterated lipids.

We performed experiments on the neutron reflectometer at OFFSPEC at ISIS, the pulsed neutron and muon source at the Rutherford Appleton Laboratory in Oxfordshire, UK [94]. The samples were stacked DMPC bilayers hydrated with water, and they were deuterated as follows; (1) DMPC/H_2O, (2) DMPC/D_2O, and (3) tail-deuterated DMPC/H_2O. These three samples having different deuterium labelling were assessed and the extent of the water layer, head group, acyl chains were determined [2]. This structure is contained within the submission entitled "*Anomalous and Anisotropic Nanoscale Diffusion of Hydration Water Molecules in Fluid Lipid Membranes*". Our experiment used OFFSPEC in reflectometer mode. OFFSPEC can be used in multiple modes like neutron spin echo spectrometer, which is not covered in this thesis.

3.3.2 Triple-Axis Spectrometer: N5 at Canadian Neutron Beam Center

Bertram Brockhouse built the first triple-axis spectrometer in 1955 at Chalk River Laboratories in Chalk River, Ontario Canada. This spectrometer design has been widely used and is invaluable for studying thermal and magnetic fluctuations by measuring inelastic scattering, or structure and dynamics by measuring elastic and quasi-elastic scattering. Our main use of the triple-axis spectrometer was to determine the structure of solid-supported, highly oriented membrane samples by measuring

in-plane scattering. The three axes referred to are the rotation axes of the monochromator, sample, and analyser. These are shown in a schematic of a triple-axis spectrometer in Figure 3.8. The monochromator selects a beam of a single energy from the broad distribution of energies in the main beam (called a white beam). A single crystal material, such as copper, silicon, pyrolytic graphite (PG), Bragg reflects the neutrons at an angle θ_m. Absorptive shielding houses the monochromator, while an opening allows for the monoenergetic neutron beam with well-defined wave vector $\vec{k}_i$ is incident on the sample.

After the neutrons have scattered from the sample, these neutrons subtending a Bragg angle of θ_s will then be Bragg reflected by the analyser (scattered at angle θ_a) to the detector [87]. However, only those with a scattered wave vectors that satisfy the Bragg condition of the analyser reach the detector. On the N5 triple-axis spectrometer incident and final neutron energies are defined by the Bragg reflections from PG monochromator and analyzer crystals. Soller collimators were positioned on each leg of the beam, labeled c_{1-4} in Figure 3.8, and determined the beam divergence.

The goal of the monochromator to select single-wavelength (or single energy) beam is impractical due to low flux. In practice, typical experiments wanting to achieve high monochromaticity or energy resolution will try to minimize the spread in wavelengths, $\Delta\lambda$, which equates to minimizing the spread in energy, ΔE. Minimizing ΔE serves to maximize the energy resolution $\frac{\Delta E}{E}$.

We can define the longitudinal coherence length ξ which is dependent on the monochromaticity as [95, 10]

$$\xi = \frac{\lambda^2}{\Delta\lambda} \sim \frac{18\sqrt{E}}{\Delta E}\,. \tag{3.4}$$

The coherence length can be described as the length scale upon which two waves coherently interfere and in practice this amounts to the length scale over which the beam is averaging over the structure of the sample. The energy spread, ΔE is determined by the incident wavelength, the angular divergence of the beam, and the resolution of the monochromator and analyser. Thus in order to change the coherence length, these quantities must be changed.

In hard condensed matter experiments where samples are crystalline and have long range order, a long coherence length is desirable. However, in a soft matter system such as the lipid and cholesterol system outlined in the publication entitled "*Cholesterol Structure in Lipid Rafts*", a long coherence length can lead to the observation of an average structure dominated by the surrounding structure causing the small domains to possibly be averaged out [4]. By reducing the incident wavelength, the coherence length was decreased and we were able to observe both small domains and the surrounding structure. In our study, the wavelength was changed from 2.37 Å to 1.48 Å and 1.44 Å while the collimation was fixed at c_1=30′, c_2=18′, c_3=28′, c_4=60′ and the monochromator and analyzer resolutions stayed constant. Coherence lengths calculated for each wavelength are ξ=90.9, 33.9, and 32.1 Å respectively. The energy resolutions used to calculate the coherence lengths were calculated using the ResLib software package [96], adapted for the N5 spectrometer.

The elastic mode was used in these structural measurements of oriented samples, where the monochromator and analyzer were fixed and $\vec{Q}$ was scanned by changing the angle of the detector,

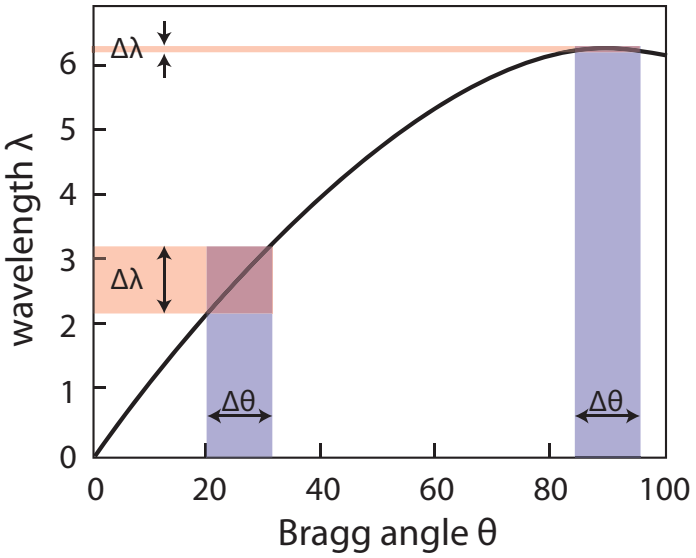

Figure 3.9: Plot of wavelength λ, as a function of Bragg scattering angle θ. For a range of $\sim 10°$ of incident wave vector directions (i.e., a 10° divergence) the reflected wavelength will have a much less spread in wavelengths i.e., a more monochromatic beam, close to backscattering (90°) than at a lower angle. Adapted from "*Neutron and X-ray Spectroscopy*" [98]

carving out an arc around the sample. The comparison of measurements at different wavelengths has previously been reported to efficiently integrate over small structures while providing the high spatial resolution to detect them [9, 10, 97].

3.3.3 Backscattering spectrometer: HFBS at NIST

Heinz Maier-Leibnitz in 1966 was first to suggest the neutron backscattering spectrometer in order to drastically increase energy resolution [99]. This high energy resolution is the main advantage of backscattering spectrometers, which allows physical properties of samples to be measured out to long time scales. The geometry of the system serves to fix the wave vector incident on the sample, $|\vec{k}_i|$, and measure a variety of scattered wave vectors, $|\vec{k}_f|$, determining the values of these wave vectors very precisely. For the case of a collimated neutron beam, the backscattering spectrometer uses a white beam (whether pulsed or continuous), which is sent to a single-crystal monochromator from which it is Bragg reflected such that the Bragg angle is $\theta = 90°$, i.e., the difference between the directions of wave vectors incident and scattered from the monochromator is 180°. The reasoning behind this configuration is illustrated in Figure 3.9, which shows that the spread in wavelength at a Bragg angle around 90° is much smaller than at a lower angle 25°.

From the monochromator, the single-wavelength beam is incident on the sample. After the neutrons are scattered from the sample they travel to the analyser, which selects a single wavelength of neutron, and directs only this selection through the sample to the detector as shown in Figure 3.10. It should be noted that beams typically have some divergence $\Delta\theta$, and focussing and/or steering

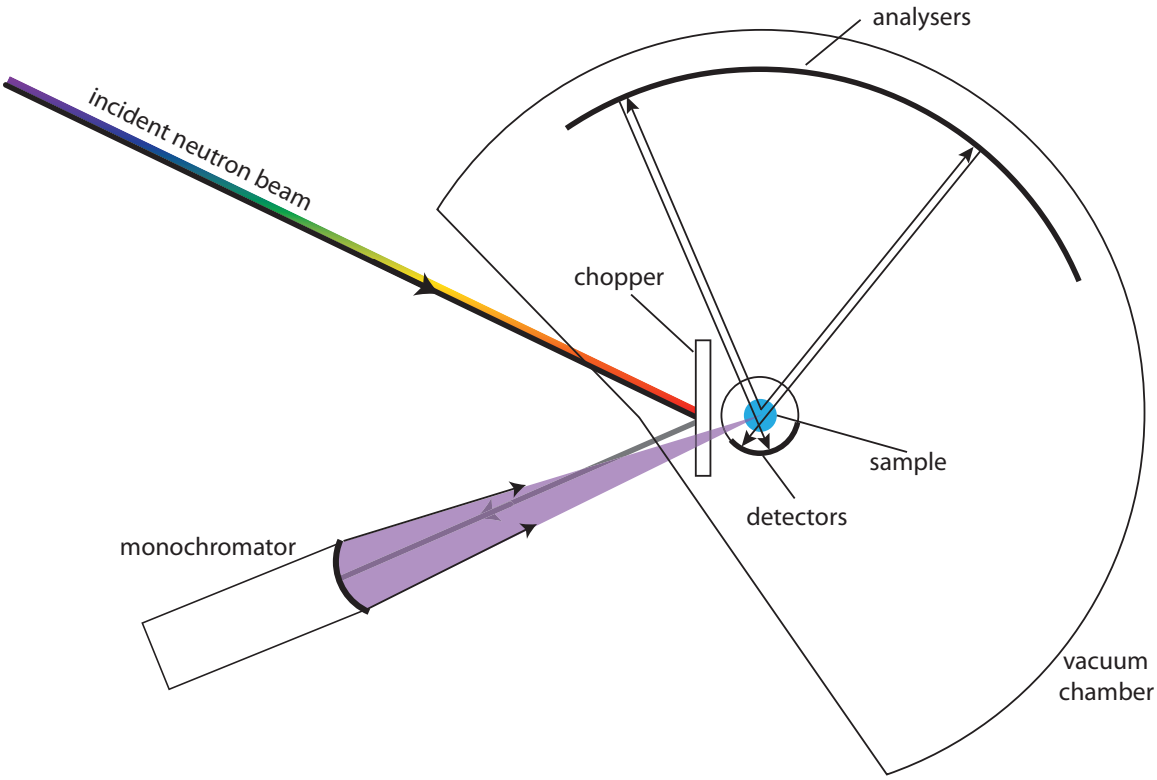

Figure 3.10: Schematic of a backscattering spectrometer with the geometry and configuration of the high-flux backscattering spectrometer (HFBS) at NIST. A white beam of neutrons is deflected by the chopper which sends the main beam to the monochromator where it exits as a single wavelength. This monochromatic beam is incident on the sample (blue), where the scattered neutrons are scattered from the analysers back through the sample to the detectors.

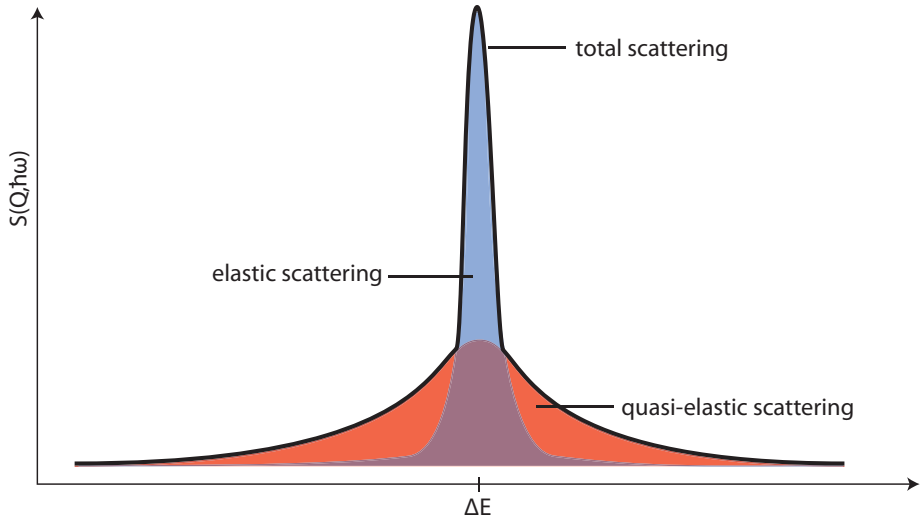

Figure 3.11: Schematic of elastic and quasi-elastic scattering from neutrons. Elastic scattering from a sample is typically modeled by a narrow Gaussian curve. Quasi-elastic scattering occurs as lower-amplitude with broad wings, commonly modeled as a Lorentzian function.

elements are present along the beam line and the backscattering angle of 180° cannot always be met in every instrument i.e., the Bragg scattering occurs at θ=90° + ϵ.

In practice, perfect collimation is not attainable and a neutron beam will have a spread of incident neutron angles $\Delta\theta$, which will have the same $\Delta\theta$ after the monochromator, but will introduce variation in k, Δk. By taking the differential of Bragg's law ($n\lambda = 2d\sin\theta$) we find [98, 100]

$$\frac{\Delta\lambda}{\lambda} = \frac{\Delta\theta}{\tan\theta} + \frac{\Delta d}{d} \sim \frac{\Delta k}{k}\,. \tag{3.5}$$

If θ approaches 90°, $\Delta\lambda/\lambda$ only depends on the spread of lamellar (or lattice) spacings Δd divided by the average lamellar spacing d. For a small $\Delta\theta$, the energy resolution is

$$\frac{\Delta E}{E} = \frac{k_{max} - k_{min}}{k} = \frac{1}{\cos(\Delta\theta/2)} - 1 \approx \frac{(\Delta\theta)^2}{8}\,. \tag{3.6}$$

Backscattering spectrometers similar to the High Flux Backscattering Spectrometer (HFBS) at NIST focus the white beam such that the flux of the beam is large; however, the divergence is also high. The problem of reflecting a highly divergent beam from a flat surface is solved by reflecting from a spherical monochromator, in this way the backscattering condition can be satisfied and flux can remain high [98]. In this setup, the energy resolution is determined by the waist of the focus and the distance from the focus to the monochromator. After scattering from the sample, the neutrons encounter a spherical set of analyzer crystals which focuses the neutrons onto the detectors. On the way to the sample, the beam is intercepted by a deflecting chopper which allows the detector to discriminate between neutrons scattered from the analyzer and directly from the sample.

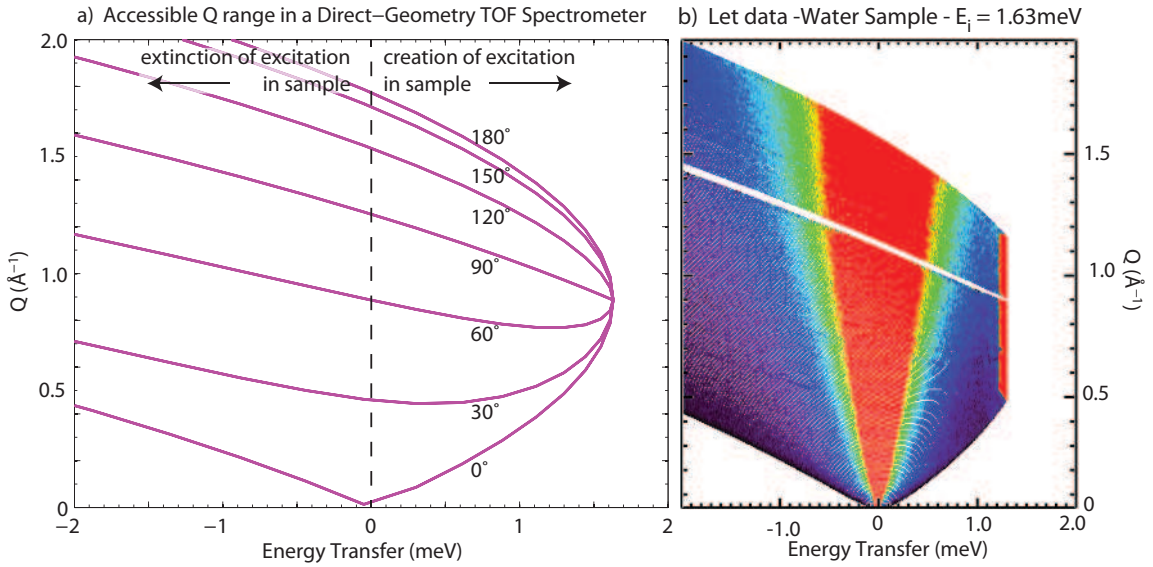

Figure 3.12: Plot of the accessible ranges of momentum transfer. a) Theoretical accessible range for momentum transfer, Q and energy transfer $\hbar\omega$ using Equations (2.6,2.2); for an incident neutron energy of 1.63meV and an angular range of 0°-180°. b) Data from Let time-of-flight spectrometer for an incident neutron energy of 1.63 meV.

The neutron experiment carried out at the high-flux neutron backscattering spectrometer HFBS at the NIST Center for Neutron Research (NCNR), Gaithersburg, [100] is used in two publications covered in this thesis where both elastic and quasi-elastically scattered neutrons were measured, these types of scattering are illustrated in Figure 3.11. The standard setup for this instrument uses Si(111) both for monochromator and analyzer crystals. The instrument is set with a wavelength of $\lambda = 6.27$ Å, corresponding to an incident energy of 2.08 meV and can reach sub-μeV energy resolution. HFBS is used in "*Hydration water freezing in single supported lipid bilayers*" to measure the intensity of elastically scattered neutrons within a fixed energy window as a function of temperature to determine dynamics of various membrane components [1]. This backscattering instrument was also employed in "*Partitioning of ethanol into lipid membranes and its effect on fluidity and permeability as seen by X-ray and neutron scattering*" to measure incoherent quasi-elastic scattering from the lipids (hydrated with and without ethanol) producing spectra of $S_{inc}(Q, \hbar\omega)$, which was modeled to find the diffusive motions of the bilayers [3].

3.3.4 Time-of-Flight Spectrometer: Low Energy Transfer at ISIS

The general properties of a direct-geometry time-of-flight (TOF) spectrometer are discussed concerning the measurement of incoherent quasi-elastic neutron scattering and details of the Let spectrometer at ISIS will follow.

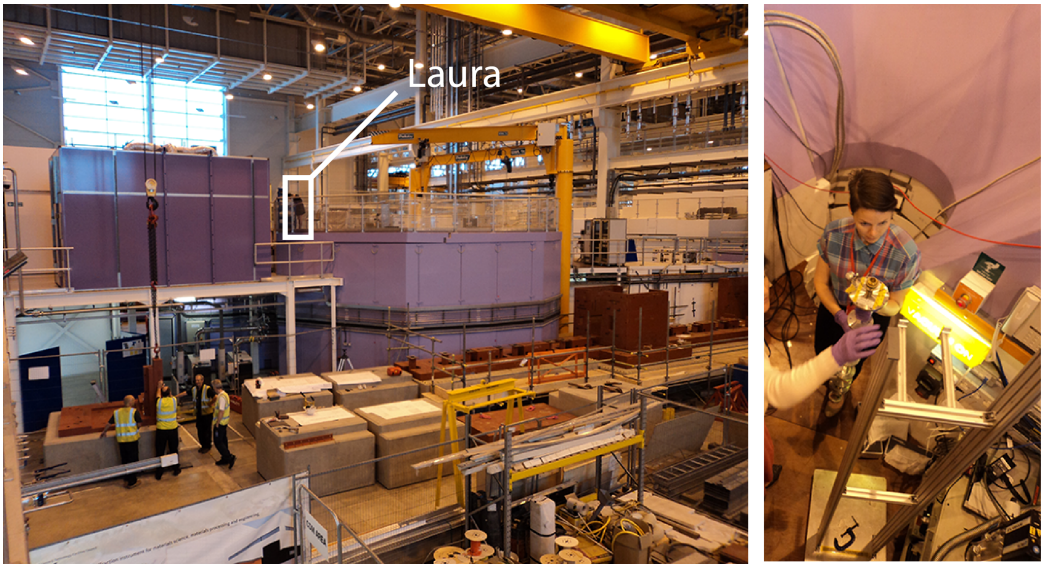

Figure 3.13: Photographs of Let. Left photograph shows the scale of the instrument from its exterior. I stand $5'6''$ atop of the instrument. Right photograph is the aluminum sample stick, having screwed our sample can to the bottom, the sample is ready to be put into the beam.

Two quantities are commonly measured on TOF spectrometers, the momentum transfer and energy transfer

$$\begin{aligned} \hbar\vec{Q} &= \hbar(\vec{k}_f - \vec{k}_i)\,, \\ \hbar\omega = E_f - E_i &= \frac{\hbar^2}{2m_n}\left(k_f^2 - k_i^2\right)\,, \end{aligned}$$

where subscripts i and f denote quantities prior to and after scattering and m_n is the neutron mass. Positive $\hbar\omega$ denotes the sample losing energy to the neutron, which gains that energy. However, energy transfer is commonly discussed with respect to the sample as opposed to the neutron as is shown in Figure 3.12.

Travelling from the reactor or spallation source, the white neutron beam is monochromated by a series of mechanical choppers that rotate with a specific frequency in order to select the allowed neutron velocity. The choppers are commonly coated with a neutron absorbing material such that the neutrons that are not permitted through the chopper cannot be erroneously scattered through the choppers. These choppers also serve to pulse the neutron beam in time, and each pulse is scattered from the sample and the scattered neutrons are timed, as they travel the known sample-detector distance [87]. For the case of spectrometers, such as Let at ISIS or IN5 at the Institut Laue-Langevin, two-dimensional detector banks with long, straight rods set on the arc of a circle making the detector a partial cylinder, this arrangement is illustrated in Figure 3.14.

The resolution of such spectrometers is limited by how well the velocity of the neutrons can be measured. This is determined by the speed with which the choppers can rotate and the divergence

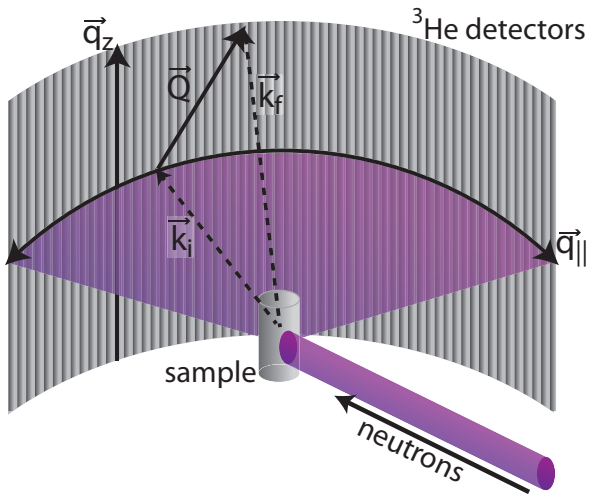

Figure 3.14: Schematic of the low energy transfer time-of-flight instrument at ISIS. Schematic shows a neutrons incident on the sample in the center and the scattered neutrons incident upon position sensitive ^{3}He detectors.

of the beam incident on the sample i.e., the uncertainties in the neutron flight paths.

The observable range of $\vec{Q}$ is illustrated in Figure 3.12 for a fixed incident neutron energy. Here, the energy transfer is with respect to the sample, positive energy transfer is a gain in energy to the sample while a negative transfer is a loss. Figure 3.12 (a) shows the kinematic limits for E_i=1.63 meV calculated from Eq. 2.7 and Figure 3.12 (b) is data from a bulk water sample at Let with incident energy E_i=1.63 meV [2]. The positive energy transfer denotes the increase in energy of the sample and hence "turns over" at 1.63 meV since the sample cannot gain more energy than that possessed by the incident neutron. The negative side of the energy transfer represents the sample losing energy, thus the neutron acquires this energy. A large range of energy can be transferred from excitations of the sample as there can be many populated excitations in the sample.

The incoherent quasi-elastic neutron scattering experiments in the submission entitled "*Anomalous and Anisotropic Nanoscale Diffusion of Hydration Water Molecules in Fluid Lipid Membranes*" were carried out at the direct-geometry Low-energy-transfer (Let) spectrometer [101, 102, 103] at ISIS, the pulsed neutron and muon source at the Rutherford Appleton Laboratory in Oxfordshire, UK. Some pictures of the instrument are shown in Figure 3.13. Disc-choppers were set to speeds of 200 Hz and 80 Hz (pulse removal) in order to select 5 pulses of neutrons with energies 0.64, .96, 1.62, 3.28, and 9.80 meV. The chopper frequencies were chosen such that frame-overlap did not occur, thus ensuring scattering from a particular pulse could not be mistakenly detected from another incident pulse.

The detectors on Let are position-sensitive detectors where the in-plane and out-of-plane scattering from our oriented samples can be distinguished. A schematic of the general setup of Let is shown in Figure 3.14. The detectors are filled with ^{3}He which acts as an absorbing material to foster

the reaction [87]

$$^3\text{He} + \text{neutron} \rightarrow ^3\text{He} + \text{proton} + 0.8\text{MeV}\,. \tag{3.7}$$

This reaction causes the products to be ejected in opposite directions having resultant energies which are inversely proportional to their masses. These particles ionize the surrounding gas and a high-voltage anode collects the ionized particles. Because of the high voltage of the anode, the electrons are highly accelerated and ionize the gas causing an electron avalanche [87]. The detector tubes are pressurised to 10 bar partial pressure and the scattered neutrons are collected with an angular range vertically of $\pm 30^\circ$ and horizontally from -10° to 70°; however, after increasing the number of detector banks, the horizontal range was increased to 120°. The detectors are 3.5 m from the sample and the tubes are 4 m high and 2.5 cm in diameter.

Chapter 4

Properties of Hydration Water in Fluid Lipid Membranes: Publications I & II

4.1 Introduction

Biological membranes are complex entities, having many components serving many functions reflected by various dynamic properties. We model a biological membrane by using a hydrated lipid bilayer, where motions of lipids and water can be observed. Biological membranes are modelled throughout this thesis by hydrated phospholipid bilayers in their fluid phase. Though the lipids form the bilayer that acts as the envelope to protect cells from their external environment, water is essential for the biological relevance of the bilayer as cells are surrounded by fluid. Water is not simply a structureless solvent for the membrane, but, forms hydration shells around phospholipid head groups that are less dense than the bulk water, as is evidenced by our elastic scattering experiment [1]. However even bulk water forms a hydrogen bonded network and it is this network that is responsible for bilayer formation [13].

The two papers discussed in this chapter focus on the properties of hydration water in model membrane systems. We set out to characterize the diffusive motions of hydration water and how the motions of lipids and the hydrating water are related. We found that the hydration water (D_2O) of single, solid-supported phospholipid bilayers has two freezing transitions suppressed below the freezing transition temperature of bulk D_2O, T_m=277 K. These suppressed transitions and their coupling to the membrane dynamics from these elastic experiments are evidence for the existence of water that is tightly and loosely bound to the phospholipid head groups. The behaviour of hydration water observed in Publication I was the impetus for the investigation of quasi-elastic scattering from membrane hydration water in Publication II. It was in this second publication that we observed the

anomalous behaviour of the hydration water due to its experience of different environments, such as water near or far from the membrane. We also found that motion of the hydration water of these solid-supported membranes is anisotropic due to geometrical confinement due to the presence of the membrane.

The following publications are contained in this chapter.

Publication I: "*Hydration Water Freezing in Single Supported Lipid Bilayers*", Laura Toppozini, Clare L. Armstrong, Martin D. Kaye, Madhusudan Tyagi, Timothy Jenkins, and Maikel C. Rheinstädter ISRN Biophysics, vol. 2012, Article ID 520307, 7 pages

Publication II: "*Anomalous and Anisotropic Nanoscale Diffusion of Hydration Water in Fluid Lipid Membranes*", Laura Toppozini, Felix Roosen-Runge, Robert Bewley, Robert Dalgliesh, Henry R. Glyde, Toby Perring, Victoria García Sakai and Maikel C. Rheinstädter Soft Matter, DOI: 10.1039C5SM01713K

4.2 Preface to Publication I: "*Hydration Water Freezing in Single Supported Lipid Bilayers*"

In order to study the interaction between this model membrane and its hydration water, we model a biological interface: a highly-oriented single bilayer membrane attached supported by a silicon substrate. This perfect model interface allowed for the investigation of basic properties and interactions in great detail. Using single bilayers in dynamical neutron scattering experiments is challenging, predominantly due to the small scattering signals from the small amount of sample material. However, neutron instruments with large flux and good energy resolution, such as the High-Flux Backscattering Spectrometer (HFBS) at NIST, Gaithersburg, Maryland, USA have made it possible for single bilayers to be studied.

In this publication, we report the freezing and melting transitions of hydration water of single, solid-supported, lipid membranes. A freezing transition was observed at T = 271 K, suppressed from bulk D_2O's freezing transition at T=277 K, upon slow cooling of the sample from 290 K to 240 K. This transition has been observed in other studies of single lipid bilayers, such as that by Armstrong *et al.* [90]. Lipid diffusion, lipid tail dynamics, and hydration water dynamics were observed simultaneously by analysing the length scale dependence of elastic neutron scattering from single lipid bilayers hydrated with D_2O. Elastic scattering from a fixed energy-window (FEW) centered around zero energy transfer was collected as the sample temperature was scanned through the freezing transition; this is referred to as a fixed energy window scan. We observed nanosecond motions of membrane components from elastic coherent and incoherent neutron scattering on the HFBS instrument at NIST. Additional freezing and melting transitions observed were assigned membrane motions, such as membrane dynamical degrees of freedom. By comparing freezing and melting temperatures in the various detectors, we were able to assign transitions to the corresponding membrane

dynamics and study coupling between hydration water, lipid diffusion, and lipid acyl-tail dynamics. This technique is very sensitive to freezing and melting transitions. We observed two freezing transitions for hydration water that were suppressed below the bulk freezing transition, which gives evidence for tight and loose binding of water to lipid head groups. This observation supports the existence of hydration shells of hydration water around the lipid head group. By comparing the temperatures of the transitions for the different membrane components we observe that the membrane and the hydration water dynamics are partially decoupled. This is in opposition to the commonly held opinion that strong coupling exists between water and lipid dynamics for this hydrated single bilayer system.

Author Contributions:

- *Experimental Concept:* Maikel Rheinstädter, Madhusudan Tyagi, Timothy Jenkins
- *Sample Preparation:* Maikel Rheinstädter
- *Execution of Neutron Experiments:* Madhusudan Tyagi, Timothy Jenkins, Maikel Rheinstädter
- *Data Analysis:* **Laura Toppozini**, Maikel Rheinstädter
- *Manuscript Preparation:* **Laura Toppozini**, Maikel C. Rheinstädter, Clare L. Armstrong, Martin D. Kaye

International Scholarly Research Network
ISRN Biophysics
Volume 2012, Article ID 520307, 7 pages
doi:10.5402/2012/520307

Research Article

Hydration Water Freezing in Single Supported Lipid Bilayers

Laura Toppozini,[1] Clare L. Armstrong,[1] Martin D. Kaye,[1] Madhusudan Tyagi,[2,3] Timothy Jenkins,[2] and Maikel C. Rheinstädter[1,4]

[1] *Department of Physics & Astronomy, McMaster University, 1280 Main Street West, Hamilton, ON, Canada L8S 4M1*
[2] *NIST Center for Neutron Research, NIST, Gaithersburg, MD 20899, USA*
[3] *Department of Materials Science and Engineering, University of Maryland, College Park, MD 20742, USA*
[4] *Canadian Neutron Beam Centre, National Research Council Canada, Chalk River, ON, Canada K0J 1J0*

Correspondence should be addressed to Maikel C. Rheinstädter, rheinstadter@mcmaster.ca

Received 2 January 2012; Accepted 31 January 2012

Academic Editors: J. P. Bradshaw, L. Loura, and J. Perez-Gil

We present a high-temperature and high-energy resolution neutron scattering investigation of hydration water freezing in single supported lipid bilayers. Single supported lipid bilayers provide a well-defined biological interface to study hydration water dynamics and coupling to membrane degrees of freedom. Nanosecond molecular motions of membrane and hydration water were studied in the temperature range 240 K < T < 290 K in slow heating and cooling cycles using coherent and incoherent elastic neutron scattering on a backscattering spectrometer. Several freezing and melting transitions were observed. From the length scale dependence of the elastic scattering, these transitions could be assigned to freezing and melting of hydration water dynamics, diffusive lipid, and lipid acyl-tail dynamics. Coupling was investigated by comparing the different freezing and melting temperatures. While it is often speculated that membrane and hydration water dynamics are strongly coupled, we find that membrane and hydration water dynamics are at least partially decoupled in single bilayers.

1. Introduction

Despite the vast potential for applications of single membranes in biotechnology and fundamental research [1, 2], experiments using single membranes are challenging, mainly because of the small amounts of sample material and corresponding small sample signals. Recent developments in neutron scattering instrumentation, and the increasingly powerful neutron sources, have made it possible to experimentally address molecular dynamics in single bilayers. Lipid diffusion in single supported bilayers made of DMPC (1,2-dimyristoyl-sn-glycero-3-phosphatidylcholine) was studied recently using quasielastic neutron scattering [3]. A freezing transition at T = 271 K was reported and associated with freezing of hydration water molecules. Here, we used solid-supported single-lipid bilayers as a well-defined biological interface to study freezing and melting of hydration water and membrane.

We report a high-energy and temperature-resolution neutron scattering study using a backscattering spectrometer in a temperature range between 240 K and 290 K. While the temperature range 100 K < T < 220 K was investigated thoroughly in the literature to study the so-called "dynamical transition" in hydrated protein and membrane systems, much less attention was paid to the onset of freezing at 271 K in the past. By analyzing the length scale dependence of the elastic coherent and incoherent scattering, freezing of hydration water and membrane dynamics was observed, and the corresponding freezing and melting temperatures determined. Single supported bilayers of the model membrane system DMPC were prepared on silicon wafers, as shown in Figure 1. Diffusion of lipid molecules, lipid acyl-tail dynamics, and dynamics of hydration water molecules were studied simultaneously using protonated lipids, hydrated by heavy water (D_2O). We measured nanosecond molecular dynamics on the High Flux Backscattering Spectrometer (HFBS) at the

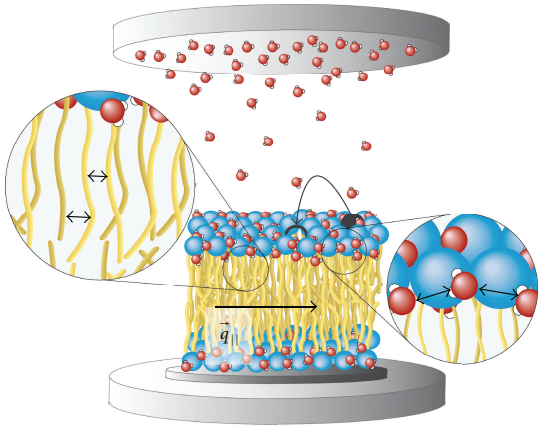

Figure 1: Sketch of a hydrated, single supported lipid bilayer, as suggested by [4–6]. Some of the hydration water molecules are drawn. The momentum transfer, $\vec{Q}$, in the neutron scattering experiments was in the plane of the bilayers ($\vec{q}_{\parallel}$) to detect in-plane motions of lipid and hydration water molecules. The experiment was sensitive to lipid diffusion, lipid acyl chain and hydration water dynamics.

NIST Center for Neutron Research, Gaithersburg, via elastic neutron scattering experiments. Fixed energy-window scans (FEW-scans) centered at zero energy transfer were recorded as a function of sample temperature to probe molecular motions on a time scale as long as ~1 ns. A freezing transition at $T = 271$ K was observed upon slow cooling of the sample. This transition has previously been observed not only in single supported [3] but also in stacked membrane systems [7–10] and was assigned to freezing of membrane hydration water. We find evidence for additional freezing and melting transitions that we assign to hydration water molecules and membrane dynamical degrees of freedom. Coupling between hydration water, lipid diffusion, and lipid acyl-tail dynamics was studied by comparing the corresponding freezing and melting temperatures.

2. Materials and Methods

2.1. Sample Preparation. Single supported bilayers of the model system DMPC supported on silicon wafers were prepared by vesicle fusion [11–13] using the protocol reported in [3]: Double-side polished, 2″ Si(100)—wafers were cleaned by immersing the wafers in an H_2O_2 + sulfuric acid mixture (volume fraction of 70% concentrated H_2SO_4, 30% H_2O_2 at 90°C for 30 min). This strongly oxidizing combination removes all organic contaminants on the surface but does not disturb the native silicon oxide layer. The wafers were then rinsed and stored under distilled water before use [14]. 200 mL of a $5 \cdot 10^{-3}$ mol/L Hepes, $5 \cdot 10^{-3}$ mol/L $MgCl_2$, and $100 \cdot 10^{-3}$ mol/L KCl buffer solution was prepared and heated to 55°C. 1,2-dimyristoyl-sn-glycero-3-phosphatidylcholine (DMPC) was added to the buffer solution up to a concentration of 1.5 mg/mL. The milky suspension, which initially contained multilamellar lipid suspensions, was sonicated (50% duty cycle, power level 4) for 15 h until the suspension became transparent and small unilamellar vesicles formed. The hydrophilic Si wafers were then completely immersed in the suspension for 1 hour. The lipid suspension was kept at 55°C during the whole process to keep the bilayers in their fluid phase. After 1 h, the wafers were thoroughly rinsed with ~2 L of ultra pure water to remove excess vesicles from the surface. By applying this procedure, small bilayer patches initially develop on the substrate, which eventually undergo a transition into a large uniform single bilayer after approximately 20–25 min [12]. The substrates were then annealed for 72 h at 55°C in an oven in air before mounting in an aluminum sample can, and rehydrated. To check the existence of a a single supported bilayer, the quality of the samples was checked by atomic force microscopy (AFM) and X-ray reflectivity. AFM pictures showed a defect-free uniformly covered surface. From the absence of sharp Bragg peaks in the X-ray experiment, a multilamellar structure could be excluded.

To increase the scattering signal, 100 double-sided, polished wafers (resulting in 200 single bilayers) were mounted horizontally into the neutron spectrometer, with the plane of the bilayers in the scattering plane, as depicted in Figure 1. The sample was sealed in an aluminum sample can and placed inside a closed-cycle refrigerator (CCR) during the experiment. The experimental temperature range extended from of 240 K to 290 K, where freezing of the hydration water molecules was expected. 120 μL of heavy water was added before closing to ensure full hydration of the bilayers. The sample can used in this study was designed such that the formation of bulk ice is discouraged in the experimental setup, such as on the windows of the sample can or on the sample, and would occur outside of the neutron beam.

2.2. Neutron Scattering Experiment. The neutron experiment was carried out at the high flux neutron backscattering spectrometer HFBS at the NIST Center for Neutron Research (NCNR), Gaithersburg, [16] in its standard setup with Si(111) monochromator and analyzer crystals corresponding to an incident and analyzed neutron energy of 2.08 meV (λ = 6.27 Å). At the resolution of 0.8 μeV, only molecular motions with characteristic times slower than 1 ns are monitored. The experiment covered lateral length scales of 3.5 Å to 12 Å to study in-plane dynamics down to nearest neighbor distances of lipid acyl tails and hydration water molecules. Performing so-called "elastic" scans, which record the elastic scattering intensity as a function of temperature, reveals dynamical changes on different length scales. Freezing and melting of molecular degrees of freedom can easily be identified because they lead to jumps or kinks in the recorded intensity. The counting time per scan was 5 minutes. Using cooling and heating ramps of 0.04 K/min, this results in a temperature resolution of 0.2 K. The 16 HFBS detectors (D1–D16) cover a total Q range of 0.14 Å^{-1} to 1.81 Å^{-1}. The Table 1 lists the center Q values and the corresponding length scales. Each analyzers covers an angular range of approximately 8deg.

Table 1: Neutron detectors (D1–D16), corresponding center $q_{||}$-value, length scales, and type of scattering and motion detected. The lipid acyl chain correlation peak is centered $q_{||} \sim 1.5\,\text{Å}^{-1}$. The hydration water correlation peak was reported at $q_{||} = 1.85\,\text{Å}^{-1}$ [9, 10, 15].

Detector	$q_{\|\|}$ (Å^{-1})	Lateral distance (Å)	Dominant scattering	Motion detected
D1	0.25	25	Coherent small angle scattering	
D2	0.36	17		
D3	0.47	13		
D4	0.56	11		
D5	**0.62**	**10**		
D6	**0.75**	**8**		
D7	**0.87**	**7**	Incoherent	Lipid diffusion
D8	**0.99**	**6.3**		
D9	1.11	5.7		
D10	1.22	5.2		
D11	1.32	4.8		
D12	1.42	4.4		
D13	**1.51**	**4.2**	Lipid tail correlation peak	Lipid tail dynamics
D14	1.60	3.9		
D15	1.68	3.7		
D16	**1.75**	**3.6**	Hydration water correlation peak	Hydration water dynamics

As the membranes were oriented with the membrane plane in the scattering plane, the observed Q values were all oriented in the plane of the membranes, $q_{\|}$.

Different types of motion fall into the length scales covered by the HFBS spectrometer. Atomic and molecular motions in membranes can be classified as local, self-correlated, and collective, pair-correlated dynamics. Local dynamics correspond to the motion of molecules or functional groups in local energy potentials. The force and time constants involved are determined by the local friction and restoring forces. This type of dynamics is called incoherent because the particles move independently in their local environments. Examples are vibration, rotation, libration (hindered rotation), and diffusion of individual lipid molecules. Coupled, collective molecular motions arise due to an interaction between particles or functional groups. This type of dynamics is called coherent. Collective molecular motions determine, for instance, elasticity of membranes [17] and interactions between membrane embedded proteins [18], and are important for membrane transport [19, 20]. Within the scattering formalism, incoherent, autocorrelated dynamics is described by the incoherent scattering function, $S_{\text{inc}}(Q, \hbar\omega)$, while the coherent scattering, $S_{\text{coh}}(Q, \hbar\omega)$, describes dynamics involving different molecules [21, 22].

Different types of dynamics can be distinguished based on their length scale dependence: Gaspar et al. have recently shown that incoherent and coherent scattering contributions in proteins can be discriminated by using neutron polarization analysis [15]. By using protein powders at different levels of hydration, scattering contributions due to the hydration water could be identified: The nearest neighbor distance of the hydration water molecules leads to a correlation peak centered at $1.85\,\text{Å}^{-1}$, corresponding to a distance of 3.4 Å between hydration water molecules. Detector D16 was, therefore, assigned to dynamics of hydration water molecules.

The lipid acyl chain correlation peak in DMPC is the result of a close packing of the lipid tails in the hydrophobic membrane core. The corresponding correlation peak occurs at $\sim 1.5\,\text{Å}^{-1}$ in the gel phase [10, 19] (below the main phase transition at $T = 294\,\text{K}$), corresponding to a nearest neighbor distance of 4.2 Å. Detector D13, which covers this length scale, was, therefore, assigned to lipid tail dynamics. Lipid and water dynamics were studied previously using backscattering spectrometers by analyzing elastic scattering at the positions of the lipid acyl chain and hydration water correlation peaks [9, 10, 23]. These studies demonstrated that the different length scales and corresponding detectors are decoupled and that lipid and water dynamics can be studied separately but simultaneously.

Incoherent scattering is dominant at intermediate $q_{\|}$ values, between 0.3 and $1.5\,\text{Å}^{-1}$, where no correlation peak occurs. This range of length scales between ~4 and 21 Å is often used in neutron scattering studies (see, e.g., [7, 8]) to study diffusion and molecular mean square displacements of lipid molecules. We assigned the Q range from $0.6\,\text{Å}^{-1}$ to $1.05\,\text{Å}^{-1}$ (detectors D5–D8), covering length scales from 6.3 Å–10 Å to incoherent dynamics due to diffusion of lipid molecules.

Lipid diffusion and lipid and hydration water dynamics were studied simultaneously by analyzing different detectors. Table 1 lists the dominant scattering contribution for the different length scales, and the corresponding type of motion observed in the various detectors. The HFBS analyzers cover an angular range of approximately 8° each. The experiment was, therefore, not sensitive to shifts of the lipid and water

correlation peak with temperature within this $q_{\parallel}$ resolution due to potential structural changes of the bilayers with temperature.

3. Results

Data were collected during cooling and heating cycles, using a temperature ramp of 0.04 K/min. The temperature ramp of 0.04 K/min was determined to be in thermal equilibrium as there were no observed differences to data taken at even slower speeds. Note that faster ramps could lead to partial dehydration of the membranes because of a possible temperature gradient inside of the sample can.

Figure 2 depicts the elastic scattering collected from detectors D5–D8, D13, and D16, which represent lipid diffusion, (a), lipid tail dynamics, (b), and hydration water dynamics, (c). The elastic scattering due to lipid diffusion increases upon cooling until a freezing transition is observed at T = 264 K (3). A second step occurs at T = 252 K (5). The membrane shows a hysteresis in the heating curve, which was shifted upward on the intensity axis for clarity. During the heating cycle, the melting transition is observed to begin at T = 271 K (2). The membranes transition back into their high temperature state at 279 K (1).

Lipid tail dynamics were studied in detector D13, which collects scattering at the $q_{\parallel}$ position of the lipid acyl chain correlation peak. The freezing curve in Figure 2(b) shows two pronounced anomalies corresponding to freezing transitions, the first at T = 264 K (3), and the second at T = 255 K (4). The temperature of transition (3) in D13 agrees with the transition observed in detectors D5–D8. The heating curve (shifted upward on the intensity axis for clarity) shows transitions at T = 247 K (6), T = 252 K (5), T = 271 K (2) and T = 279 K (1).

Hydration water dynamics were observed in detector D16 in Figure 2(c). The elastic intensity in Figure 2(c) shows a first kink at T = 271 K (2) in cooling. A second freezing transition is observed at T = 252 K (5). Two kinks corresponding to melting transitions can be assigned to the heating curve, at 252 K and 271 K. We note that the hydration water correlation peak occurs at $q_{\parallel}$ =1.85 Å^{-1} [9, 10, 15]. D16 does, therefore, not cover the entire water correlation peak. We argue, however, that D16 covers part of the broad hydration water peak (see [15]) to capture hydration water dynamics. All transition temperatures are listed in Table 2.

An empty aluminum can consisting of silicon wafers (without membranes), and heavy water was measured as a reference. Scattering of the sample, was constant, and no freezing or melting transitions were observed in the temperature range 240 K < T < 290 K.

The system was cycled several times through the temperature range 240 K < T < 290 K. Note that the heating curves in Figure 2 have been shifted upward on the intensity axis to distinctly show the transition locations. The original data shows closed loops for all plots, and the system always returned to its initial high-temperature state. The number of particles in the beam was constant, as the intensities of the elastic scattering at the beginning and end of the temperature cycle coincide, resulting in perfectly reproducible data. The cooling and heating rate of 0.04 K/min was slow enough such that the observed states were thermodynamic states rather than determined by hydration kinetics. The absence of a freezing transition at T = 277 K, the freezing and melting transition of heavy water, in Figures 2(a), 2(b), and 2(c) excludes the presence of bulk D_2O in the beam. The dynamical changes in Figure 2 were, therefore, attributed to

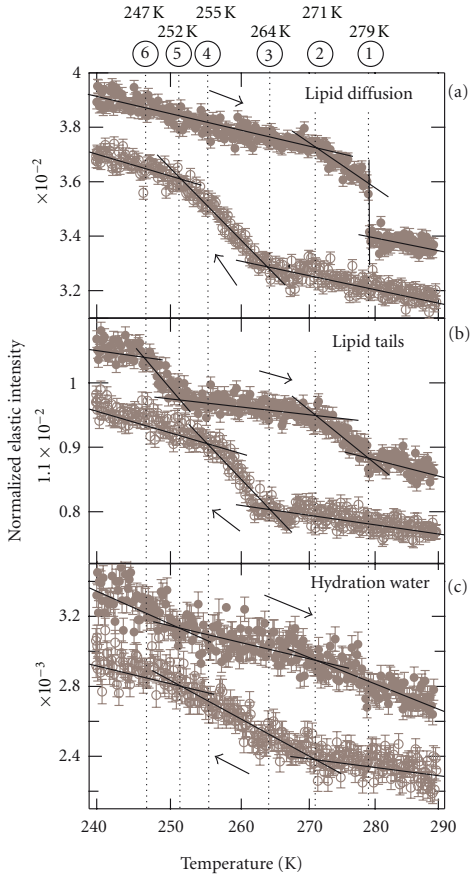

Figure 2: Elastic neutron scattering as determined in slow cooling and heating cycles. (a) Detectors D5–D8 cover lipid diffusion. (b) Lipid acyl-tail dynamics were observed in D13. (c) D16 covered hydration water dynamics. Freezing and melting transitions are labeled (1)–(6) and the corresponding temperatures are given. All heating curves are shifted upward in intensity for clarity; the original data show closed loops. Error bars represent one standard deviation. The experimental temperature resolution was 0.2 K. The error in the determination of the transition temperatures is related to the determination of the intersection of the different slopes. For lipid dynamics we estimate the maximum error to be ∼2 K. The hydration water data in (c) has slightly larger statistical errors and the maximum error in the determination of the transition temperature was estimated to be ∼4 K.

Table 2: Freezing and melting temperatures of hydration and membrane dynamics in the temperature range 240 K < T < 290 K as determined from the data in Figure 2.

Motion	Freezing temperature (K)	Melting temperature (K)	Hysteresis ΔT (K)
Hydration water dynamics	271 (2)	271 (2)	0
	252 (5)	252 (5)	0
Diffusive membrane dynamics	264 (3)	279 (1)	15
	252 (5)	271 (2)	19
Membrane dynamics	—	247 (6)	—
	264 (3)	279 (1)	15
	255 (4)	271 (2)	19

dynamical changes of the hydrophobic membrane core and the hydration water molecules.

4. Discussion

The onset of freezing at transition (2) in the hydration water scan in Figure 2(c) can be compared to freezing of membrane hydration water in stacked membrane systems as reported from neutron diffraction [7] and elastic neutron scattering experiments [8–10]. The transition temperature of 271 K agrees well with the temperatures reported. Freezing of these hydration water molecules is supercooled by 6 K as freezing and melting of bulk D_2O occurs at 277 K. A second freezing transition was observed at lower temperatures of T = 252 K.

Lipid diffusion and the lipid tail dynamics start to freeze at T = 264 K (3). The onset of freezing of membrane dynamical degrees of freedom appears to be decoupled from the hydration water freezing. Lipid diffusion shows a second freezing transition at 252 K, which coincides with the low-temperature hydration water freezing transition. Freezing of the hydration water molecules seems to have a strong effect on the displacement of lipid molecules. Lipid tail dynamics, however, appear to be less sensitive to hydration water dynamics, as the low temperature freezing in Figure 2(b) occurs at T = 255 K, slightly higher than the water freezing. Freezing transitions at ∼250 K were also observed in the elastic neutron scattering and computer simulation data by Wood et al. [8] obtained in purple membrane. However, the relatively coarse temperature resolution in this study does not allow a quantitative comparison with the values in Table 2.

No hysteresis was found in freezing and melting of the hydration water; freezing and melting temperatures coincide in the scan in Figure 2(c). Hysteresis of 15 K and 19 K were observed for diffusive membrane and acyl-tail dynamics, as listed in Table 2. These values are significantly larger than the experimental temperature resolution, possible hysteresis of the experimental setup, and the maximum error in the determination of the transition temperatures and must, therefore, be attributed to the membrane.

Diffusive lipid and tail dynamics show a first melting transition at T = 271 K (2), the temperature of the first hydration water melting transition. Membrane dynamics fully melt and return to their high temperature state at T = 279 K (1), and diffusive and tail dynamics appear to be coupled in heating. The melting transition of lipid diffusion appears as a pronounced step in the data in Figure 2(a), while all other transitions manifest as kinks. An additional transition at T = 247 K in the tail dynamics is observed in the heating curve in Figure 2(b), which has no analogue in cooling. Taking into account a possible hysteresis, this points to further freezing transitions in the correlated tail dynamics at lower temperatures, outside the temperature window of this experiment.

As this is the first study of freezing and melting of hydration water and membrane dynamics in solid supported lipid bilayers, we can, at this point, not provide a full explanation and a detailed molecular model. In particular, computer simulations are needed to unambiguously identify hydration water molecules inside the lipid head group region and possibly assign the transitions observed to freezing of water molecules in different hydration shells and their coupling to membrane dynamics. We argue, however, that the two main conclusions of this work are robust: (1) the observation that diffusive and correlated lipid dynamics are to some extent decoupled and show different freezing temperatures, and (2) that hydration water and membrane freezing are at least to some extent de-coupled in single supported lipid bilayers and show different freezing and melting temperatures.

A comment is in order: while one leaflet of the bilayer is directly exposed to water molecules, the other is closely interacting with the silicon substrate, with only a few water molecules available to interact. This is likely to affect the motional freedom of the lipid head groups of the lower layer and their hydration water molecules. The technique presented in this paper is not capable of easily resolving signals from different leaflets. The observed freezing and melting transitions may, therefore, also be related to molecular freezing and melting in different leaflets. It is, for instance, well known that confinement can lead to a suppression or lowering of freezing transitions as a result of competing interactions with the confining surface.

Protein powders, proteins in suspension, or multilamellar membranes are often used as model systems to investigate the structure and dynamics of the hydration water, and

its impact on membrane and protein dynamics [8, 24–28]. Here, we have for the first time used single phospholipid bilayers supported on a solid surface to study freezing and melting of membrane and hydration water. The upper leaflet of the bilayer, and with it the water adsorption sites in the lipid head group region, is in direct contact with saturated water vapor. By preparing such a well-defined biological interface, it will in future experiments be possible to obtain detailed information about structure and dynamics of the hydration water and its impact on membrane dynamics and dynamics of membrane-embedded proteins.

5. Conclusion

In summary, we studied freezing and melting of hydration water and membrane dynamics in single supported lipid bilayers using high energy resolution neutron scattering on a backscattering spectrometer. Membrane and hydration water dynamics were studied in the temperature range $240\,\text{K} < T < 290\,\text{K}$ in slow heating and cooling cycles. Several freezing and melting transitions were observed. From the length scale dependence of the elastic scattering, these transitions could be assigned to freezing and melting of the hydration water and freezing of lipid diffusion and lipid acyl-tail dynamics. The different dynamics appear to be partially decoupled in this single bilayer system as we observe different freezing and melting temperatures. The onset of hydration water freezing was found at $T = 271\,\text{K}$. Freezing of lipid diffusion and lipid tail dynamics was observed at a slightly lower temperature of $T = 264\,\text{K}$. Single-supported lipid bilayers present a well-defined biological interface to study hydration water dynamics and their coupling to membrane degrees of freedom. Because of its simplicity, this system should in particular be highly suited for computer simulations.

Acknowledgments

The authors thank the NIST Center for Neutron Research for the allocation of beam time. This paper utilized facilities supported in part by the National Science Foundation under Agreement no. DMR-0944772. This paper was partially funded by the Natural Sciences and Engineering Research Council of Canada (NSERC) and the National Research Council Canada (NRC).

References

[1] E. Sackmann, "Supported membranes: scientific and practical applications," *Science*, vol. 271, no. 5245, pp. 43–48, 1996.

[2] M. Tanaka and E. Sackmann, "Polymer-supported membranes as models of the cell surface," *Nature*, vol. 437, no. 7059, pp. 656–663, 2005.

[3] C. L. Armstrong, M. D. Kaye, M. Zamponi et al., "Diffusion in single supported lipid bilayers studied by quasi-elastic neutron scattering," *Soft Matter*, vol. 6, no. 23, pp. 5864–5867, 2010.

[4] N. Kučerka, Y. Liu, N. Chu, H. I. Petrache, S. Tristram-Nagle, and J. F. Nagle, "Structure of fully hydrated fluid phase DMPC and DLPC lipid bilayers using x-ray scattering from oriented multilamellar arrays and from unilamellar vesicles," *Biophysical Journal*, vol. 88, no. 4, pp. 2626–2637, 2005.

[5] G. A. Yeghiazaryan, A. H. Poghosyan, and A. A. Shahinyan, "The water molecules orientation around the dipalmitoylphosphatidylcholine head group: a molecular dynamics study," *Physica A*, vol. 362, no. 1, pp. 197–203, 2006.

[6] E. Nováková, K. Giewekemeyer, and T. Salditt, "Structure of two-component lipid membranes on solid support: an x-ray reflectivity study," *Physical Review E*, vol. 74, no. 5, Article ID 051911, 2006.

[7] M. Weik, U. Lehnert, and G. Zaccai, "Liquid-like water confined in stacks of biological membranes at 200 K and its relation to protein dynamics," *Biophysical Journal*, vol. 89, no. 5, pp. 3639–3646, 2005.

[8] K. Wood, M. Plazanet, F. Gabel et al., "Coupling of protein and hydration-water dynamics in biological membranes," *Proceedings of the National Academy of Sciences of the United States of America*, vol. 104, no. 46, pp. 18049–18054, 2007.

[9] M. C. Rheinstädter, T. Seydel, F. Demmel, and T. Salditt, "Molecular motions in lipid bilayers studied by the neutron backscattering technique," *Physical Review E*, vol. 71, no. 6, Article ID 061908, pp. 1–8, 2005.

[10] M. C. Rheinstädter, T. Seydel, and T. Salditt, "Nanosecond molecular relaxations in lipid bilayers studied by high energy-resolution neutron scattering and in situ diffraction," *Physical Review E*, vol. 75, no. 1, Article ID 011907, 2007.

[11] T. H. Watts, A. A. Brian, and J. W. Kappler, "Antigen presentation by supported planar membranes containing affinity-purified I-A(d)," *Proceedings of the National Academy of Sciences of the United States of America*, vol. 81, no. 23, pp. 7564–7568, 1984.

[12] R. Richter, A. Mukhopadhyay, and A. Brisson, "Pathways of lipid vesicle deposition on solid surfaces: a combined QCM-D and AFM study," *Biophysical Journal*, vol. 85, no. 5, pp. 3035–3047, 2003.

[13] V. Oliynyk, U. Kaatze, and T. Heimburg, "Defect formation of lytic peptides in lipid membranes and their influence on the thermodynamic properties of the pore environment," *Biochimica et Biophysica Acta*, vol. 1768, no. 2, pp. 236–245, 2007.

[14] I. M. Tidswell, B. M. Ocko, P. S. Pershan, S. R. Wasserman, G. M. Whitesides, and J. D. Axe, "X-ray specular reflection studies of silicon coated by organic monolayers (alkylsiloxanes)," *Physical Review B*, vol. 41, no. 2, pp. 1111–1128, 1990.

[15] A. M. Gaspar, S. Busch, M. S. Appavou et al., "Using polarization analysis to separate the coherent and incoherent scattering from protein samples," *Biochimica et Biophysica Acta*, vol. 1804, no. 1, pp. 76–82, 2010.

[16] A. Meyer, R. M. Dimeo, P. M. Gehring, and D. A. Neumann, "The high-flux backscattering spectrometer at the NIST Center for Neutron Research," *Review of Scientific Instruments*, vol. 74, no. 5, pp. 2759–2777, 2003.

[17] M. C. Rheinstädter, W. Häußler, and T. Salditt, "Dispersion relation of lipid membrane shape fluctuations by neutron spin-echo spectrometry," *Physical Review Letters*, vol. 97, no. 4, Article ID 048103, 2006.

[18] M. C. Rheinstädter, K. Schmalzl, K. Wood, and D. Strauch, "Protein-protein interaction in purple membrane," *Physical Review Letters*, vol. 103, no. 12, Article ID 128104, 2009.

[19] M. C. Rheinstädter, C. Ollinger, G. Fragneto, F. Demmel, and T. Salditt, "Collective dynamics of lipid membranes studied by inelastic neutron scattering," *Physical Review Letters*, vol. 93, no. 10, Article ID 108107, 4 pages, 2004.

[20] M. D. Kaye, K. Schmalzl, V. C. Nibali, M. Tarek, and M. C. Rheinstädter, "Ethanol enhances collective dynamics of lipid

membranes," *Physical Review E*, vol. 83, Article ID 050907, 4 pages, 2011.

[21] C. L. Armstrong, E. Sandqvist, and M. C. Rheinstädter, "Protein-protein interactions in membranes," *Protein and Peptide Letters*, vol. 18, no. 4, pp. 344–353, 2011.

[22] M. C. Rheinstädter, "Collective molecular dynamics in proteins and membranes," *Biointerphases*, vol. 3, no. 2, pp. FB83–FB90, 2008.

[23] M. C. Rheinstädter, J. Das, E. J. Flenner, B. Brüning, T. Seydel, and I. Kosztin, "Motional coherence in fluid phospholipid membranes," *Physical Review Letters*, vol. 101, no. 24, Article ID 248106, 4 pages, 2008.

[24] M. Tarek and D. J. Tobias, "Role of protein-water hydrogen bond dynamics in the protein dynamical transition," *Physical Review Letters*, vol. 88, no. 13, Article ID 138101, 4 pages, 2002.

[25] D. Russo, G. Hura, and T. Head-Gordon, "Hydration dynamics near a model protein surface," *Biophysical Journal*, vol. 86, no. 3, pp. 1852–1862, 2004.

[26] P. Kumar, Z. Yan, L. Xu et al., "Glass transition in biomolecules and the liquid-liquid critical point of water," *Physical Review Letters*, vol. 97, no. 17, Article ID 177802, 26 pages, 2006.

[27] S. H. Chen, L. Liu, E. Fratini, P. Baglioni, A. Faraone, and E. Mamontov, "Observation of fragile-to-strong dynamic crossover in protein hydration water," *Proceedings of the National Academy of Sciences of the United States of America*, vol. 103, no. 24, pp. 9012–9016, 2006.

[28] S. Ebbinghaus, J. K. Seung, M. Heyden et al., "An extended dynamical hydration shell around proteins," *Proceedings of the National Academy of Sciences of the United States of America*, vol. 104, no. 52, pp. 20749–20752, 2007.

4.3 Preface to Publication II: "*Anomalous and Anisotropic Nanoscale Diffusion of Hydration Water in Fluid Lipid Membranes*"

In the previous study, we observed properties of the hydration water of single, hydrated membranes and its coupling to the other dynamics of the membrane. By measuring changes in the intensity of the elastic scattering we were able to determine various transitions and found that the hydration water was not well-coupled to the lipid dynamics. This interesting finding motivated us to continue to explore hydration water dynamics in more detail. In this publication, quasi-elastic scattering is used to investigate relaxational dynamics, including diffusion, of hydration water molecules in stacked, oriented, fluid membranes.

Diffusion is a fundamental process in nature and the mechanism by which lipids, proteins and water molecules move in a cell membrane. Our aim was to measure diffusion of hydration water in a fluid lipid membrane made from chain-deuterated DMPC. Incoherent quasi-elastic neutron scattering was used to measure the diffusion of the water and large two-dimensional detectors of Let allowed us to simultaneously measure scattering in the plane and perpendicular to the plane of the membranes.

In this publication we present evidence from experiments and simulations for anomalous, anisotropic diffusion of membrane hydration water. The dynamic structure factor, $S(Q, E)$ of the hydration water was measured and diffusion was modelled by fitting the Fourier transform of the Kohlrausch-Williams-Watts function to the quasi-elastic scattering component of the structure factor data. The fitting was done directly in the energy domain and compared to bulk H_2O using the same model. This model has two characteristic parameters: β and τ. β is called the stretching exponent and can have a value between 0 and 1 where the farther away from 1 β is, the slower the motion i.e, the more sub-diffusive and less Brownian. The τ parameter is the relaxation time of the motion, the smaller the relaxation time, the quicker the relaxation happens. Ranges of β for hydration water were observed to be from 1 to as low as $\sim$0.5. In simulations, both hydration and bulk water are modelled. Hydration water is modelled using coarse-grained Brownian dynamics with a potential function that is approximated from our structural measurements and a distribution of diffusion constants span the hydration layer and the bilayer. From these simulations, it was observed that anomalous diffusion was present as well as anisotropy on large length scales due to geometrical confinement from the bilayer. Bulk water is modelled using molecular dynamics in full atomistic detail, only isotropic and intrinsic anomalous behaviour was observed.

Author Contributions:

- *Experimental Concept:* Maikel Rheinstädter, Victoria García Sakai
- *Sample Preparation:* **Laura Toppozini**, Maikel Rheinstädter
- *Neutron Experiments:* **Laura Toppozini**, Maikel Rheinstädter, Victoria García Sakai, Robert Bewley, Robert Dalgliesh
- *Simulations:* Felix Roosen-Runge
- *Theoretical Framework:* Henry Glyde, **Laura Toppozini**, Maikel Rheinstädter, Felix Roosen-Runge
- *Data Analysis:* **Laura Toppozini**, Felix Roosen-Runge, Toby Perring
- *Manuscript Preparation:* **Laura Toppozini**, Felix Roosen-Runge, Henry R. Glyde, Victoria García Sakai, Maikel C. Rheinstädter

Soft Matter

PAPER

View Article Online
View Journal

Cite this: DOI: 10.1039/c5sm01713k

Anomalous and anisotropic nanoscale diffusion of hydration water molecules in fluid lipid membranes†

Laura Toppozini,[a] Felix Roosen-Runge,[b] Robert I. Bewley,[c] Robert M. Dalgliesh,[c] Toby Perring,[c] Tilo Seydel,[b] Henry R. Glyde,[d] Victoria García Sakai[c] and Maikel C. Rheinstädter*[a]

Received 11th July 2015,
Accepted 18th August 2015

DOI: 10.1039/c5sm01713k

www.rsc.org/softmatter

We have studied nanoscale diffusion of membrane hydration water in fluid-phase lipid bilayers made of 1,2-dimyristoyl-3-phosphocholine (DMPC) using incoherent quasi-elastic neutron scattering. Dynamics were fit directly in the energy domain using the Fourier transform of a stretched exponential. By using large, 2-dimensional detectors, lateral motions of water molecules and motions perpendicular to the membranes could be studied simultaneously, resulting in 2-dimensional maps of relaxation time, τ, and stretching exponent, β. We present experimental evidence for anomalous (sub-diffusive) and anisotropic diffusion of membrane hydration water molecules over nanometer distances. By combining molecular dynamics and Brownian dynamics simulations, the potential microscopic origins for the anomaly and anisotropy of hydration water were investigated. Bulk water was found to show intrinsic sub-diffusive motion at time scales of several picoseconds, likely related to caging effects. In membrane hydration water, however, the anisotropy of confinement and local dynamical environments leads to an anisotropy of relaxation times and stretched exponents, indicative of anomalous dynamics.

1 Introduction

Diffusion is the fundamental mechanism of motion for lipids, proteins and water molecules throughout a membrane. While diffusion describes a stochastic, intrinsically non-directed motion, many biological processes are related to highly directed motions. The incoherent interaction between active processes in the cytoplasm was recently shown to lead to random fluctuation forces,[1] which in return may change the character of a directed motion into a thermally-induced diffusion process.

In biology, diffusion often occurs in crowded media, which for instance, have been found to lead to anomalous diffusion of proteins.[2–4] The dynamics of the atoms in protein or lipid molecules are more complex than those in ordinary liquids. In a simple liquid, atoms move ballistically at short times, followed by a crossover to Brownian diffusion. In dense fluids a "caging" effect is observed, where the atoms can be trapped momentarily by their neighbours. The motions of protein and lipid atoms are further complicated by their polymeric structure, characterized by connectivity and flexibility.

Sub-diffusion of lipid molecules in membranes has been observed in computer simulations.[8–10] The experimental observation of sub-diffusive lipid or hydration water motion, however, has turned out to be more difficult and a conclusive observation has yet to be reported.[11,12]

While numerous studies addressed nanoscale lipid dynamics, see, *e.g.*,[5–7,13–21] significantly less work has been done to study dynamics of membrane hydration water, most likely due to the corresponding computational and in particular experimental challenges. However, hydration water was shown to have distinct properties as compared to bulk water, such as a slower diffusion,[22] reduced freezing temperature[23,24] and glassy dynamics.[25]

Properties of hydration water play an important role for the dynamics of biological systems up to the point that their corresponding dynamics have been suggested to be "slaved" by the solvent's fluctuations.[26] Protein dynamics and folding were reported to strongly depend to hydration water dynamics.[27–29] Lipid structural dynamics have a complex relationship with hydration water[30] and coupling of membrane and hydration water dynamics has been reported.[24,31]

From computer simulations of lipid bilayers, sub-diffusive and ballistic regimes of hydration water motions have been predicted on short time scales and correspondingly small distances.[32,33] Water molecules are expected to move anisotropically when diffusing along the membranes or approaching and penetrating the bilayers, as reported from nuclear magnetic resonance imaging[34] and are shown to slow further from the introduction

[a] *Department of Physics and Astronomy, McMaster University, Hamilton, Ontario, Canada. E-mail: rheinstadter@mcmaster.ca*
[b] *Institut Laue-Langevin, Grenoble, France*
[c] *ISIS, Rutherford Appleton Laboratory, Didcot, UK*
[d] *Department of Physics and Astronomy, University of Delaware, Newark, Delaware, USA*

† 87.16.D-, 87.15.Vv, 83.85.Hf, 87.15.A-

View Article Online

Paper Soft Matter

of proteins by sum frequency generation spectroscopy.[35] Time-resolved vibrational spectroscopy has shown that water in DOPC membranes is distributed anisotropically and forms nano-clusters[36] for a range of hydration levels, supported by molecular dynamics simulations.[37]

While water molecules can penetrate lipid bilayers,[38] the perpendicular diffusion, $D_{\perp}$, is typically at least an order of magnitude lower than lateral diffusion along the bilayers. Water motion through a bilayer is not a simple diffusion process as free energy and diffusion rate strongly depend on the position in the bilayer.[39]

In this work we combined neutron diffraction, incoherent quasi-elastic neutron scattering and computer modelling to study nanoscale diffusion of hydration water molecules throughout lipid bilayers on length scales of ~3–100 Å. By preparing oriented membranes, the experimental results give unambiguous access to the anisotropic local molecular confinement geometry to which the diffusive processes are restricted. Large, 2-dimensional detector arrays further enabled us to differentiate between motions of water molecules along and across the membranes separately.

Hydration water diffusion was also modelled using Brownian dynamics in a coarse-grained simulation of the trajectory of water molecules represented by center of mass coordinate for 10 μs (in time steps of 0.1 ps). Diffusion constants and potentials for water molecules are specific to the region, such as hydrophobic core and hydration water layer, with friction included as an effective term. From the computer model, we find that the anisotropy of confinement and local dynamical environments of membrane hydration water lead to an anisotropy of relaxation times and stretched exponents, indicative of anomalous diffusion.

2 Materials & methods

2.1 Experimental sample preparation

2.1.1 Bulk water sample. The bulk water sample consisted of a cylindrical aluminum annulus filled with ultra pure H_2O with a resistivity of 18.2 MΩ cm. The walls of the annulus were separated by 0.1 mm and the can was held at room temperature (T = 21 °C = 294 K) during the measurement. Vanadium foil was bent to the same shape as the annulus and used to measure the energy resolution at the different incident neutron energies.

2.1.2 Membrane samples. Highly oriented, multi-lamellar stacks of 1,2-dimyristoyl-3-phosphocholine (DMPC) and chain deuterated DMPC (DMPC-d54) were prepared on 2″ single-side polished Si wafers of thickness 300 μm. A solution of 16.7 mg mL^{-1} DMPC in 1 : 1 chloroform and 2,2,2-trifluoroethanol (TFE) was prepared. The Si wafers were cleaned by alternate 12 minute sonications in ultra pure water and methanol at 40 °C (313 K). This process was repeated twice. The cleaned wafers were placed on a heated sample preparation surface, which was kept at 35 °C (308 K). This temperature is well above the main phase transition for DMPC that occurs at 23.4 °C (296.4 K), thus the heated substrates ensured that the lipids were in the fluid phase during deposition and the self-assembly of the lipids. An aliquot of 1.2 mL of the lipid solution was deposited on each Si wafer and allowed to dry. The wafers were kept under vacuum overnight to remove all traces of solvent. Following this protocol, ~3000 highly-oriented, stacked membranes were supported on each wafer with a total thickness of ~10 μm.

Deuterated lipids, DMPC-d54, hydrated with H_2O, were used for the incoherent experiment to emphasize the incoherent scattering of the hydration water molecules. In order to study water dynamics from the quasi-elastic neutron scattering experiments, eighteen Si wafers were stacked with two 0.3 mm aluminum spacers placed in between each wafer to allow for the membranes to be properly hydrated. Wafers and spacers were stacked into an aluminum sample can, as shown in Fig. 1(a)–(c). Aluminum foil between the wafers and sample can lid provided tension to keep the wafers in place. Samples were then hydrated with ultra pure H_2O and incubated at 30 °C (303 K) for 24 hours before the measurements. Energy resolution was determined by cooling a sample with a large incoherent scattering contribution consisting of protonated lipids hydrated with H_2O down to 15 K to freeze all molecular dynamics, such that the observed scattering was considered to be purely elastic.

In this experiment, the bilayers were hydrated from water vapor to avoid high absorption and background signals from bulk solvent hydration.[40] Solvent-saturated filter paper was

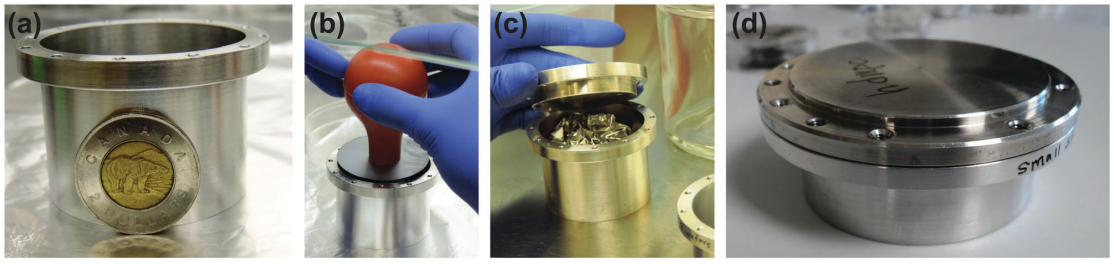

Fig. 1 Sample cans used for the neutron scattering experiments. (a) A cylindrical sample can was used for the incoherent neutron scattering experiments. (b) 18 2″, 300 μm thick Si wafers were loaded into the aluminium cans. (c) Wafers were separated by 0.3 mm thick aluminum spacers to allow for hydration and the remaining space was filled with aluminum foil. (d) Sample can used for the neutron reflectivity where a single 2″ wafer was mounted.

placed above loosely packed balls of aluminum foil and cadmium shields were mounted carefully to avoid scattering of the filter paper and bulk water. The can was mounted inside of a temperature controlled cryostat with a temperature stability of ±0.01 K. Data were taken while the membranes were fully hydrated and in their fluid phase, at a temperature of T = 30 °C (303 K). Due to the typically low scattering of the sample (~10%), we did not observe evidence of multiple scattering events.

The membrane structure was determined *via* neutron diffraction in which a single Si wafer was mounted in an aluminum can, as shown in Fig. 1(d) and aligned in a temperature controlled chamber on a neutron reflectometer. Temperature was set to T = 30 °C (303 K) and controlled by a circulating water bath to better than ±0.1 K. Samples were hydrated with ultra pure H_2O or heavy water (D_2O), and incubated at 30 °C (303 K) for 24 hours before the measurements.

2.2 Elastic and quasi-elastic neutron scattering

2.2.1 Neutron diffraction on OFFSPEC. The structure of the bilayers was studied through neutron reflectivity at the OFFSPEC reflectometer at ISIS, the pulsed neutron and muon source at the Rutherford Appleton Laboratory in Oxfordshire, UK.[41,42] OFFSPEC is a vertical, flexible, low background, reflectometer and was used in its unpolarized mode.

We used OFFSPEC to probe the structure of the lamellar bilayers perpendicular to the plane of the bilayers. The thickness of the hydration water layer and water distribution throughout the bilayers, bilayer head group and tail region thickness were determined from these measurements. Neutron scattering has the advantage of scattering differently from hydrogen and deuterium atoms due to their vastly different scattering cross sections. This difference allows measurements to highlight the structure of particular atoms and functional groups through deuterium labelling. The corresponding reflectivity profiles are shown in Fig. 2: (red) chain-deuterated DMPC hydrated with H_2O to emphasise the scattering contribution of the hydrophobic membrane core, (blue) DMPC hydrated with heavy water (D_2O) to highlight contribution of the hydration water, and (green) DMPC and H_2O to emphasise the head group in the bilayers.

The equally spaced Bragg peaks are indicative of a well organized lamellar membrane structure. While up to 12 diffraction orders can be observed in partially-hydrated DMPC membranes,[43–46] thermal fluctuations in fully hydrated fluid lipid membranes usually strongly suppress higher diffraction orders.[47] Four to five diffraction orders were observed in each diffractrogram in Fig. 2 and used for Fourier synthesis of the scattering length density.

The OFFSPEC measurements covered a q_z range from 0.04 to 1.10 Å^{-1}, however Bragg peaks could be observed only to a maximum of $q_z \sim 0.50$ Å^{-1}. The out-of-plane and in-plane component of the total scattering vector, Q, are denoted q_z and q_{xy}, respectively, in what follows. Fitting of Lorentzian peak profiles was used to determine the location of each reflection. The peak areas were integrated by manual determination of the corresponding peak bounds. An example of such an area is marked in Fig. 2 in the third reflection of the DMPC-d54/H_2O sample (red).

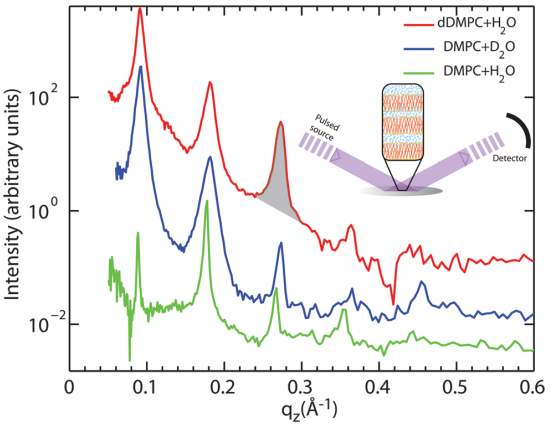

Fig. 2 Neutron diffraction data collected at the OFFSPEC reflectometer are shown for three hydrated lipid bilayer samples: (red) deuterated DMPC hydrated by H_2O, (blue) DMPC hydrated by D_2O, and (green) DMPC hydrated by H_2O. The neutron scattering length profiles in Fig. 5 were calculated from these data by using the location and areas (as shown by the shading under the peak) under each peak. All measurements were taken at T = 30 °C (303 K).

The neutron scattering length density (NSLD), $\rho(z)$, can be approximated by a 1-dimensional Fourier analysis, where the different Fourier components are observed in the experiment as the integrated intensities of the reflectivity Bragg peaks:

$$\begin{aligned}\rho(z) &= \frac{2}{d_z}\sum_{n=1}^{N} F(q_n)\nu_n \cos(q_n z) \\ &= \frac{2}{d_z}\sum_{n=1}^{N} \sqrt{I_n q_n}\nu_n \cos\left(\frac{2\pi n z}{d_z}\right),\end{aligned} \tag{1}$$

where N is the highest order of the Bragg peaks observed in the experiment. This method is equivalent to determining electron densities from X-ray scattering.[24,45,48] The square root of the integrated peak intensities I_n, multiplied by q_n give the form factors, $F(q_{z,n})$.[49,50] The bilayer component form factor $F(q_z)$, which is in general a complex quantity, is real-valued in the case of centro-symmetry. The phase problem of crystallography, therefore, simplifies to the sign problem $F(q_{z,n}) = \nu_n|F(q_{z,n})|$, where the phases, ν_n, can only take values ±1. These phases are used to reconstruct the neutron scattering length density profiles from the diffraction pattern following eqn (1).

When the form factor $F(q_z)$ is measured at several q_z values, $T(q_z)$, which is proportional to $F(q_z)$, can be fit:

$$T(q_z) = \sum_n \sqrt{I_n q_n}\,\mathrm{sinc}\left(\frac{1}{2}d_z q_z - \pi n\right). \tag{2}$$

In order to determine the phases quantitatively, the form factor has to be observed at different q_z-values by measuring at different contrast conditions or using the so-called swelling technique.[46]

View Article Online
Paper Soft Matter

Here, fitting the experimental peak intensities and comparing them to the analytical expression for $T(q_z)$ in eqn (2) allowed us to assess the phases, ν_n. Up to 5 evenly spaced diffraction peaks were observed for these curves and were used to determine the neutron scattering length density profiles for each sample. Each peak in the diffraction pattern has a corresponding phase of ± 1. Phase arrays for each sample were as follows: DMPC-d54/H_2O, $[-1\ 1\ 1\ -1]$; DMPC/D_2O, $[1\ -1\ 1\ 1\ -1]$; DMPC/H_2O, $[-1\ -1\ -1\ 1\ -1]$.

The lamellar spacings, d_z, were determined from the peak spacing in Fig. 2 to be: DMPC-d54 hydrated with H_2O: d_z = 69.22 Å, DMPC hydrated with D_2O: d_z = 70.92 Å, and DMPC hydrated with H_2O: d_z = 68.98 Å. As the lamellar spacing includes the thickness of the bilayer plus the thickness of the water layer between the stacked bilayer, it is an established measure of the level of hydration reached. Values of d_z as a function of hydration are well documented for DMPC by the Nagle group and d_z for DMPC was reported to show a power-law dependence on membrane hydration.[51] d_z values in excess of 63 Å denote a significant increase in the thickness of the water layer. The different membranes prepared for this study can, therefore, be considered to be fully hydrated with more than 25 water molecules per lipid molecule such that the results of each system can directly be compared.

2.2.2 Incoherent quasi-elastic neutron scattering on Let. The incoherent quasi-elastic neutron scattering experiments were carried out at the Low-energy-transfer (Let) spectrometer[52,53] at ISIS, the pulsed neutron and muon source at the Rutherford Appleton Laboratory in Oxfordshire, UK.

In order to cover as large a range of momentum transfer, Q, and dynamical range as possible different incident neutron energies, E_i, were combined: 0.64, 0.96, 1.62, 3.28, and 9.8 meV corresponding to neutron wavelengths of λ = 11.3, 9.23, 7.11, 4.99 and 2.89 Å, respectively. Position- and time-sensitive ^{3}He detectors collected scattered neutrons with an angular range of -10° to 70° (up to 140° for bulk water) horizontally and $\pm 30^\circ$ vertically.

A 3-dimensional spectrum (E, Q, $S(Q, E)$) for each incident energy was acquired in .nxspe (Nexus event-mode) format. A Matlab (Mathworks Inc.) script tailored to stacked membranes used a cylindrical geometry where the components of scattering vector, Q, are the membrane plane, q_{xy}, and the cylindrical axis, q_z.

Bulk water data were sliced using a powder geometry in DAVE (Data Analysis and Visualization Environment) software from NIST Center for Neutron Research.[54] All data were cut into ten equal slices in q_z and up to 22 equal slices in q_{xy} to make a grid of 220 squares in reciprocal space. For E_is of 0.64, 0.96, 1.62, 3.28, 9.80 meV the widths in q_z and q_{xy} were 0.027, 0.033, 0.043, 0.062, and 0.106 Å, respectively.

Each square results in a spectrum of $S(q_{(xy,z)}, E)$ *vs.* E and was fit with functions that will be described in detail in the next section (Section 2.2.3). Only data from detector positions of greater than $\sim 10^\circ$ (the sixth slice and greater) in the lateral direction were used in the analysis due to contributions of the super mirror guides. The super mirror guides cause a beam divergence, which in turn affects the lower scattering angles.

As the membranes were disordered in the plane of the bilayers (lateral average), the lateral Q-range was scaled by $\sqrt{2}$ to convert the lateral scale from $q_{xy} = \sqrt{{q_x}^2 + {q_y}^2} = \sqrt{2}q_x$ to q_x. The q_x-range for each of the incident energies was as follows: 0.10–0.34 Å^{-1} (0.64 meV), 0.12–0.42 Å^{-1} (0.96 meV), 0.15–0.54 Å^{-1} (1.62 meV), 0.22–0.79 Å^{-1} (3.28 meV), and 0.37–1.35 Å^{-1} (9.80 meV). The q_z-ranges for each of the incident energies were: 0–0.27 Å^{-1} (0.64 meV), 0–0.33 Å^{-1} (0.96 meV), 0–0.43 Å^{-1} (1.62 meV), 0–0.62 Å^{-1} (3.28 meV), and 0–1.06 Å^{-1} (9.80 meV).

Resolution measurements for the membrane system were taken using a $\sim$15 K DMPC/H_2O sample and bulk H_2O resolution measurements using a vanadium sample. Resolutions and quasi-elastic spectra were cut to the same dimensions in reciprocal space. The fits are based on the Matlab nonlinear least-squares minimization algorithm ''lsqnonlin''. Fits were a numerical convolution of the resolution (Gaussian function(s)) with the δ-shaped function and the model for the QENS, with the addition of a background. The resolution function of Let depends on the incident energy and scattering angle and may deviate from a simple Gaussian function. Therefore, the resolution spectra were fit with one Gaussian function (E_i = 0.64, 0.96, 1.62 meV) or two Gaussian functions (E_i = 3.28, 9.80 meV). A Toeplitz matrix was constructed from each resolution spectrum, forming a square matrix dependent on the size of the scattering function spectrum. Convolution was carried out by multiplication of the Toeplitz matrix with the sum of the δ-shaped function and broadening model.

2.2.3 Diffusion models. There are different models used to describe diffusive motions.[55] For a particle diffusing *via* thermally-induced Brownian motion, the 1-dimensional mean squared displacement (MSD) of the particle is a function linear in time,

$$\langle[\delta r(t)]^2\rangle = 2Dt, \tag{3}$$

where D is the translational diffusion coefficient. With this characteristic length scale, one can define a self time-dependent pair-correlation function for incoherent scattering,

$$F_d(r, t) = (4\pi Dt)^{-\frac{1}{2}} \exp\left(\frac{-r^2}{4Dt}\right), \tag{4}$$

which is a solution of Fick's law,

$$\frac{\partial F_d(r, t)}{\partial t} = D\nabla^2 F_d(r, t). \tag{5}$$

The corresponding intermediate scattering function decays exponentially,

$$I_d(Q, t) = \exp(-Q^2 Dt), \tag{6}$$

and can be Fourier transformed to give a Lorentzian-shaped incoherent scattering function

$$S_d(Q, E) = \frac{1}{\pi\hbar}\left(\frac{Q^2 D}{(Q^2 D)^2 + (E/\hbar)^2}\right). \tag{7}$$

Thus, quasi-elastic scattering, which exhibits itself as Lorentzian broadening with a full-width at half-maximum (FWHM) that

has a Q^2 dependence, is indicative of a continuous diffusion process with $E_{\mathrm{FWHM}} = 2\hbar DQ^2$.

Water dynamics are more complex than that of ordinary liquids. In a simple liquid[56] atoms move ballistically at short times. The ballistic MSD $\langle[\delta r(t)]^2\rangle \propto \langle(vt)^2\rangle \propto t^2$ of the single molecule is eventually followed by a crossover to Brownian diffusion, characterized by $\langle[\delta r(t)]^2\rangle \propto t$, for long times. In dense or strongly interacting fluids, the caging effect leads to a plateau in $\langle[\delta r(t)]^2\rangle$. The motion in this regime is sub-diffusive with $\langle[\delta r(t)]^2\rangle \propto t^{\beta}$ with an exponent $\beta < 1$. This anomalous regime of hydration water dynamics was observed in computer simulations of lipid bilayers.[32,33]

The models used to fit the incoherent neutron data incorporate a constant background, a resolution function, $R(t)$ (in the time domain) or $R(E - E')$ (in energy domain), which is numerically convolved with the sum of a δ-like function and a function that describes the quasi-elastic broadening.

In the first model, motion of the water molecules is modelled by a single relaxation time, τ:

$$S_{\mathrm{R}}(Q,E) = \frac{1}{2\pi\hbar}\int \mathrm{d}t \mathrm{e}^{iEt/\hbar}\left[I_{\infty}(Q) + A(Q)\mathrm{e}^{-t/\tau}\right]R(t). \quad (8)$$

$E = \hbar\omega$, $A(Q) = (1 - I_{\infty}(Q))$, and $I_{\infty}(Q)$ is the so-called elastic incoherent structure factor, that represents effects of confinement, *i.e.*, correlations in the long-time limit[57,58] and $S_{\mathrm{R}}(Q, E)$ is the resolution-broadened incoherent scattering function. Eqn (8) describes a single Brownian diffusion process of the water molecules with a Lorentzian quasi-elastic broadening:

$$S_{\mathrm{R}}(Q,E) = C_{\mathrm{bkgnd}} + R(E - E') \otimes \left\{ B\delta(E - E') + A\frac{1}{\pi}\frac{\left(\frac{1}{2}\Gamma\right)}{(E')^2 + \left(\frac{1}{2}\Gamma\right)^2}\right\}, \quad (9)$$

where B is the amplitude of the δ-like function and is equal to $I_{\infty}(Q)$. A and C_{bkgnd} are constants and Γ is the FWHM of the Lorentzian function.

In the second model, the observed dynamics are described by two Brownian diffusion processes,

$$S_{\mathrm{R}}(Q,E) = \frac{1}{2\pi\hbar}\int \mathrm{d}t \mathrm{e}^{iEt/\hbar}\left[I_{\infty}(Q) + A_1(Q)\mathrm{e}^{-t/\tau_1} + A_2(Q)\mathrm{e}^{-t/\tau_2}\right]R(t), \quad (10)$$

resulting in two Lorentzian functions:

$$S_{\mathrm{R}}(Q,E) = C_{\mathrm{bkgnd}} + R(Q, E - E') \otimes \left\{ B\delta(E - E') + A_1\frac{1}{\pi}\frac{\left(\frac{1}{2}\Gamma_1\right)}{(E')^2 + \left(\frac{1}{2}\Gamma_1\right)^2} + A_2\frac{1}{\pi}\frac{\left(\frac{1}{2}\Gamma_2\right)}{(E')^2 + \left(\frac{1}{2}\Gamma_2\right)^2}\right\}. \quad (11)$$

Here, A_1 and A_2 are constants. These functions typically describe a slow motion (narrow width, Γ_1) and a fast process of the molecules (broad width, Γ_2).

In the third model, we used the Kohlrausch–Williams–Watts (KWW) function to describe motion of the water molecules.[59] This function describes a distribution of relaxation processes characterized by relaxation time τ and stretching exponent β. Values of β less than unity signify a sub-diffusive regime, where a stretching exponent of unity is indicative of Brownian diffusion.

Using this model one obtains

$$S_{\mathrm{R}}(Q,E) = \frac{1}{2\pi\hbar}\int \mathrm{d}t \mathrm{e}^{iEt/\hbar}\left[I_{\infty}(Q) + A(Q)\mathrm{e}^{-(t/\tau)^{\beta}}\right]R(t), \quad (12)$$

resulting in

$$S_{\mathrm{R}}(Q,E) = C_{\mathrm{bkgnd}} + R(Q, E - E') \otimes \left\{ B\delta(E - E') + FFT\left[A\mathrm{e}^{-(t/\tau)^{\beta}}\right]\right\}. \quad (13)$$

The choice of which of the above functions to use to model incoherent quasi-elastic neutron scattering data is not a purely mathematical problem. The use of a single Lorentzian peak implies a relaxation process with a single relaxation time τ. Two Lorentzian peaks imply two well defined dynamical processes. Stretched exponential correlation functions are often more appropriate to describe dynamics in heterogeneous systems to take into account the heterogeneous local structure in which water molecules move. β exponents of less than 1 describe a distribution of relaxation times. The dynamics are then "glassy" and the corresponding diffusion dynamics slower than a Brownian diffusion. This regime is referred to as "sub-diffusive". The difference in the distribution of relaxation times between a single and stretched exponentials, is pictured in Fig. 3 for different values of β.

A clear distinction between the different models often turns out to be difficult due to low statistics in experiments. Examples of different models fit to quasi-elastic scattering are shown in Fig. 4. While the one-Lorentzian fit shown in parts (a)–(c) fits the data reasonably well, fitting with two Lorentzians (parts (d–f)) or the Fourier transform of the KWW function (in parts (g–i)) provides a significantly better fit.

In order to quantitatively compare the different models, the reduced chi-squared values ($\tilde{\chi}^2$) of the different models were calculated using[61]

$$\tilde{\chi}^2 = \frac{1}{N - n}\sum^{N}\left(\frac{y_{\mathrm{dat}} - y_{\mathrm{fit}}}{\Delta y_{\mathrm{dat}}}\right)^2, \quad (14)$$

where N is the number of data points summed over and n is the number of constraints in the fits. The reduced χ^2 value gives a statistically valid measure of the goodness of fit: in the ideal case of $\tilde{\chi}^2 = 1$, the fit is within the error bars of the spectrum. For $\tilde{\chi}^2 > 1$, the spectrum is under-fitted, *i.e.*, there is more information in the spectrum that has not been reproduced in the fit. For $\tilde{\chi}^2 < 1$, the spectrum is over-fitted.

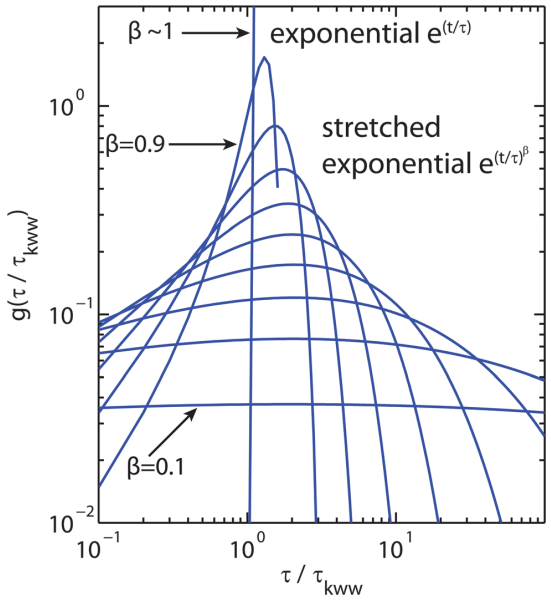

Fig. 3 Plot of the relaxation time probability density function (pdf) as a function of τ/τ_{KWW} where τ_{KWW} is the relaxation time introduced in eqn (12) and (13).[60] β values range from 0.1 to ~1 to illustrate the range of relaxation distributions for sub-diffusive systems as opposed to the δ-like distribution for Brownian diffusion (approximated by β = 0.9999).

Each spectrum was fit with all three models and the corresponding reduced χ^2 calculated. The results are listed in Table 1. A detailed list is given for the q_x-averaged $\tilde{\chi}^2$ for an incident energy of 3.28 meV to show that the fit quality also depends on q_z. Mean $\tilde{\chi}^2$s were calculated and are given for all energies. It is observed that the fit of a single Lorentzian provides a significantly poorer fit while two Lorentzian peaks and a KWW function seem to adequately describe the quasi-elastic data with almost identical $\tilde{\chi}^2$s.

We note that this problem is not unique to incoherent quasi-elastic neutron scattering experiments. Lipid motion determined by fluorescence correlation spectroscopy (FCS), for instance, was reported to be equally well described by anomalous diffusion or two Brownian diffusion processes.[11]

Following eqn (9), (11) and (13), the corresponding fitting functions involve 2, 4 and 3 free parameters. While a larger number of free parameters typically leads to a better fit, the fundamental question is if motion of molecules in anisotropic and heterogeneous environments is more reasonably described by a series of Brownian diffusion processes or rather by a distribution of relaxation times, as described by the KWW function. We will present evidence that the KWW provides the correct description of hydration water dynamics based on results from the neutron experiment and computer simulations further below. In the remaining sections, the quasi-elastic broadening is characterized by the Fourier transform of a KWW function to describe anomalous dynamics, and τ and β parameters are determined.

2.2.4 The effect of instrumental resolution. If there is an instrumental energy resolution, $R(E)$, then the resolution broadened dynamical structure factor, $S_R(Q, E)$ is given by

$$S_R(Q,E) = \int_{-\infty}^{+\infty} dE' S(Q,E') R(E-E'). \quad (15)$$

By introducing the Fourier transform, $R(t)$ of $R(E)$,[62]

$$R(E) = \frac{1}{2\pi\hbar}\int_{-\infty}^{+\infty} dt\, e^{iEt/\hbar} R(t), \quad (16)$$

$S_R(Q, E)$ can be written as,

$$S_R(Q,E) = \frac{1}{2\pi\hbar}\int_{-\infty}^{+\infty} dt\, e^{iEt/\hbar} I(Q,t) R(t). \quad (17)$$

When assuming a Gaussian resolution function, common in quasi-elastic incoherent neutron scattering experiments, $R(E)$ can be written as

$$R(E) = \left[2\pi\sigma^2\right]^{-\frac{1}{2}} e^{-\frac{E^2}{2\sigma^2}}, \quad (18)$$

where σ is the Gaussian width of the energy resolution. This resolution has the Fourier transform

$$R(t) = e^{-\frac{1}{2}\sigma^2 t^2/\hbar^2} = e^{-\frac{1}{2}t^2/{\tau_R}^2}. \quad (19)$$

When $R(t)$ is substituted into $R(E)$, the integral in eqn (17) is cut off after a time τ_R. For a Gaussian $R(t)$, the "cut-off" time (the experimental observation time τ_R) is related to the FWHM of $R(E)$ by

$$\tau_R = \frac{\hbar}{\sigma} = \hbar\frac{2\sqrt{2\ln 2}}{E_{FWHM}}. \quad (20)$$

where σ and E_{FWHM} are in energy units.

Experimental observation time windows, τ_R, for the bulk water sample were calculated from the average σ of the resolution peaks of 4.3, 6.8, 12.7, 20.0, 96.4 μeV to be 154.2, 97.2, 51.7, 23.5, 6.6 ps, respectively. The membrane samples have average σ resolution peaks of 4.3, 6.8, 12.6, 25.8, 96.0 μeV corresponding to observation time windows of 151.6, 97.4, 52.3, 25.5, 6.9 ps, respectively. The slight difference in the experimental resolution and observation time for the two samples is a purely geometrical effect as the experimental resolution depends on the size (mainly the diameter) of the sample used.

Molecular motions slower than the experimental observation time can still be accessed in experiments, however potential additional statistical noise in a spectrum can lead to a systematic error, which tends to overestimate the actual relaxation time, τ, as will be discussed below.

2.3 Simulations

2.3.1 Atomic-detail molecular dynamics simulations of bulk water diffusion. In order to study the intrinsic character of water diffusion, the motion of water in bulk was studied using molecular dynamics at full atomic detail. We employed GROMACS to simulate 895 water molecules (SPCE model) in a NPT ensemble with the built-in Nose–Hoover thermostat (T = 300 K, τ = 1 ps) and the built-in Parrinello–Rahman barostat (p = 1 bar, compressibility 4.5 × 10^{-5}/bar, τ = 1 ps).

View Article Online
Soft Matter Paper

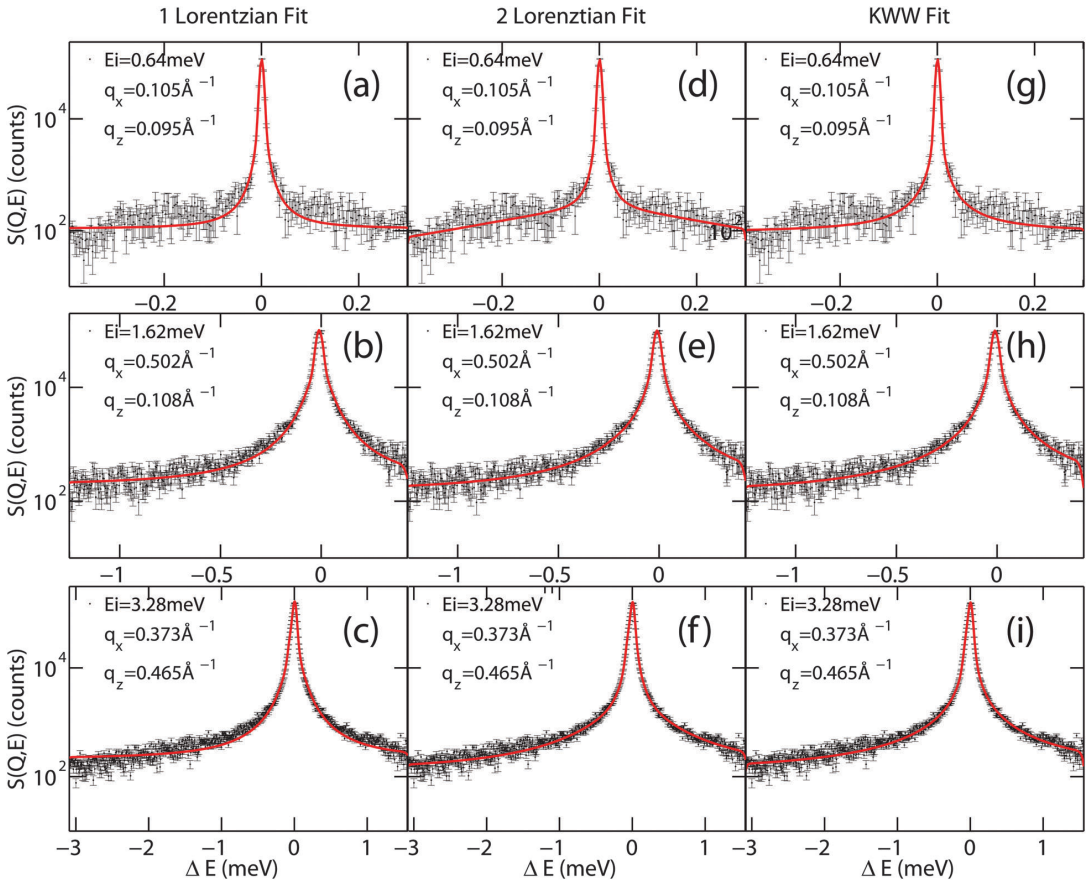

Fig. 4 Comparison between a one-Lorentzian peak fit, two-Lorentzian peak fit and Fourier transform of KWW fit of quasi-elastic broadening spectra of water diffusing in a lipid membrane. Values for q_x and q_z are indicated in each plot.

We used a time step of 1 fs and simulated for 50 ns. To ensure proper equilibration, only the trajectory beyond 1 ns was further analyzed. The start configuration is constructed with standard GROMACS routines for SPC water.

2.3.2 Coarse-grained Brownian dynamics simulations of water diffusion in a membrane system. In order to focus on the dynamical features introduced by the membrane due to different local dynamical environments and geometrical confinement, profiles for diffusivity $D(z)$ and free energy $V(z)$ were chosen to mimic those obtained in atomic-detail molecular dynamics simulations[32] and neutron reflectivity.

In particular, we choose:

$$D(z) = D_{\text{in}} + (D_{\text{bulk}} - D_{\text{in}})\frac{1+\cosh[b]}{\cosh[b]+\cosh[az]} \quad (21)$$

and

$$V(z) = cz^{2.75}, \quad (22)$$

with the bulk diffusion coefficient D_{bulk} = 2.7 nm^2 ns^{-1}, the inner-membrane diffusion coefficient D_{in} = 0.12 nm^2 ns^{-1}, and the parameters a = 4/nm, b = 3.6, c = 0.43/nm$^{2.75}$. $V(z)$ is given in units of k_BT. The potential $V(z)$ is shown in Fig. 5(b) and was modelled based on the experimentally determined distribution of water molecules in the bilayers. Note that since on sub-nanosecond time scales the crossing of water through membranes is negligible, these profiles describing only one water layer between two membranes is appropriate.

The displacement Δr of the center-of-mass of one water molecule within a time step Δt is calculated *via*

$$\Delta r = -D(z)\nabla V(z)\Delta t + \nabla D(z)\Delta t + \sqrt{2D(z)\Delta t}\Delta W, \quad (23)$$

where the Wiener increment ΔW is drawn from a normal distribution with $\langle \Delta W \rangle = 0$ and $\langle \Delta W^2 \rangle = 1$. Note that the second summand is the apparent drift term from the Ito interpretation of the Langevin equation[63] which ensures relaxation to equilibrium at long times.

The trajectory for one water molecule is simulated with Δt = 0.1 ps for a time of 10 μs. As starting condition we choose the center of the water layer, in agreement with the experimental data in Fig. 5.

Table 1 Listing of $\tilde{\chi}^2$ values (mean $\tilde{\chi}_x^2$). All q_z values are listed for an incident neutron energy of 3.28 meV; averages are shown for other energies, only. Mean $\tilde{\chi}^2$s are calculated from fits to one Lorentzian (eqn (9)), two Lorentzians (eqn (11)) and the KWW function (eqn (13)) of each spectrum. Exemplary fits are shown in Fig. 4

		Mean $\tilde{\chi}^2$		
Energy (meV)	q_z (Å^{-1})	1 Lorentzian	2 Lorentzians	KWW
0.64		1.21	1.07	1.15
0.96		2.14	2.06	2.03
1.62		5.58	5.03	5.15
3.28	0.0310	16.5	9.73	10.6
	0.0930	15.6	8.56	8.85
	0.155	14.6	7.41	7.73
	0.217	15.2	8.13	8.25
	0.279	13.6	6.49	6.58
	0.341	12.2	5.34	5.37
	0.403	12.7	5.93	5.86
	0.465	11.5	5.67	5.47
	0.527	12.5	7.48	7.30
	0.589	13.7	7.99	8.17
Mean $\tilde{\chi}^2$		13.7	7.27	7.41
9.80		71.0	30.7	41.7
Total $\tilde{\chi}^2$		**18.7**	**9.21**	**11.5**

2.3.3 Intermediate scattering function and fitting procedure. From the simulation trajectories, the intermediate scattering function $I(Q, t)$ was calculated directly for each combination of q_x and q_z, respectively. For the case of bulk water, $I(q_x, q_z, t)$ was calculated for the center-of-mass of each molecule for an exponential time range from 0.05 ps to 30 ns, respectively, as shown in Fig. 6, and then averaged over all molecules. For the case of membrane water, an exponential time range from 0.1 ps to 300 ns was used.

The intermediate scattering functions were fitted with a stretched exponential plus a constant (non-zero only for $q_x = 0$), consistent with the experimental analysis as laid out in eqn (13). To render the fitting more robust, we employed the following fit procedure: first, for the case of hydration water and $q_x = 0$, $I_\infty(q_x, q_z)$ is fixed to the mean of the last 3 points of the correlation function. For all other cases, $I_\infty(q_x, q_z)$ is set to zero. Second, we fit a stretched exponential to the re-scaled data.

In order to investigate conditions closer to the experiment, we include a hypothetical Gaussian experimental resolution *via* fitting weights $R(t) = \exp(-\frac{1}{2}t^2/\tau_R^2)$ with $\tau = 500$ ps. Fig. 6 shows a set of $I(Q, t)$ profiles with corresponding fits and artificial resolution function. Except for very small correlation times, the model of a stretched exponential provides good fits over several decades in times.

2.3.4 Mean-squared displacement and time-dependent stretch exponent. The MSDs parallel, $\langle \delta x^2 \rangle + \langle \delta y^2 \rangle$, and perpendicular, $\langle \delta z^2 \rangle$, to the membrane were calculated from the center-of-mass coordinate separately. In the case of bulk water, the MSDs are averaged over all molecules. According to the MSD for an anomalous diffusion, $\langle \delta r^2 \rangle = 2(Dt)^{\beta(t)}$, we calculate the time-dependent stretch exponent

$$\beta(t) = \frac{\mathrm{d}\log[\langle \delta r^2 \rangle]}{\mathrm{d}\log[t]} \quad (24)$$

as an alternative measure of motional anomaly.

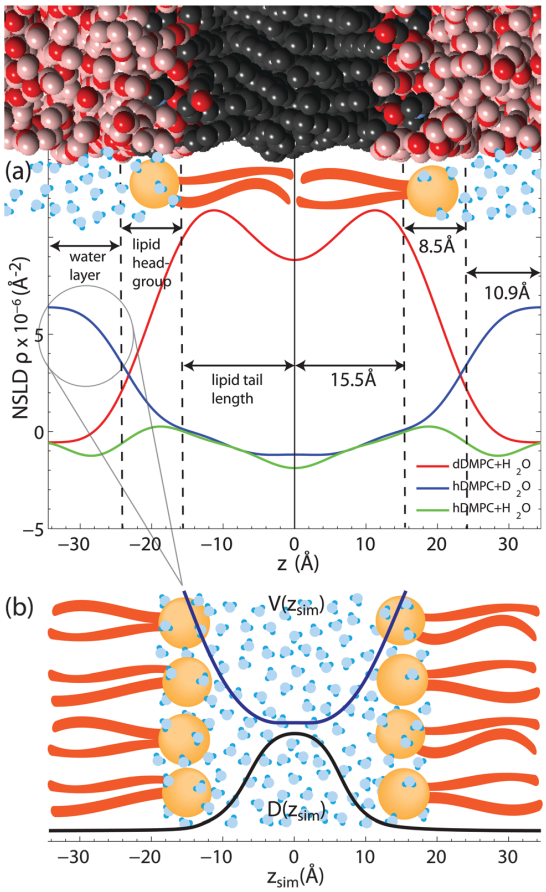

Fig. 5 (a) Scattering length density profiles as synthesized through Fourier transformation of the reflectivity curves in Fig. 2. Selective labelling of hydration water and lipid tails highlights the hydration water layer and the hydrophobic membrane core. Fully protonated membranes enable the determination of the lipid head groups as phosphate and carbonyl groups have larger coherent neutron scattering cross section. (b) The shape of the water segment of the D_2O/DMPC sample was used to model the shape of the potential, $V(z)$, in the simulations.

3 Results & discussion

3.1 Membrane structure

In order to confirm fully hydrated bilayers neutron reflectivity measurements were done to determine the bilayer structure. Fig. 5 shows the scattering length density profiles, as determined from the reflectivity curves in Fig. 2.

The DMPC/H_2O sample allowed us to determine the extent of the head group, the water layer and lipid tail regions. A combination of X-ray scattering, neutron scattering and simulations have been used to determine bilayer structures of a variety of phospholipids (PC).[64–66] Since these lipids have the same PC head group, these publications were instructive in finding the extent of our head group region. We define the extent of the head

View Article Online
Soft Matter Paper

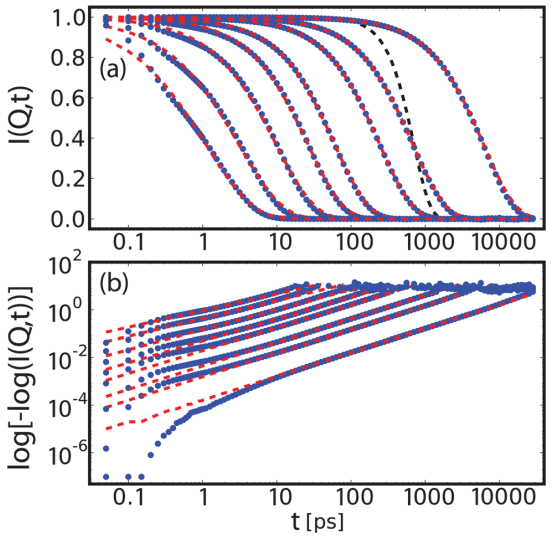

Fig. 6 Intermediate scattering function for bulk water at q_x = 0 and q_z = 0.025, 0.075, 0.125, 0.25, 0.375, 0.6, 1.0, 1.5 Å^{-1} in lin–log (a) and log–log (b) representation. These data (blue dots) are fitted corresponding to eqn (12) with a stretched exponential plus constant (red dashed line). The linear scaling over decades in time in the log–log representation supports the applicability of a stretched exponential as fit function, although deviations are observed at low times. The artificial resolution function is plotted as a black dashed line.

group to be the center of the distributions of its most interior/exterior molecules: carbonyl/choline groups.

The probability distributions for the head group components[65,66] show the head group/water boundary at approximately the centre of the choline distributions. The head group/water boundary should be approximately at the inflection point of the head group peak bordering the water at z = 24 Å, as shown in Fig. 5.

We assumed the maximum of our NSLD peak is centered between the phosphate and carbonyl groups. As the distribution of the carbonyl[64–66] has a half-width at half-maximum of ~3 Å, we approximate the head group/tail boundary at 15.5 Å. Half the average lamellar repeat distance minus the head group/water boundary (34.9–24.0 Å) results in half a water layer of 10.9 Å. Based on this analysis, the membrane core was found to have a thickness of 31 Å (15.5 Å per leaflet), the head group region was 8.5 Å thick and the hydration water layer had a total thickness of 21.8 Å (10.9 Å on each side of the density profile). These values were used in the simulations and confirm that the phospholipid bilayers were in their fully hydrated fluid phase. We note that the values for the bilayer dimensions are in excellent agreement with reference values for DMPC by the Nagle group[51] of D_{HH} = 35.3 Å, D_W = 19.2 Å and 9 Å for the head group thickness.

The raw NSLDs for each sample were scaled in the following way: the profile edges were scaled to the density of bulk water ($\rho_{H_2O} = -5.6 \times 10^{-7}$ Å^{-2} or $\rho_{D_2O} = +6.39 \times 10^{-6}$ Å^{-2}) and bilayer centers were scaled to a CH_3 (or CD_3) group ($\rho_{CH_3} = -1.83 \times 10^{-6}$ Å^{-2}) or ($\rho_{CD_3} = +8.89 \times 10^{-6}$ Å^{-2}) plus the NSLD of 0.10 water molecule. The center of the bilayer in the NSLD profiles are typically scaled to a CH_3 group, however, differences between tail regions of DMPC/H_2O and DMPC/D_2O profiles point to non-zero water content at the center of the hydrophobic core.

We determine the water content at the center of the hydrophobic core to be 0.10 solvent molecules (H_2O or D_2O) per lipid such that the NSLD profiles of the two DMPC samples overlap from ~6 Å to 10 Å.

Though this technique cannot determine the absolute number of water molecules in the entire tail group region, our experiments provide evidence for ~1 water molecule for every 10 lipids. The presence of water in the center of lipid bilayers is supported by IR spectroscopy experiments,[36] as well as simulations.[37,39] While the density of water molecules in the hydrophobic core is low compared to the hydration water layer, the center of the bilayer is a region of low lipid density, with a larger free volume fraction[39] and consequently lower free energy and higher probability for water molecules to be present.

The NSLD profiles in Fig. 5 are in very good agreement with results from recent computer simulations in the same system by Hansen *et al.*[33] and Yang, Calero and Marti.[67] Both our experiment and simulations agree that water molecules penetrate the bilayer into head group and tail region, however the simulations do not provide evidence for an increased water density in the center of the bilayers. We note that the simulations used a potential to implicitly model the membrane where water was not explicitly accounted for within the membrane core.

3.2 Water dynamics from experiments

3.2.1 Bulk water. The diffusion of water molecules in two systems are discussed in this section: (1) the isotropic diffusion of bulk water (H_2O) contained in a cylindrical annulus at room temperature, and (2) the anisotropic diffusion of hydration water (H_2O) in fluid, oriented, deuterated lipid bilayers at T = 30 °C (303 K). In order to describe motion of water molecules in crowded or strongly interacting environments, which may induce a distribution of relaxation times, the dynamics were fit directly in the energy domain using the Fourier transform of a KWW function, where β is the exponent of the stretched exponential and τ the corresponding relaxation time.

Fig. 7(a) and (b) show the results for bulk water. A sketch of the scattering geometry is shown in Fig. 7(c). Stretching exponent (Fig. 7(a)) and relaxation time (part (b)) are displayed in 2-dimensional maps as a function of parallel and perpendicular momentum transfer, q_x and q_z. τ is plotted in units of picoseconds and on a logarithm scale due to its multiple orders of magnitude range. The map covers motions of water molecules from ~3 Å to ~100 Å in the x-direction and from ~6 Å to ~60 Å in the z-direction.

Motions over longer distances (small $q_{x,z}$-values) are slower and require longer observation times (higher energy resolution or longer neutron wavelength, λ) as compared to short-range motions at larger $q_{x,z}$-values. Following Bragg's equation ($q = 4\pi \sin(\theta)/\lambda$ or $2d \sin(\theta) = \lambda$ with $d = 2\pi/q$), the accessible q_x and q_z-range strongly depends on the incident neutron wavelength.

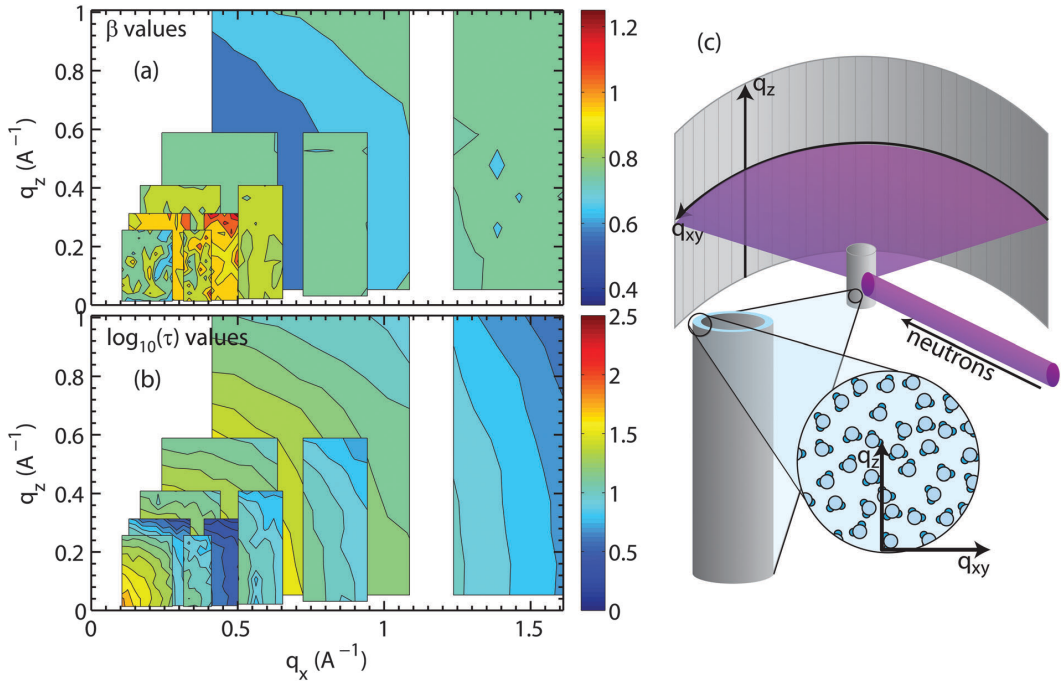

Fig. 7 Values of (a) β and (b) $\log_{10}(\tau)$ (τ in ps), fit from each bulk water spectrum, are plotted as a function of q_z and q_x. Measurements were made with five different energy resolutions. The isotropic nature of the bulk water dynamics can be seen in the concentric rings in (b). (c) Sketch of the scattering geometry. We note that the 17th slice in each measurement was taken out because the detector array at this scattering angle was, unfortunately, malfunctioning during the experiment.

The larger λ, the larger the observation time and the higher the energy resolution, however, the smaller the $q_{x,z}$-range covered. In order to cover the largest range of length and time scales, results from different energy resolutions must, therefore, be combined, as has been done in Fig. 7. The pattern of concentric rings of relaxation times in Fig. 7(b) is indicative of an isotropic motion of water molecules with longer relaxation times at longer length scales.

The values for β in Fig. 7(a) between 0.85 and 1 indicate that the corresponding nanoscale dynamics of water molecules is slightly sub-diffusive. Sub-diffusive dynamics is often found in supercooled water. Simulations of supercooled bulk water[68–70] show sub-diffusive behaviour with exponents in the range of β = 0.85–1 for our parameter ranges. Chen *et al.*[69,70] found that β stayed close to 1 for low Q values and low temperatures $T <$ 225 K, however Sciortino *et al.*[68] reported that supercooled bulk water at 285 K at $Q \sim 1.5$ Å^{-1} reached $\beta = 0.85$. Experiments using light scattering[71] and neutron scattering[71,72] observed $1 \geq \beta \geq 0.6$ for bulk water in our temperature range (293–313 K[72]) for $Q \sim 0.25$–1.5 Å^{-1}.

The bulk water measurements prove that diffusion can be studied by analyzing different areas on the large 2-dimensional detector array. We note that it is not trivial to determine a diffusion constant in the sub-diffusive regime as the standard approach is to use eqn (7) and plot the quasi-elastic broadening as a function square of the scattering vector, Q^2; this approach fails in the case of sub-diffusion and non-Lorentzian fit functions.

3.2.2 Membrane hydration water. Fig. 8(a) and (b) depict β and τ-values for the membrane hydration water as a function of q_x and q_z. The membranes were aligned horizontally in the spectrometer, such that q_x denotes the scattering vector of the lateral motions and q_z denotes motions transverse to the bilayers, as shown in Fig. 8(c). As for bulk water, five measurements with different energy resolution were combined to maximize the accessible $q_{x,z}$-range. While concentric circles were observed for bulk water, the pattern of βs and τs is clearly anisotropic for hydration water in the lateral and transverse direction. β-values of $\sim$0.5 were observed at high q_x and q_z-values in part (a) corresponding to small distances, indicative of a sub-diffusive dynamics. β continuously increases towards longer lengths (smaller $q_{x,z}$ values) until Brownian diffusion with $\beta = 1$ is observed.

The relaxation times in Fig. 8(b) show fast hydration water dynamics at large q_x, which continuously slows down towards longer length scales (smaller q-values). In contrast to the bulk water results in Fig. 7, the relaxation times along q_x and q_z are anisotropic with clear deviations from the circular pattern. The most striking feature is a localized region with slow relaxation times at $q_x \sim 0.15$ Å^{-1} (equivalent to a length scale of 40 Å). The feature is also seen in the β data in part (a) and exhibits small values of β of less than 0.40. Shape and position of this feature agrees well with the feature observed in the computer model of

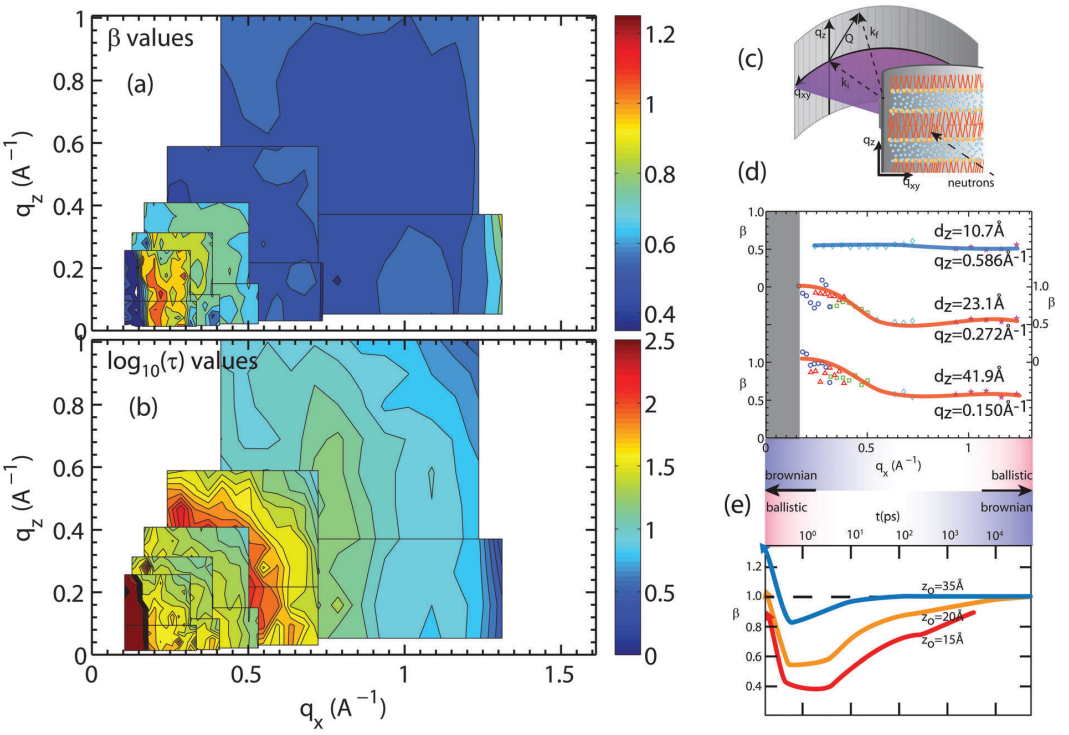

Fig. 8 Plots of the (a) stretching exponent, β, and (b) the logarithm of the relaxation time $\log_{10}(\tau)$, τ in ps, from fits of hydration water spectra that have been integrated over q_z and q_x. The smallest map corresponds to the highest resolution measurement (E_i = 0.64 meV) while the largest map corresponds to the lowest resolution measurement (E_i = 9.80 meV). The experimental error on determining the β- and τ-values depends on the actual Q-value and the resolution of the spectrometer. Relative standard error values for β and τ were between 5% to 10%. (c) A schematic of the membrane system in the Let spectrometer. (d) β values for slices in q_z of 0.15, 0.272, and 0.586 Å^{-1} for water motion varying in q_x. (e) β values adapted from simulations done by von Hansen *et al.*[32] plotted as a function of time.

the stacked bilayers and is a result of confinement, as will be discussed below.

Fig. 8(d) shows q_x-slices at different q_z-values, which allow access to different water molecules. Based on the structural results in Fig. 5, the highest density of water molecules in the hydrated bilayer stack is found in the center of the hydration water layer. Different values of the transverse momentum transfer, q_z, then correspond to the spread of z-values that the molecules explore when diffusing. q_z = 0.586 Å^{-1} corresponds to a vertical distance of $d_z = 2\pi/0.586$ = 10.7 Å, within the hydration water layer. The slice centered at q_z = 0.272 Å^{-1} contains water molecules that penetrate the head group region of the bilayers; q_z = 0.15 Å^{-1} molecules, which migrate to the lipid acyl chains. Based on Fig. 8(d), water molecules, which diffuse laterally in the hydration water layer show a sub-diffusive behaviour with a β exponent of $\sim$0.50. This β-value is significantly lower than the value that we measured for bulk water, indicative that hydration water motion is significantly anomalous. Water molecules in contact with lipid head groups and hydrophobic core show a sub-diffusive regime at small distances with a transition to Brownian motion at larger distances of $\sim$14 Å. We note that ballistic motion of water molecules with β-values of 2 is expected to occur at larger q_x-values, outside of the experimentally accessible range in this experiment.

The results are in qualitative agreement with a recent computer simulation study by von Hansen, Gekle and Netz,[32] which reports a sub-diffusive regime for hydration water dynamics, however in the time domain, as shown in Fig. 8(e) (data adapted from ref. 32). The simulation data were evaluated for water molecules at different distances from the bilayer center, z_0 = 15 Å being located in the lipid head group region and z_0 = 35 Å, at the farthest distance from the bilayer. We note that simulations were conducted in a single hydrated bilayer, where water dynamics away from the bilayer are more likely Brownian, as compared to the confined water layer in our experiment. Water molecules diffusing along the head group region or within the lipid tails show a distinct sub-diffusive regime, with β values of 0.50, in good agreement with the experimental results in Fig. 8(d).

Corresponding cuts of the relaxation time, τ, at q_z-values of 0.15 Å^{-1} and 0.586 Å^{-1} (corresponding to z motions over 10.7 Å and 41.9 Å, respectively) are shown in Fig. 9. Again, slices were centered in the hydration water layer and q_z-values are a measure of the corresponding slice width. The relaxation time for hydration

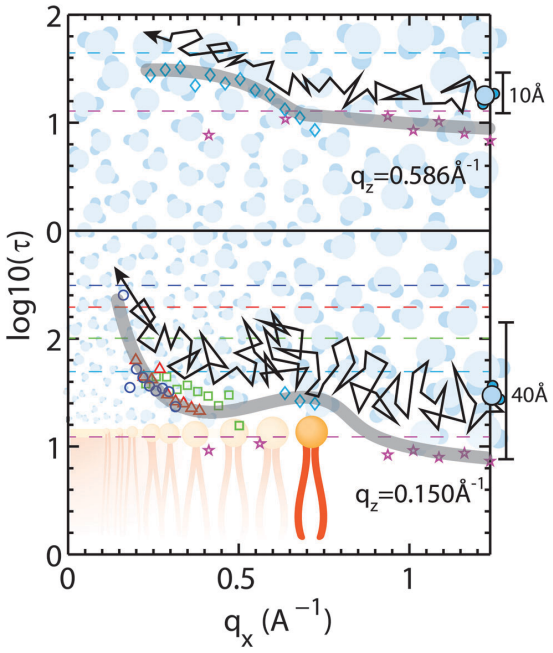

Fig. 9 Lateral diffusion of membrane water molecules as shown by relaxation time τ (τ in ps). Slices along q_x are shown for two values of q_z. The lower curve occurs at q_z = 0.15 Å^{-1} corresponding to length scale of ~40 Å. The lateral motion of a water molecule is slowed significantly for a lateral length scale of ~10 Å denoted by an increase in τ at q_x = 0.6 Å^{-1}; most likely due to the water's interaction with the head group, where hydrogen bonding occurs. The upper curve occurs at q_z = 0.586 Å^{-1} corresponding to ~10 Å. This signal is most likely dominated by water molecules diffusing in the hydration water layer. Dashed lines correspond to maximum viable τ; lines and symbols have corresponding colors.

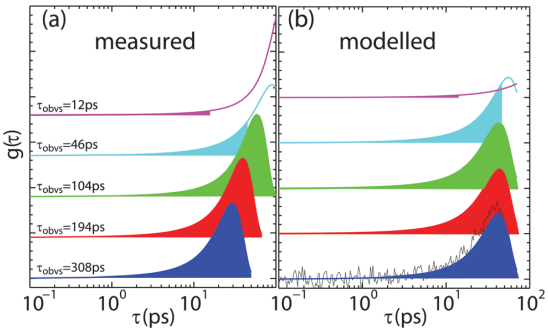

Fig. 10 (a) Plot of relaxation time probability density functions using β and τ_{KWW} values obtained from fits of QENS data for an area of reciprocal space bounded by Δq_z = 0.2–0.1 Å^{-1} and Δq_x = 0.4–0.3 Å^{-1} for each resolution probed. (b) Plot of fits to relaxation time pdfs with β = 0.8 with noise. Values of τ_{KWW} and amplitude were obtained for fits to the noisy pdf within each resolution range. Blocks of color represent the observation time window for that particular resolution setup. Observation times (τ_R) are given.

water molecules diffusing laterally with small z motions (large q_z), inside the water layer, was found to be almost q_x independent. A slight slowing down of the water molecules at a q_x-value of ~0.70 Å^{-1} is likely related to the presence of the bilayer interface as a disturbance caused by the lipid head groups. This feature corresponds to the slight decrease in β-values in Fig. 8(e) in the computer simulations by von Hansen, Gekle and Netz[32] at z_0 = 35 Å.

A hydration water molecule that moves about a range of z = 40 Å while diffusing laterally penetrates the bilayer to the lipid acyl chains. Its motion appears to slow down at a q_x value corresponding to the distance between two lipid head groups indicated by the peak in the relaxation time. The relaxation times then increase significantly towards larger length scales.

3.2.3 Effect of experimental resolution. A resolution effect is observed in Fig. 8(b): while the general trend is that motions become faster over smaller distances (larger Q-values), τ values between the different resolution frames do not seem to fit seamlessly. When switching from a higher to a lower resolution (moving from a smaller into a larger rectangle in Fig. 8(b)), the relaxation time becomes slower again. Thus, it seems that different relaxation times can be obtained when the same length scale is measured at two different energy resolutions equivalent to different experimental observation times.

Fig. 10 illustrates the effect: Fig. 10 (a) shows τ distributions of the fit function to data measured at the same (q_x, q_z) position in reciprocal space from the data in Fig. 8 (which should have the same relaxation time), however, measured at different experimental resolution times, τ_R. τ_R-values are given in the figure and marked by the shaded areas. For some resolutions, the peak in the time distribution is outside of the experimentally covered window and the corresponding relaxation time was extrapolated by the fit. As a consequence, when the quasi-elastic broadening was too small to be properly resolved by the instrumental resolution, the relaxation time was found to be systematically over-estimated.

Though counterintuitive, this behaviour is a systematic effect that can be modelled. If there is little or no noise or error, fit functions can typically be determined correctly even when the function is not fully covered by the experimentally accessible range of data. This is the case when the relaxation time is outside the experimental resolution window, as defined in eqn (20). The combination of experimental noise and partial coverage, however, may cause a systematic error in the determination of relaxation times in quasi-elastic incoherent neutron scattering experiments. In Fig. 10(b), the τ-distribution from part (a) was generated and a window equivalent to the experimentally accessible time window was selected. Statistical noise was added to the generated data to mimic experimental conditions. The resulting data were then fitted again with the original distribution that was used to create the distribution (and should reproduce the original data). The results are shown as solid lines in part (b) and well reproduce the systematic deviation: the relaxation time tends to be over-estimated when the distribution is outside of the experimental window and experimental noise is present.

3.3 Water dynamics from computer modelling

In order to consolidate the picture of anisotropy and anomaly of water dynamics obtained by the neutron scattering experiments,

View Article Online

Soft Matter Paper

we employed two sets of computer modelling. First, using full-atomic detail molecular dynamics, we studied the intrinsically anomalous character of isotropic, bulk water diffusion at picosecond time scales.

For hydration water dynamics, we used a coarse-grained Brownian dynamics simulation to investigate the effects of geometrical confinement and locally varying dynamical environments of water molecules interacting with lipid bilayers. The corresponding systems are inherently larger in size and the number of molecules involved, therefore, making full atomistic simulations challenging.

3.3.1 Bulk water. Fig. 11 summarizes the results for the atomistic bulk water simulations. β-values are shown in part (a) and the corresponding relaxation times in part (b). As expected for bulk water in isotropic and unconfined conditions, no angular dependence is observed in the relaxation time τ and the stretch exponent β. Patterns of concentric circles are observed, in agreement with the experimental data. τ increases monotonically with decreasing q_x or q_z, *i.e.*, increasing length scale. In agreement with the experimental results bulk water dynamics on picosecond time scales and over Ångström distances (large $q_{x,z}$-values) is sub-diffusive, with β exponents of $\sim$0.75. The diffusive nature changes to Brownian at low $q_{x,z}$.

The MSD and the derived time-dependent stretch exponent β are shown in Fig. 11(c) and (d). The displacements along different directions ($\langle\delta x^2\rangle$, $\langle\delta y^2\rangle$ and $\langle\delta z^2\rangle$) coincide, indicative of an isotropic motion. After a ballistic regime at sub-picosecond time scales, a sub-diffusive regime at time scales of several picoseconds follows, and, finally, normal diffusion is reached at nanosecond time scales, in agreement with computer simulations by von Hansen *et al.*[32] Thus, both experiments and simulations consistently indicate that water diffusion has an intrinsically sub-diffusive character on picosecond time scales, also under ambient conditions.

3.3.2 Membrane hydration water. Fig. 12 shows the results for the simulations of water in proximity to membranes. Before discussing the 2-dimensional maps, we stress that the computational framework used here involved Brownian dynamics, and can, therefore, not account for the intrinsic sub-diffusive character of water diffusion in the bulk. Consistently, the mean-squared displacement and the time-dependent stretch exponent β should indicate normal diffusion at small times (with $\beta = 1$).

However, the stretch exponent β in Fig. 12(a) shows sub-diffusive behaviour at all q_x values, with a trend of stronger sub-diffusive motion at higher q_x. Pronounced anisotropic behaviour is observed at low q_x. The constant $I_\infty(Q)$ is zero except for $q_x = 0$ Å^{-1} and $q_z \lesssim 0.2$ Å^{-1}, indicating geometrical confinement due to the membrane on a length scale of $\sim$30 Å. The relaxation time τ (plotted in units of 1 ps in Fig. 12(b)) shows anisotropic behaviour at low q_x. Water motion is overall slower than in bulk water in Fig. 11(b).

The significantly longer τ results from the slowing down of dynamics close to the membrane, and a longer average relaxation time. The value of β indicates a distribution of local dynamical environments, and thus a distribution of relaxation times. This finding is consistent with the observed trend of β approaching 1 with lowering $q_{x,z}$, since the molecule explores a larger space and thus performs a temporal average of dynamical environments, finally reaching normal diffusion with the average diffusion coefficient.

With increasing correlation time, the molecules experience confinement due to the membrane, which induces an apparent sub-diffusive character for the diffusion displacement. We note that this factor is only caused by the z coordinate, as shown in the MSD in Fig. 12(c), while diffusion along x and y is normal diffusion, as expected from the simulation framework.

At low $q_{x,z}$, distinct anisotropic features appear in τ, β and I_∞, mirroring the features observed in experiments. In particular, when cutting along the q_x axis for small q_z, a non-monotonous behaviour is observed for β and τ. The evolution of β as a function of time is plotted in Fig. 12(d). This non-monotonicity seems to be directly related to confinement effects, since its

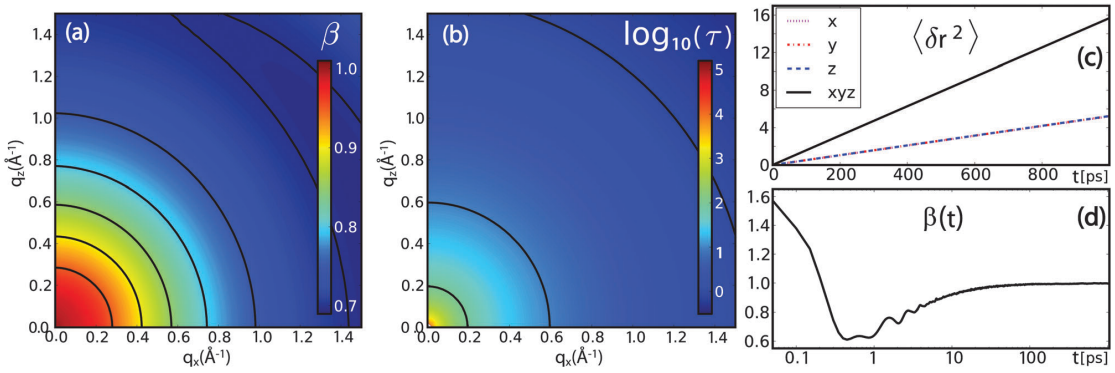

Fig. 11 Results from full atomistic molecular dynamics simulations of bulk water using the SPCE model: (a) intrinsic anomaly of water diffusion: the stretch exponent β indicates a transition from normal diffusion at low q_x-value to predominantly sub-diffusive behaviour at larger q_x. (b) The relaxation time τ (plotted in units of 1 ps) shows no anisotropic behaviour, as expected for bulk water. (c) and (d) The time-dependent stretch exponent as extracted from the MSD $\langle\delta r^2\rangle$ *via* eqn (24) changes from a super-diffusive, ballistic regime at times below 0.5 ps to a sub-diffusive regime for several ps before approaching the normal diffusive regime for longer time scales.

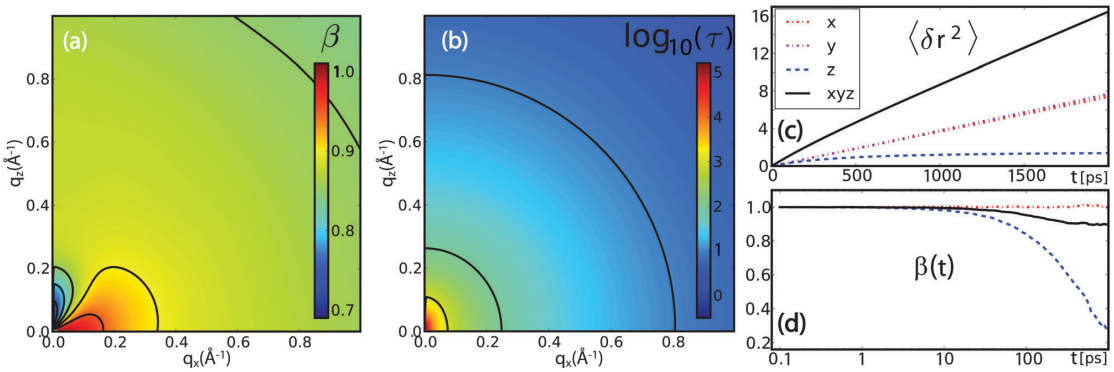

Fig. 12 Results from coarse-grained Brownian dynamics simulation for water confined in a membrane system: (a) anomaly of water diffusion due to dynamical heterogeneity and confinement: the stretch exponent β shows sub-diffusive behaviour at all visible q_x values, with a trend of stronger sub-diffusive motion at higher q_x. Anisotropic behaviour is observed at low q_x due to geometrical confinement of the membranes. (b) The relaxation time τ (plotted in units of 1 ps) shows a slight anisotropic behaviour at low q_x. Water diffusion is overall slower than in bulk (see Fig. 11(a)). (c) and (d) Mean-squared displacements $\langle \delta r^2 \rangle$ and time-dependent stretch exponents $\beta(t)$ (see eqn (24)) for different coordinate directions evidence a confined motion in z-direction (blue dashed), while the MSD in xy-direction (red dash-dotted) resembles that of normal diffusion. The resulting overall MSD (black solid) has an apparent sub-diffusive character emerging solely from the confinement of hydration water molecules.

appearance coincides with a non-zero I_∞, *i.e.*, a non-vanishing correlation at long times.

This relation of geometrical confinement and dynamical effects can be understood when considering the role of Q in the calculation of the intermediate scattering function if one coordinate is confined:

$$I(Q,t) = \langle \exp[-i\vec{Q}\cdot(\vec{r}(t) - \vec{r}(0))] \rangle \sim \exp[-q_x{}^2\langle \delta x^2 \rangle - q_y{}^2\langle \delta y^2 \rangle - q_z{}^2\langle \delta z^2 \rangle] + \ldots, \quad (25)$$

where the second line is the first term of the so-called cumulant expansion, the so-called Gaussian approximation. For a fluctuation with wave vector Q to relax, the MSD has to increase sufficiently. For the case of the membrane system, the z motion is confined on the experimental time scales, *i.e.* $\langle \delta z^2 \rangle$ settles at $L_{\text{layer}} \sim 40$ Å for long times, in perfect agreement with the experiments. Consequently, for $q_x = q_y = 0$, correlation remains for long times, which is represented by $I_\infty(Q)$ from eqn (8). At large q_x, the remaining long-time correlations are relaxed only through the x motion, *i.e.*, diffusion in z and x direction play a fundamentally different role. Small q_z corresponds to a larger remaining correlation in the z direction, which in turn means that a longer time is needed to relax the fluctuation *via* the other coordinates. We note that the argument is not dependent on the Gaussian approximation, but similarly holds for higher cumulants, since all z cumulants are constant and confined in the long time limit.

3.4 Motion of water molecules

Lipid diffusion has been studied for decades and it is commonly accepted that the Brownian motion of lipid molecules over long, micrometer length scales is characterized by a continuous diffusion process.[13–17,21] Although this is a well studied fundamental process, our understanding of nanoscale diffusion in membranes is still being challenged by new results from experiments and simulations.

Experimental evidence that lipids move coherently in loosely bound clusters, rather than as independent molecules was presented.[7,18–20] A "hopping" diffusion of lipids into nearest neighbour sites was observed in single supported bilayers.[6] Ballistic lipid motion in fluid membranes was recently reported.[5] It has also been suggested that there is a flow-like component to the motion of the lipid molecules over long length scales.[7]

Significantly less work has been done to study dynamics of hydration water molecules, most likely due to the experimental and computational challenges. We find that lateral water diffusion is affected at all distances from the bilayers and motions of hydration water molecules differs significantly from the isotropic diffusion of bulk water.

3.4.1 Anomalous dynamics of hydration water. By labelling water molecules, lipid head groups, and lipid tails through selective deuteration, dimensions of hydration water layer, bilayer head group and tail region were determined by neutron reflectivity. While the highest water density is found in the center of the hydration water layer, the NSLDs give evidence for water molecules that are able to penetrate the hydrophobic membrane core; ~1 water molecule per 10 lipid molecules were found in the center of the fully hydrated membranes.

From the quasi-elastic neutron scattering experiments and computer simulations, we obtain a consistent picture of the phenomenology of water diffusion in membrane systems, as well as different origins of anomaly and anisotropy. As a first origin of anomaly, water shows an intrinsic anomalous diffusion on pico-second time scales, as also observable in bulk water. The second origin of anomalous diffusion is related to the distribution of local dynamical environments of hydration water molecules, which leads to a distribution of relaxation times and sub-diffusive behaviour. The anisotropic effects of confinement and local dynamical environments on the motions in different directions give rise to direction-dependent relaxation times and stretch exponents due to the varying sampling time of the system along the unconfined coordinates.

View Article Online
Soft Matter Paper

3.4.2 Anomalous diffusion models. Different models are typically used in the literature to describe membrane and hydration water dynamics in quasi-elastic neutron scattering experiments. Through a comparison between a single Lorentzian, two Lorentzians and the KWW function to fit the quasi-elastic broadening, the single Lorentzian was found to give the poorest agreement, while two Lorentzians and the KWW function both provided a satisfying fit. The fundamental difference between the two models is the description of relaxation times in the time domain. The two Lorentzian peaks typically correspond to a slow and a fast process, each with a single relaxation time. While the slow process is well captured, the observed fast process typically partially lies outside of the instrumentally accessible energy window and basically leads to a broad, curved background. This procedure is often used in the literature. While the KWW function fits 3 parameters, the model using two Lorentzian functions has 4 free parameters. Fitting more free parameters typically provides better fits with smaller χ^2-values.

A clear distinction of which model to use is often difficult in QENS data because of the limited statistics in the data, such that different models fit the data equally well. We note that FCS suffers from the same issue and cannot unambiguously determine the basic character of lipid dynamics in membranes.[11] However, we argue that motion of water molecules in anisotropic and heterogeneous environments is physically better described by a distribution of relaxation times (a KWW function) rather than a sum of individual Brownian processes (several Lorentzian functions). This interpretation is supported by the computer simulations, *i.e.*, by the linear scaling of intermediate scattering function in the log–log representation over several decades which is indicative of a single stretched exponential.

We further tested the hypothesis of Lorentzian *vs.* KWW function in the experiment by using different instrumental resolutions. If the processes fitted by the 2 Lorentzian peak broadenings were actual physical processes, their corresponding width should be constant and they should be independent of the instrumentally available energy window. However, each energy resolution was well fit by a narrow and a broad Lorentzian peak, with no correlation between the broad peaks at different resolutions. This is strong evidence that the broad Lorentzian is likely a fitting artefact in the case of hydration water. We can, of course, not make a statement about lipid dynamics as this was not part of the current study.

Measurements at different hydrations could possibly be used to distinguish between Lorentzian and KWW models in QENS experiments in the future. One may expect that de-hydration leads to a more heterogeneous environment of water molecules and correspondingly smaller values of β, possibly up to the point where Lorentzians no longer describe the data.

4 Conclusion

Diffusion of hydration water molecules in hydrated phospholipid bilayers was studied using 2-dimensional incoherent quasi-elastic neutron scattering combined with computer modelling. By aligning the membranes horizontally in the spectrometer, lateral and transverse molecular motions can be studied separately, but simultaneously, by analyzing different positions on the 2-dimensional detector array. The dynamics were described in the energy domain by KWW functions, corresponding to stretched exponentials in the time domain.

The nanoscale dynamics of hydration water molecules is anisotropic, and shows a sub-diffusive behaviour on nanometer length scales. As a first origin of the anomalous character of hydration water we have identified the intrinsic sub-diffusion of water at picosecond time scales, as also observed in bulk water. Secondly, a dynamically heterogeneous environment causes a distribution of relaxation times that finally appear as a sub-diffusive motion. These 2-dimensional data show a distinct regime of very slow dynamics at small Q-values, related to the geometry of the stacked bilayers used for the experiment.

Diffusion experiments using 2-dimensional detectors will in the future be used to precisely measure penetration and permeability of water molecules across bilayers as a function of bilayer composition,[40,73] and to study the interaction of water with membrane inclusions, such as proteins and peptides.

Acknowledgements

Experiments were funded by the Natural Sciences and Engineering Research Council (NSERC) of Canada, the National Research Council (NRC), the Canada Foundation for Innovation (CFI), and the Ontario Ministry of Economic Development and Innovation. L.T. is the recipient of an NSERC Canada Graduate Scholarship, M.C.R. is the recipient of an Early Researcher Award from the Province of Ontario. H.R.G. was supported by the United States DOE, Office of Basic Energy Sciences under Contract No. 46680. We profited from discussions with Jean-Louis Barrat (Grenoble) on the general interpretation.

References

1 M. Guo, A. J. Ehrlicher, M. H. Jensen, M. Renz, J. R. Moore, R. D. Goldman, J. Lippincott-Schwartz, F. C. Mackintosh and D. A. Weitz, Probing the stochastic, motor-driven properties of the cytoplasm using force spectrum microscopy, *Cell*, 2014, **158**, 822–832.
2 F. Höfling and T. Franosch, Anomalous transport in the crowded world of biological cells, *Rep. Prog. Phys.*, 2013, **76**, 046602.
3 D. S. Banks and C. Fradin, Anomalous diffusion of proteins due to molecular crowding, *Biophys. J.*, 2005, **89**, 2960–2971.
4 F. Roosen-Runge, M. Hennig, F. Zhang, R. M. J. Jacobs, M. Sztucki, H. Schober, T. Seydel and F. Schreiber, Protein self-diffusion in crowded solutions, *Proc. Natl. Acad. Sci. U. S. A.*, 2011, **108**, 11815.
5 C. L. Armstrong, M. Trapp, J. Peters, T. Seydel and M. C. Rheinstädter, Short range ballistic motion in fluid lipid bilayers studied by quasi-elastic neutron scattering, *Soft Matter*, 2011, **7**, 8358–8362.

6 C. L. Armstrong, M. D. Kaye, M. Zamponi, E. Mamontov, M. Tyagi, T. Jenkins and M. C. Rheinstädter, Diffusion in single solid supported lipid bilayers studied by quasi-elastic neutron scattering, *Soft Matter*, 2010, **6**, 5864–5867.

7 S. Busch, C. Smuda, L. C. Pardo and T. Unruh, Molecular mechanism of long-range diffusion in phospholipid membranes studied by quasielastic neutron scattering, *J. Am. Chem. Soc.*, 2010, **132**, 3232–3233.

8 E. Flenner, J. Das, M. C. Rheinstädter and I. Kosztin, Subdiffusion and lateral diffusion coefficient of lipid atoms and molecules in phospholipid bilayers, *Phys. Rev. E: Stat., Nonlinear, Soft Matter Phys.*, 2009, **79**, 011907.

9 G. R. Kneller, K. Baczynski and M. Pasenkiewicz-Gierula, Communication: consistent picture of lateral subdiffusion in lipid bilayers: molecular dynamics simulation and exact results, *J. Chem. Phys.*, 2011, **135**, 141105.

10 J.-H. Jeon, H. M.-S. Monne, M. Javanainen and R. Metzler, Anomalous diffusion of phospholipids and cholesterols in a lipid bilayer and its origins, *Phys. Rev. Lett.*, 2012, **109**, 188103.

11 P. Schwille, J. Korlach and W. W. Webb, Fluorescence correlation spectroscopy with single-molecule sensitivity on cell and model membranes, *Cytometry*, 1999, **36**, 176–182.

12 D. S. Martin, M. B. Forstner and J. A. Käs, Apparent subdiffusion inherent to single particle tracking, *Biophys. J.*, 2002, **83**, 2109–2117.

13 S. König, W. Pfeiffer, T. Bayerl, D. Richter and E. Sackmann, Molecular dynamics of lipid bilayers studied by incoherent quasi-elastic neutron scattering, *J. Phys. II*, 1992, **2**, 1589–1615.

14 S. König, E. Sackmann, D. Richter, R. Zorn, C. Carlile and T. M. Bayerl, Molecular dynamics of water in oriented dppc multilayers studied by quasielastic neutron scattering and deuterium-nuclear magnetic resonance relaxation, *J. Chem. Phys.*, 1994, **100**, 3307–3316.

15 S. König, T. M. Bayerl, G. Coddens, D. Richter and E. Sackmann, Hydration dependence of chain dynamics and local diffusion in l-alpha-dipalmitoylphosphatidylcholine multilayers studied by incoherent quasi-elastic neutron scattering, *Biophys. J.*, 1995, **68**, 1871–1880.

16 W. Pfeiffer, Th. Henkel, E. Sackmann and W. Knorr, Local dynamics of lipid bilayers studied by incoherent quasi-elastic neutron scattering, *Europhys. Lett.*, 1989, **8**, 201–206.

17 W. Pfeiffer, S. König, J. F. Legrand, T. Bayerl, D. Richter and E. Sackmann, Neutron spin echo study of membrane undulations in lipid multibilayers, *Europhys. Lett.*, 1993, **23**, 457–462.

18 E. Falck, T. Róg, M. Karttunen and I. Vattulainen, Lateral diffusion in lipid membranes through collective flows, *J. Am. Chem. Soc.*, 2008, **130**, 44–45.

19 M. C. Rheinstädter, J. Das, E. J. Flenner, B. Brüning, T. Seydel and I. Kosztin, Motional coherence in fluid phospholipid membranes, *Phys. Rev. Lett.*, 2008, **101**, 248106.

20 C. L. Armstrong, L. Toppozini, H. Dies, A. Faraone, M. Nagao and M. Rheinstädter, Incoherent neutron spin-echo spectroscopy as an option to study long-range lipid diffusion, *ISRN Biophys.*, 2013, **2013**, 9.

21 U. Wanderlingh, G. D'Angelo, C. Branca, V. C. Nibali, A. Trimarchi, S. Rifici, C. Finocchiaro, D. ad Crupi, J. Ollivier and H. D. Middendorf, Multi-component modeling of quasielastic neutron scattering from phospholipid membranes, *J. Chem. Phys.*, 2014, **140**, 174901.

22 S. R. Wassall, Pulsed field gradient-spin echo NMR studies of water diffusion in a phospholipid model membrane, *Biophys. J.*, 1996, **71**, 2724.

23 M. Weik, U. Lehnert and G. Zaccai, Liquid-like water confined in stacks of biological membranes at 200 K and its relation to protein dynamics, *Biophys. J.*, 2005, **89**, 3639–3646.

24 L. Toppozini, C. L. Armstrong, M. D. Kaye, M. Tyagi, T. Jenkins and M. Rheinstädter, Hydration water freezing in single supported lipid bilayers, *ISRN Biophys.*, 2012, **2012**, 520307.

25 M. C. Rheinstädter, T. Seydel, F. Demmel and T. Salditt, Molecular motions in lipid bilayers studied by the neutron backscattering technique, *Phys. Rev. E: Stat., Nonlinear, Soft Matter Phys.*, 2005, **71**, 061908.

26 P. W. Fenimore, H. Frauenfelder, B. H. McMahon and F. G. Parak, Slaving: solvent fluctuations dominate protein dynamics and functions, *Proc. Natl. Acad. Sci. U. S. A.*, 2002, **99**, 16047–16051.

27 P. W. Fenimore, H. Frauenfelder, B. H. McMahon and R. D. Young, Bulk-solvent and hydration-shell fluctuations, similar to α- and β-fluctuations in glasses, control protein motions and functions, *Proc. Natl. Acad. Sci. U. S. A.*, 2004, **101**, 14408–14413.

28 H. Frauenfelder, P. W. Fenimore, G. Chen and B. H. McMahon, Protein folding is slaved to solvent motions, *Proc. Natl. Acad. Sci. U. S. A.*, 2006, **103**, 15469–15472.

29 G. Zaccai, The effect of water on protein dynamics, *Philos. Trans. R. Soc., B*, 2004, **359**, 1269–1275.

30 O. Kel, A. Tamimi, M. C. Thielges and M. D. Fayer, Ultrafast structural dynamics inside planar phospholipid multibilayer model cell membranes measured with 2D IR spectroscopy, *J. Am. Chem. Soc.*, 2013, **135**, 11063–11074.

31 K. Wood, M. Plazanet, F. Gabel, B. Kessler, D. Oesterhelt, D. J. Tobias, G. Zaccai and M. Weik, Coupling of protein and hydration-water dynamics in biological membranes, *Proc. Natl. Acad. Sci. U. S. A.*, 2007, **104**, 18049–18054.

32 Y. von Hansen, S. Gekle and R. R. Netz, Anomalous anisotropic diffusion dynamics of hydration water at lipid membranes, *Phys. Rev. Lett.*, 2013, **111**, 118103.

33 F. Y. Hansen, G. H. Peters, H. Taub and A. Miskowiec, Diffusion of water and selected atoms in DMPC lipid bilayer membranes, *J. Chem. Phys.*, 2012, **137**, 204910.

34 P. Wästerby, G. Orädd and G. Lindblom, Anisotropic water diffusion in macroscopically oriented lipid bilayers studied by pulsed magnetic field gradient NMR, *J. Magn. Reson.*, 2002, **157**, 156–159.

35 A. Ghosh, R. Kramer Campen, M. Sovago and M. Bonn, Structure and dynamics of interfacial water in model lung surfactants, *Faraday Discuss.*, 2009, **141**, 145–159.

36 L. Piatkowski, J. de Heij and H. J. Bakker, Probing the distribution of water molecules hydrating lipid membranes with ultrafast förster vibrational energy transfer, *J. Phys. Chem. B*, 2013, **117**, 1367–1377.

37 S. M. Gruenbaum and J. L. Skinner, Vibrational spectroscopy of water in hydrated lipid multi-bilayers. iii. water clustering and vibrational energy transfer, *J. Chem. Phys.*, 2013, **139**, 175103.

38 J. Andrasko and S. Forsén, NMR study of rapid water diffusion across lipid bilayers in dipalmitoyl lecithin vesicles, *Biochem. Biophys. Res. Commun.*, 1974, **60**, 813–819.

39 S.-J. Marrink and H. J. C. Berendsen, Simulation of water transport through a lipid membrane, *J. Phys. Chem.*, 1994, **98**, 4155–4168.

40 M. D. Kaye, K. Schmalzl, V. C. Nibali, M. Tarek and M. C. Rheinstädter, Ethanol enhances collective dynamics of lipid membranes, *Phys. Rev. E: Stat., Nonlinear, Soft Matter Phys.*, 2011, **83**, 050907.

41 J. R. P. Webster, S. Langridge, R. M. Dalgliesh and T. R. Charlton, Reflectometry techniques on the second target station at ISIS: methods and science, *Eur. Phys. J. Plus*, 2011, **126**, 1–5.

42 R. Dalgliesh, S. Langridge, J. Plomp, V. O. de Haan and A. A. van Well, Offspec, the ISIS spin-echo reflectometer, *Phys. B*, 2011, **406**, 2346–2349.

43 M. A. Barrett, S. Zheng, G. Roshankar, R. J. Alsop, R. K. R. Belanger, C. Huynh, N. Kučerka and M. C. Rheinstädter, Interaction of aspirin (acetylsalicylic acid) with lipid membranes, *PLoS One*, 2012, **7**, e34357.

44 M. A. Barrett, S. Zheng, L. A. Toppozini, R. J. Alsop, H. Dies, A. Wang, N. Jago, M. Moore and M. C. Rheinstädter, Solubility of cholesterol in lipid membranes and the formation of immiscible cholesterol plaques at high cholesterol concentrations, *Soft Matter*, 2013, **9**, 9342–9351.

45 R. J. Alsop, M. A. Barrett, S. Zheng, H. Dies and M. C. Rheinstädter, Acetylsalicylic acid (ASA) increases the solubility of cholesterol when incorporated in lipid membranes, *Soft Matter*, 2014, **10**, 4275–4286.

46 R. J. Alsop, C. Armstrong, A. Maqbool, L. Toppozini, H. Dies and M. C. Rheinstadter, Cholesterol expels ibuprofen from the hydrophobic membrane core and stabilizes lamellar phases in lipid membranes containing ibuprofen, *Soft Matter*, 2015, **11**, 4756–4767.

47 K. Hristova and S. H. White, Determination of the hydrocarbon core structure of fluid dioleoylphosphocholine (dopc) bilayers by x-ray diffraction using specific bromination of the double-bonds: effect of hydration, *Biophys. J.*, 1998, **74**, 2419–2433.

48 S. Tristram-Nagle, Y. Liu, J. Legleiter and J. F. Nagle, Structure of gel phase DMPC determined by X-ray diffraction, *Biophys. J.*, 2002, **83**, 3324–3335.

49 J. F. Nagle and M. C. Wiener, Relations for lipid bilayers, *Biophys. J.*, 1989, **55**, 309–313.

50 J. F. Nagle, R. Zhang, S. Tristram-Nagle, W. Sun, H. I. Petrache and R. M. Suter, X-ray structure determination of fully hydrated lα phase dipalmitoylphosphatidylcholine bilayers, *Biophys. J.*, 1996, **70**, 1419–1431.

51 N. Kučerka, Y. Liu, N. Chu, H. I. Petrache, S. Tristram-Nagle and J. F. Nagle, Structure of fully hydrated fluid phase DMPC and DLPC lipid bilayers using X-ray scattering from oriented multilamellar arrays and from unilamellar vesicles, *Biophys. J.*, 2005, **88**, 2626–2637.

52 R. I. Bewley, J. W. Taylor and S. M. Bennington, Let, a cold neutron multi-disk chopper spectrometer at ISIS, *Nucl. Instrum. Methods Phys. Res., Sect. A*, 2011, **637**, 128–134.

53 R. I. Bewley, J. W. Taylor and S. M. Bennington, Let: a low energy multiple chopper spectrometer at ISIS, *Notiziario Neutroni e Luce di Sincrotrone*, 2011, **16**, 4–13.

54 R. T. Azuah, L. R. Kneller, Y. Qiu, P. L. W. Tregenna-Piggott, C. M. Brown, J. R. D. Copley and R. M. Dimeo, Dave: a comprehensive software suite for the reduction, visualization, and analysis of low energy neutron spectroscopic data, *J. Res. Natl. Inst. Stand. Technol.*, 2009, **114**, 341–358.

55 M. Bée, *Quasielastic Neutron Scattering: Principles and Applications in Solid State Chemistry*, Biology and Materials Science, Taylor & Francis, 1988.

56 J. Hansen and I. McDonald, *Theory of Simple Liquids*, Elsevier, Oxford, 2006.

57 D. Vural and H. R. Glyde, Intrinsic mean-square displacements in proteins, *Phys. Rev. E: Stat., Nonlinear, Soft Matter Phys.*, 2012, **86**, 011926.

58 D. Vural, L. Hong, J. C. Smith and H. R. Glyde, Long-time mean-square displacements in proteins, *Phys. Rev. E: Stat., Nonlinear, Soft Matter Phys.*, 2013, **88**, 052706.

59 G. Williams and D. C. Watts, Non-symmetrical dielectric relaxation behaviour arising from a simple empirical decay function, *Trans. Faraday Soc.*, 1970, **66**, 80–85.

60 C. P. Lindsey and G. D. Patterson, Detailed comparison of the Williams–Watts and Cole–Davidson functions, *J. Chem. Phys.*, 1980, **73**, 3348.

61 J. R. Taylor, *A Introduction to Error Analysis: the study of uncertainties in physical measurements*, University Science Books, 1997.

62 D. Vural, L. Hong, J. C. Smith and H. R. Glyde, Motional displacements in proteins: the origin of wave-vector-dependent values, *Phys. Rev. E: Stat., Nonlinear, Soft Matter Phys.*, 2015, **91**, 052705.

63 J. M. Sancho, Brownian colloidal particles: ITO, stratonovich, or a different stochastic interpretation, *Phys. Rev. E: Stat., Nonlinear, Soft Matter Phys.*, 2011, **84**, 062102.

64 N. Kučerka, J. F. Nagle, J. N. Sachs, S. E. Feller, J. Pencer, A. Jackson and J. Katsaras, Lipid bilayer structure determined by the simultaneous analysis of neutron and X-ray scattering data, *Biophys. J.*, 2008, **95**, 2356–2367.

65 H. Petrache, S. Feller and J. Nagle, Determination of component volumes of lipid bilayers from simulations, *Biophys. J.*, 1997, **70**, 2237–2242.

66 J. F. Nagle and S. Tristram-Nagle, Structure of lipid bilayers, *Biochim. Biophys. Acta*, 1469, **2000**, 159–195.

67 J. Yang, C. Calero and J. Marti, Diffusion and spectroscopy of water and lipids in fully hydrated dimyristoylphosphatidylcholine bilayer membranes, *J. Chem. Phys.*, 2014, **140**, 104901.

68 F. Sciortino, P. Gallo, P. Tartaglia and S.-H. Chen, Supercooled water and the kinetic glass transition,

Phys. Rev. E: Stat. Phys., Plasmas, Fluids, Relat. Interdiscip. Top., 1996, **54**, 6331–6343.

69 F. Y. Chen, W. C. Hung and H. W. Huang, Critical swelling of phospholipid bilayers, *Phys. Rev. Lett.*, 1997, **79**, 4026–4029.

70 S.-H. Chen, C. Liao, F. Sciortino, P. Gallo and P. Tartaglia, Model for single-particle dynamics in supercooled water, *Phys. Rev. E: Stat. Phys., Plasmas, Fluids, Relat. Interdiscip. Top.*, 1999, **59**, 6708–6714.

71 V. Crupi, D. Majolino, P. Migliardo and V. Venuti, Diffusive relaxations and vibrational properties of water and h-bonded systems in confined state by neutrons and light scattering: state of the art, *J. Phys. Chem. A*, 2000, **104**, 11000–11012.

72 V. Crupi, D. Majonlino, P. Migliardo and V. Venuti, Neutron scattering study and dynamic properties of hydrogen-bond liquids in mesoscopic confinement. 1. The water case, *J. Phys. Chem. B*, 2002, **106**, 10884–10894.

73 L. Toppozini, C. L. Armstrong, M. A. Barrett, S. Zheng, L. Luo, H. Nanda, V. Garcia Sakai and M. Rheinstädter, Partitioning of ethanol into lipid membranes and its effect on fluidity and permeability as seen by X-ray and neutron scattering, *Soft Matter*, 2012, **8**, 11839–11849.

Chapter 5

The Location and Effect of Ethanol in Single-Component Lipid Bilayers: Publication III

"*Partitioning of ethanol into lipid membranes and its effect on fluidity and permeability as seen by X-ray and neutron scattering*", Laura Toppozini, Clare L. Armstrong, Matthew A. Barrett, Songbo Zheng, Lindy Luo, Hirsh Nanda, Victoria García Sakai, Maikel C. Rheinstädter Soft Matter, 2012, **8**(47), 11839-11849

5.1 Preface

Ethanol is a ubiquitous substance in our society and some common uses are alcoholic beverages, antiseptics, and anaesthetics. Ethanol has been used as an early anaesthetic and is implicated as a drug-enhancer; though ethanol has been used medically for these properties, the mechanisms for either of these effects are largely unknown.

Our goals in this publication were to present observations that quantify the effect that ethanol has on model lipid membranes. Our membranes were solid-supported, however, not oriented as is common in the Laboratory of Membrane and Protein Dynamics. Due to ethanol's volatility, hydrating from the vapour phase is non-trivial to control and may result in a different concentration of ethanol than in the vapour or solution. The sample was, therefore, prepared as a hydrated powder (see Section 3) to ensure the DMPC membranes were in contact with the 2mol% water/ethanol solution.

Structural measurements were carried out by high-resolution X-ray scattering which allowed us to determine the location and quantity of additional solvent molecules in the bilayers in both their gel and fluid phases. Though we cannot directly observe ethanol molecules in these measurements, we

view an increase in electron density in the head groups as due to the presence of ethanol molecules. Evidence of increased permeability is given by the observation of increased electron density amongst the membrane's hydrophobic core in the presence of ethanol.

Dynamical measurements were carried out using elastic and quasi-elastic neutron scattering from a neutron backscattering spectrometer which allowed us to observe slow, nanosecond dynamics. The range of the backscattering instrument allowed us to probe length scales corresponding to lipid diffusion, acyl chain dynamics and solvent dynamics. The membranes were observed to have slower diffusion in the gel phase, giving rise to a higher degree of order in the gel phase while no discernible change was observed in the fluid lipid dynamics.

Author Contributions:

- *Experimental Concept:* Maikel Rheinstädter, Victoria García Sakai, Hirsh Nanda
- *Sample Preparation:* **Laura Toppozini**, Maikel Rheinstädter, Victoria Garía Sakai, Lindy Luo
- *X-ray Experiment:* **Laura Toppozini**, Maikel Rheinstädter
- *Neutron Experiment:* Victoria García Sakai, Hirsh Nanda
- *Data Analysis:* **Laura Toppozini**, Clare Armstrong, Matthew Barret, Songbo Zheng
- *Manuscript Preparation:* **Laura Toppozini**, Maikel Rheinstäter, Victoria García Sakai, Clare Armstrong

Soft Matter

Cite this: *Soft Matter*, 2012, **8**, 11839

www.rsc.org/softmatter

PAPER

Partitioning of ethanol into lipid membranes and its effect on fluidity and permeability as seen by X-ray and neutron scattering

Laura Toppozini,*[a] Clare L. Armstrong,[a] Matthew A. Barrett,[a] Songbo Zheng,[a] Lindy Luo,[a] Hirsh Nanda,[b] Victoria García Sakai*[c] and Maikel C. Rheinstädter*[ad]

Received 3rd July 2012, Accepted 11th September 2012
DOI: 10.1039/c2sm26546j

We present a combined neutron and X-ray scattering investigation to study the effect of ethanol on the molecular structure and dynamics of lipid membranes. 1,2-Dimyristoyl-*sn-glycero*-3-phoshatidylcholine (DMPC) powder hydrated with a 5 wt% ethanol solution (corresponding to 2 mol% of ethanol) was used in this study. From high-resolution X-ray experiments the position and partitioning of the ethanol molecules in the phospholipid bilayers was determined in their gel and fluid phases. We find that the ethanol molecules reside in the head group region of the bilayers, with 1.6 ethanol molecules per lipid molecule in the gel phase and 1.2 ethanol molecules per lipid molecule in the fluid phase. We find evidence for enhanced permeability in both fluid and gel phases of the phospholipid bilayers in the presence of ethanol molecules. Elastic and quasi-elastic neutron scattering data, obtained using a neutron backscattering spectrometer, was used to study slow, nanosecond molecular dynamics on length scales corresponding to lipid diffusion, acyl chain dynamics and solvent dynamics. While the presence of ethanol molecules had no observable effect on these types of dynamics in the fluid (L_α) phase, the membranes appeared to have a higher degree of order in gel (L_β) and ripple ($P_{\beta'}$) phases. In particular, lipid diffusion was found to be slower by a factor of two in the more rigid gel phase when ethanol was present.

1 Introduction

Our knowledge about interactions between ethanol and lipid membranes on the molecular scale mainly stems from two techniques: nuclear magnetic resonance (NMR) experiments[1–3] and molecular dynamics (MD) simulations.[4–9] In particular, experiments using neutron and X-ray scattering to probe molecular dynamics and structure are scarce,[10–12] most likely due to experimental challenges.

When partitioning into the bilayer, ethanol has been found to reside predominately at the membrane–water interface. Ethanol's hydrophilic nature causes it to exhibit a lower degree of partitioning into the hydrophobic core of the bilayer, differing from longer chain alcohols that insert into the hydrophobic core with their hydrophobic chains aligned parallel to the lipid hydrocarbon chains.[7,13] The ethanol molecules can form hydrogen bonds with the lipid head groups with bond lifetimes of about 1 nanosecond.[7,14] It has been reported that ethanol has

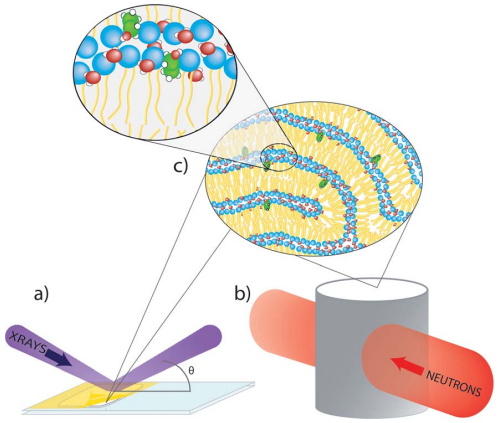

Fig. 1 Schematic diagram of the X-ray and neutron scattering experiments performed on a hydrated lipid powder. (a) The powder was applied to a ~0.5 mm depression in a glass slide for X-ray experiments. A 13 μm thick Kapton sheet was placed over the depression to avoid evaporation. (b) In the neutron scattering experiment, hydrated powder was applied to the sides of a annular aluminium sample holder. (c) Cartoon of the membrane structure in the hydrated powder, notice the non-oriented bilayer formation. DMPC: blue; H_2O: red; ethanol: green.

[a]*Department of Physics and Astronomy, McMaster University, Hamilton, ON, Canada. E-mail: toppozl@mcmaster.ca; rheinstadter@mcmaster.ca*
[b]*NIST Center for Neutron Research, National Institute of Standards and Technology, Gaithersburg, MD, USA*
[c]*ISIS Pulsed Neutron and Muon Source, Rutherford Appleton Laboratory, Didcot, UK. E-mail: victoria.garcia-sakai@stfc.ac.uk*
[d]*Canadian Neutron Beam Centre, National Research Council Canada, Chalk River, ON, Canada*

numerous effects on the lipid bilayer: it decreases the gel-to-fluid transition temperature,[1,4] it has a weak effect on the area per lipid, and it increases membrane fluidity and disorder.[7] Finally, and perhaps most importantly, ethanol has been found to increase membrane permeability.[7,15,16]

The aim of this study is to determine molecular structure and dynamics of phospholipid membranes hydrated by a 5 wt% ethanol solution. This concentration is significantly larger than the typical, very low alcohol concentrations of ~0.092 wt% (~0.036 mol%) found in human blood.[2] However, 5 wt% can be considered a moderate alcohol concentration to which skin and mucous membranes in the mouth and digestive system can be exposed. We combined elastic and quasi-elastic neutron scattering and X-ray diffraction to study the properties of multi-lamellar lipid bilayers containing ethanol. Using neutron scattering, we determined the impact of ethanol on slow, nanosecond membrane dynamics at different length scales, such as lipid diffusion, nanoscale tail dynamics and hydration water dynamics. While ethanol did not alter dynamics in the fluid phase, the ripple and gel phases exhibited a higher degree of molecular order with slower dynamics. The lipid diffusion constant showed a significant 50% decrease in the gel phase of the membranes. From the X-ray scattering experiments, we were able to determine the position of the ethanol molecules in the membrane and determine their partitioning, *i.e.*, the number of ethanol molecules per lipid molecule, in the bilayer. In addition, we found experimental evidence to suggest an increase in the permeability of the membranes due to the presence of ethanol.

2 Materials and methods

2.1 Sample preparation

To ensure a well defined ethanol concentration in the membranes, it is necessary that the bilayers are in direct contact with a water–ethanol solution. For this reason, hydrated lipid powders were used in this study. Highly concentrated suspensions of 1,2-dimyristoyl-*sn-glycero*-3-phoshatidylcholine (DMPC) were prepared by hydrating the lipid powder. Four types of samples were prepared, two for each scattering technique. In the dynamical neutron scattering experiments, lipids were hydrated with D_2O and D_2O–d-ethanol (deuterated ethanol) 5 wt%. In the X-ray scattering experiments, lipids were hydrated with ultra pure H_2O and an H_2O–5 wt% ethanol solution. The typical sample mass was ~300 mg for the neutron and ~15 mg for the X-ray experiment. A 3 : 1 mass ratio of water or water–ethanol solution to lipid powder was mixed to ensure full hydration of the bilayers. We envision the structure of the hydrated powder as depicted in the cartoon in Fig. 1 as a randomly oriented multi-lamellar structure. The number of water and ethanol molecules that attach to and incorporate into the bilayers change the concentration of the solution. About 7–8 water molecules per lipid molecule are found in the head group region of the bilayers;[2,17] we find about 1.6 ethanol molecules per lipid molecule (as will be shown below). Using these numbers the concentration of the water–ethanol solution changes from 2 mol% to ~1 mol% when it is in contact with the lipid powder. The concentration of ethanol molecules in the membranes is, therefore, not limited by the total number of ethanol molecules available in the solution.

An annular sample cell made of aluminium was used for the neutron experiments. The suspension was applied as a film to the inner wall of the hollow cylinder after which, an inner cylinder was inserted to form a seal. The sample was mounted inside of a cryostat. A temperature range between 280 K $<T<$ 335 K was used, which covers the temperatures of gel (L_β), ripple ($P_{\beta'}$) and fluid (L_α) phases of the bilayers. Temperature was controlled to better than 0.1 K.

In the X-ray experiments, the lipid mixture was spread on a ~20 mm × 20 mm × 0.5 mm square well ground into a Quartz glass slide. The hydrated powder was sealed with a 13 μm thick Kapton polyimide foil acting as an X-ray window using vacuum grease for adhesion. The sample was mounted in a temperature controlled humidity chamber during the X-ray experiments. Temperature was controlled using a circulating water bath controller with a temperature stability of better than 0.1 K. The structure of the lipid–ethanol system was studied at two temperatures: 293 K, allowing observation of the gel (ripple, $P_{\beta'}$) phase of the membranes, and 303 K, to observe their fluid (L_α) phase. Fig. 1 shows schematics of the neutron and X-ray scattering sample and the experimental geometries.

2.2 Neutron scattering experiment

The neutron experiments were carried out at the High Flux Neutron Backscattering Spectrometer (HFBS)[21] at the NIST Center for Neutron Research (NCNR), Gaithersburg, in its standard set-up with Si(111) monochromator and analyzer crystals corresponding to an incident and analyzed neutron energy of 2.08 meV ($\lambda = 6.27$ Å). Two types of experiments were conducted: so-called elastic (fixed energy window, FEW) scans and quasi-elastic neutron scattering (QENS).

Elastic incoherent neutron scattering is an established tool for the detection of molecular freezing and melting,[18,19,22–25] where sample scattering is recorded as a function of temperature. At the energy resolution of ~0.9 μeV, only molecular motions with characteristic times slower than ~1 ns are monitored. The experiment covered lateral length scales of 3.5–12 Å to study dynamics down to nearest-neighbour distances of both lipid acyl tails and hydration water molecules. Performing elastic scans as a function of temperature, reveals dynamical changes on different length scales. Freezing and melting of molecular degrees of freedom can easily be identified because they lead to jumps or kinks in the recorded intensity, as shown below.

The 16 HFBS detectors (D1–D16) cover a total Q range of 0.14 $Å^{-1}$ to 1.81 $Å^{-1}$. Table 1 lists the centre Q-values and the corresponding length scales. Each detector covers an angular range of approximately 8°. Different types of motion fall into the length scales covered by the HFBS spectrometer.

Slow nanosecond dynamics of lipid and water molecules were studied previously using backscattering spectrometers by analyzing elastic scattering at the positions of the lipid acyl chain and hydration water correlation peaks.[18–20,25,26] Based on these results, different types of dynamics can be distinguished based on their length scale dependence:

• Incoherent scattering is dominant at intermediate Q values, between about 0.3 and 1.5 $Å^{-1}$, where no correlation peak occurs. This range of length scales between ~4 and 21 Å is often used in neutron scattering studies (see, *e.g.* ref. 22 and 24) to study diffusion and molecular mean square displacements of

Table 1 Neutron detector (D1–D16), corresponding centre Q-value, length scales and type of scattering and motion detected. The lipid acyl chain correlation peak is centred at $Q \sim 1.5$ Å^{-1}. The hydration water correlation peak was reported at $Q = 1.85$ Å^{-1} (ref. 18–20)

Detector	Q (Å^{-1})	Distance (Å)	Dominant scattering	Associated motion
D1	0.25	25		
D2	0.36	17		
D3	0.47	13		
D4	0.56	11		
D5	0.62	10		
D6	**0.75**	**8**	**Incoherent**	**Lipid diffusion**
D7	**0.87**	**7**		
D8	**0.99**	**6.3**		
D9	**1.11**	**5.7**		
D10	1.22	5.2		
D11	1.32	4.8		
D12	1.42	4.4		
D13	**1.51**	**4.2**	**Lipid tail correlation peak**	**Lipid tail dynamics**
D14	1.60	3.9		
D15	1.68	3.7		
D16	**1.75**	**3.6**	**Hydration water correlation peak**	**Hydration water dynamics**

lipid molecules. We assigned the Q-range from 0.69 Å^{-1} to 1.17 Å^{-1} (detectors D6–D9), to incoherent dynamics due to diffusion of lipid molecules, covering length scales from 5.6–9.2 Å. These values take into account the Q-range for each detector.

- Detector D13, covers the Q range of the lipid acyl chain correlation peak (~1.5 Å^{-1}) and was assigned to lipid tail fluctuations.
- The nearest-neighbour distance of the hydration water molecules leads to a correlation peak centred at 1.85 Å^{-1}, corresponding to a nearest-neighbour distance of 3.4 Å between hydration water molecules, slightly larger than bulk water. Detector D16 was, therefore, assigned to dynamics of hydration water molecules. We note that D16 is centred at 1.75 Å^{-1}, however it covers the hydration correlation peak partially.

The multi-lamellar Bragg reflections due to stacking of the membranes are veritable Bragg peaks related to an order on basically infinite time scales, in both gel and fluid phases. The in-plane correlations related to lipid tails and water molecules, which lead to in-plane correlation peaks at high Q values above ~0.7 Å^{-1}, however, are dynamic in nature. It has been shown using energy resolved neutron diffraction[18] that these correlations exist on time scales only up to nanoseconds in the fluid phase of the membranes. The absence of "true" elastic scattering is the fingerprint of a fluid structure; it is well known that lipid membranes show properties of a 2D fluid in their fluid phases. The corresponding reflections are usually observed in neutron and X-ray diffraction experiments as relatively weak and broad peaks as compared to the out-of-plane Bragg peaks. The scattering, which occurs at the peak positions of lipid acyl chain and hydration water molecules in our experiment is, therefore, not static but can be used to characterize the time scale of the underlying molecular degrees of freedom, as suggested in ref. 18, 19, 25 and 26 and in Table 1.

Lipid diffusion, and lipid tail and hydration water dynamics were studied simultaneously by analyzing different detectors. Table 1 lists the dominant scattering contribution for different length scales and corresponding motion observed in the various detectors. Because the HFBS detectors have a coarse angular (Q) resolution of approximately 8° each, the experiment was not sensitive to shifts of the lipid and water correlation peak with temperature due to potential structural changes of the bilayers with temperature. The measured elastic intensity at the Q position for diffusion, lipid tail and hydration water dynamics is shown in Fig. 2. The scans cover a temperature range of 280 K < T < 335 K. Data were taken in heating and cooling scans at a rate

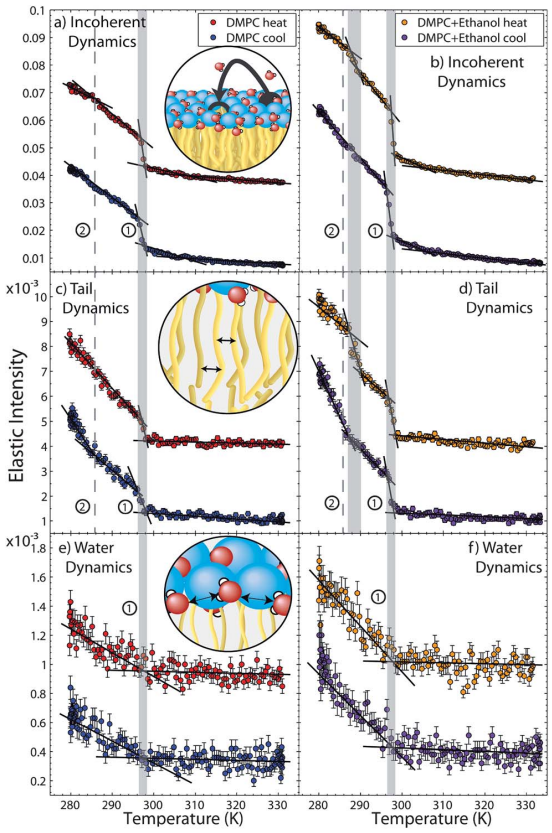

Fig. 2 The elastic neutron scattering experiment was sensitive to lipid diffusion, lipid acyl chain and hydration water dynamics. As listed in Table 1, data from detectors D6 through D9 were summed to create the lipid diffusion plots, detector D13 data for lipid acyl chain dynamics, and detector D16 data for hydration water dynamics. Heating and cooling scans are shown. All heating curves are shifted upward in intensity for clarity; the original data show closed loops. Error bars represent one standard deviation. The experimental temperature resolution was 0.5 K. The temperature of the pre-transition in pure DMPC is marked by a dashed line. The shaded areas marks the ranges of pre- and main transitions. The error in the determination of the transition temperatures is related to the determination of the intersection of the different slopes. For lipid dynamics we estimate the maximum error to be ~2 K as determined by min./max. slopes. The hydration water data in (c) has slightly larger statistical errors (*i.e.* lower detector counts due to its placement within the instrument) and the maximum error in the determination of the transition temperature was estimated to be ~4 K.

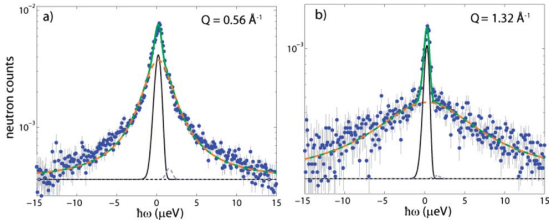

Fig. 3 QENS spectra of the DMPC–ethanol sample at $T = 308$ K recorded at low (a) and high (b) Q-values. The instrumental resolution is fit with two functions: an asymmetric Gaussian (solid black curve) and a second Gaussian function (dashed grey curves). The quasi-elastic broadening is fit with a Lorentzian (dashed orange curve) and a constant background (dashed black line), and the total fit is shown as a solid green curve.

of 0.5 K min^{-1}. Because the counting time was set to 1 min, the temperature resolution of the experiment is determined to be 0.5 K.

Quasi-elastic neutron scattering is a powerful tool to gain access to slow nanosecond molecular dynamics in soft-matter and biophysics, see *e.g.* ref. 27 for a recent review. Neutron spectra are recorded in quasi-elastic neutron scattering experiments. A mechanical Doppler drive was employed to produce an oscillatory motion of the monochromator in order to vary the incident energy of the neutrons. A dynamic range of -15 μeV < $\hbar\omega$ < 15 μeV is accessible using this set-up. The corresponding spectra are shown in Fig. 3. By analyzing the shape of the inelastic scattering, detailed information about nanosecond molecular dynamics in the membranes can be obtained. We used quasi-elastic scattering to determine lipid diffusion coefficients at selected temperatures, as will be shown below. Phase transitions were determined first using the elastic scans. Diffusion was then measured in the gel and fluid phases using QENS.

2.3 X-ray scattering experiment

X-ray scattering data were obtained using the Biological Large Angle Diffraction Experiment (BLADE) in the Laboratory for Membrane and Protein Dynamics at McMaster University. BLADE uses a 9 kW (45 kV, 200 mA) CuKα rotating anode at a wavelength of 1.5418 Å. Both source and detector are mounted on movable arms ensuring the sample stay horizontal during the measurements. Multi-layer focussing optics provide a high intensity beam with monochromatic X-ray intensities up to 10^{10} photons/(mm^2 × s). Data were obtained in reflection geometry using a collimated X-ray beam. A schematic of the scattering geometry is shown in Fig. 1(a).

The scans, as shown in Fig. 4, cover a Q range up to 2.5 Å^{-1}, which extends over length scales from intermolecular distances to the lamellar spacing between neighbouring membranes. As the multi-lamellar membranes are not oriented, Bragg peaks due to the lamellar stacking perpendicular to the membranes and in-plane correlation peaks due to molecular alignment in the plane of the membranes, are observed simultaneously. The lamellar Bragg peaks are observed in the Q range between ~0.1 and ~0.75 Å^{-1}, corresponding to lamellar spacings of ~65 Å. The lipid acyl chain correlation peak in DMPC occurs at a Q value

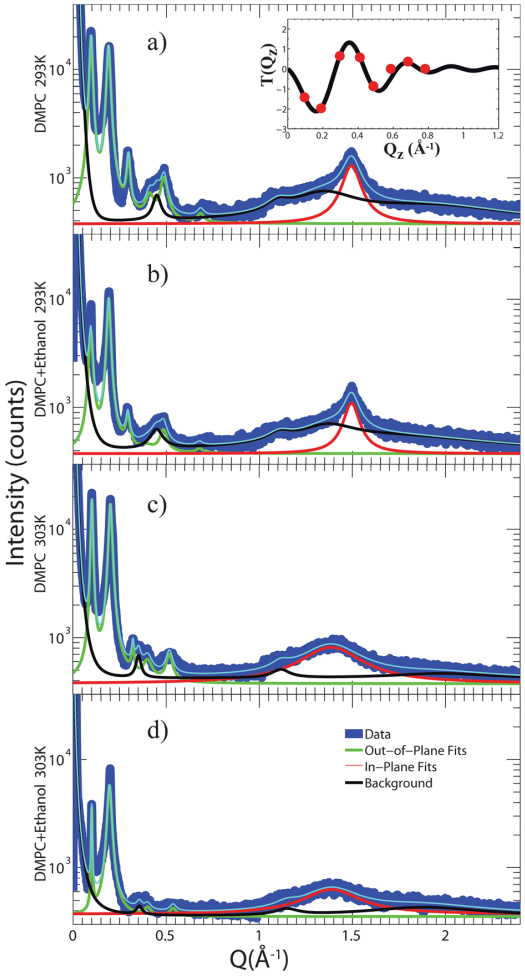

Fig. 4 Overview of the X-ray data. (a) DMPC at $T = 293$ K (gel phase). The inset shows $T(q_z)$, as defined in eqn (2). (b) DMPC–ethanol at $T = 293$ K (gel phase), (c) DMPC at $T = 303$ K (fluid phase), (d) DMPC–ethanol at $T = 303$ K (fluid phase). Background of the sample holder was subtracted from the data in (a)–(d). The total fit is shown in light blue. The low-Q scans were assigned to a multi-lamellar membrane structure and shown in green. The inter-acyl chain correlation peak at Q values of ~1.5 Å^{-1} is shown in red. The weak intensity at ~1.1 Å^{-1} stems from the Kapton window and did not subtract perfectly.

of ~1.5 Å^{-1} in the gel phase,[18,28] below the main phase transition at $T = 296.6$ K.

The multi-lamellar Bragg peaks allow for the determination of the structure perpendicular to the plane of the membranes (see, *e.g.* ref. 29 and 30 for recent reviews). Because of the membrane stacking, *i.e.* the convolution with the lamellar structure factor, the Fourier transform is not continuous but discrete. The different Fourier components are observed in the experiment as the integrated intensities of the out-of-plane Bragg peaks. The electron density, $\rho(z)$, can be approximated by a 1D Fourier analysis:[31]

$$\rho(z) = \rho_W + \frac{F(0)}{d_z} + \frac{2}{d_z}\sum_{n=1}^{N} F(q_n)\nu_n \cos(q_n z)$$
$$= \rho_W + \frac{F(0)}{d_z} + \frac{2}{d_z}\sum_{n=1}^{N} \sqrt{I_n q_n}\nu_n \cos\left(\frac{2\pi n z}{d_z}\right) \quad (1)$$

N is the highest order of the Bragg peaks observed in the experiment and ρ_W the electron density of water or solution. The integrated peak intensities, I_n, are multiplied by q_n and square rooted to obtain the form factors, $F(q_n)$.[32,33] The bilayer form factor $F(q_z)$, which is in general a complex quantity, is real-valued in the case of centro-symmetry. The phase problem of crystallography, therefore, simplifies to the sign problem $F(q_z) = \pm|F(q_z)|$. The phases, ν_n, can only take the values ± 1. When the membrane form factor $F(q_z)$ is measured at several q_z values, a continuous function, $T(q_z)$, which is proportional to $F(q_z)$, can be fit to the data:[10,32–34]

$$T(q_z) = \sum_n \sqrt{I_n q_n}\,\mathrm{sinc}(\pi d_z q_z - \pi n). \quad (2)$$

Once an analytical expression for $T(q_z)$ has been determined from fitting the experimental peak intensities, the phases ν_n can be determined from $T(q_z)$.

X-ray scans were measured for the pure DMPC bilayers and the DMPC–ethanol sample at two temperatures, namely $T = 293$ K, the gel phase for DMPC bilayers, and $T = 303$ K, their fluid phase. Data are shown in Fig. 4. A background scan of the glass substrate with Kapton polyimide foil was subtracted from the data shown in parts (a)–(d). The pronounced Bragg peaks at Q values up to $\sim$0.75 Å^{-1} were assigned to a multi-lamellar membrane structure in the powder. We find lamellar d_z spacings of $d_z^{DMPC} = 64.27$ Å, $d_z^{DMPC\text{–}ethanol} = 64.89$ Å in the gel phase at $T = 293$ K and $d_z^{DMPC} = 61.10$ Å and $d_z^{DMPC\text{–}ethanol} = 62.02$ Å in fluid membranes. The measured d_z spacing for DMPC is in excellent agreement to lamellar spacings reported for fully hydrated bilayers.[35]

The Bragg peaks were fit using Lorentzian peak profiles. Up to eight peaks could be fit and were used to reconstruct the electron density. $T(q_z)$ was fit to the experimentally determined peak intensities using eqn (2), where an array of ν_n values was determined out of the corresponding 2^8 combinations, assuming a phase of +1 or −1. The inset in Fig. 4(a) shows the best fit of $T(q)$ for DMPC in its gel phase as example. All samples were well fitted using the following combination of phases: $\bar{1}\bar{1}11\bar{1}\bar{1}11$. The resulting electron densities are plotted in Fig. 5.

We assign the additional correlation peak at higher Q values to the in-plane structure of the membranes. The lipid acyl chain positional correlation peak is the result of closely packed acyl chains making up the hydrophobic core of the membrane. The corresponding correlation peaks were observed at 1.49 Å^{-1} in both the DMPC and DMPC–ethanol systems at $T = 293$ K, corresponding to a distance between neighbouring acyl chains of $\sim$4.21 Å in the gel phase. In the fluid phase, the lipid tail positional correlation peaks occur at 1.39 Å^{-1} in the DMPC and DMPC–ethanol samples at $T = 303$ K, corresponding to an increased distance between neighbouring acyl chains of $\sim$4.53 Å. The acyl chain correlation peak is more pronounced in the gel phase indicating a higher degree of order. The broad fluid peak is the fingerprint of the disordered L_α phase. The acyl chain packing is not significantly affected by the presence of ethanol as the position of the peak does not change with addition of ethanol within the resolution of this experiment. The weak peak at $\sim$1.1 Å^{-1} in Fig. 4 stems from the Kapton window and did not subtract perfectly; it is not related to a lipid membrane structure.

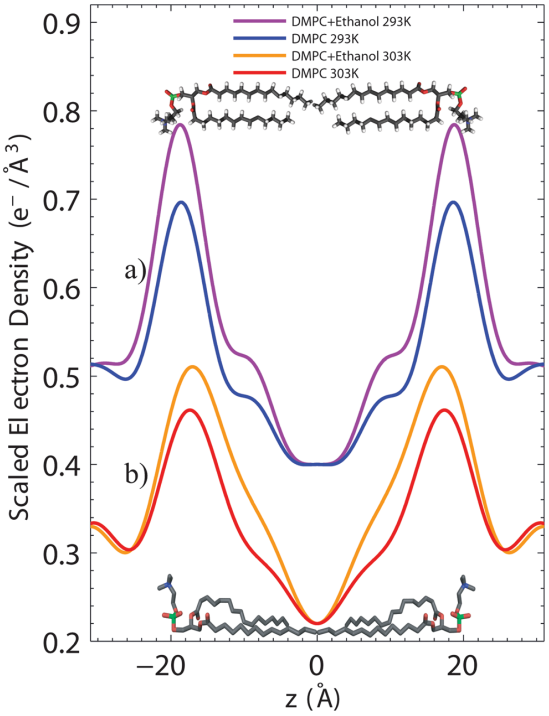

Fig. 5 Electron densities $\rho(z)$ for all sample variations, as determined from the data in Fig. 4, using eqn (1) and (2). $\rho(z)$ was scaled to the electron density of a CH_3 group in the centre (*i.e.* where lipid tail ends meet) and water or ethanol–water electron density at the ends (*i.e.* between the hydrophilic headgroups of adjacent bilayers). The 293 K data in (a) are shifted by +0.18 e$^-$ Å^{-3} on the y-axis for clarity. $\rho(z)$ is increased in the presence of ethanol in the head-group region and at z-values around $\sim$9 Å.

3 Results

3.1 Molecular freezing and melting studied by elastic neutron scattering

Elastic scattering data, during heating and cooling, are shown in Fig. 2. The heating curves have been shifted upward on the intensity axis to distinguish the transition locations. The original data shows closed loops for all plots indicating that the number of particles in the beam was constant during the experiments. Also, the system always returned to its initial high-temperature intensity.

Elastic scattering related to lipid diffusion is shown in Fig. 2(a) for pure DMPC and Fig. 2(b) for DMPC–ethanol. A pronounced step is observed at a temperature of $T = 297$ K. This temperature coincides well with the temperature of the main

transition in fully hydrated bilayers made of DMPC, which was reported at $T = 296.6$ K in multi-lamellar DMPC systems.[19,22] The transition temperatures in Fig. 2(a) and (b) coincide, showing that within the temperature resolution of this experiment, ethanol does not change the temperature of the transition at this length scale. When comparing the pure DMPC and DMPC–ethanol, the introduction of ethanol does not change the elastic intensity in the fluid phase. In the gel phase, however, the elastic intensity changes drastically with the addition of ethanol. This is indicated by an increase in the slopes of the transitions at these lower temperatures and points to enhanced order in both gel and ripple phase due to ethanol.

An additional kink is observed at a temperature of $T = 286$ K, which can be assigned to the pre-transition in DMPC, *i.e.*, the transition between the gel (L_β) and ripple ($P_{\beta'}$) phases of the bilayers. The pre-transition appears to be more pronounced in the presence of ethanol molecules and shifted by ~2.5 K towards higher temperatures (~288.5 K). No hysteresis was observed between the cooling and heating curve within the experimental resolution.

Nanoscale lipid tail dynamics are observed in Fig. 2(c) and (d). A pronounced step in the elastic intensity is observed at $T = 297$ K, related to the main transition. The transition temperatures in DMPC and DMPC–ethanol coincide; within the instrumental resolution, ethanol does not change the temperature of freezing or melting of the lipid acyl chains on nearest-neighbour distances of acyl chains. The step in the elastic scattering is, however, more pronounced in the presence of ethanol indicating a better ordered state in the $P_{\beta'}$ phase. No precise pre-transition temperature can be assigned to the data in Fig. 2(c) for pure DMPC on this length scale. However, a pronounced step associated with the transition into the L_β phase is observed in the presence of ethanol in Fig. 2(d) at ~288.5 K. In addition, the pre-transition temperature is slightly shifted towards higher temperatures. The transition appears more pronounced in the heating curve.

Dynamics of the hydration water are observed in Fig. 2(e) and (f). This detector is located at a Q position of ~1.85 $Å^{-1}$. This length scale is mainly sensitive to hydration water, which has a slightly lower density as compared to bulk water. A pronounced kink in the elastic intensity is observed at $T = 297$ K. The hydration water dynamics follow that of the lipid molecules and ethanol does not seem to change their dynamical behaviour. No hysteresis is observed; the ethanol does not seem to have an impact on the freezing and melting of the hydration water within the temperature resolution of this experiment.

3.2 Nanosecond membrane dynamics and diffusion studied quasi-elastic neutron scattering

QENS allows for the determination of lipid diffusion in the membranes. Exemplary QENS spectra of the DMPC–ethanol system at $T = 308$ K, in the fluid phase of the bilayers, are shown in Fig. 3 for two selected Q values. The instrumental resolution was determined from a Vanadium sample and it was found that rather than exhibiting a simple Gaussian peak shape, the resolution had a slight gradual asymmetry at negative $\hbar\omega$ values (fit with an asymmetric Gaussian) and a small shoulder at positive $\hbar\omega$ values (fit with an additional small Gaussian). The asymmetric Gaussian used to accommodate the gradual asymmetry in the resolution function was composed of a Gaussian with an exponential function on one side of the peak,[36]

$$y = y_o + H(\hbar\omega_o - \hbar\omega)Ae^{-\left(\frac{(\hbar\omega-\hbar\omega_o)^2}{2\sigma^2+\tau|\hbar\omega-\hbar\omega_o|}\right)} + H(\hbar\omega - \hbar\omega_o)Ae^{-\left(\frac{(\hbar\omega-\hbar\omega_o)^2}{2\sigma^2}\right)}, \quad (3)$$

where A is the amplitude, ω_o the elastic energy peak position, σ the Gaussian standard deviation, H is the Heaviside function, and τ the asymmetry parameter. For $\tau = 0$, a symmetric Gaussian function is obtained. Values of τ used to fit this gradual asymmetry ranged from ~0.030 to 0.217. A Q range of 0.55 $Å^{-1} < Q <$ 1.35 $Å^{-1}$ was used for the determination of the diffusion constant.

The scattering obtained from the DMPC–ethanol sample is described by a narrow central component, corresponding to the instrumental resolution (~0.9 μeV), a constant background, and a quasi-elastic broadening due to relaxational dynamics of the

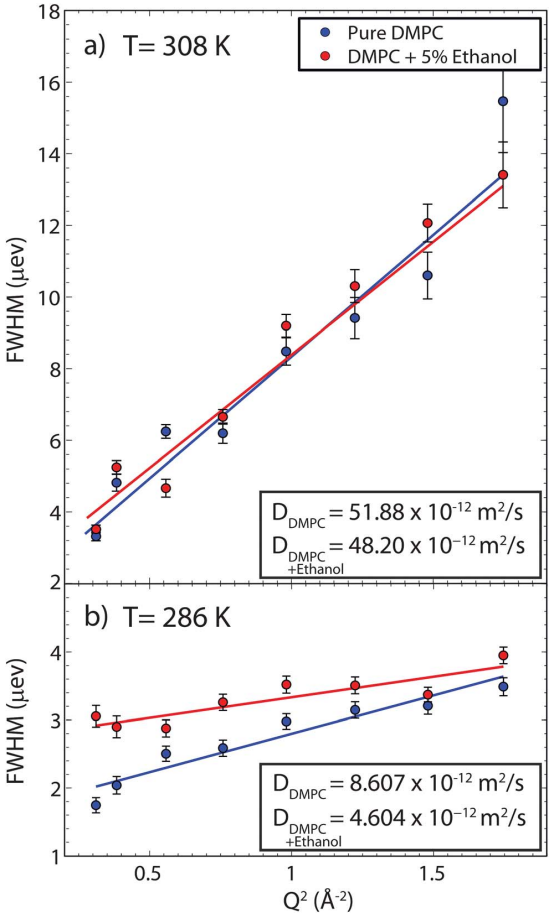

Fig. 6 FWHM of the quasi-elastic broadening as determined from the data in Fig. 3. Data are plotted as function of Q^2 such that the slope of the line is directly proportional to the diffusion coefficients.

lipid molecules. This broadening is fit with a Lorentzian function, convolved with the Gaussian instrumental resolution. It should be noted that the FWHM of the Lorentzian functions quoted in the paper are the deconvoluted values.

Fig. 6 displays the FWHM for all measured Q-values as a function of Q^2. In this plot the FWHM scale linearly with Q^2, a behaviour indicative of continuous diffusion ($FWHM_L = 2\hbar DQ^2$), as previously explained in great detail in, *e.g.*, ref. 37. This behaviour was observed for the quasi-elastic broadening in the gel ($P_{\beta'}$) and fluid phases of the DMPC and DMPC–ethanol bilayers, as shown in Fig. 6. The data fit is depicted by a blue line for the pure DMPC and red line for the DMPC–ethanol. From this linear fit the diffusion coefficients could be extracted and are displayed in Fig. 6. The values are in good agreement with diffusion coefficients quoted in the literature for similar systems.[38–42] We note that the linear fit in Fig. 6 does not pass through the origin, as one would expect, and the offset is larger than the instrumental resolution. This effect is often observed in the literature, however no consistent explanation has been offered. We also note that the accessible Q range of the HFBS spectrometer is not sensitive to the ballistic diffusion regime[37] or a potential flow-like diffusion, as reported recently.[40]

No difference in the diffusion constants in the fluid phase with or without ethanol was observed within the resolution of this experiment. The experimental values of the diffusion constants in the fluid phase are found to be $D_{DMPC–ethanol} = 48.20 \times 10^{-12}$ m^2 s^{-1} and $D_{DMPC} = 51.88 \times 10^{-12}$ m^2 s^{-1}. Diffusion constants in the gel phase are significantly slower than in the fluid phase for both samples, with and without ethanol. However, diffusion in the gel phase in the presence of ethanol is slowed down by a factor of ~2 as compared to pure DMPC, as shown in Fig. 6(b). The diffusion constants in the gel phase are found to be $D_{DMPC–ethanol} = 4.604 \times 10^{-12}$ m^2 s^{-1} and $D_{DMPC} = 8.607 \times 10^{-12}$ m^2 s^{-1}.

3.3 Electron densities and location of the ethanol molecules from X-ray scattering

The integrated intensities of out-of-plane Bragg peaks in Fig. 4 were used to calculate the electron density profile perpendicular to the bilayers following eqn (1). Position and partitioning of the ethanol molecules in the bilayers can then be determined from the different $\rho(z)$, shown in Fig. 5. In order to put $\rho(z)$ on an absolute scale, the electron densities were scaled to fulfil the condition $\rho(0) = 0.22$ e$^-$ Å^{-3} (the electron density of a CH_3 group at the end of a lipid tail) in the centre of the bilayer, and the electron density of the solution outside the bilayers. The electron densities for water and water–5 wt% ethanol solution are calculated in Table 2. We find $\rho(d_z/2) = 0.330$ e$^-$ Å^{-3} for water–5 wt% ethanol, and the well known $\rho(d_z/2) = 0.334$ e$^-$ Å^{-3} for pure water.

The normalized electron density profiles for DMPC in its gel phase are depicted in Fig. 5(a). The profile corresponds to a DMPC molecule in the well ordered gel state with both chains in all-*trans* configuration, as has been reported previously.[31] The electron rich phosphorous group in the head group region can be identified by the peak in the electron density at ~22 Å. $\rho(z)$ monotonically decreases towards the bilayer centre at $z = 0$; only CH_3 groups at the end of the lipid tails are found in the centre. The electron density profiles in the fluid phase in Fig. 5(b) agree well with profiles reported in the literature.[31,43,44] The sharp dip at the centre is the tell-tale sign of a fluid membrane, *i.e.*, the increasing number of kink-defects lower the density of the lipid tails in the bilayer centre.

Table 2 Properties of water, ethanol and the water–ethanol solution. The ethanol concentration is given as wt%, vol% and mol%. The calculated electron density is used to normalize the electron densities of the bilayers in Fig. 5 and 7

	Water (H_2O)	Ethanol (C_2H_6O)	Water–ethanol
% by weight (wt%)	—	—	5
% by volume (vol%)	—	—	6.25
% by moles (mol%)	—	—	2.02
Molecular weight (g mol^{-1})	18.0153	46.06844	18.58104
Molecules/Å^3	3.34×10^{-2}	1.03×10^{-2}	3.20×10^{-2}
Number of electrons	10	26	10.3
Electrons density (e$^-$ Å^{-3})	0.334	0.268	0.330

The presence of ethanol leads to an increase in electron density in the head group region of the bilayers. $\rho(z)$ is also increased around z values of ~9 Å, representing the presence of molecules that have permeated the membrane. The dip in the electron densities at z values of ~27 Å is most likely related to a reduced density of the hydration water and solvent at the lipid–solvent interface, as will be discussed below.

For a quantitative comparison, Fig. 7 shows the electron density profile of a single leaflet for each temperature in more detail. The increase in electron density is the result of the presence of additional molecules in the bilayers. The addition of two Gaussian peak profiles ($\rho(z) = \rho_0 \exp[-(z - z_0)^2/2\sigma^2]$) to the

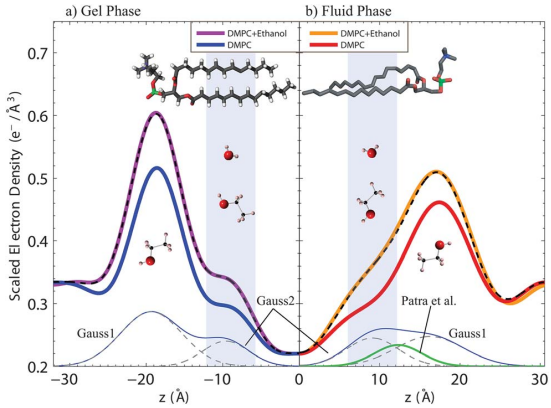

Fig. 7 Bilayer electron densities in gel and fluid phases. Each density is scaled to the electron density of CH_3 at the centre of the bilayer and the electron density of the respective solutes. One leaflet of a bilayer is shown. (a): In the gel phase, the electron density is increased in the presence of ethanol. The increase can be described by the addition of two Gaussian functions to the DMPC density (dashed black line). (b): In the fluid phase, an increase is seen in the presence of ethanol, which can also be described by two Gaussian distributions. The two Gaussians can be assigned to the presence of ethanol and possibly water molecules in the bilayers. The green Gaussian function is extrapolated from a mass density plot determined by a molecular dynamics simulation of DPPC and ethanol from Patra *et al.*[7]

Table 3 Parameters of the Gaussian peaks, $\rho(z) = \rho_0 \exp[-(z - z_0)^2/2\sigma^2]$, as determined from the fits in Fig. 7. Gaussian 1 is assigned to the presence of ethanol molecules in the head group region of the bilayers. Gaussian 2 can be assigned to additional ethanol (scenario ①) or water molecules (scenario ②) in the hydrophobic membrane core. Numbers are provided for both scenarios. Literature values have been used for the lipid areas in gel and fluid phase

	z_0 (Å)	ρ_0	σ (Å)	$\rho_0\sigma\sqrt{2\pi}$ (Å^2)	d_z (Å)	A_L (Å^2)	#Electrons	#Molecules
Gauss 1 (gel)	19.35	0.087	4	0.872	64.89	47.2 (ref. 43)	0.654	1.58 ethanol–lipid
Gauss 2 (gel)	9.6	0.04	3	0.301	64.89	47.2 (ref. 43)	0.226	① 0.55 ethanol–lipid, ② 1.42 water–lipid
Gauss 1 (fluid)	16.25	0.0475	4.25	0.506	62.02	60.6 (ref. 31)	0.506	1.18 ethanol–lipid
Gauss 2 (fluid)	9.1	0.045	3.25	0.367	62.02	60.6 (ref. 31)	0.367	① 0.85 ethanol–lipid, ② 2.22 water–lipid

electron density profiles of pure DMPC in Fig. 7(a) and (b) results in the dashed black lines, which show excellent agreement to the DMPC–ethanol data. In the gel phase, Gauss 1 is centred at 19.35 Å and Gauss 2 is centred at 9.6 Å, whereas for the fluid phase we obtain the Gauss 1 centred at 16.25 Å and Gauss 2 centred at 9.1 Å. While Gauss 1 is dominant in the gel phase, Gauss 1 becomes comparable to Gauss 2 in the fluid phase in Fig. 7. Position, width and area of the Gaussian distributions in the different samples are summarized in Table 3.

The electron density of the lipid bilayer is defined by $\rho = e^-/V_L = e^-/(A_L d_z)$, where V_L is the volume of a lipid molecule, A_L is the lipid area and d_z the lamellar spacing, *i.e.*, the size of the unit cell. One unit contains two lipid molecules and their hydration water molecules, as depicted in Fig. 5. The integral $e^- = A_L \int_0^{d/2} \rho(z) dz$ gives the total number of electrons in one leaflet. For pure DMPC this number is calculated to be $e^-_{gel} = 514$ and $e^-_{fluid} = 622$ in respective gel and fluid phases. Using the number of electrons per lipid (374, $C_{36}H_{72}NO_8P$) and water molecule (10, H_2O), these numbers refer to 1 lipid molecule hydrated by 14 water molecules in the gel phase, and 1 lipid molecule hydrated by 25 water molecules in the fluid phase, in excellent agreement to literature values.[17] This agreement proves that our technique is capable to quantitatively determine electron densities, which is an important point for the discussion of partitioning of molecules below.

We note that the determination of lipid areas is an important field in membrane research. As discussed in detail in the literature,[45,46] it is not straightforward to determine the area per lipid molecule directly from the inter-acyl chain correlation peak from the data in Fig. 4. Lipid areas can be determined with high accuracy by a combined approach using X-ray and neutron scattering and computer simulations, see ref. 29 for a recent review. We, therefore, used lipid areas published for DMPC in gel and fluid phases by the Nagle group[31,43] (listed in Table 3). We also note that lipid areas can be determined from the chain correlation peaks in dehydrated gel phases, in the absence of lipid fluctuations.[47]

The number of electrons related to the electron density in the Gaussian peaks can be calculated to $e^- = A_L \int_{Gauss} \rho(z) dz$. By dividing this number by the number of electrons of an ethanol or water molecule, the number of ethanol or equivalent water molecules per lipid molecule can be determined. As the X-ray experiment is averaging over a large number of those unit cells, a non-integer occupancy means that ethanol (or water) molecules can be shared between lipids. Partitioning of ethanol and water molecules in the lipid bilayers can be determined from these parameters and are calculated in Table 3.

4 Discussion

By combining X-ray diffraction and elastic and quasi-elastic neutron scattering, the molecular structure and dynamics of lipid membranes containing ethanol were determined. To the best of our knowledge this is the first extensive scattering study of the interaction of ethanol with lipid membranes. The bilayers were in contact with a 5 wt% water–ethanol solution, corresponding to 2 mol% of ethanol.

Electron density profiles in Figs. 5 and 7 allowed for the determination of the position of the ethanol molecules and their partition in lipid membranes. The presence of the ethanol molecules leads to an increase of the electron densities in both gel and fluid phases. The difference between $\rho(z)$ with and without ethanol is well described by the addition of two Gaussian distributions to the electron densities of pure DMPC bilayers. Gaussian 1 is centred at ~19 Å and ~16 Å in gel and fluid phases, in the head group region of the membrane. Gaussian 2 is centred at ~9 Å in gel and fluid phase, in the hydrophobic membrane core.

The positions of the two Gaussians can be compared to results from NMR[1–3] and molecular dynamics simulations:[7,8] Barry and Gawrisch located the ethanol molecules from NMR experiments close to the lipid–water interface for bilayers in the fluid phase in the region of the headgroup, glycerol backbone and the uppermost chain methylene groups. The position of ethanol molecules as determined from molecular dynamics (MD) simulations by Patra *et al.* (interpolated from Fig. 6 in ref. 7 and scaled by the ratio of the electron density to mass density of ethanol) is marked by the solid green distribution in Fig. 7(b). The MD simulations localize the ethanol molecules slightly closer to the membrane core, while NMR and X-ray diffraction experiments show good agreement finding the ethanol closer to the head group region in the membrane water interface. Therefore, we assign Gaussian 1 to ethanol molecules in the head group region of the bilayers in agreement with NMR studies.

The number of ethanol molecules in the head group region can be determined by further analysis of the areas of the Gaussian peaks. As listed in Table 3, the increase in electron density corresponds to ~1.6 ethanol molecules per lipid molecule in the gel phase at $T = 293$ K. Therefore, immersion of DMPC in a 2 mol% ethanol solution was found to result in a 1.6 molar concentration of ethanol in the head group region of the membranes. The number of ethanol molecules assigned to Gaussian 1 in the fluid phase is slightly less, ~1.2 ethanol molecules per lipid molecule.

Measuring membrane–ethanol and membrane–water partition coefficients in the presence of ethanol has proven to be difficult

due to experimental challenges, mainly related to the small volumes and the volatility of the ethanol molecule. Partition coefficients must be measured *in situ*, directly on lipid bilayers. Partitioning of ethanol in bilayers has been measured using different techniques:[2] radioisotopes,[48,49] calorimetry[9,50,51] and vapour pressure measurements.[2,52] The molar coefficient of ethanol partitioning into lipid bilayers, K_p, is defined as $K_p = X^{Et}_{lipid}/X^{Et}_{water}$, where X^{Et}_{lipid} and X^{Et}_{water} are the mole fractions of ethanol in lipid and water phases, respectively. K_p can also be expressed using molar ratios $K_p = \frac{677.933}{18.015} \times \text{molar ratio}^{Et}_{lipid}/\text{molar ratio}^{Et}_{water}$, with $M_{lipid} = 677.933$ g mol^{-1} and $M_{water} = 18.015$ g mol^{-1} the molar masses of DMPC and water.

A K_p value of $K_p = 19$ was reported recently for POPC bilayers[2] at a water–ethanol concentration of 0.036 mol%. K_ps of $K_p \sim 8$,[49] $K_p \sim 15$ (ref. 9) and $K_p \sim 28$ (ref. 51) were reported in DMPC. These coefficients correspond to molar concentrations on the order of ~1 mol%, *i.e.*, concentrations of 1 ethanol molecule per about 100 lipid molecules in the bilayers. We find 1.6 and 1.2 ethanol molecules per lipid molecule in gel and fluid phase, respectively. The fact that the coefficients reported in the literature[9,49] have been determined in solutions with much smaller ethanol concentrations may point to a nonlinear partitioning of ethanol in lipid bilayers, in particular at higher alcohol concentrations. Our result is in agreement with computer simulations by Terama *et al.*,[9] who observed almost complete partitioning of the ethanol molecules under similar conditions.

We now address the origin of the second Gaussian, inside the membrane core. The solubility of ethanol in the hydrophobic membrane core was found to be small in NMR experiments[1,2] and computer simulations.[6] However, Gaussian 2 partially overlaps with the z position of ethanol molecules reported from MD simulations,[7] as shown in Fig. 7. In a more recent MD study using DPPC membranes in contact with a 1.9 mol% ethanol solution (see Fig. 4 in ref. 8) an additional peak was observed in the mass density of the bilayers near the bilayer centre, in agreement with the data in Fig. 7(b). The second Gaussian contribution might, therefore, be related to the presence of ethanol molecules in the hydrophobic membrane core. On the other hand, ethanol is also known to increase the permeability of lipid membranes for water molecules.[53–56] Alternatively, the increase in electron density may, therefore, be due to an increase of the number of water molecules in the membrane in a 1.9 mol% water–ethanol solution.

Because we cannot unambiguously assign Gaussian 2 to the presence of either ethanol or water molecules, we would like to discuss two scenarios to explain the second Gaussian contribution centred at ~9 Å:

(1) Gaussian 2 can be assigned to additional ethanol molecules in the hydrophobic membrane core.

(2) Gaussian 2 can tentatively be attributed to water molecules in the bilayer, which have traveled into the hydrophobic core due to ethanol's effect of increased membrane permeability.

If Gaussian 2 is related to the presence of additional ethanol molecules in the membrane core, the increase in electron density corresponds to 0.55 ethanol molecules per lipid molecule in the gel phase and 0.85 ethanol molecules per lipid molecule in the fluid phase. It is believed that general anaesthetics, such as ethanol, dissolve in membranes thereby changing their physical properties and altering membrane function.[57] Changes in lateral pressure is speculated to be relevant for protein function and binding sites, and in particular functioning of ion channels.[58] The potential presence of ethanol molecules in the hydrophobic core, as listed in Table 3, is likely to be important to distinguish between different theories.[58–61] The presence and solubility of ethanol molecules in the hydrophobic core might also be relevant to model ethanol crossing event, as discussed in refs. 7–9.

When we assign Gaussian 2 to the presence of water molecules in the hydrophobic membrane core, the increase in electron density corresponds to 1.42 water molecules per lipid molecule in the gel state of the phospholipid membranes. In the fluid phase at $T = 303$ K (Fig. 7(b)), 2.22 water molecules per lipid molecule is dissolved in the hydrophobic membrane core.

The results from elastic and quasi-elastic neutron scattering give access to molecular membrane dynamics in the presence of alcohol. Lipid diffusion in the fluid phase is not altered by the presence of ethanol molecules in the bilayers, as shown in Fig. 6. The diffusion constant of $D \sim 50 \times 10^{-12}$ m^2 s^{-1} agrees well with diffusion constants reported in the literature for similar systems.[38–42] This result is in excellent agreement to MD simulations, where no change in lateral diffusion coefficient was observed in the fluid phase of a DPPC membrane in contact with a 1.9 mol% ethanol solution.[8] A similar behaviour was reported from MD simulations in DPPC, however, at very low ethanol concentrations.[9] Diffusion is significantly slower in the gel phase when ethanol is present, consistent with the elastic data in Fig. 2. The inclusion of additional molecules to the head group region of the bilayers reduces the mobility of the lipid molecules in the more rigid gel phase, leading to a smaller diffusion constant.

Molecular freezing and melting is observed in the elastic neutron scattering experiments in Fig. 2. Molecular motions slower than about 1 nanosecond contribute to the elastic intensity. An increase in the recorded intensity is, therefore, caused by slowing down or freezing of molecular dynamics and can be used to assign phase transition temperatures and determine the "stiffness" of molecular interactions. The data in Fig. 2 show the effect of ethanol molecules on slow, nanosecond dynamics of the membranes on different length scales, corresponding to lipid diffusion, lipid tail and hydration water dynamics. Another important finding is that ethanol does not seem to change membrane properties in the fluid L_α phase as the elastic data coincide for DMPC and DMPC–ethanol for temperatures above 297 K. However, the absolute values of the elastic intensity are higher on all length scales in ripple and gel phase when ethanol is present, indicative of a better ordered lipid structure. This increased ordering in the ripple phase has been speculated to be a sign of interdigitation.[12]

The presence of ethanol molecules has a distinct effect on pre-transition (L_β to $P_{\beta'}$) and main transition ($P_{\beta'}$ to L_α) of the membranes. All transitions appear more pronounced with ethanol. While the temperature of the main transition is not changed within the temperature resolution of 0.5 K of this experiment, the pre-transition was found to be shifted by ~2.5 K toward higher temperatures due to the presence of ethanol molecules.

These results lead us to the conclusion that ethanol has little effect on the nanosecond dynamics in the fluid phase of lipid

membranes. This type of dynamics includes diffusion, however also motions related to the elastic properties (*e.g.* undulation of the membranes), and molecular reorientations, which show relaxational dynamics. In a recent inelastic neutron scattering study ethanol was found to significantly increase the collective nanoscale dynamics of the lipid tails in the fluid phase of the membranes.[11] These dynamics are significantly faster than the dynamics probed here and happen on picosecond time scales and between neighbouring hydrocarbon tails. A new, low-energy phonon branch was observed in the presence of ethanol and speculated to be related to the mobility of kink defects perpendicular to the membranes, possibly responsible for the increased permeability for small molecules. While ethanol enhances molecular order in gel and ripple phases, likely ordering into a more densely packed structure, ethanol seems to mainly affect the fast collective dynamics in the physiologically relevant fluid phase.

Dynamics of the hydration water are observed in Fig. 2(e) and (f). A freezing and melting transition is observed as a kink in the elastic intensity curve at $T = 297$ K. This temperature coincides with the temperature of the main transition of the membranes. Hydration water dynamics, therefore, seem to be coupled to freezing and melting of membrane dynamics at the temperature of the main transition.

The freezing and melting transition of water, observed in detector D16, indicates that a significant fraction of the water molecules in our hydrated powder samples can be considered to be hydration water or membrane-bound water as opposed to bulk water. While a water–water correlation peak in bulk water would be observed at Q value $Q \sim 2$ Å^{-1} (3.14 Å), we observe the nearest-neighbour distance between hydration water molecules to be increased by ~8% to 1.85 Å^{-1} (3.4 Å) form the bulk water value. The dip in the electron densities in Fig. 5 and 7 at the lipid–solution interface at $z \sim 27$ Å, points to a reduced density of the hydration water density close to the lipid head groups. From the electron density plots, the dip is decreased by about 10% at the lipid–water interface, which agrees well with the decrease in density of the hydration solvent due to the increased nearest-neighbour distance.

5 Conclusion

In summary, we studied structure and dynamics of phospholipid membranes hydrated with a 5 wt% water–ethanol solution. Elastic and quasi-elastic neutron scattering was used to study slow, nanosecond molecular motions. By analyzing different length scales the effects of ethanol on diffusion, lipid acyl chain dynamics, and hydration water dynamics are determined. Lipid diffusion is found to be unaltered in the fluid phase ($D \sim 50 \times 10^{-12}$ m^2 s^{-1}) however, decreased in the gel phase of the bilayers by 50%: from $D_{\mathrm{DMPC}} = 8.607 \times 10^{-12}$ m^2 s^{-1} to $D_{\mathrm{DMPC+ethanol}} = 4.604 \times 10^{-12}$ m^2 s^{-1}. Ethanol is found to lead to a stiffer, better ordered structure in ripple and gel phases of the membranes. Another important finding is that the dynamics of membrane and hydration water are not significantly affected by the presence of ethanol in the physiologically relevant fluid phase of the membranes at this alcohol concentration.

However, our neutron experiments find the presence of ethanol molecules to have a distinct effect on the pre-transition (L_β to $P_{\beta'}$) and main transition ($P_{\beta'}$ to L_α) of the membranes: all transitions appear more pronounced with the addition of ethanol. While the temperature of the main transition is not affected by ethanol, the pre-transition appears to be shifted to higher temperatures when ethanol is present.

From X-ray scattering experiments we determined the position of the ethanol molecules and their partitioning in the bilayers in gel and fluid phases. We find that the ethanol molecules are located in the head group region of the membranes, at a concentration of 1.6 ethanol molecules per lipid molecule in the gel phase, and 1.2 ethanol molecules per lipid molecule in the fluid phase. The electron densities give experimental evidence for an increased permeability in the presence of ethanol, related to either ethanol molecules in the hydrophobic membrane core or an enhanced permeability to water molecules. In future experiments neutron diffraction will be used to determine the number of ethanol and water molecules in the hydrophobic core by selectively deuterating ethanol molecules with respect to water in order to provide contrast between the two molecules. Partitioning of water and ethanol molecules is essential in better understanding the physiological effect of ethanol as a drug enhancer and an anaesthetic.

Acknowledgements

This research was funded by the Natural Sciences and Engineering Research Council of Canada (NSERC), the National Research Council Canada (NRC), the Canada Foundation for Innovation (CFI) and the Ontario Ministry of Economic Development and Innovation. We thank the NIST Center for Neutron Research for the allocation of beam time. This work utilized facilities supported in part by the National Science Foundation under Agreement No. DMR-0944772.

References

1 J. A. Barry and K. Gawrisch, *Biochemistry*, 1994, **33**, 8082–8088.
2 D. T. Nizza and K. Gawrisch, *Gen. Physiol. Biophys.*, 2009, **28**, 140–145.
3 L. L. Holte and K. Gawrisch, *Biochemistry*, 1997, **36**, 4669–4674.
4 S. E. Feller, C. A. Brown, D. T. Nizza and K. Gawrisch, *Biophys. J.*, 2002, **82**, 1396–1404.
5 J. Chanda and S. Bandyopadhyay, *Chem. Phys. Lett.*, 2004, **392**, 249.
6 A. N. Dickey and R. Faller, *J. Polym. Sci., Part B: Polym. Phys.*, 2005, **43**, 1025–1032.
7 M. Patra, E. Salonen, E. Terama, I. Vattulainen, R. Faller, B. W. Lee, J. Holopainen and M. Karttunen, *Biophys. J.*, 2006, **90**, 1121–1135.
8 A. N. Dickey and R. Faller, *Biophys. J.*, 2007, **92**, 2366–2376.
9 E. Terama, O. H. S. Ollila, E. Salonen, A. C. Rowat, C. Trandum, P. Westh, M. Patra, M. Karttunen and I. Vattulainen, *J. Phys. Chem. B*, 2008, **112**, 4131–4139.
10 T. Adachi, *Chem. Phys. Lipids*, 2000, **107**, 93–97.
11 M. D. Kaye, K. Schmalzl, V. C. Nibali, M. Tarek and M. C. Rheinstädter, *Phys. Rev. E: Stat., Nonlinear, Soft Matter Phys.*, 2011, **83**, 050907.
12 H. Seto, M. Hishida, H. Nobutou, N. L. Yamada, M. Nagao and T. Takeda, *J. Phys. Soc. Jpn.*, 2007, **76**, 054602.
13 P. Westerman, J. Pope, N. Phonphok, J. Doane and D. Dubro, *Biochim. Biophys. Acta, Biomembr.*, 1988, **939**, 64–78.
14 B. W. Koenig and K. Gawrisch, *J. Phys. Chem. B*, 2005, **109**, 7540–7547.
15 H. Komatsu and S. Okada, *Chem. Phys. Lipids*, 1997, **85**, 67–74.
16 H. V. Ly and M. L. Longo, *Biophys. J.*, 2004, **87**, 1013–1033.
17 E. Nováková, K. Giewekemeyer and T. Salditt, *Phys. Rev. E: Stat., Nonlinear, Soft Matter Phys.*, 2006, **74**, 051911.

18 M. C. Rheinstädter, T. Seydel and T. Salditt, *Phys. Rev. E: Stat., Nonlinear, Soft Matter Phys.*, 2007, **75**, 011907.
19 M. C. Rheinstädter, T. Seydel, F. Demmel and T. Salditt, *Phys. Rev. E: Stat., Nonlinear, Soft Matter Phys.*, 2005, **71**, 061908.
20 A. M. Gaspar, S. Busch, M.-S. Appavou, W. Haeussler, R. Georgii, Y. Su and W. Doster, *Biochim. Biophys. Acta*, 2010, **1804**, 7682.
21 A. Meyer, R. M. Dimeo, P. M. Gehring and D. A. Neumann, *Rev. Sci. Instrum.*, 2003, **74**, 2759–2777.
22 M. Weik, U. Lehnert and G. Zaccai, *Biophys. J.*, 2005, **89**, 3639–3646.
23 M. Doxastakis, V. García Sakai, S. Ohtake, J. Maranas and J. de Pablo, *Biophys. J.*, 2007, **92**, 147–161.
24 K. Wood, M. Plazanet, F. Gabel, B. Kessler, D. Oesterhelt, D. J. Tobias, G. Zaccai and M. Weik, *Proc. Natl. Acad. Sci. U. S. A.*, 2007, **104**, 18049–18054.
25 L. Toppozini, C. L. Armstrong, M. D. Kaye, M. Tyagi, T. Jenkins and M. Rheinstädter, *ISRN Biophysics*, 2012, **2012**, 520307.
26 M. C. Rheinstädter, J. Das, E. J. Flenner, B. Brüning, T. Seydel and I. Kosztin, *Phys. Rev. Lett.*, 2008, **101**, 248106, 4 pages.
27 V. García Sakai and A. Arbe, *Curr. Opin. Colloid Interface Sci.*, 2009, **14**, 381–390.
28 M. C. Rheinstädter, C. Ollinger, G. Fragneto, F. Demmel and T. Salditt, *Phys. Rev. Lett.*, 2004, **93**, 108107.
29 G. Pabst, N. Kučerka, M.-P. Nieh, M. Rheinstädter and J. Katsaras, *Chem. Phys. Lipids*, 2010, **163**, 460–479.
30 G. Fragneto and M. Rheinstädter, *C. R. Phys.*, 2007, **8**, 865–883.
31 S. Tristram-Nagle, Y. Liu, J. Legleiter and J. F. Nagle, *Biophys. J.*, 2002, **83**, 3324–3335.
32 J. F. Nagle and M. C. Wiener, *Biophys. J.*, 1989, **55**, 309–313.
33 J. Nagle, R. Zhang, S. Tristram-Nagle, W. Sun, H. Petrache and R. Suter, *Biophys. J.*, 1996, **70**, 1419–1431.
34 G. I. King and C. R. Worthington, *Phys. Lett. A*, 1971, **35**, 259–260.
35 N. Chu, N. Kučerka, Y. Liu, S. Tristram-Nagle and J. F. Nagle, *Phys. Rev. E: Stat., Nonlinear, Soft Matter Phys.*, 2005, **71**, 041904.
36 K. Lan and J. Jorgenson, *J. Chromatogr., A*, 2001, **915**, 1–13.
37 C. L. Armstrong, M. Trapp, J. Peters, T. Seydel and M. C. Rheinstädter, *Soft Matter*, 2011, **7**, 8358–8362.
38 C. L. Armstrong, M. D. Kaye, M. Zamponi, E. Mamontov, M. Tyagi, T. Jenkins and M. C. Rheinstädter, *Soft Matter*, 2010, **6**, 5864–5867.
39 W. Pfeiffer, T. Henkel, E. Sackmann and W. Knorr, *Europhys. Lett.*, 1989, **8**, 201–206.
40 S. Busch, C. Smuda, L. Pardo and T. Unruh, *J. Am. Chem. Soc.*, 2010, **132**, 3232–3233.
41 A. Buchsteiner, T. Hauß, S. Dante and N. Dencher, *Biochim. Biophys. Acta*, 2010, **1798**, 1969–1976.
42 S. König, W. Pfeiffer, T. Bayerl, D. Richter and E. Sackmann, *J. Phys. II*, 1992, **2**, 1589–1615.
43 N. Kučerka, Y. Liu, N. Chu, H. I. Petrache, S. Tristram-Nagle and J. F. Nagle, *Biophys. J.*, 2005, **88**, 2626–2637.
44 N. Kucerka, S. Tristram-Nagle and J. F. Nagle, *Biophysical Journal: Biophysical Letters*, 2006, **90**, L83–L85.
45 A. Spaar and T. Salditt, *Biophys. J.*, 2003, **85**, 1576–1584.
46 T. T. Mills, G. E. S. Toombes, S. Tristram-Nagle, D.-M. Smilgies, G. W. Feigenson and J. F. Nagle, *Biophys. J.*, 2008, **95**, 669–681.
47 M. A. Barrett, S. Zheng, G. Roshankar, R. J. Alsop, R. K. Belanger, C. Huynh, N. Kučerka and M. C. Rheinstädter, *PLoS One*, 2012, **7**, e34357.
48 Y. Katz and J. M. Diamond, *J. Membr. Biol.*, 1974, **17**, 69–86.
49 Y. Katz and J. M. Diamond, *J. Membr. Biol.*, 1974, **17**, 101–120.
50 E. S. Rowe, *Mol. Pharmacol.*, 1982, **22**, 133–139.
51 C. Trandum, P. Westh, K. Jörgensen and O. G. Mouritsen, *Biochim. Biophys. Acta*, 1999, **1420**, 179–188.
52 P. Westh and C. Trandum, *Biochim. Biophys. Acta*, 1999, **1421**, 261–272.
53 D. Huster, J. Jin, Albert, K. Arnold and K. Gawrisch, *Biophys. J.*, 1997, **73**, 855–864.
54 B. Deamer and J. Bramhall, *Chem. Phys. Lipids*, 1986, **40**, 167–188.
55 S. Paula, A. Volkov, A. Van Hoek, T. Haines and D. Deamer, *Biophys. J.*, 1996, **70**, 339–348.
56 G. Lahajnar, P. Macek, P. Smid and I. Zupancic, *Biochim. Biophys. Acta*, 1995, **1235**, 437–442.
57 P. Seeman, *Pharmacol. Rev.*, 1972, **24**, 583–655.
58 H. Jerabek, G. Pabst, M. Rappolt and T. Stockner, *J. Am. Chem. Soc.*, 2010, **132**, 7990–7997.
59 K. Pang, *Mol. Pharmacol.*, 1980, **18**, 84.
60 J. Trudell, *Anesthesiology*, 1977, **46**, 5.
61 D. Mountcastle, *Proc. Natl. Acad. Sci. U. S. A.*, 1978, **75**, 4906.

Chapter 6

The Structure of Cholesterol in Lipid Rafts: Publication IV

"*The Structure of Cholesterol in Lipid Rafts*", Laura Toppozini, Sebastian Meinhardt, Clare L. Armstrong, Zahra Yamani, Norbert Kučerka, Friederike Schmid, and Maikel C. Rheinstädter Phys. Rev. Lett. **113**, 228101 (2014) http://dx.doi.org/10.1103/PhysRevLett.113.228101

6.1 Preface

Model membranes are far from the complex, multi-component envelopes that are biological membranes; however, fundamental properties such as a bilayer structure with a hydrophobic core, where the lipids are hydrated and fluid, can give insight into the fundamental properties of membranes. By utilizing this simple, single-phospholipid bilayers model we can characterize our simplest construct of a membrane and add molecules to increase complexity. Cholesterol provides much of the structural rigidity in biological membranes and is also implicated in lipid rafts, which are suggested to facilitate specific cellular processes.

Rafts, as mentioned in Section 2.2, are the elusive cholesterol-rich biological structures that are thought to be important for many functions of the cell and were first introduced by Simons and Ikonen [7]. Cholesterol is the single most abundant species of lipid in the plasma membrane, commonly found in molar concentrations of ∼30%. Being so common, the long-standing question of how cholesterol is involved in regulating membrane structure and function is of wide-spread interest.

Previous studies have looked at simplistic systems of ternary (saturated, unsaturated and cholesterol) [25, 104, 105] and more recently binary mixtures (cholesterol and lipid) using experiments and simulations alike [10, 106, 28]. Such structures are transient, lasting on the order of 100 ns and with a size of approximately 10 nm which have proved difficult to measure. However, a new technique

pioneered by Armstrong *et al.* [9, 10] employs a change in the coherence length of the incident neutrons via a change in neutron wavelength in order to detect small structures. These small structures would otherwise be averaged over in the case of large coherence length and information about their structure lost.

The simulations and experiments in this publication are performed in the liquid-ordered phase and heterogeneities are observed in each of the coarse-grained molecular simulations as well as the neutron diffraction measurements. The simulations are very large simulations, incorporating 20,000 molecules, which is quite an impressive system size considering typical molecular dynamics simulations have only hundreds of lipid molecules. In order to have such a large system, the molecules were coarse-grained model in lieu of fully atomistic models. Thus, these simulations describe the long range order of the l_o systems, complementing the local structural observations of our neutron experiments. The structures of the cholesterol within the different types of lateral heterogeneities are determined by neutron diffraction experiments on deuterium labeled cholesterol in lipid bilayers. It should be noted that within the publication the simulations are ambiguously referred to as molecular dynamics; however they are Monte Carlo simulations of a coarse-grained molecular model of lipids and cholesterol that form lipid bilayers.

We observed strongly-bound lipid-cholesterol complexes, as suggested by the umbrella model [23] (two cholesterol molecules bound to a lipid molecule) and cholesterol bilayers. We find a total of three different structures: (1) lipid-cholesterol complexes distributed in a low concentration amongst lipids in a liquid-disordered phase, (2) a monoclinic structure of ordered lipid-cholesterol complexes of alternating direction in equilibrium with (3) triclinic cholesterol bilayers. The fact that domains exist in these simple model membranes has contributed to the understanding of the principles governing phase behaviour and lipid raft formation in biological membranes.

Author Contributions:

- *Project Concept:* Maikel Rheinstädter, Friederike Schmid
- *Sample Preparation:* Clare Armstrong, **Laura Toppozini**
- *X-ray Experiment:* **Laura Toppozini**, Maikel Rheinstädter, Zahra Yamani, Norbert Kučerka
- *Simulations:* Sebastian Meinhardt, Friederike Schmid
- *Data Analysis:* **Laura Toppozini**, Sebastian Meinhardt
- *Manuscript Preparation:* **Laura Toppozini**, Sebastian Meinhardt, Friederike Schmid, Maikel Rheinstädter

PRL **113,** 228101 (2014) PHYSICAL REVIEW LETTERS week ending 28 NOVEMBER 2014

Structure of Cholesterol in Lipid Rafts

Laura Toppozini,[1] Sebastian Meinhardt,[2] Clare L. Armstrong,[1] Zahra Yamani,[3] Norbert Kučerka,[3,4] Friederike Schmid,[2,†] and Maikel C. Rheinstädter[1,3,*]

[1]*Department of Physics and Astronomy, McMaster University, Hamilton, Ontario, L8S 4M1, Canada*
[2]*KOMET 331, Institute of Physics, Johannes Gutenberg-Universität Mainz, 55099 Mainz, Germany*
[3]*Canadian Neutron Beam Centre, Chalk River, Ontario, K0J 1J0, Canada*
[4]*Faculty of Pharmacy, Comenius University, 832 32 Bratislava, Slovakia*

(Received 17 March 2014; published 25 November 2014)

Rafts, or functional domains, are transient nano-or mesoscopic structures in the plasma membrane and are thought to be essential for many cellular processes such as signal transduction, adhesion, trafficking, and lipid or protein sorting. Observations of these membrane heterogeneities have proven challenging, as they are thought to be both small and short lived. With a combination of coarse-grained molecular dynamics simulations and neutron diffraction using deuterium labeled cholesterol molecules, we observe raftlike structures and determine the ordering of the cholesterol molecules in binary cholesterol-containing lipid membranes. From coarse-grained computer simulations, heterogenous membranes structures were observed and characterized as small, ordered domains. Neutron diffraction was used to study the lateral structure of the cholesterol molecules. We find pairs of strongly bound cholesterol molecules in the liquid-disordered phase, in accordance with the umbrella model. Bragg peaks corresponding to ordering of the cholesterol molecules in the raftlike structures were observed and indexed by two different structures: a monoclinic structure of ordered cholesterol pairs of alternating direction in equilibrium with cholesterol plaques, i.e., triclinic cholesterol bilayers.

DOI: 10.1103/PhysRevLett.113.228101 PACS numbers: 87.16.dt, 83.85.Hf, 87.15.ap

The liquid-ordered (l_o) phase of membranes in the presence of cholesterol was brought to the attention of the life science community in 1997 when Simons and Ikonen [1] proposed the existence of so-called rafts in biological membranes. Rafts were thought to be small, molecularly organized units, providing local structure in fluid biological membranes and hence furnishing platforms for specific biological functions [1–10]. These rafts were supposed to be enriched in cholesterol making them more ordered, thicker and, thus, appropriate anchoring places for certain acylated and hydrophobically matched integral membrane proteins. The high levels of cholesterol in these rafts led to the proposal that rafts are local manifestations of the l_o phase, although in most cases the nature of the lipid ordering and the phase state were not established in cells, nor in most model membrane studies [10–12].

Rafts are generally interpreted as self-assembled clusters floating around in an otherwise structureless liquid membrane. However, early work in the physical chemistry of lipid bilayers pointed to the possibility of dynamic heterogeneity [13–16] in thermodynamic one-phase regions of binary systems. The sources of dynamic heterogeneity are cooperative molecular interactions and thermal fluctuations that lead to density and compositional fluctuations in space and time.

A number of ternary phase diagrams have been determined for systems involving cholesterol and two different lipid species. Usually these systems contain a lipid species with a high melting point, such as a long-chain saturated phospholipid or sphingolipid, and a lipid species with a low melting point, such as an unsaturated phospholipid [17], resulting in the observations of micrometer-sized, thermodynamically stable domains [4,18–21]. Much less work has been done on cholesterol-lipid binary mixtures, which although seemingly simpler, have proven to be more difficult to study. Evidence for a heterogeneous structure of the l_o phase, similar to a microemulsion, with ordered lipid nanodomains in equilibrium with a disordered membrane was recently supported both by theory and experiment. The computational work by Meinhardt, Vink, and Schmid [22] and Sodt *et al.* [23] and the experimental papers by Armstrong *et al.* [24–26] using neutron scattering were conducted using binary DPPC/cholesterol and dimyristoylphosphocholine (DMPC)/cholesterol systems.

We combined coarse-grained molecular dynamics (MD) simulations including 20 000 lipid-cholesterol molecules with neutron diffraction using deuterium labeled cholesterol molecules to study the cholesterol structure in the liquid-ordered phase of dipalmitoylphosphatidylcholine (DPPC) bilayers. The simulations present evidence for a heterogenous membrane structure at 17 and 60 mol% cholesterol and the formation of small, transient domains enriched in cholesterol. The molecular structure of the cholesterol molecules within these domains was determined by neutron diffraction at 32.5 mol% cholesterol. Three structures were observed: (1) a fluidlike structure with strongly bound pairs of cholesterol molecules as manifestation of the liquid-disordered (l_d) phase; (2) a highly ordered lipid-cholesterol phase where the lipid-cholesterol

complexes condense in a monoclinic structure, in accordance with the umbrella model; and (3) triclinic cholesterol plaques, i.e., cholesterol bilayers coexisting with the lamellar lipid membranes.

The simulations use a simple coarse-grained lipid model [27] that reproduces the main phases of DPPC bilayers including the nanostructured ripple phase $P_{\beta'}$ [27] and has similar elastic properties in the fluid phase [28]. In this model, lipids are represented by short linear chains of beads, with a "head bead" and several "tail beads" [Fig. 1(a)], which are surrounded by a structureless solvent. The model was recently extended to binary lipid-cholesterol mixtures. The cholesterol molecules are modeled shorter and stiffer than DPPC, and they have an affinity to phospholipid molecules, reflecting the observation that sterols in bilayers tend to be solubilized by lipids [29]. In our previous work, we have reported on the behavior of mixed bilayers with low cholesterol content [22]. Locally, phase separation was observed between an l_o and an l_d phase. On large scales, however, the system assumes a two-dimensional microemulsion-type state, where nanometer-sized cholesterol-rich domains are embedded in an l_d environment. These domains are stabilized by a coupling between monolayer curvature and local ordering [22], suggesting that raft formation is closely related to the formation of ripples in one-component membranes. In the following, we will discuss the behavior of our model membranes at larger cholesterol concentrations and discuss the implications for experiments.

The simulations were done at constant pressure, constant temperature, and constant zero surface tension in a semi-grandcanonical ensemble where lipids and cholesterol molecules can switch their identities. The cholesterol content is thus driven by a chemical potential parameter μ. Simulation results are given in units of $\sigma \approx 6$ Å [28] and the thermal energy k_BT. Typical equilibrated simulation snapshots (side view and top view) are shown in Figs. 1(b) and 1(c). At low cholesterol concentration ($\mu = 8.5k_BT$), one observes small rafts as discussed earlier. At higher cholesterol concentration (lower μ), the cholesterol-rich rafts grow and gradually fill up the system, but they still remain separated by narrow cholesterol-poor "trenches." The side view shows that these trenches have the structure of line defects where opposing monolayers are connected. Such line defects are also structural elements of the ripple phase in one-component bilayers [30,31].

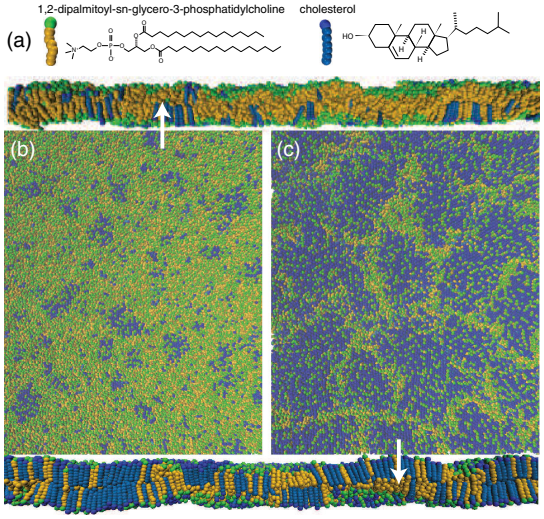

FIG. 1 (color online). (a) Schematic representation of DPPC and cholesterol molecules used in the simulations. (b) Snapshot of the simulation at $\mu = 8.5k_BT$, resulting in a cholesterol concentration of ≈17 mol%. (c) Snapshot of the simulation at $\mu = 7.8k_BT$ resulting in a cholesterol concentration of ≈60 mol%.

With increasing cholesterol concentration, the structure of the rafts changes qualitatively. This is demonstrated in Fig. 2(a), which shows that the cholesterol concentration inside rafts remains constant (around 25%) for a range of chemical potentials $\mu > 8.5k_BT$, but then increases rapidly at $\mu \leq 8k_BT$. Along with this concentration increase, the peaks in the lateral structure factor of cholesterol head groups in Fig. 2(b) become more pronounced, indicating a substantial increase in molecular order. We should note that the coarse-grained model used in the simulations is not suitable for studying details of the molecular arrangement inside the ordered structures. However, one can analyze the transition between states with high and low μ by analyzing the distribution of local cholesterol densities [Fig. 2(a), inset]. At high μ, the histogram has a maximum at cholesterol density c close to zero and decays for higher c with a broad tail that reflects the contribution of the rafts. At low μ, it exhibits a marked maximum at $c \approx 1\sigma^{-2}$, corresponding to bilayer regions consisting purely of cholesterol. In the intermediate regime, corresponding to the situation shown in Fig. 1(c), the histogram of cholesterol densities features two broad peaks around $c \approx 0.4\sigma^{-2}$ and $c \approx 0.7\sigma^{-2}$. In this regime, almost pure cholesterol plaques coexist with regions having cholesterol

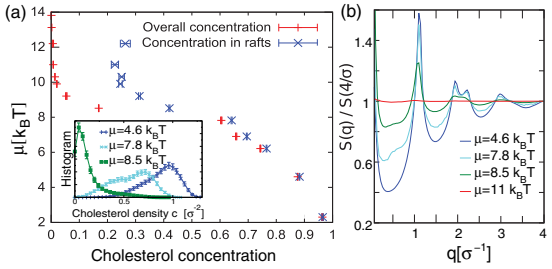

FIG. 2 (color online). (a) Total cholesterol concentration and cholesterol concentration inside rafts for different chemical potential μ. Inset shows a histogram of local cholesterol densities, taken using squares of area $25\sigma^2 \approx 9$ nm^2. (b) Radially averaged two-dimensional lateral structure factor of cholesterol head groups for different μ as indicated. The level of molecular order increases with decreasing μ, i.e., increasing cholesterol concentration.

PRL **113,** 228101 (2014) PHYSICAL REVIEW LETTERS week ending 28 NOVEMBER 2014

compositions that are close to those of rafts in cholesterol-poor membranes [high μ limit in Fig. 2(a)].

The experimental observation of the l_o phase in a cholesterol-lipid binary mixture was initially reported by Vist and Davis [32]. The quantitative determination of binary lipid-cholesterol phase diagrams has remained elusive. In phospholipid membranes, most studies report the l_o phase at cholesterol concentrations of more than 30 mol% [17]. The formation of cholesterol plaques, phase-separated cholesterol bilayers coexisting with the membrane, was reported to occur at ≈37.5 mol% cholesterol in model lipid membranes [33]. That leaves a relatively small range of cholesterol concentrations in the experiment (between about 30 and 37.5 mol%), where the l_o phase can be studied. Phase separation may be driven in experiments by certain boundary conditions, not present in computer simulations. The simulations in Fig. 2 can, therefore, access a much larger range of cholesterol concentrations and by studying concentrations slightly lower and higher than the experimentally accessible range, the corresponding structures could be emphasized in the computer model.

We used neutron diffraction to measure the lateral cholesterol structure in DPPC bilayers containing 32.5 mol% at $T = 50\,°\mathrm{C}$ and a D_2O relative humidity of ≈100%, ensuring full hydration of the membranes. Deuterium labeled cholesterol (d7) was used such that the experiment was sensitive to the arrangements of the cholesterol molecules. Schematics of the two molecules are shown in Fig. 3(a). Highly oriented, solid supported membrane stacks on silicon wafers were prepared, as detailed in the Supplemental Material [34]. The sample was aligned in the neutron beam such that the scattering vector, $\vec{Q}$, was placed in the plane of the membranes [Fig. 3(b)]. This in-plane component of the scattering vector is referred to as $q_\parallel$.

Two setups were used: a conventional high-energy and momentum resolution setup using a neutron wavelength of $\lambda = 2.37$ Å and a low-energy and momentum resolution setup with smaller wavelengths of $\lambda = 1.44$ and 1.48 Å. The latter setup was reported to efficiently integrate over small structures and provide a high spatial resolution capable of detecting small structures and weak signals [12,25,46]. The two setups could be readily switched during the experiment by changing the incoming neutron wavelength, λ, without altering the state of the membrane sample. Data taken using the conventional setup are shown in Fig. 3(c) and display a diffraction pattern with broad peaks, typical of a fluidlike structure.

Peaks T_1, T_2, and T_3 in Fig. 3(c) correspond to the hexagonal arrangement of the lipid tails with a unit cell of $a_{\mathrm{lipid}-l_d} = b_{\mathrm{lipid}-l_d} = 5.58$ Å and $\gamma = 120°$, in agreement with Armstrong *et al.* [25]. By calculating the (coherent) scattering contributions (Table S3 [34]), cholesterol and lipid molecules contribute almost equally to the scattering in the l_d phase such that the corresponding signals are observed simultaneously in Fig. 3(c). Peak H agrees well with an

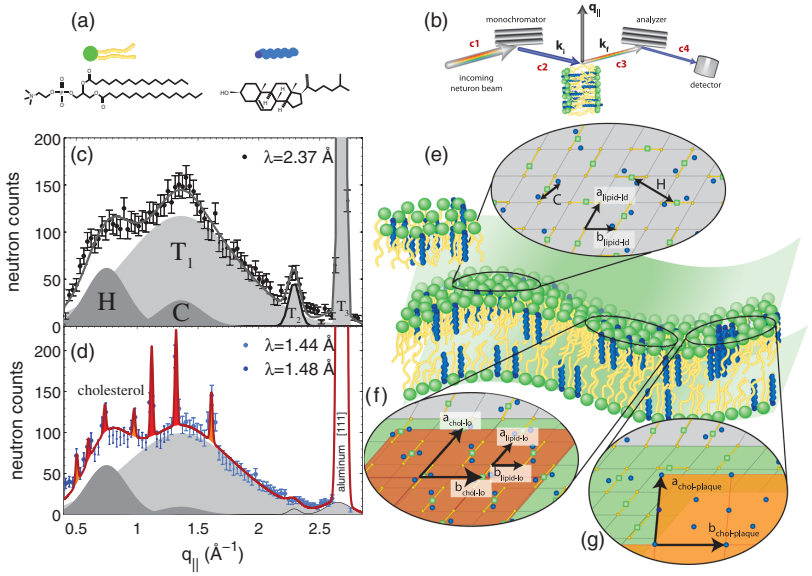

FIG. 3 (color online). (a) Schematics of DPPC and (deuterated) cholesterol molecules. (b) Sketch of the scattering geometry. $q_\parallel$ denotes the in-plane component of the scattering vector. (c) Diffraction measured at $\lambda = 2.37$ Å showing broad, fluidlike peaks. (d) Data measured at $\lambda = 1.44$ and 1.48 Å. Several pronounced Bragg peaks are observed in addition to the broad peaks in (a). (e) Illustration of the different molecular structures: pairs of cholesterol molecules in the liquid-disordered regions of the membrane in equilibrium with highly ordered cholesterol structures such as the umbrella structure (f) and cholesterol plaques (g). An aluminum Bragg peak due to the windows of the humidity chamber and the sample holder is present at $q_\parallel = 2.68$ Å^{-1}. Aluminum forms a face-centered cubic lattice with lattice parameter $a = 4.04941$ Å [45].

average nearest neighbor head group-head group distance of ≈8.4 Å. Peak *C* only occurs in the presence of deuterated cholesterol molecules. It was, therefore, assigned to a nearest neighbor distance of ≈4.6 Å (±0.5 Å) of cholesterol molecules in the l_d phase, i.e., to pairs of strongly bound cholesterol molecules, as shown in Fig. 3(e). Details of the fitting procedure are given in the Supplemental Material [34].

Several pronounced Bragg peaks are observed at neutron wavelengths of $\lambda = 1.44$ and 1.48 Å in Fig. 3(d) in addition to the broad correlation peaks. Because of the high cholesterol concentration in l_o-type structures and plaques and the scattering lengths of DPPC and *d*-cholesterol molecules, the corresponding coherent scattering signal in Fig. 3(d) is dominated by the deuterated cholesterol molecules. As listed in Table I, the peak pattern is well described by a superposition of two 2-dimensional structures: a monoclinic unit cell with lattice parameters $a_{\text{chol-lo}} = b_{\text{chol-lo}} = 11$ Å and $\gamma = 131°$ and a triclinic unit cell with $a_{\text{chol-plaque}} = b_{\text{chol-plaque}} = 12.8$ Å and $\gamma = 95°$ (the values for α and β could not be determined from the measurements but were taken from [33,47] to be $\alpha = 91.9°$ and $\beta = 98.1°$).

The lipid structure in the l_o-type structures in binary DPPC/32.5 mol% cholesterol bilayers was recently reported by Armstrong *et al.* from neutron diffraction using deuterium labeled lipid molecules [25]. The lipid tails were found in an ordered, gel-like phase organized in a monoclinic unit cell with $a_{\text{lipid-lo}} = b_{\text{lipid-lo}} = 5.2$ Å and $\gamma = 130.7°$, as shown in Fig. 3(f). The cholesterol unit cell determined from the diffraction data in Fig. 3(c) is indicative of a doubling of the lipid tail unit cell for the cholesterol molecules. The corresponding cholesterol structure consists of cholesterol pairs alternating between two different orientations.

The l_d-and the l_o-type structures can be related to the well-known umbrella model [48], where one lipid molecule is assumed to be capable to "host" two cholesterol molecules, which leads to a maximum cholesterol solubility of 66 mol% in saturated lipid bilayers. In this scenario the term umbrella model refers to two cholesterol molecules closely interacting with one lipid molecule. Cholesterol plaques, i.e., cholesterol bilayers coexisting with the lamellar membrane phase, were reported recently by Barrett *et al.* [33] in model membranes containing high amounts of cholesterol, above 40 mol% for DMPC and 37.5 mol% for DPPC. The triclinic peaks in Fig. 3(d) agree well with the structures published and were, therefore, assigned to cholesterol plaques.

Hence both coarse-grained molecular simulations and neutron diffraction data suggest the coexistence of a liquid disordered membrane with two types of highly ordered cholesterol structures: One with some lipid content [Fig. 3(f)], corresponding to the first shoulder in the density histogram at $\mu = 7.8 k_B T$ [Fig. 2(a), inset], and one almost exclusively made of cholesterol [Fig. 3(g)], corresponding to the second peak at $\mu = 7.8 k_B T$ in Fig. 2(a). The existence of these structures in the experiment should be robust in binary systems and not depend on, for instance, the sample preparation protocol [49].

The neutron diffraction data present evidence for pairs of strongly bound cholesterol molecules. We note that the scattering experiment was not sensitive to *single* cholesterol molecules; however, the formation of cholesterol dimers with a well-defined nearest neighbor distance leads to a corresponding peak in the data in Figs. 3(c) and 3(d). An attractive force between cholesterol molecules in a 1-palmitoyl-2-oleoylphosphatidylcholine (POPC) bilayer and the formation of cholesterol dimers was reported from MD simulations [50]. Such a force is likely related to the formation of lipid-cholesterol complexes [51] and the umbrella model. However, it is not straightforward to estimate the percentage of dimers from the experiments. A dynamical equilibrium between dimers and monomers is a likely scenario [52].

The dynamic domains observed in this study are not biological rafts, which are thought to be more complex, multi-component structures in biological membranes. In the past, domains have been observed in simple model systems, but only those designed to be "raft-forming" mixtures. In these cases the domains that form are stable equilibrium structures, and are not likely related to the rafts that exist in real cells [12]. The small and fluctuating domains observed in binary systems may be more closely related to what rafts are thought to be [10], and are potentially the nuclei that lead to the formation of rafts in biological membranes. The characteristic overall length scale for nanodomains in the simulations is around 20σ, corresponding to 10–20 nanometers. Both simulations and experiments indicate that there are two types of cholesterol-rich patches coexisting with cholesterol-poor liquid-disordered regions, i.e., ordered l_o-type regions containing both lipids and cholesterol, and cholesterol plaques. The transition between these two is gradual in the coarse-grained simulations. In real membranes, they have different

TABLE I. Peak parameters of the correlation peaks observed in Figs. 3(c) and 3(d) and the association with the different cholesterol structures, such as l_d-, l_o-type structure and cholesterol plaque. *H* and *C* label the nearest neighbor distances of lipid head groups and cholesterol molecules, respectively; T_1, T_2, and T_3 denote the unit cell of the lipid tails in the l_d regions of the membrane. Peaks were fitted using Gaussian peak profiles and widths are listed as Gaussian widths, σ_G.

	Amplitude (counts)	Center (Å^{-1})	σ_G (Å^{-1})	l_d	monoclinic cholesterol l_o-type structure	triclinic cholesterol plaque
Fig. 3(c)	62	0.75	0.17	*H*		
	117	1.360	0.46	T_1		
	27.5	1.360	0.17	*C*		
	46.6	2.289	0.05	T_2		
	15.0	2.650	0.10	T_3		
Fig. 3(d)	19.8	0.5	0.01			[1 0 0]
	34.8	0.55	0.01		[1 $\bar{1}$ 0]	
	34.3	0.74	0.01		[1 0 0]	[1 1 0]
	33.5	0.98	0.01			[2 0 0]
	110	1.12	0.01		[2 $\bar{1}$ 0]	
	117.8	1.32	0.01		[1 1 0]	
	60.0	1.61	0.01			[1 3 0]

local structures (monoclinic in l_o-type regions, triclinic in plaque regions), which may stabilize distinct domains.

This work was supported by the German Science Foundation within the collaborative research center SFB-625. Simulations were carried out at the John von Neumann Institute for Computing (NIC) Jülich and the Mogon Cluster at Mainz University. Experiments were funded by the Natural Sciences and Engineering Research Council (NSERC) of Canada, the National Research Council (NRC), the Canada Foundation for Innovation (CFI), and the Ontario Ministry of Economic Development and Innovation. L. T. is the recipient of an NSERC Canada Graduate Scholarship; M. C. R. is the recipient of an Early Researcher Award from the Province of Ontario.

*Corresponding author.
rheinstadter@mcmaster.ca
†friederike.schmid@uni-mainz.de

[1] K. Simons and E. Ikonen, Nature (London) **387**, 569 (1997).
[2] K. Simons and E. Ikonen, Science **290**, 1721 (2000).
[3] D. M. Engelman, Nature (London) **438**, 578 (2005).
[4] P. S. Niemelä, S. Ollila, M. T. Hyvönen, M. Karttunen, and I. Vattulainen, PLoS Comput. Biol. **3**, e34 (2007).
[5] L. J. Pike, J. Lipid Res. **50**, S323 (2009).
[6] D. Lingwood and K. Simons, Science **327**, 46 (2010).
[7] C. Eggeling, C. Ringemann, R. Medda, G. Schwarzmann, K. Sandhoff, S. Polyakova, V. N. Belov, B. Hein, C. von Middendorf, A. Schönle, and S. W. Hell, Nature (London) **457**, 1159 (2009).
[8] F. G. van der Goot and T. Harder, Seminars in immunology **13**, 89 (2001).
[9] P.-F. Lenne and A. Nicolas, Soft Matter **5**, 2841 (2009).
[10] K. Simons and M. J. Gerl, Nat. Rev. Mol. Cell Biol. **11**, 688 (2010).
[11] O. G. Mouritsen, Biochim. Biophys. Acta **1798**, 1286 (2010).
[12] M. C. Rheinstädter and O. G. Mouritsen, Curr. Opin. Colloid Interface Sci. **18**, 440 (2013).
[13] A. Dibble, A. K. Hinderliter, J. J. Sando, and R. L. Biltonen, Biophys. J. **71**, 1877 (1996).
[14] O. G. Mouritsen and R. L. Biltonen, New Compr. Biochem. **25**, 1 (1993).
[15] O. G. Mouritsen and K. Jørgensen, Chem. Phys. Lipids **73**, 3 (1994).
[16] O. G. Mouritsen and K. Jørgensen, Curr. Opin. Struct. Biol. **7**, 518 (1997).
[17] D. Marsh, Biochim. Biophys. Acta Biomembr. **1798**, 688 (2010).
[18] H. J. Risselada and S. J. Marrink, Proc. Natl. Acad. Sci. U.S.A. **105**, 17367 (2008).
[19] M. L. Berkowitz, Biochim. Biophys. Acta Biomembr. **1788**, 86 (2009).
[20] W. Bennett and D. P. Tieleman, Biochim. Biophys. Acta Biomembr. **1828**, 1765 (2013).
[21] F. A. Heberle, R. S. Petruzielo, J. Pan, P. Drazba, N. Kucerka, R. F. Standaert, G. W. Feigenson, and J. Katsaras, J. Am. Chem. Soc. **135**, 6853 (2013).
[22] S. Meinhardt, R. L. C. Vink, and F. Schmid, Proc. Natl. Acad. Sci. U.S.A. **110**, 4476 (2013).
[23] A. J. Sodt, M. L. Sandar, K. Gawrisch, R. W. Pastor, and E. Lyman, J. Am. Chem. Soc. **136**, 725 (2014).
[24] C. L. Armstrong, M. A. Barrett, A. Hiess, T. Salditt, J. Katsaras, A.-C. Shi, and M. C. Rheinstädter, Eur. Biophys. J. **41**, 901 (2012).
[25] C. L. Armstrong, D. Marquardt, H. Dies, N. Kučerka, Z. Yamani, T. A. Harroun, J. Katsaras, A.-C. Shi, and M. C. Rheinstädter, PLoS One **8**, e66162 (2013).
[26] C. L. Armstrong, W. Häußler, T. Seydel, J. Katsaras, and M. C. Rheinstädter, Soft Matter **10**, 2600 (2014).
[27] F. Schmid, D. Düchs, O. Lenz, and B. West, Comput. Phys. Commun. **177**, 168 (2007).
[28] B. West, F. L. H. Brown, and F. Schmid, Biophys. J. **96**, 101 (2009).
[29] G. Lindblom and G. Orädd, Biochim. Biophys. Acta **1788**, 234 (2009).
[30] A. H. de Vries, S. Yefimov, A. E. Mark, and S. J. Marrink, Proc. Natl. Acad. Sci. U.S.A. **102**, 5392 (2005).
[31] O. Lenz and F. Schmid, Phys. Rev. Lett. **98**, 058104 (2007).
[32] R. Vist and J. H. Davis, Biochemistry **29**, 451 (1990).
[33] M. Barrett, S. Zheng, L. Toppozini, R. Alsop, H. Dies, A. Wang, N. Jago, M. Moore, and M. Rheinstädter, Soft Matter **9**, 9342 (2013).
[34] See Supplemental Material at http://link.aps.org/supplemental/10.1103/PhysRevLett.113.228101 for details of molecular dynamics simulations and data analysis from the neutron scattering experiment, which includes Refs. [35–44].
[35] N. Chu, N. Kučerka, Y. Liu, S. Tristram-Nagle, and J. F. Nagle, Phys. Rev. E **71**, 041904 (2005).
[36] D. Frenkel and B. Smit, *Understanding Molecular Simulation: From Algorithms to Applications* (Academic, New York, 2001).
[37] L. Hosta-Rigau, Y. Zhang, M. T. Boon, A. Postma, and B. Städler, Nanoscale **5**, 89 (2012).
[38] J. Katsaras, R. F. Epand, and R. M. Epand, Phys. Rev. E **55**, 3751 (1997).
[39] O. Lenz and F. Schmid, J. Mol. Liq. **117**, 147 (2005).
[40] S. Mabrey and J. Sturtevant, Proc. Natl. Acad. Sci. U.S.A. **73**, 3862 (1976).
[41] W. D. Ness, Chem. Rev. **111**, 6423 (2011).
[42] H. Rauch, Found. Phys. **23**, 7 (1993).
[43] J. R. Taylor, *An Introduction to Error Analysis: The Study of Uncertainties in Physical Measurements* (University Science Books, Sausalito, 1982).
[44] A. Zheludev, "Reslib," http://www.neutron.ethz.ch/research/resources/reslib (2009).
[45] W. Witt, Z. Naturforschg. **22a**, 92 (1967).
[46] C. L. Armstrong, M. A. Barrett, L. Toppozini, N. Kučerka, Z. Yamani, J. Katsaras, G. Fragneto, and M. C. Rheinstädter, Soft Matter **8**, 4687 (2012).
[47] H. Rapaport, I. Kuzmenko, S. Lafont, K. Kjaer, P. B. Howes, J. Als-Nielsen, M. Lahav, and L. Leiserowitz, Biophys. J. **81**, 2729 (2001).
[48] J. Huang and G. W. Feigenson, Biophys. J. **76**, 2142 (1999).
[49] E. Elizondo, J. Larsen, N. S. Hatzakis, I. Cabrera, T. Børnholm, J. Veciana, D. Stamou, and N. Ventosa, J. Am. Chem. Soc. **134**, 1918 (2012).
[50] Y. Andoh, K. Oono, S. Okazaki, and I. Hatta, J. Chem. Phys. **136**, 155104 (2012).
[51] H. M. McConnell and A. Radhakrishnan, Biochim. Biophys. Acta Biomembr. **1610**, 159 (2003).
[52] J. Dai, M. Alwarawrah, and J. Huang, J. Phys. Chem. B **114**, 840 (2010).

Chapter 7

Conclusions & Outlook

7.1 Conclusions

Using lipid bilayers to model biological membranes has been a field of its own for many years and much progress has been made in the attempt to quantify basic characteristics of model membranes. We have constructed experiments in order to observe fundamental properties of model membranes in an attempt to build a solid foundation on which future experiments using model membranes can rest. Our goals were not only to quantify interactions between the bilayer and incorporated molecules, but to also push the boundaries of these experimental models and measurement techniques. This thesis explores both the structure and dynamics of phospholipid bilayers, how these properties change in the presence of various molecules, and observations from various scattering techniques.

The dynamics of hydration water using high-resolution neutron spectrometry was accomplished by observation of hydration water phase transitions and their coupling to the membrane using a backscattering spectrometer, which showed that water and the membrane phase transitions are largely decoupled. Our two-dimensional mapping of the hydration water of fluid bilayers was achieved with a time-of-flight spectrometer with position-sensitive detectors and revealed that hydration water has an anomalous and anisotropic behaviour compared to bulk water.

The interaction of ethanol and a hydrated lipid bilayer was studied by using a high-resolution X-ray diffractometer and neutron backscattering spectrometer, which revealed the ethanol's affinity to lipid head groups and its role in increasing solvent molecules within the membrane's hydrophobic core. A decrease in the diffusion of the lipids was also observed as a result of ethanol in the bilayer.

Finally, the interaction of lipids and cholesterol in a high-concentration binary mixture was studied using a new technique whereby a neutron beam with a relatively short coherence length was able to uncover the structure of small domains. This experiment elucidated the heterogeneous nature of the liquid-ordered phase and uncovered cholesterol structures in the heterogeneous domains, giving possible insight into complex biological systems.

These outcomes are valuable in the fundamental understanding and characterizing of the sim-

plistic model membrane. Experimental modelling of biological membranes tends to be done in small progressions: first, simple lipid bilayers made of a single lipid species, then perhaps the complexity of the model is increased by adding different types of lipid to the mixture such as unsaturated or charged phospholipids, sterols, sphingolipids, or glycolipids, the last progression being to use extracted biological membranes where the environment is the model component. These are obvious long term goals; however we now make more detailed and directed goals for these experimental paths directly from these publications.

A next step in the investigation of the temperature-dependent transitions of the components of single membranes using FEW scans to discover their degree of coupling, as discussed in Publication I, is to increase the membrane complexity. From this point, by adding cholesterol to the bilayer, one could experiment with concentrations that have been explored using X-ray or neutron diffraction to investigate the lateral structure of the membranes. This structural information could help guide the data analysis and give more insight into the liquid-ordered phase. For instance, "*Structure of Cholesterol in Lipid Rafts*" details the structure of membranes with a cholesterol concentration of 32.5% and may be able to inform the temperature-dependent measurements proposed [4].

The second paper discussed in this thesis, "*Anomalous and Anisotropic Nanoscale Diffusion of Hydration Water Molecules of Fluid Lipid Bilayers*", utilized position-sensitive detectors to characterize the motions of hydration water in a bilayer. By using time-of-flight spectroscopy one could build upon the work presented here by measuring the incoherent quasi-elastic scattering from lipids to characterize the diffusion of lipids in a hydrated, fluid membrane. The KWW function was used to describe the quasi-elastic scattering instead of the conventional Lorentzian functions to characterize the diffusion of hydration water due to the wide variation of environments experienced by the water. An interesting finding would be to observe whether lipid diffusion is seen to be described better by the conventional Brownian (Lorentzian) or sub-diffusive (KWW) regimes.

The same sample preparation as the samples in Publication II could be used and the composition of samples would be changed from H_2O-hydrated DMPC-d54 to D_2O-hydrated DMPC. This composition would highlight incoherent scattering from the lipids in order to characterize the dynamics of the lipid bilayers. This experiment could also be done on Let at ISIS, or a similar instrument IN5 at the Institut Laue-Langevin (ILL). This lipid dynamics investigation would also allow for the comparison between water and lipid dynamics in the same system.

A couple of experiments will be suggested here which could be done following the success of Publication III in characterizing the partitioning and diffusion effects due to incorporating ethanol into the membrane. This same system could be compared to hydrated DMPC bilayers using the same technique described in Publication II, where the diffusion of water, and possibly lipids, can be measured to observe differences brought on by ethanol. The primary purpose of this experiment would be to infer increased permeability of the membranes by observing an increase in diffusion perpendicular to the membranes. Two samples could be measured at Let at ISIS (or IN5 at ILL): (1) DMPC hydrated by D_2O with 2mol% deuterated ethanol, and (2) deuterated DMPC hydrated with H_2O and 2mol% deuterated ethanol. With data from these two experiments, analysis and

observation of the change in hydration water and lipid diffusion in the presence of ethanol may be investigated. In addition, single-wafer samples of samples (1) and (2) can be measured on OFFSPEC at ISIS, this data would be used to determine more precisely partitioning in the center of the membrane which could not be distinguished with X-ray scattering in Publication III.

Another path that could follow Publication III is a set of experiments that would focus on the interaction of the membrane with general anaesthetics like ethanol and ethers, for instance. Specifically, preparing samples for X-ray and neutron reflectometry measurements, commonalities between experiments may arise, giving insight into a mechanisms of general anaesthetics. However, this path will surely be faced with challenges as general anaesthetics are highly volatile compounds. Current opinion on the mechanism of action of anaesthetics is an increase in the lateral pressure of the membrane interior [13], this mechanism can be supported by the increase in electron density in the hydrophobic core in Publication III.

From the work described in "*Structure of Cholesterol in Lipid Rafts*", which assessed the structure of cholesterol in a the liquid-ordered phase, two paths will be suggested to build upon the results of this experiment. First, since the liquid-ordered phase was observed to be inhomogeneous, it is suggested that other concentrations of cholesterol be probed to observe possible inhomogeneity and describe the structures at lower concentrations. Second, incorporation of peptides and proteins is an obvious next step as one of our reasons for probing the 32.5% cholesterol membrane was to investigate raft formation. In biological rafts, proteins are thought to also play a major role and it would therefore be interesting to observe any change of raft structure or arrangement of the proteins, i.e., are rafts more favourable and hence aggregation of proteins is observed or can we observe curvature changes.

Appendix A

Supplementary Information of Publications

A.1 Supplementary Material for "*Structure of Cholesterol in Lipid Rafts*"

Supplementary Material to: The Structure of Cholesterol in Lipid Rafts

Laura Toppozini,[1] Sebastian Meinhardt,[2] Clare L. Armstrong,[1] Zahra Yamani,[3] Norbert Kučerka,[3] Friederike Schmid,[2,*] and Maikel C. Rheinstädter[1,3,†]

[1] *Department of Physics and Astronomy, McMaster University, Hamilton, Ontario, Canada*

[2] *KOMET 331, Institute of Physics, Johannes Gutenberg-Universität Mainz, Mainz, Germany*

[3] *Canadian Neutron Beam Centre, Chalk River, Ontario, Canada*

(Dated: October 24, 2014)

MATERIALS AND METHODS

Coarse-Grained Simulation Model

The model is defined in terms of the length unit $\sigma \approx$0.6 nm and the energy unit $\epsilon \approx 0.36 \cdot 10^{-20}$ J [15]. Phospholipid molecules (P) are represented by simple flexible chains of beads with a hydrophilic head and a hydrophobic tail, which self-assemble in the presence of structureless solvent beads [8]. Cholesterol molecules (C) have the same basic structure, but they are shorter and stiffer except for one flexible end. All lipids are linear chains of six tail beads attached to one head bead, connected by finite extension nonlinear elastic (FENE) springs with the spring constant $k_b = 100\frac{\epsilon}{\sigma^2}$, equilibrium bond lengths $r_0 = 0.7\sigma$ (P lipid) and $r = 0.6\sigma$ (C lipid), and logarithmic cutoffs at $\Delta r_{\max} = 0.2\sigma$ (P) and $\Delta r_{\max} = 0.15\sigma$ (C). We have established in previous work that membranes containing pure P lipids roughly reproduce the behavior of DPPC bilayers [7, 15]. Fully stretched C-lipid chains have a length of 3.6σ, corresponding to $\sim$ 22 Å, which is reasonably close to the estimated length $\sim$ 19 Å of cholesterol molecules [5, 11]. Consecutive bonds in a chain with angle θ are subject to a stiffness potential $\mathrm{UBA}(\theta) = k_\theta(1 - \cos(\theta))$ with stiffness constant $k_\theta = 4.7\epsilon$ (P lipids), $k_\theta = 100\epsilon$ (C lipids, first four angles), and $k_\theta = 4.7\epsilon$(C lipid, last angle). Beads that are not directly bonded with each other interact via a Lennard-Jones potential $U_{LJ}(r/\zeta) = \epsilon_{LJ}\left(\left(\frac{\zeta}{r}\right)^{12} - 2\left(\frac{\zeta}{r}t\right)^{6}\right)$, which is truncated at a cutoff radius r_c and shifted such that it remains continuous. At $r_c = 1$, one recovers the purely repulsive Weeks-Chandler-Anderson potential [13]. The interaction parameters for pairs of P or C beads (head or tail) and solvent beads are taken from [10] and given in Table S1.

* friederike.schmid@uni-mainz.de

† rheinstadter@mcmaster.ca

Bead type-bead type	ϵ/ϵ	ζ/σ	r_c/ζ
Head(any)-head(any)	1.0	1.1	1.0
Head(any)-tail(any)	1.0	1.05	1.0
Head(any)-solvent	1.0	1.1	1.0
Tail(P)-tail(P)	1.0	1.0	2.0
Tail(P)-tail(C)	1.0	1.0	2.0
Tail(C)-tail(C)	0.9	1.0	2.0
Tail(any)-solvent	1.0	1.05	1.0
Solvent-solvent	0	0	0

Supplemental Material, Table S1. Interaction parameters of the coarse-grained molecular dynamics simulations.

Hence, all non-bonded interactions except the tail-tail interactions are repulsive, and the attraction between C tail beads is weaker than that between other tail beads, which effectively leads to an enhanced affinity between C-chains and P-chains. The model was studied by Monte Carlo simulations at constant pressure $P = 2\epsilon/\sigma^3$ and constant zero surface tension in a fluctuating box of variable size and shape [13]. The total number of lipids was kept fixed, but the composition was allowed to fluctuate (semi-grand canonical ensemble). This was implemented by means of configurational bias Monte Carlo moves [4], during which the identity of a lipid was switched between P and C. The use of the semi-grand canonical ensemble was necessary to ensure that the configurations could be equilibrated and that the finite domains were not simply the result of an incomplete phase separation. Even in the semi-grand canonical ensemble, the equilibration times were still of order 1-3 million Monte Carlo sweeps. Simulations were carried out at the John von Neumann Institute for Computing (NIC) Jülich and the Mogon Cluster at Mainz University.

Sample Preparation and Neutron Diffraction Experiment

Deuterated cholesterol (d7) was used to enhance the intensity of the out-of-plane and in-plane neutron Bragg diffraction peaks. Highly oriented, multi-lamellar stacks of 1,2-dipalmitoyl-sn-glycero-3-phosphocholine (DPPC) with 32.5 mol% cholesterol-d7 were prepared on 2″ single-side polished Si wafers of thickness 300 μm. A solution of 16.7 mg/mL DPPC with 32.5 mol% cholesterol in 1:1 chloroform and 2,2,2-trifluoroethanol (TFE) was prepared. The Si wafers were cleaned by alternate 12 minute sonications in ultra pure water and methanol at 313 K. This process was repeated twice. The cleaned wafers were placed on a heated sample preparation surface, which was kept at 50°C. This temperature is well above the main phase transition for DPPC, thus the heated substrates ensured that the lipids were in the fluid phase after deposition. 1.2 mL of the lipid solution was deposited on each Si wafer and allowed to dry. The wafers were kept under vacuum overnight to remove all traces of the solvent. Samples were then hydrated with heavy water, D_2O, and annealed in an incubator at 328 K for 24 hours. Following this protocol, each wafer contained ≈3,000 highly oriented stacked membranes with a total thickness of ≈10 μm. Sixteen such Si wafers were stacked with two 0.3 mm aluminum spacers placed in between each wafer to allow for the membranes to be properly hydrated. The "sandwich" sample was kept in a sealed temperature and humidity controlled aluminum chamber.

Hydration of lipid membranes from water vapor was achieved by independently adjusting the temperature of the heavy water reservoir, the sample and the chamber cover. Temperature sensors were installed close to the sample. A water bath was used to control the temperature of the D_2O reservoir, and the temperatures of the sample and its cover were controlled using Peltier elements.

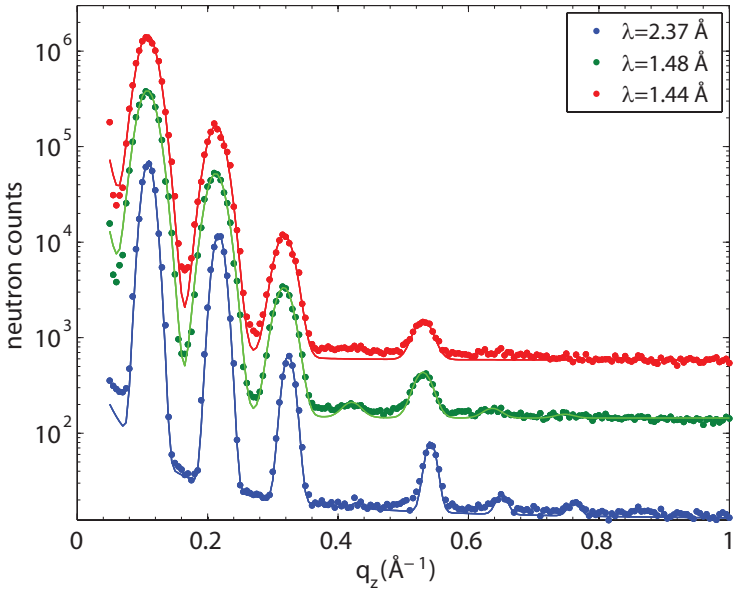

Supplemental Material, Figure S1. Neutron diffraction data for each scattering wavelength used to probe the out-of-plane structure along the membrane normal, q_z. The wavelength 2.37 Å is the wavelength used in conventional neutron scattering setups, while wavelengths 1.48 Å and 1.44 Å were used in for the low energy, low Q resolution setups.

Sample Characterization

The sample was mounted vertically in the neutron beam such that the scattering vector, Q, could either be placed in the plane of the membranes ($q_{||}$), or perpendicular to it (q_z), as shown in Fig. 3 b). The out-of-plane and in-plane structures could be measured by simply rotating the sample by 90°. The lamellar spacing, d_z, i.e., the distance between two neighboring membranes in the stack, was determined from neutron diffraction along the membrane normal, q_z. The corresponding scans are shown in Fig. S1 and show a series of pronounced and equally spaced Bragg peaks indicative of uniform and well developed lamellar membrane stacks. A concentration of 32.5 mol% cholesterol was previously carefully checked by Armstrong *et al.* and confirmed to be in the liquid-ordered state for DPPC membranes [2]. Scans were measured for different neutron wavelengths, λ, and over the duration of the experiment of about 3 weeks. The bilayer spacing stayed within the range of 57.8 Å and 59.2 Å, corresponding to a hydration of the bilayers to better than 99.6% [3]. The main transition temperature, T_m, of DPPC is reported to be $T = 314.4$ K [6, 9].

All measurements reported here were done at $T = 323.2$ K (50°C), well above T_m.

Scattering Cross Sections of the Different Molecular Components

To determine the contribution of lipid and cholesterol molecules to the scattering signals, the corresponding scattering lengths were calculated and are listed in Table S2. Scattering lengths for protonated and deuterated lipid, cholesterol and water molecules are included for completeness. Scattering from lipid molecules dominates the scattering signal in a DPPC-d62/32.5 mol% cholesterol system. Lipid and cholesterol molecules have equal scattering contributions in the liquid-disordered phase at DPPC/66 mol% cholesterol-d7 and both signals were observed in the data in Fig. 3 c). However, cholesterol molecules dominate at higher concentrations of, e.g., DPPC/66 mol% cholesterol-d7 in l_o-type or plaque structures (as seen in Fig. 3 d)).

	Molecule	Chemical Formula	Scattering Length (fm)
	DPPC	$C_{40}H_{80}NO_8P$	27.63
	DPPC-d62	$C_{40}H_{18}D_{62}NO_8P$	673.1
	Cholesterol	$C_{27}H_{46}O$	13.25
	Cholesterol-d7	$C_{27}H_{39}D_7O$	86.12
	Water	H_2O	-1.68
	Heavy Water	D_2O	19.15
DPPC/32.5 mol% Cholesterol-d7	DPPC	$C_{40}H_{80}NO_8P$	18.65
	Cholesterol-d7	$C_{27}H_{39}D_7O$	27.99
DPPC/66 mol% Cholesterol-d7	DPPC	$C_{40}H_{80}NO_8P$	9.11
	Cholesterol-d7	$C_{27}H_{39}D_7O$	56.84

Supplemental Material, Table S2. Scattering lengths of the different membrane components.

Neutron Diffraction Experiment

Experiments were conducted using the N5 triple-axis spectrometer at the Canadian Neutron Beam Centre (Chalk River, ON, Canada). The three axes of the spectrometer refer to the axis of rotation of the monochromator, the sample and the analyzer. The incident and final neutron energies are defined by the Bragg reflections from pyrolytic graphite (PG) crystals. The divergence of the neutron beam was controlled by Soller collimators. A schematic of the instrument's configuration is shown in Fig. 3 b). The instrumental parameters for the two setups used in this experiment are listed in Table S3. Energy and Q-resolution (given as FWHM) were calculated using the ResLib software package by A. Zheludev [16] adapted to the N5 spectrometer.

λ (Å)	E (meV)	ΔE (meV)	ΔQ (Å^{-1})
2.37	14.6	0.757	0.020
1.44	39.5	3.521	0.033
1.48	37.3	3.239	0.032

Supplemental Material, Table S3. Instrumental parameters of the triple-axis spectrometer.

The ΔE and ΔQ of a neutron triple-axis spectrometer are determined by: (1) the incident energy of the neutron beam; (2) the divergence of the neutron beam; and (3) the wavelength resolution of the monochromator and analyzer. Collimation was kept constant during the course of the experiment and set to (c1-c2-c3-c4): 30-18-28-60 (in minutes). Small and large ΔE setups were achieved by varying the incident energy of the incoming neutrons. The longitudinal coherence length of the neutron beam, ξ, is defined by $\xi = \lambda^2/\Delta\lambda$ [12]. For a neutron spectrometer with incident neutron energy E and instrumental energy resolution ΔE, ξ can be estimated to be $\xi \approx 18\sqrt{E}/\Delta E$ [1], where E and ΔE are in meV.

Note that the reason for the typically low monochromaticity of neutron beams is to avoid further compromising the already low-flux "white" neutron beam, a situation that is very different for synchrotron X-rays. Switching between the high and low energy resolution setups was done by changing instrumental settings of the neutron triple-axis spectrometer, which has an effect on ΔQ and ΔE of the beam. A smaller neutron wavelength leads to strongly relaxed ΔQ and ΔE. In addition, the longitudinal coherence length of the neutron beam decreases. The most significant changes between the high and low energy resolution setups are: (1) a more efficient integration over smaller $q_{||}$ ranges to enhance small signals; and (2) a reduction of the coherently added scattering volume.

Details of the Fitting of In-Plane Diffraction Data

λ (Å)	Lorentzian Amplitude (counts)	Lorentzian Width (Å^{-1})	Constant Offset (counts)
2.37	730	0.45	135
1.44	1060	0.29	170
1.48	1000	0.29	175

Supplemental Material, Table S4. Parameters of the background used to fit the in-plane diffraction data. The incoherent scattering contribution was accounted for by a Lorentzian peak shape centered at $q_{||}$=0 Å^{-1}.

The in-plane diffraction data in Figure 3 c) and d) were fit by using a series of Gaussian peak shapes to determine the scattering contributions of lipid and cholesterol molecules. The high total scattering of the sample, due to the large percentage of protonated material, resulted in a large constant, Q-independent background. While small collimation was used, beam size was 2 inches by 2 inches to optimally illuminate the silicon wafers, leading to a significant scattering contribution at small Q-values, close to the direct beam. The background was accounted for by a Lorentzian peak centered at $q_{||}$=0 Å^{-1} including a constant. Details of the background for the different wavelengths

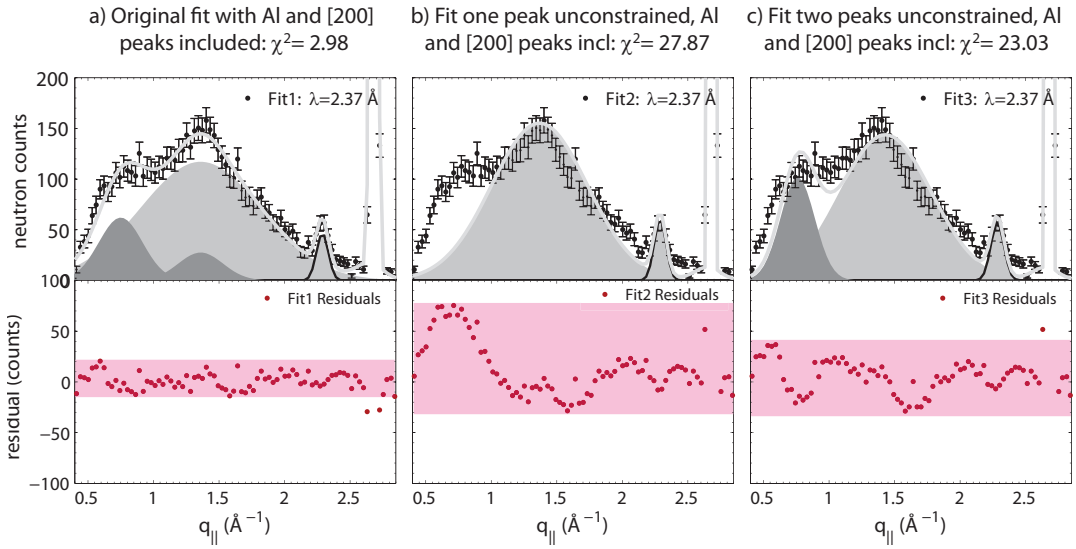

Supplemental Material, Figure S2. Comparison of fitting different models to the in-plane diffraction data (Fig. 3 in the main paper). The fit including Gaussians peak profiles from lipid tails and head groups and cholesterol best describes the data with a significantly better χ^2-value.

used are given in Table S4. In contrast to coherent scattering, incoherent scattering is isotropic, Q-independent and well accounted for by a constant background at larger Q-values of $Q \gtrsim 0.45$ Å^{-1}.

The in-plane diffraction data were tentatively fit with only lipid tail peaks, lipid tail and head group peaks, and lipid tail, head group and cholesterol peaks, as shown in Fig. S2. The corresponding residuals, $\left(y_i^{data} - y_i^{fit}\right)$, are plotted and χ^2-values are given in the figure. Based on the comparison, the model suggested in the main paper including contributions from lipid tails, head groups and cholesterol best describes the experimental data, with a significantly smaller χ^2-value.

The uncertainly in the determination of the position of the cholesterol peak (the C-peak in Fig. 3 c) can tentatively be estimated by fixing the position of the cholesterol peak (C) and shifting it by ± 10% with respect to the C peak position in the original fit. All peak amplitudes were allowed to vary, however, all peak locations were fixed except for the lipid tail (T_1) peak. The result of this procedure is shown in Fig. S3. In order to estimate the quality of the fitted curve, the mean (see Eq. (1) from [14]) and standard deviation of the residuals (Eq. (2) from [14]) were calculated:

$$\bar{y} = \frac{\sum_{i=1}^{n} (y_i^{data} - y_i^{fit})}{n} \quad \text{and} \tag{1}$$

$$\sigma = \sqrt{\frac{\sum_{i=1}^{n} \left((y_i^{data} - y_i^{fit}) - \bar{y}\right)^2}{n-1}}, \tag{2}$$

where $\bar{y}$ is the mean of the deviation of the data from the fit, σ is the standard deviation from the mean, and n is the number of data points used in the calculation. The result is shown in Fig. S3. The residuals and standard

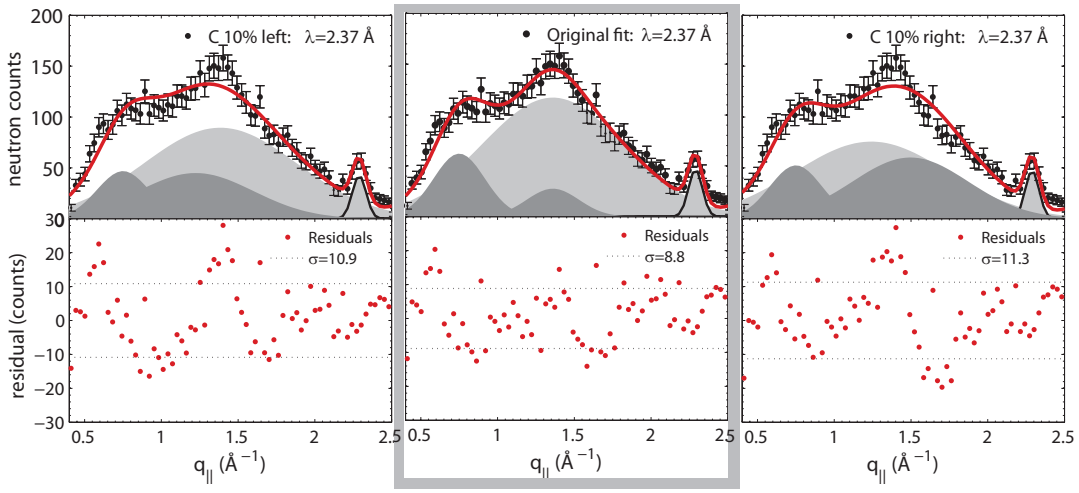

Supplemental Material, Figure S3. The uncertainty in determining the position of the cholesterol peak (C) can tentatively be estimated by shifting and constraining the peak away from its fitted position and evaluating the quality of the observed fit. The residuals ($(y_i^{data} - y_i^{fit}) - \bar{y}$) are plotted below each fit and the corresponding standard deviations, σ, are listed in the legend.

deviation are plotted below the fit. Both the fits where the C peak is fixed to $q_{||}$=1.22 Å (equivalent to a shift of 10% to the left) and where the C peak is fixed to $q_{||}$=1.50 Å (equivalent to a 10% to the right) show a significant increase in the standard deviation. We note that the data range used in these calculations does not include the aluminum peak as its high intensity drowns out the quantitative differences in the aforementioned fits.

The analysis can be summarized as follows: the in-plane diffraction data are best described by peaks related to ordering of lipid tails, lipid head groups and cholesterol molecules. Based on the above analysis the uncertainty in the correlation distance between cholesterol molecules in a cholesterol-lipid-cholesterol complex in the liquid disordered phase was tentatively estimated to be 10%, resulting in 4.6 ± 0.5 Å.

[1] Clare L. Armstrong, Matthew A. Barrett, Laura Toppozini, Norbert Kučerka, Zahra Yamani, John Katsaras, Giovanna Fragneto, and Maikel C. Rheinstädter. Co-existence of gel and fluid domains in single-component phospholipid membranes. *Soft Matter*, 8:4687–4694, 2012.

[2] Clare L. Armstrong, Drew Marquardt, Hannah Dies, Norbert Kučerka, Zahra Yamani, Thad A. Harroun, John Katsaras, An-Chang Shi, and Maikel C. Rheinstädter. The observation of highly ordered domains in membranes with cholesterol. *PLOS ONE*, 8:e66162, 2013.

[3] Nanjun Chu, Norbert Kučerka, Yufeng Liu, Stephanie Tristram-Nagle, and John F. Nagle. Anomalous swelling of lipid bilayer stacks is caused by softening of the bending modulus. *Phys. Rev. E*, 71:041904, 2005.

[4] D. Frenkel and B. Smit. *Understanding molecular simulation: from algorithms to applications*. Academic, 2001.

[5] Leticia Hosta-Rigau, Yan Zhang, M. Teo Boon, Almar Postma, and Brigitte Städler. Cholesterol – a biological compound as a building block in bionanotechnology. *Nanoscale*, 5:89–109, 2013.

[6] J. Katsaras, R. F. Epand, and R. M. Epand. Absence of chiral domains in mixtures of dipalmitoylphosphatidylcholine molecules of opposite chirality. *Phys. Rev. E*, 55:3751–3753, 1997.

[7] O. Lenz and F. Schmid. Structure of symmetric and asymmetric ripple phases in lipid bilayers. *Phys. Rev. Lett.*, 98:058104, 2007.

[8] Olaf Lenz and Friederike Schmid. A simple computer model for liquid lipid bilayers. *Journal of molecular liquids*, 117(1):147–152, 2005.

[9] S. Mabrey and J.M. Sturtevant. Investigation of phase transitions of lipids and lipid mixtures by high sensitivity differential scanning calorimetry. *Proc. Natl. Acad. Sci. USA*, 73:3862–3866, 1976.

[10] Sebastian Meinhardt, Richard L. C. Vink, and Friederike Schmid. Monolayer curvature stabilizes nanoscale raft domains in mixed lipid bilayers. *Proc. Natl. Acad. Sci. U.S.A.*, 110(12):4476–4481, 2013.

[11] W. D. Ness. Biosynthesis of cholesterol and other sterols. *Chemical Reviews*, 111(10):6423–6451, 2011.

[12] H. Rauch. Reality in neutron interference experiments. *Foundation of Physics*, 23:7–36, 1993.

[13] D. Schmid, F. and. Düchs and B. West. A generic model for lipid monolayers, bilayers and membranes. *Comput Phys Commun*, 1177:168–171, 2007.

[14] John R. Taylor. *An Introduction to Error Analysis: The Study of Uncertainties in Physical Measurements.* University Science Books, Sausalito, 1982.

[15] B. West, F. L. H. Brown, and F. Schmid. Membrane-protein interactions in a generic coarse-grained model for lipid bilayers. *Biophys. J.*, 96:101–115, 2009.

[16] Andrey Zheludev. Reslib. `http://www.neutron.ethz.ch/research/resources/reslib`, 2009.

Appendix B

Copyright Information for Publications

B.1 ISRN Publication

Excerpt from http://www.hindawi.com/journals/isrn/2012/520307/ regarding the reproduction of this article:

"Copyright ©2012 Laura Toppozini *et al.* This is an open access article distributed under the Creative Commons Attribution License, which permits unrestricted use, distribution, and reproduction in any medium, provided the original work is properly cited."

B.2 Soft Matter Publications

Excerpt from http://pubs.rsc.org/en/content/requestpermission?msid=c2sm26546j and http://pubs.rsc.org/en/content/requestpermission?msid=c5sm01713k regarding permission request information:

"Authors contributing to RSC publications (journal articles, books or book chapters) do not need to formally request permission to reproduce material contained in this article provided that the correct acknowledgement is given with the reproduced material."

"If you are the author of this article you still need to obtain permission to reproduce the whole article in a third party publication with the exception of reproduction of the whole article in a thesis or dissertation."

B.3 Physical Review Letters Publication

The licence agreement below details between myself and American Physical Society that show and terms of reproduction of "*Structure of Cholesterol in Lipid Rafts*" for use in this thesis.

American Physical Society License Details

Jul 15, 2015

This is an Agreement between Laura Toppozini ("You") and American Physical Society ("Publisher"). It consists of your order details, the terms and conditions provided by American Physical Society, and the payment instructions.

License Number	3664810164461
License date	Jul 02, 2015
Licensed Content Publisher	American Physical Society
Licensed Content Publication	Physical Review Letters
Licensed Content Title	Structure of Cholesterol in Lipid Rafts
Licensed copyright line	© 2014 American Physical Society
Licensed Content Author	Laura Toppozini et al.
Licensed Content Date	Nov 25, 2014
Volume number	113
I would like to...	Thesis/Dissertation
Requestor type	Student
Format	Print, Electronic
Portion	chapter/article
Rights for	Main product
Duration of use	Life of current/future editions
Creation of copies for the disabled	yes
With minor editing privileges	yes
For distribution to	Worldwide
In the following language(s)	Original language of publication
With incidental promotional use	no
The lifetime unit quantity of new product	0 to 499
The requesting person/organization is:	Laura Toppozini / McMaster University
Order reference number	None
Title of your thesis / dissertation	Effects of various molecules on the structure and dynamics of lipid membranes
Expected completion date	Sep 2015
Expected size (number of pages)	120
Total	**0.00 CAD**
Terms and Conditions	

Terms and Conditions

The American Physical Society (APS) is pleased to grant the Requestor of this license a non-exclusive, non-transferable

Bibliography

[1] L. Toppozini, C. L. Armstrong, M. D. Kaye, M. Tyagi, T. Jenkins, and M. Rheinstädter. Hydration water freezing in single supported lipid bilayers. *ISRN Biophysics*, 2012(0):520307, 2012.

[2] L. Toppozini, F. Roosen-Runge, R. I. Bewley, R. M. Dalgliesh, T. Perring, H. Glyde, V. García Sakai, and M. C. Rheinstädter. Anomalous and anisotropic nanoscale diffusion of hydration water molecules in fluid lipid membranes. *Soft Matter*, 2015.

[3] L. Toppozini, C. L. Armstrong, M. A. Barrett, S. Zheng, L. Luo, H. Nanda, V. García Sakai, and M. Rheinstädter. Partitioning of ethanol into lipid membranes and its effect on fluidity and permeability as seen by x-ray and neutron scattering. *Soft Matter*, 8:11839–11849, 2012.

[4] L. Toppozini, S. Meinhardt, C. Armstrong, Z. Yamani, N. Kučerka, F. Schmid, and M. rheinstädter. Structure of cholesterol in lipid rafts. *Physical Review Letters*, 113:228101, 2014.

[5] S.J. Singer and G.L. Nicolson. The fluid mosaic model of the structure of cell membranes. *Science*, 175:720–731, 1972.

[6] G. Nicolson. Transmembrane control of receptors on normal and tumour cells. *BBA*, 457:57–108, 1976.

[7] K. Simons and E. Ikonen. Functional rafts in cell membranes. *Nature*, 387:569–572, 1997.

[8] G. Nicolson. The fluid-mosaic model of membrane structure: still relevant to understanding the structure, function, and dynamics of biological membranes after more than 40 years. *BBA-Biomembranes*, 1838:1451–1466, 2014.

[9] C. L. Armstrong, M. A. Barrett, L. Toppozini, N. Kučerka, Z. Yamani, J. Katsaras, G. Fragneto, and M. C. Rheinstädter. Co-existence of gel and fluid domains in single-component phospholipid membranes. *Soft Matter*, 8:4687–4694, 2012.

[10] C. L. Armstrong, D. Marquardt, H. Dies, N. Kučerka, Z. Yamani, T. A. Harroun, J. Katsaras, A-C Shi, and M. C. Rheinstädter. The observation of highly ordered domains in membranes with cholesterol. *PLOS ONE*, 8:e66162, 2013.

[11] C. L. Wennberg, D. van der Spoel, and J. S. Hub. Large influence of cholesterol on solute partitioning into lipid membranes. *J. Am. Chem. Soc.*, 134:5351–5361, 2012.

[12] G. van Meer, D.R. Voelker, and G.W. Feigenson. Membrane lipids: where they are and how they behave. *Nat Rev Mol Cell Biol*, 9:112–124, 2008.

[13] Ole G Mouritsen. *Life-as a matter of fat: the emerging science of lipidomics*. Springer, 2005.

[14] N. Kučerka, Y. Liu, N. Chu, H. I. Petrache, S. Tristram-Nagle, and J. F. Nagle. Structure of fully hydrated fluid phase DMPC and DLPC lipid bilayers using X-ray scattering from oriented multilamellar arrays and from unilamellar vesicles. *Biophys. J.*, 88:2626–2637, 2005.

[15] N. Kučerka, J. F. Nagle, J. N. Sachs, S. E. Feller, J. Pencer, A. Jackson, and J. Katsaras. Lipid bilayer structure determined by the simultaneous analysis of neutron and X-ray scattering data. *Biophysical Journal*, 95(5):2356 – 2367, 2008.

[16] D. Marsh. *CRC Handbook of Lipid Bilayers*. CRC Press, 1990.

[17] J. F. Nagle and S. Tristram-Nagle. Structure of lipid bilayers. *Biochim. Biophys. Acta*, 1469:159–195, 2000.

[18] J Katsaras and T. Gutberlet. *Lipid Bilayers: Structure and interactions*. Springer, 2001.

[19] A. Tardieu, V. Luzzati, and F.C. Reman. Structure and polymorphism of the hydrocarbon chains of lipids: a study of lecithin-water phases. *Journal of Molecular Biology*, 75:711–718, 1973.

[20] M.J. Janiak, D.M. Small, and G.G. Shipley. Temperature and compositional dependence of the structure of hydrated dimyristoyl lecithin. *The Journal of Biological Chemistry*, 254:6068–6078, 1979.

[21] R. Vist and J. H. Davis. Phase equilibria of cholesterol/dipalmitoylphosphotidylcholine mixtures: ^{2}H NMR and DSC. *Biochemistry*, 29:451, 1990.

[22] J. L. Thewalt and M. Bloom. Phosphatidylcholine: cholesterol phase diagrams. *Biophysical Journal*, 63:1176–118, 1992.

[23] Juyang Huang and Gerald W. Feigenson. A microscopic interaction model of maximum solubility of cholesterol in lipid bilayers. *Biophysical Journal*, 76:2142–2157, 1999.

[24] D. Marsh. Liquid-ordered phases induced by cholesterol: A compendium of binary phase diagrams. *Biochimica et Biophysica Acta- Biomembranes*, 1798(3):688 – 699, 2010.

[25] S. L. Veatch and S.L. Keller. Separation of liquid phases in giant vesicles of ternary mixtures of phospholipids and cholesterol. *Biophys. J.*, 85:3074–3083, 2003.

[26] G. W. Feigenson and J. T. Buboltz. Ternary phase diagram of dipalmitoyl-PC/dilauroyl-PC/cholesterol: Nanoscopic domain formation driven by cholesterol. *BiophysJ*, 80:2775–2788, 2001.

[27] S. L. Veatch, I. V. Polozov, K. Gawrisch, and S. L. Keller. Liquid domains in vesicles investigated by NMR and fluorescence microscopy. *Biophys J*, 86:2910–2922, 2004.

[28] S. Meinhardt, R. L. C. Vink, and F. Schmid. Monolayer curvature stabilizes nanoscale raft domains in mixed lipid bilayers. *Proc. Natl. Acad. Sci. U.S.A.*, 110(12):4476–4481, 2013.

[29] R.A. Demel and B. de Kryuff. The function of sterols in membranes. *BBA - Biomembranes*, 457:109–132, 1976.

[30] P.F.F. Almeida, W.L.C. Vaz, and T.E. Thompson. Lateral diffusion in the liquid phases of dimyristoylphosphatidylcholine/cholesterol lipid bilayers: a free volume analysis. *Biochemistry*, 31:6739–6747, 1992.

[31] M.B. Sankaram and T. Thompson. Cholesterol-induced fluid-phase immicibility in membranes. *Proc Natl Acad Sci U.S.A.*, 88:8686–8690, 1991.

[32] A.M. Smondyrev and M.L. Berkowitz. Structure of dipalmitoylphosphatidylcholine/cholesterol bilayer at low and high cholesterol concentrations: Molecular dynamics simulation. *Biophys. J.*, 77:2075–2089, 1999.

[33] P. Somerharju, J. A. Virtanen, and K. H. Cheng. Lateral organisation of membrane lipids the superlattice view. *BBA*, 1440:32–48, 1999.

[34] P. Somerharju, J. A. Virtanen, K. H. Cheng, and M. Hermansson. The superlattice model of lateral organization of membranes and its implications on membrane lipid homeostasis. *BBA - Biomembranes*, 1788(1):12 – 23, 2009.

[35] J. Huang. Exploration of molecular interactions in cholesterol superlattices: Effect of multibody interactions. *Biophys. J.*, 83:1014–1025, 2002.

[36] L. L. Holte and K. Gawrisch. Determining ethanol distribution in phospholipid multilayers with MAS-NOESY spectra. *Biochemistry*, 36:4669–4674, 1997.

[37] D. T. Nizza and K. Gawrisch. A layer model of ethanol partitioning into lipid membranes. *Gen. Physiol. Biophys.*, 28:140–145, 2009.

[38] M. Patra, E. Salonen, E. Terama, I. Vattulainen, R. Faller, B. W. Lee, J. Holopainen, and M. Karttunen. Under the influence of alcohol: The effect of ethanol and methanol on lipid bilayers. *Biophys. J.*, 90:1121–1135, 2006.

[39] J. Chanda and S. Bandyopadhyay. Perturbation of phospholipid bilayer properties by ethanol at a high concentration. *Langmuir*, 22:3775–3781, 2006.

[40] M. Ruiz. A detailed diagram of the cell. Wikimedia Commons, January 2007. Image Credit.

[41] A. Jan Fijalkowski. Lipid raft organisation scheme. Wikimedia Commons, December 2006. Image credit.

[42] K. Simons and D. Toomre. Lipid rafts and signal transduction. *Nature Reviews Molecular Cell Biology*, 1:31–39, 2000.

[43] K. Simons and M. J. Gerl. Revitalizing membrane rafts: new tools and insights. *Nat Rev Mol Cell Biol*, 11(10):688–699, 2010.

[44] R. Cotterill. *Biophysics. An introduciton.* Wiley, 2002.

[45] T. Bayerl and M. Bloom. Physical properties of single phospholipid bilayers adsorbed to micro glass beads. a new vesicular model system studied by ^{2}H-nuclear magnetic resonance. *Biophy. J.*, 58:357–362, 1990.

[46] D. Chapman and N.J. Salsbury. Physical studies of phospholipids. part 5.proton magnetic resonance studies of molecular motion in some 2,3-diacyl-DL-phosphatidylethanolamines. *Trans. Faraday. Soc.*, 62:2607–2621, 1966.

[47] Z. Veksli, N. Salsbury, and D. Chapman. Physical studies of phospholipids: XII. nuclear magnetic resonance studies of molecular motion in some pure lecithin-water systems. *BBA-Biomembranes*, 183:434–446, 1969.

[48] D. Chapman and J.A. Hayward. New biophysical techniques and their application to the study of membranes. *Biochem. J*, 228:281–295, 1985.

[49] A. Seelig and J. Seelig. Dynamic sturcture of fatty acyl chains in a phospholipid bilayer measured by deuterium magnetic resonance. *Biochem.*, 13:4839–4845, 1974.

[50] B. Bechinger and J. Seelig. Conformation changes of the phosphotidylcholine headgroup due to membrane dehydration. a ^{2}H NMR study. *Chemistry and Physics of Lipids*, 58:1–5, 1991.

[51] J. Seelig and P. Macdonald. Phospholipids and proteins in biological membranes. ^{2}H NMR as a method to study structure, dynamics and interactions. *Accounts of Chemical Research*, 20:221–228, 1987.

[52] H.I. Petrache, S.W. Dodd, and M.F. Brown. Area per lipid and acyl length distributions in fluid phosphatidylcholines determined by ^{2}H NMR spectroscopy. *Biophys. J.*, 79:3172–3192, 2000.

[53] R.M. Epand, K. D'Souza, B. Berno, and M. Schlame. Membrane curvature modulation of protein activity determined by NMR. *BBA-Biomembranes*, 1848:220–228, 2014.

[54] G. Da Costa, L. Mouret, S. Chevance, L. Le Rumeur, and A. Bondon. NMR of molecules interacting with lipids in small unilamellar vesicles. *European Biophysics Journal*, 36:933, 2007.

[55] H.A. Scheidt and D. Huster. The interaction of small molecules with phospholipid membranes studied by ^{1}H NOESY NMR under magic angle spinning. *Acta Pharmacologica Sinica*, 29:35–49, 2008.

[56] A. Léonard and E. Dufourc. Interactions of cholesterol with the membrane lipid matrix. a solid-state NMR approach. *Biochimie*, 73:1295–1302, 1991.

[57] R.R. Vold, R.S. Prosser, and A.J. Deese. Isotropic solutions of phospholipid bicelles: a new membrane mimetic for high-resolution NMR studies of polypeptides. *Journal of Biomolecular NMR*, 9:329–335, 1997.

[58] L.A. Bagatolli. To see or not to see: Lateral organizaiton of biological membranes and fluorescence microscopy. *BBA - Biomembranes*, 1758:1541–1556, 2006.

[59] S. Mabrey and J.M. Sturtevant. Investigation of phase transitions of lipids and lipid mixtures by high sensitivity differential scanning calorimetry. *Proc. Natl. Acad. Sci. USA*, 73:3862–3866, 1976.

[60] I.N. Serdyuk, N. Zaccai, and J. Zaccai. *Methods in molecular biophysics: Structure, dynamics and function*. Cambridge University Press, 2007.

[61] Y. Mély and G. Duportail, editors. *Fluorescent Methods to Study Biological Membranes*. Springer, 2012.

[62] D.M. Owen, M.A.A. Neil, P.M.W. French, and A.I. Magee. Optical techniques for imaging membrane lipid microdomains in living cells. *Seminars in Cell & Developmental Biology*, 18:591–598, 2007.

[63] E. Sezgin and P. Schwille. Fluorescence techniques to study lipid dynamics. *Cold Spring Harbor Perspectives in Biology*, 3:a009803, 2011.

[64] L. Loura, R.F. de Almeida, L.C. Silva, and M. Prieto. FRET analysis of domain formation and properties in complex membrane systems. *BBA-Biomembranes*, 1788:209–224, 2009.

[65] L. Loura and M. Prieto. FRET in membrane biophysics: an overview. *Frontiers in physiology*, 2:1–10, 2011.

[66] J. Korlach, P. Schwille, W. Webb, and G. Feigenson. Characterization of lipid bilayer phases by confocal microscopy and fluorescence correlation spectroscopy. *PNAS*, 96:8461–8466, 1999.

[67] Daniel S. Banks and C'ecile Fradin. Anomalous diffusion of proteins due to molecular crowding. *Biophysical Journal*, 89(5):2960 – 2971, 2005.

[68] L. Toppozini, V. García Sakai, R. Bewley, R. Dalgliesh, T. Perring, and M. Rheinstädter. Diffusion in membranes: Toward a two-dimensional diffusion map. *EPJ Web of Conferences*, 83:02019, 2015.

[69] D. Axelrod, D.E. Koppel, J. Schlessinger, E. Elson, and W. Webb. Mobility measurement by analysis of fluorescence photobleaching recovery kinetics. *Biophys. J.*, 16:1055–1069, 1976.

[70] D.P. Tieleman and H.J.C. Berendsen. A computer perspective of membranes: molecular dynamics studies of lipid bilayer systems. *BBA-Biomembranes*, 1331:235–270, 1997.

[71] S.E. Feller. Molecular dynamics simulations of lipid bilayers. *Current Opinion in Colloid & Interface Science*, 5:217–223, 2000.

[72] J. F. Nagle. Introductory lecture: Basic quantities in model biomembranes. *Faraday Discuss.*, 161:11–29, 2013.

[73] S. Baoukina, S.J. Marrink, and D.P. Tieleman. *Structure and dynamics of lipid monolayers: Theory and applications*, chapter 3, page 25. Humana Press, 2009.

[74] S. Baoukina, S.J. Marrink, and D.P. Tieleman. Lateral pressure profiles in lipid monolayers. *Faraday Discuss.*, 144:393–406, 2010.

[75] S.-J. Marrink and H. J. C. Berendsen. Simulation of water transport through a lipid membrane. *The Journal of Physical Chemistry*, 98(15):4155–4168, 1994.

[76] F.Y. Hansen, G.H. Peters, H. Taub, and A. Miskowiec. Diffusion of water and selected atoms in DMPC lipid bilayer membranes. *The Journal of Chemical Physics*, 137:204910, 2012.

[77] Y. Von Hansen, S. Geckle, and R. R. Netz. Anomalous anisotropic diffusion dynamics of hydration water at lipid membranes. *Phys. Rev. Lett.*, 111:118103, 2013.

[78] E. Terama, O. H. S. Ollila, E. Salonen, A. C. Rowat, C. Trandum, P. Westh, M. Patra, M. Karttunen, and I. Vattulainen. Influence of ethanol on lipid membranes: From lateral pressure profiles to dynamics and partitioning. *J. Phys. Chem. B*, 112:4131–4139, 2008.

[79] A.M. Smondyrev and M.L. Berkowitz. Molecular dynamics simulation of the structure of dimyristoylphosphatidylcholine bilayers with cholesterol, ergosterol, and lanosterol. *Biophys. J.*, 80:1649–1658, 2001.

[80] S.W. Chiu, E. Jakobsson, R.J. Mashl, and H.L. Scott. Cholesterol-induced modifications in lipid bilayers: A simulation study. *Biophys. J.*, 83:1842–1853, 2002.

[81] D. Wüstner and H. Sklenar. Atomistic monte carlo simulation of lipd membranes. *Int. J. Mol. Sci.*, 15:1767–1803, 2014.

[82] M. Bée. *Quasielastic Neutron Scattering: Principles and Applications in Solid State Chemistry, Biology and Materials Science.* Taylor & Francis, 1988.

[83] V.F. Sears. Neutron scattering lengths and cross sections. *Neutron News*, 3:26–37, 1992.

[84] J.H. Hubbell, W.J. Veigele, E.A. Briggs, R.T. Brown, D.T. Cromer, and R.J. Howerton. Atomic form factors, incoherent scattering functions, and photon scattering cross sections. *J. Phys. Chem. Ref. Data*, 4:471–538, 1975.

[85] G.L. Squires. *Introduction to the theory of thermal neutron scattering.* Dover Publications, Inc., Mineola, New York, 1978.

[86] Jens Als-Nielsen and Des McMorrow. *Elements of Modern X-Ray Physics.* John Wiley & Sons, Ltd, New York, 2001.

[87] B.T.M. Willis and C. J. Carlile. *Experimental Neutron Scattering.* Oxford University Press, 2009.

[88] G. Perozziello, R. Catalano, G. Simone, P. Candeloro, N. Malara, S. Santoriello, R. La Rocca, F. De Angelis, A. Accardo, M. Burghammer, E. Di Cola, G. Cuda, C. Riekel, and E. Di Fabrizio. Microfluidic polyimide chips fabricated by lamination processes for X-ray scattering applications, October 2012.

[89] R. Richter, A. Mukhopadhyay, and A. Brisson. Pathways of lipid vesicle deposition on solid surfaces: A combined QCM-D and AFM study. *Biophys. J.*, 85:3035–3047, 2003.

[90] C. L. Armstrong, M. D. Kaye, M. Zamponi, E. Mamontov, M. Tyagi, T. Jenkins, and M. C. Rheinstädter. Diffusion in single solid supported lipid bilayers studied by quasi-elastic neutron scattering. *Soft Matter*, 6:5864–5867, 2010.

[91] D.E. Vance and J.E. Vance, editors. *Biochemistry of lipids, lipoproteins, and membranes.* Elsevier, 1996.

[92] Rigaku Corporation. Powder diffraction optics for SmartLab X-ray diffractometer. *The Rigaku Journal*, 26:29–30, 2010.

[93] S. Kobayashi and K. Inaba. X-ray thin-film measurement techniques VIIi. detectors and series summary. *The Rigaku Journal*, 28:8–13, 2012.

[94] J.R.P. Webster, S. Langridge, R.M. Dalgliesh, and T.R. Charlton. Reflectometry techniques on the second target station at ISIS: Methods and science. *The European Physical Journal Plus*, 126(11):1–5, 2011.

[95] H. Rauch. Reality in neutron interference experiments. *Foundation of Physics*, 23:7–36, 1993.

[96] Andrey Zheludev. Reslib, 2009.

[97] M. C. Rheinstädter and O. G. Mouritsen. Small-scale structures in fluid cholesterol-lipid bilayers. *Curr. Opin. Colloid Interface Sci.*, 18:440–447, 2013.

[98] F. Hippert. *Neutron and X-ray Spectroscopy.* Springer, 2006.

[99] H. Maier-Leibnitz. *Nukleonik*, 8:61–67, 1966.

[100] A. Meyer, R. M. Dimeo, P. M. Gehring, and D. A. Neumann. The high flux backscattering spectrometer at the NIST center for neutron research. *Rev. Sci. Instrum.*, 74:2759–2777, 2003.

[101] R.I. Bewley, J.W. Taylor, and S.M. Bennington. LET, a cold neutron multi-disk chopper spectrometer at ISIS. *Nuclear Instruments and Methods in Physics Research Section A: Accelerators, Spectrometers, Detectors and Associated Equipment*, 637(1):128–134, 2011.

[102] R.I. Bewley, J.W. Taylor, and S.M. Bennington. LET: A low energy multiple chopper spectrometer at ISIS. *Notiziario Neutroni e Luce di Sincrotrone*, 16(1):4–13, 2011.

[103] A. Boothroyd, G. Aeppli, R. Bewley, and S. Bennington. LET: A cold neutron multi-chopper spectrometer.

[104] M. H. Jensen, E.J. Morris, and A.C. Simonsen. Domain shapes, couarsening, and random patterns in ternary memebranes. *Langmuir*, 23:8135–8141, 2007.

[105] F.M. Goñi, A. Alonso, L.A. BAgatoli, R.E. Brown, D. Marsh, and M. Prieto. Phase diagrams of lipid mixtures relevant to the study of membrane rafts. *BBA-Biomembranes*, 1781:665–684, 2008.

[106] C. L. Armstrong, W. Häußler, T. Seydel, J. Katsaras, and M. C. Rheinstädter. Nanosecond lipid dynamics in membranes containing cholesterol. *Soft Matter*, 10:2600–2611, 2014.